Conductance and noise in magnetic tunnel junctions with inorganic and organic barriers

A Thesis submitted in partial fulfillment of the requirements for the degree of Doctor of Philosophy

Juan Pedro Cascales Sandoval

FACULTAD DE CIENCIAS
UNIVERSIDAD AUTÓNOMA DE MADRID

Departamento de Física de la Materia Condensada
Universidad Autónoma de Madrid, Madrid, Spain

Thesis supervisor: **Farkhad Aliev Kazanski**

January 2015

Publications relevant for the thesis

1. **J.P. Cascales**, J-Y. Hong, I. Martínez, M-T Lin, T. Szczepański, V.K. Dugaev, J. Barnaś, and F.G. Aliev, "Superpoissonian shot noise in organic magnetic tunnel junctions", *Appl. Phys. Lett.*, **105**, 233302 (2014)

2. F.G. Aliev, **J.P. Cascales**, H. Ali, M. Chshiev, S. Andrieu, "Band edge noise spectroscopy of a magnetic tunnel junction", *Phys. Rev. Lett.*, **112**, 216801 (2014)

3. **J.P. Cascales**, L. Martin, A. Dulluard, M. Hehn, C. Tiusan, T. Szczepański, V. Dugaev, J. Barnaś, F. G. Aliev, "Shot noise in epitaxial double-barrier magnetic tunnel junctions", *IEEE Transactions on Magnetics*, **49**, 7, (2013)

4. T. Szczepański , V. Dugaev, J. Barnaś, **J.P. Cascales**, F.G. Aliev, "Shot noise in magnetic double-barrier tunnel junctions", *Phys. Rev. B*, **87**, 155406 (2013)

5. **J.P. Cascales**, D. Herranz, J.L. Sambricio, U. Ebels, J.A. Katine, F.G. Aliev. "Magnetization reversal in sub-100nm magnetic tunnel junctions with ultrathin MgO barrier biased along the hard axis", *Appl. Phys. Lett.*, **102**, 092404 (2013)

6. **J.P. Cascales**, D. Herranz, F.G. Aliev, T. Szczepański, V.K. Dugaev, J. Barnaś, A. Duluard, M. Hehn and C. Tiusan. "Controlling shot noise in double-barrier magnetic tunnel junctions", *Phys. Rev. Lett.*, **109**, 066601 (2012)

Other publications

7. **J.P. Cascales**, I. Martínez, D. Díaz, J.A. Rodrigo, and F. G. Aliev, "Transient lateral photovoltaic effect in patterned metal-oxide-semiconductor films", *Appl. Phys. Lett.*, **104**, 231118 (2014)

8. D. Herranz, R. Guerrero, **J.P. Cascales**, F.G. Aliev, M. Hehn and C. Tiusan. "Strong reduction of 1/f noise by carbon doping in epitaxial Fe/MgO(100)/Fe magnetic tunnel junctions with barrier defects", *Acta Physica Polonica A*, **121**, 981 (2012)

A mis padres.

"You can't always get what you want
but if you try sometimes
you just might find
you get what you need"

Mick Jagger and Keith Richards

Agradecimientos

En primer lugar, me gustaría agradecer a mi director de tesis, Farkhad Aliev, todo lo que ha hecho por mí durante estos cuatro años. Desde que me dió su voto de confianza concediéndome una beca FPI hasta la escritura de esta tesis, he aprendido con él lo que significa ser un científico, como conocer y exprimir al máximo un experimento y la importancia del rigor al presentar un resultado. Siempre bromeo que entramos al laboratorio siendo niños y salimos siendo hombres. Ojalá el laboratorio siga funcionando igual de bien con sus consejos.

En segundo lugar, he de mencionar a David Herranz, que fue mi *maestro Jedi* al llegar al laboratorio. David es un ejemplo de trabajo, paciencia y buen humor que debería exigirse a todos los trabajadores de cualquier sitio. Además, está siempre contando chistes. También gracias a Rubén Guerrero, que empezó las medidas de ruido en nuestro laboratorio, y que nos ha dado sugerencias periódicamente.

He tenido mucha suerte con el resto de los compañeros de mi grupo. Ahmad siempre muestra mucho entusiasmo tanto para la física como para hablar de libros, poemas o chistes del hombre azul. Antonio, que se está convirtiendo en un instituto de investigación autocontenido, y que tiene un *particular* sentido del humor. Isidoro (es un gato), que tiene el récord del mundo en aguantar bromas con una sonrisa. Por todos vosotros, venir al laboratorio (casi siempre) ha sido venir a pasar un buen rato.

Nuestros sistemas experimentales serían montañas de chatarra electrificada y humeante si no fuera por varias personas que trabajan desde hace tiempo en el Departamento. Gracias a José Luis, el *gurú* de la electrónica, capaz de arreglar monitores, preamplificadores o guitarras eléctricas. Andrés Buendía, muchas gracias por llevar más de 40 años diciéndole a alumnos de doctorado lo que tienen y lo que no tienen que tocar (además de arreglarnos las bombas, criostatos, etc). Gracias a Santiago por hacernos piezas como nadie, acompañando sus visitas siempre con alguna anécdota. Javi Díaz, gracias por los litros y litros de helio líquido. Macarena, que deja el laboratorio limpio como

para comer encima del criostato. También muchas gracias a Elsa y Luisa, las secretarias del Departamento, porque con ellas hacer papeleos es un poco más fácil. Gracias en general al Departamento de Materia Condensada de la UAM, me he sentido como en casa.

Estoy muy agradecido al profesor Moodera, por haberme acogido dos veranos en su laboratorio del MIT e intentar transmitirme su entusiasmo y visión competitiva de la ciencia. Durante los tres meses en su laboratorio hice un par de cientos de contactos de indio. También extiendo mi agradecimiento a sus alumnos: Peng Wei, Cui-Zu Chang, Bin Li, Ferhat Katmiss y Badih Assaf.

Gracias a toda la gente de Bajas Temperaturas, con quien bromeo diariamente. Nos hemos solucionado problemas de los experimentos, hemos comido juntos casi todos los días, contado chistes, hecho caricaturas y canciones y disfrutado de Madrid. Muchas gracias José Augusto, Edwin, Antón, Roberto, Manu, etc. Tomás y Pablo, sois un ejemplo a seguir por el trabajo, el deporte, el humor y sencillamente porque os sale todo bien.

Gracias también a mis amigos del máster. Ana Moreno y sus divertidos miedos infundados ("¡vamos a catear el máster!, ¡vamos a catear la tesis!). José Luis F. Cuñado que es como un inventor renacentista. Y Diego González, un gentleman británico oriundo de Puertollano.

Muchas gracias a Ana, parte de esta tesis también es suya: me ha criticado las figuras, los textos y ha venido al laboratorio "algún que otro" fin de semana.

A mis hermanos, Bernardo y Miguel Ángel porque siempre tienen algún chiste que hacer sobre los físicos. A mis abuelos, a pesar de que nunca he sabido contestar a la pregunta "y eso que estudias, ¿para qué vale?". A mis tíos y el resto de la familia por las comidas cuando vuelvo a Murcia y las visitas a Madrid. A mis padres, que nos han hecho a sus tres hijos personas respetuosas y responsables. Siempre nos han animado a hacer lo que nos guste y a intentar hacerlo lo mejor posible. Esta tesis es para ellos.

Contents

Resumen 1

1. Introduction 5
- 1.1. Manuscript overview and motivation . . . 5
- 1.2. A formal description of noise . . . 7
  - 1.2.1. Stochastic processes . . . 8
  - 1.2.2. Time series analysis . . . 9
- 1.3. Magnetoresistance . . . 12
  - 1.3.1. Tunnel magnetoresistance . . . 14
- 1.4. Tunneling involving magnetic materials . . . 15
  - 1.4.1. The rectangular potential barrier . . . 16
  - 1.4.2. Jullière's model . . . 18
  - 1.4.3. Coherent magnetic tunneling . . . 20

2. Noise in spintronic systems 23
- 2.1. White noise . . . 24
  - 2.1.1. Thermal noise . . . 24
  - 2.1.2. Shot noise . . . 25
  - 2.1.3. Unified equation for tunnel junctions . . . 27
- 2.2. 1/f noise . . . 30
  - 2.2.1. Thermal magnetic fluctuations . . . 33
  - 2.2.2. Magnetic noise in spintronics . . . 33
- 2.3. Random telegraph noise . . . 34
- 2.4. High frequency noise in spintronics . . . 36
  - 2.4.1. Thermal ferromagnetic resonance (T-FMR) . . . 37

2.4.2. Spin-transfer torque . . . 38
2.4.3. Phase noise . . . 39
2.5. Noise in single barrier magnetic tunnel junctions . . . 40
2.5.1. Shot noise in single barrier magnetic tunnel junctions . . . 40
2.5.1.1. AlO_x barriers . . . 40
2.5.1.2. MgO barriers . . . 42
2.5.2. 1/f noise in single barrier magnetic tunnel junctions . . . 45
2.5.3. Low frequency noise in submicron MTJs . . . 48
2.6. Noise in double-barrier magnetic tunnel junctions . . . 49
2.6.1. TMR and shot noise in double-barrier magnetic tunnel junctions . . . 49
2.6.2. 1/f noise in double-barrier magnetic tunnel junctions . . . 52
2.7. Charge and spin transport in organic materials . . . 53
2.7.1. Organic electronics . . . 53
2.7.2. Electron transport in organic materials . . . 55
2.7.3. Organic spintronics . . . 57
2.7.3.1. Organic spin valves . . . 58
2.7.3.2. Organic magnetic tunnel junctions . . . 60
2.7.3.3. Single-molecule devices and self-assembled monolayers . . . 61

3. Experimental methods 63
3.1. Introduction to the experimental techniques . . . 63
3.2. Modeling the low frequency set-up . . . 64
3.2.1. Cross-correlation . . . 66
3.3. Cryogenic low frequency noise measurements . . . 68
3.3.1. Superconducting shunt and programmable triple current source . . . 70
3.4. Room temperature low frequency noise measurements . . . 72
3.5. Room temperature high frequency noise measurements . . . 73
3.6. Calibration of the high frequency set-up . . . 74
3.6.1. Bias tee, amplifier and spectrum analyzer . . . 74
3.6.2. Picoprobe . . . 76
3.6.3. Calibration of the samples . . . 78

3.6.4. Complete transfer function . . . 78
3.7. Data analysis . . . 80
3.7.1. 1/f noise analysis . . . 80
3.7.2. Shot noise analysis . . . 81
3.7.3. Random telegraph noise analysis . . . 82
3.7.3.1. Using the time series and spectrum. . . . 82
3.7.3.2. Using only the time series. . . . 83

4. Spin-torque effects and noise in MTJs of sizes under 100nm 85
4.1. Introduction and motivation . . . 85
4.1.1. Spin transfer torque effects in nanoscale MTJs . . . 86
4.1.2. Transition from T-FMR to a steady state precession . . . 91
4.2. Sample characteristics . . . 95
4.3. External field along the easy axis of magnetization . . . 99
4.4. External field along the hard axis: current-induced magnetization reversal . . . 105
4.4.1. Micromagnetic simulations . . . 111
4.5. Discussion and conclusions . . . 114

5. Conductance and shot noise in Double-Barrier MTJs 117
5.1. Introduction . . . 117
5.2. Growth method and junction types . . . 119
5.3. Experimental results . . . 125
5.3.1. Control MTJs . . . 125
5.3.2. Shot noise in DMTJs with high barrier asymmetry . . . 126
5.3.3. DMTJs with low barrier asymmetry . . . 127
5.3.4. Tunneling through quantum well states in DMTJs . . . 128
5.4. Theoretical model . . . 132
5.4.1. Calculation of shot noise in the absence of spin relaxation 133
5.4.2. Calculation of shot noise in the presence of spin relaxation 134
5.4.3. Comparison between experiment and theory . . . 135
5.5. Conclusions . . . 138

6. Band edge noise spectroscopy of magnetic tunnel junctions 139
6.1. Introduction and motivation . . . 140
6.2. Growth and characterization of the samples . . . 141
6.3. Experimental results . . . 142
6.3.1. BENS method and phenomenological 1/f model . . . 145
6.4. Numerical calculations . . . 150
6.5. Conclusions . . . 153

7. Direct and sequential tunneling regimes through organic barriers 155
7.1. Introduction . . . 155
7.2. Organic magnetic tunnel junctions in the electron tunneling regime 158
7.2.1. Sample growth . . . 158
7.2.2. Superpoissonian shot noise . . . 161
7.2.3. Model and discussion of the results . . . 164
7.3. Sequential tunneling through thick organic layers . . . 169
7.3.1. Growth and sample characteristics . . . 169
7.3.2. Suppressed shot noise in the variable-range hopping regime 171
7.4. Conclusions . . . 173

8. Transport and noise in topological insulator/ferromagnet tunnel junctions 175
8.1. Introduction and motivation . . . 176
8.2. Growth and sample characteristics . . . 182
8.3. Transport and low frequency noise measurements . . . 184
8.3.1. $Bi_2Te_3/Al_2O_3/Co$ tunnel junctions . . . 185
8.3.2. $Bi_2Se_3/Al_2O_3/Co$ tunnel junctions . . . 190
8.4. Conclusions . . . 193

General conclusions/Conclusiones generales 195

Bibliography 225

Resumen

La motivación principal de esta tesis consiste en investigar los aspectos fundamentales del transporte electrónico en diversos tipos de uniones túnel magnéticas, a través del estudio de la conductancia y las fluctuaciones de voltaje (también conocidas como *ruido*) tanto a temperatura ambiente como a temperaturas criogénicas.

Desde que se inventó la primera unidad de disco duro en 1956, los materiales magnéticos y las películas magnéticas han constituido la base de las tecnologías de almacenamiento de datos. Los primeros trabajos sobre películas delgadas se enfocaron en el estudio de las propiedades de materiales magnéticos, y durante las últimas dos décadas, la investigación se ha centrado en el transporte a través de multicapas (o heteroestructuras). Esta tendencia ha dado origen al campo de la *espintrónica* que, a diferencia de la electrónica convencional, intenta aprovechar tanto la carga como el momento magnético (o *espín*) de los electrones. Los últimos años han revelado una gran variedad de fenómenos de transferencia de espín que son interesantes tanto desde el punto de vista fundamental como tecnológico.

El descubrimiento del acoplamiento magnético entre capas ferromagnéticas (interlayer exchange coupling o *IEC*) y la magnetorresistencia gigante (Premio Nobel de Fert y Grünberg en 2007) allanaron el camino para el estudio del transporte de espines a través de multicapas de materiales ferromagnéticos y no ferromagnéticos (metálicos o aislantes). Este descubrimiento dió paso a la fabricación de las válvulas de espín o las uniones túnel magnéticas, que presentan una resistencia eléctrica que depende del campo magnético que se les aplique, propiedad denominada *magnetorresitencia*. Estos pequeños dispositivos espintrónicos son los responsables del inmenso aumento en la capacidad de

almacenamiento de datos que experimentaron los discos duros magnéticos en torno al año 2000. La sensibilidad de las válvulas de espín a los campo magnéticos ha hecho posible leer bits grabados cada vez más pequeños, y hacerlo cada vez a velocidades más altas.

Aunque indudablemente el éxito más notable de la espintrónica ha sido su aplicación al almacenamiento de datos, se ha comenzado a aplicar en otras áreas. Las uniones túnel magnéticas se utilizan, por ejemplo, como sensores de campo magnético, como emisores de microondas, detectores de campo lejano usando la *espincaloritrónica* o incluso como sensores en el ámbito de la biología. El límite principal para el uso práctico de estos dispositivos es *la relación señal/ruido (signal to noise ratio o SNR)*. En el caso de los sensores de campo magnético, aunque la sustitución de la tecnología actual por válvulas de espín o uniones túnel magnéticas sería sencilla y bastante ventajosa (bajo consumo de energía, tamaño, lectura de datos fácil, etc) su relación señal/ruido es todavía demasiado alta para aplicaciones generales. En el caso de los osciladores espintrónicos, a pesar de su reducido tamaño, el ruido de fase y su baja potencia de salida impide su uso general en dispositivos más complejos.

Debido a estas limitaciones, el estudio de las fuentes de ruido en dispositivos espintrónicos tiene una importancia crucial. Su comprensión es fundamental para su manipulación, con el fin de lograr un mejor rendimiento en los dispositivos.

Estudiaremos las fluctuaciones del voltaje en dos rangos diferentes de frecuencia: *(i)* ruido de baja frecuencia hasta 100 kHz, que puede presentar ruido blanco (incluyendo ruido térmico y de disparo), ruido 1/f y ruido telégrafico y *(ii)* ruido de alta frecuencia hasta 18 GHz, que nos puede dar información sobre la dinámica de la imanación de los componentes ferromagnéticos de las uniones túnel magnéticas. Las uniones túnel estudiadas en esta tesis incluyen diferentes materiales y distintas configuraciones. Tanto los materiales como las configuraciones estudiadas son actualmente el foco de una intensa investigación en el área de la espintrónica. Algunos ejemplos son las uniones túnel magnéticas (con tamaños desde los 100 nanómetros hasta varias micras) con barrera sencilla o doble de MgO, barreras orgánicas cristalinas o uniones túnel con un electrodo de aislante topológico.

El manuscrito está organizado en los siguientes capítulos:

- El **Capítulo 1** incluye una breve introducción sobre la espintrónica, la motivación para realizar las medidas de ruido y los conceptos básicos sobre los dispositivos de túnel magnético.
- El **Capítulo 2** enumera las diferentes contribuciones que influyen en las fluctuaciones de voltaje y presenta un sección bibliográfica sobre los principales temas que se tratan en la Tesis.
- El **Capítulo 3** presenta las diferentes técnicas experimentales utilizadas y se describen los métodos de análisis de datos.
- El **Capítulo 4** trata sobre el estudio del ruido de alta y baja frecuencia en uniones túnel con barrera de MgO, con tamaños inferiores a 100nm, que exhiben efectos de transferencia de espín.
- El **Capítulo 5** muestra cómo el ruido de disparo puede ser controlado por el estado magnético de uniones túnel magnéticas epitaxiales con doble barrera.
- El **Capítulo 6** introduce el concepto de *band edge noise spectroscopy*, donde se observan las energías de los bordes de las bandas electrónicas de los electrodos en una unión túnel magnética.
- El **Capítulo 7** estudia por primera vez el ruido de disparo en uniones túnel magnéticas con barreras orgánicas de PTCDA, donde se observa ruido superpoissoniano.
- El **Capítulo 8** presenta uniones túnel magnéticas con un electrodo inferior de *aislante topológico* Las medidas preliminares de ruido presentan características relacionadas con la estructura de bandas del aislante topológico.

0. Resumen

Chapter 1

Introduction

1.1. Manuscript overview and motivation

The main motivation of this Thesis is to investigate different fundamental aspects of electron transport in diverse types of magnetic tunnel junctions (MTJs) with inorganic and organic barriers at both room and cryogenic temperatures through the study of their electron conductance and voltage fluctuations (referred to as *noise*).
The fluctuations of *dc* biased junctions will be studied in two different ranges of frequencies: *(i) low frequency noise* up to 100 kHz, which can present white noise (including shot and thermal noise), 1/f or random telegraph noise; *(ii) high frequency noise* up to 18 GHz which gives information about the dynamics of the magnetization of the ferromagnetic components of magnetic tunnel junctions. The MTJs studied in this Thesis include different materials or configurations all of which are currently the focus of intense investigation in the area of spintronics, such as magnetic tunnel junctions with single (both micron or nano sized) or double MgO barriers, organic crystalline barriers or junctions with a topological insulator electrode.

The manuscript is organized in the following chapters:

- **Chapter 1** includes a brief introduction of spintronics, the motivation

behind noise measurements in spintronic devices and basic concepts about magnetic tunneling devices.

- **Chapter 2** enumerates the different contributions found in voltage fluctuations and presents a bibliographical section regarding the main topics discussed in the Thesis.
- **Chapter 3** presents the different experimental and data analysis methods used.
- **Chapter 4** studies high and low frequency noise in sub-100nm sized, MgO based MTJs exhibiting spin-transfer torque effects.
- **Chapter 5** demonstrates how the shot noise could be controlled by the magnetic state of epitaxial double-barrier magnetic tunnel junctions.
- **Chapter 6** introduces the concept of *band edge noise spectroscopy* where the energies of the electrode's band edges are observed in noise.
- **Chapter 7** studies for the first time shot noise measurements through organic barriers, in PTCDA based magnetic tunnel junctions, yielding superpoissonian statistics.
- **Chapter 8** presents magnetic tunnel junctions with a *topological insulator* bottom electrode, and preliminary noise measurements which present band related features.

Since the first hard disk drive was invented back in 1956, magnetic materials and magnetic films have been at the heart of data storage technology. The first studies on thin films were focused on the properties of the magnetic materials used, but during the last two decades research has focused on the transport of spin through heterostructures. This has given rise to the field of *spintronics*, which takes advantage of both the spin and charge of electrons. A number of spin transfer processes have been discovered which are interesting from both a fundamental and a technological point of view. In this section we will briefly go over the recent history of spintronics which will serve as context and motivation for the results presented in this thesis.

The discovery of interlayer exchange coupling (IEC) and giant magnetoresistance (Fert & Grunberg's Nobel Prize in 2007) paved the road for the study of spin transport in ferromagnets and non-ferromagnetic (metallic or insulating) layers, i.e. spintronics, yielding devices such as giant magnetoresistive and

spin valves or magnetic tunnel junctions.

These devices are responsible for the immense increase in data storage of magnetic hard disk drives of the early 2000's. The sensitivity of spin valves to a magnetic field has made it possible to read from smaller and smaller recorded bits, and do it at higher data rates.

The most remarkable success of spintronic devices is probably in data storage, however spintronics has started being applied to other areas. For instance, spintronic devices may be used in magnetic field sensing or in microwave devices as oscillators (STNO), and even as biosensors[1,2] or far field meters using spincaloritronics[3]. One the main limits for these applications is the noise figure. In the case of magnetic field sensors, although the substitution of the current technology with GMR or TMR based devices would be straightforward and rather advantageous (low power consumption, size, easy data reading, etc) their signal to noise ratio (SNR) is still insufficiently high for general applications. In the case of spintronic oscillators the phase noise and the low power delivered, despite their reduced size, impedes their general use in more complex devices. Because of these limitations, the understanding (and control when possible) of the noise sources in spintronic devices (besides its manipulation to achieve a better performance) is a crucial aspect that is often overlooked.

1.2. A formal description of noise

Noise is defined as the random fluctuations of a physical quantity. In electronic devices, this quantity is the voltage and/or the current at any port of the device. In general, the random nature of this inherent noise comes from the thermal motion and intrinsic properties of the building blocks of solids, such as the generation and recombination of carriers, the discreteness of the current, the existence of deep traps or the influence of magnetic fluctuations on electron transport. Measuring noise gives information on the properties of the system that are not accessible by other techniques. Besides noise is in general a figure of merit of a device, as it determines the noise floor and thus the SNR of a system.

1.2.1. Stochastic processes

Let us define the fluctuations of a variable $x(t)$ as the expected value of the squared deviation from the mean $\langle \delta x^2 \rangle$, that is, the variance. Fluctuations appear naturally in all physical systems in contact with a thermal bath or where quantum effects (like tunneling) become important. The first of these processes ever studied was the random motion of microscopic particles submerged in a fluid, discovered by Brown and later known as brownian motion[4].

The particles that Brown observed move because of the random collisions of the liquid's molecules with the microscopic particles. This random force presents a variance that is directly proportional to the damping of the liquid. Relations of this kind between the energy dissipated by a system and the fluctuations of a generalized force are known as *fluctuation-dissipation relations*[5]. Thermal noise in a resistor is a manifestation of this theorem, where the voltage is the generalized force and the role of dissipation is played by the electrical resistance and the temperature[6]. Another example of the fluctuation dissipation theorem is the magnetic noise observed in soft ferromagnets, which comes from a frequency independent imaginary permeability at low temperature[7].

Let us consider a random or stochastic variable $X(t)$, characterized by a distribution function $F_X(x)$ which is defined as the probability P of the variable X being equal or smaller than a certain value x:

$$F_X(x) = P(X \leq x)$$

The derivative of the distribution function with respect to x is referred to as the probability density:

$$f_X(x) = \frac{dF_X(x)}{dx}$$

The different statistic moments m_n associated to the random variable may be defined by using the probability density by:

$$m_n = \int_{-\infty}^{+\infty} x^n f_X(x) dx$$

The first moment corresponds to the mean value of our random variable. The central moments μ_n of the variable are given by:

$$\mu_n = \int_{-\infty}^{+\infty} (x - m_1)^n f_X(x) dx$$

Clearly, $(x - m_1)$ corresponds to the fluctuation δx of x with respect to the mean value, so μ_1 corresponds to the average value of δx, which for a random process is zero. The second central moment μ_2 corresponds to the average value of δx^2, i.e. the variance σ^2. The meaning of the first four moments is shown in Figure 1.1.

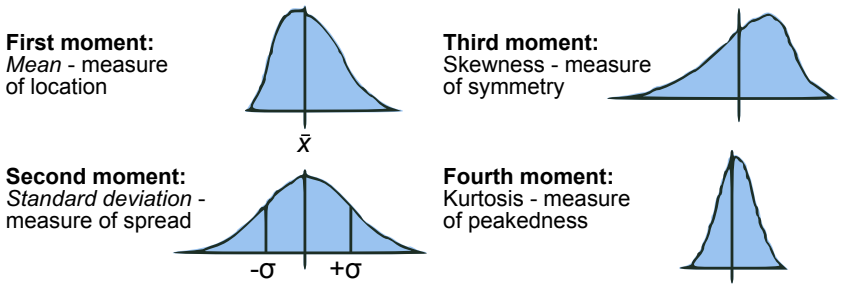

Figure 1.1: Diagram representing the meaning of the first four statistic moments.

If the process under study can be modeled as a sum of N random variables, then independently of the distribution of each variable, the distribution of the sum will approach a gaussian distribution if N is large enough (Central Limit Theorem). Only the first two moments, mean and variance, are non-zero for the gaussian distribution. *Therefore, if we can guarantee that our process has a gaussian probability density, determined by a mean m_1 and a variance μ_2, determining these two quantities experimentally will be enough to characterize the random process.* In the context of electronic transport through spintronic devices, the first and second moments may be obtained by measuring the voltage (mean) and its variance, which we extract from the Fourier transform of the voltage fluctuations (see below).

1.2.2. Time series analysis

The noise of an electronic device may be understood within the framework of the fluctuation-dissipation theorem, if, for example, the voltage is taken as

the generalized force. Then, if we design an experiment which measures the variance of our generalized force, ($\langle \Delta V^2 \rangle$), at thermal equilibrium and at some fixed range of frequency Δf, the **spectral density** *function* S_V *may be defined as the variance of the voltage per unit frequency*:

$$S_V = \frac{\langle \Delta V^2 \rangle}{\Delta f} \tag{1.1}$$

The frequency-dependent spectral density is obtained by differentiating the variance with respect to the frequency:

$$S_V(f) = \frac{d\langle \Delta V^2 \rangle}{df} \tag{1.2}$$

Thus, *the spectral density tells us how a signal or a time series is distributed with frequency.*

Let us now discuss an alternative way of defining the spectral density of a process through the correlation function.

The correlation function is a measure of similarity between two signals $X(t)$, $Y(t)$, when one of them is delayed by a lag τ. The definition slides the $Y(t)$ function along the x-axis, and calculates the integral of their product at each position. When the functions match, the correlation is maximized. It is given by:

$$R_{XY}(\tau) = \lim_{T\to\infty} \frac{1}{2T} \int_{-T}^{T} X(t)Y(t+\tau)dt \tag{1.3}$$

The autocorrelation function of a variable $X(t)$ is defined as the correlation of the signal with itself:

$$R_{XX}(\tau) = \lim_{T\to\infty} \frac{1}{2T} \int_{-T}^{T} X(t)X(t+\tau)dt \tag{1.4}$$

Finally, the Wiener-Khinchin theorem relates the autocorrelation function to the power spectral density via the Fourier transform:

$$S(f) = \int_{-\infty}^{\infty} R_{XX}(\tau) e^{-i2\pi f\tau} d\tau \tag{1.5}$$

$$R_{XX}(\tau) = \int_{-\infty}^{\infty} S(f)(\tau) e^{i2\pi f\tau} df \tag{1.6}$$

From now on we will refer the fluctuations as a spectral density instead of a variance.

With these tools in hand, the problem of studying noise in electronic devices becomes only a matter of constructing an appropriate experimental design. The signals we are mainly interested in measuring have a very small amplitude, and they need to be treated (amplified, filtered, etc) appropriately through some electronic system, say an amplifier. One could think of the amplifier as a "black box" with an input signal $V_{in}(t)$ and an output signal $V_{out}(t)$. Both are related through their power spectral densities $S_V^{in}(f)$, $S_V^{out}(f)$ and the transfer function $H(f)$ of the amplifier through the relation:

$$S_V^{out}(f) = S_V^{in}(f)|H(f)|^2 \tag{1.7}$$

valid only if the setup does not add any noise, which is never the case. How the noise of the amplifiers is modeled, and how we can get rid of it is explained further on, in Chapter 3.

The level of noise inherent to the system is called the noise floor. Therefore, the noise of the signal of interest should be significantly higher than the noise floor. The signal to noise ratio is defined as the ratio between the signal power and the noise floor power. Ideally, the SNR should be as high as possible.

There exist two main techniques of obtaining the spectral density of a signal: by the use of the fast Fourier transform (FFT) or a filtering technique.

The FFT method is used for low frequency experiments, where a resolution from a fraction of Hz up to tens of kHz is needed. In order to obtain the

spectrum, the signal of interest is sampled by $2N$ points during a time T with a resolution in time of Δt. The FFT of this discrete time trace is calculated, giving a spectrum with N data points (or bins) up to a maximum frequency $f_{max} = 1/2\Delta t$ and a frequency step of $\Delta f = 1/T$.

In the filtering technique, the spectral density for a range of frequencies (or span) is obtained by sweeping the central frequency of the filter. Since the band-width is inversely proportional to the time of taking one measurement, having a high resolution in frequency (a small frequency step) would take a very long time. So this technique is used for the detection of high frequency dynamics (in the range of GHz), where having a resolution of kHz is quite sufficient.

Let us suppose we have an AC voltage power detector which is fed our noise signal which has been transmitted through a band-pass filter. The band-pass filter has a central frequency f_0 and a width Δf. If we consider the transfer function of the filter to be 1 for $f_0 - \Delta f/2 < f < f_0 + \Delta f/2$, and 0 otherwise, the spectral density at f_0 may be estimated by the measured AC power divided by the bandwidth of the filter (equation 1.1) yielding units of V^2/Hz:

$$S_V(f_0) \sim \frac{P_{out}^{AC}}{\Delta f}$$

1.3. Magnetoresistance

Magnetoresistance is referred to as the change of the electrical resistance of a material or device when an external magnetic field is applied to it. There exist several magnetoresistance effects, including anisotropic magnetoresistance (AMR), giant magnetoresistance (GMR) and tunneling magnetoresistance (TMR). In this thesis, we will focus on TMR which is the most relevant to our interests.

Anisotropic magnetoresistance (AMR) was discovered by William Thomson in 1857 (Lord Kelvin)[8] in iron and nickel, which presented a dependence on the angle between the electric current and the magnetization direction. The magnetic anisotropy in magnetic conductors is characterized by the resistivity of the material and depends on the angle between the external applied magnetic field and current running through the material. The physical origin of the

AMR effect lies in spin orbit coupling. The electron cloud about each nucleus deforms slightly as the direction of the magnetization rotates, and this deformation changes the amount of scattering undergone by the conduction electrons when traversing the lattice. A simplified picture of the effect is shown in Fig. 1.2

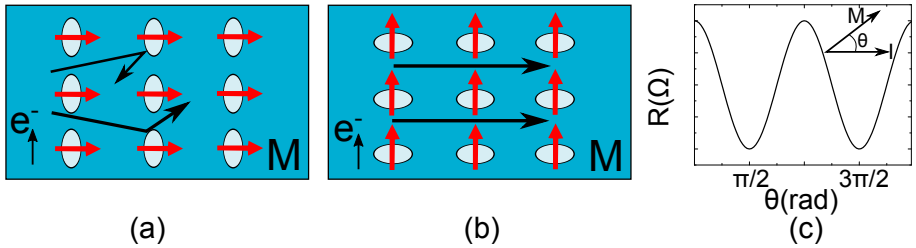

Figure 1.2: AMR effect. The distorted electron clouds of each atom scatter more electrons when the field is applied parallel (a) to the direction of the current, while the scattering is minimal when they are perpendicular (b). (c) Variation of resistance with the angle between current and magnetization.

The discovery of **giant magnetoresistance** (GMR) was done in thin-film structures composed of alternating ferromagnetic (FM) and non-magnetic (NM) conductive layers which show antiferromagnetic coupling[9–11]. This discovery earned Albert Fert and Peter Grünberg the Nobel prize in Physics in 2007.

The simplest multilayer structure is called a *spin valve*, which is composed of two ferromagnetic layers separated by a non-magnetic, metallic spacer, which provide a technologically more robust GMR. The application of GMR by the use of spin valves in 1997 by IBM (Stuart Parkin) changed the landscape of magnetic data storage by dramatically increasing storage capacity. This helped pave the way for some of todaŸs most popular devices, and it was the first application of spintronic devices to everyday technology.

The origin of the GMR effect is the spin dependent scattering of electrons in the magnetic layers which constitute the structure. Fig.1.3 presents the simplest model, referred to as the *two-current model*, where the current running through the device is presented as composed of two parallel currents, one due to spin-up and the other due to spin-down electrons. If the magnetization

directions of the FM layers are parallel (P state), the majority of electrons will have a spin parallel to this direction and they will encounter a minimum scattering (low resistance). If, on the other hand, the magnetization vectors of the layers are aligned in an antiparallel orientation (AP state), the majority of electrons coming from the the first FM layer will scatter with high probability in the second FM layer (high resistance). These two resistance states may be used to read data bits in magnetic hard disk drives.

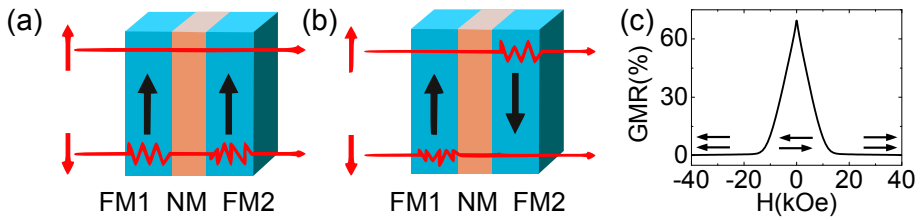

Figure 1.3: GMR effect. (a) Multilayers with alternating magnetization (antiferromagnetic system) present high scattering probabilities. (b) Minimal scattering when the magnetization of the layers are parallel. (c) Dependence of the resistance with the applied field for two exchange coupled ferromagnetic layers [12].

1.3.1. Tunnel magnetoresistance

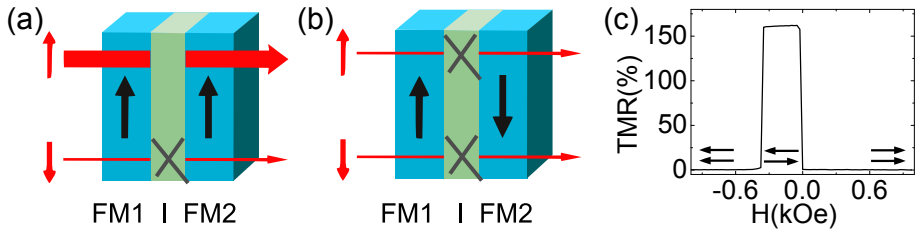

Figure 1.4: Simplified picture of the TMR effect for 100 % polarized ferromagnets. (a) In the P state the spin majority electrons from the top electrode easily find available majority states in the bottom layer to tunnel into. (b) In the AP state the spin majority electrons from the top layer may only tunnel into the scarcely available minority states of the bottom layer. (c) TMR vs external magnetic field.

If the non-magnetic metallic spacer layer of the spin valve is replaced by a sufficiently thin non-magnetic insulating layer, the electrons can tunnel from one ferromagnetic layer to the other. If tunneling conserves the spin, the device is called a *magnetic tunnel junction* or MTJ (see Figure 1.4).

Classically, these structures usually have FM electrodes with different coercive fields $H_c^1 < H_c^2$. If an external magnetic field is applied so $H_{ext} > H_c^1 > H_c^2$, the magnetization of both layers is oriented along the same direction and this is referred to as the P state. In the range $H_c^2 > H_{ext} > H_c^1$ there is an antiparallel alignment of the layers' magnetization, the AP state. The difference of coercive field is realized either by choosing a hard and a soft FM material for each layer or by exchange-coupling one of the layers to an antiferromagnet (exchange biased).

Similarly as to what happens in spin valves, the parallel or antiparallel alignment of the layers' magnetization presents a low or high resistance state. This effect is called the tunneling magnetoresistance (TMR) effect. TMR is usually given as a percentage, corresponding to the difference in resistance between the P and AP states normalized by the P state resistance (referred to as the "opt imistic" TMR):

$$TMR = \frac{R_{AP} - R_P}{R_P} \tag{1.8}$$

The following section will describe the details of tunneling between magnetic materials that are needed tu understand the TMR effect.

1.4. Tunneling involving magnetic materials

The main ingredient needed to understand the TMR effect is spin dependent quantum tunneling. After discussing the phenomenon in general, specific details of tunneling between magnetic materials will be introduced.

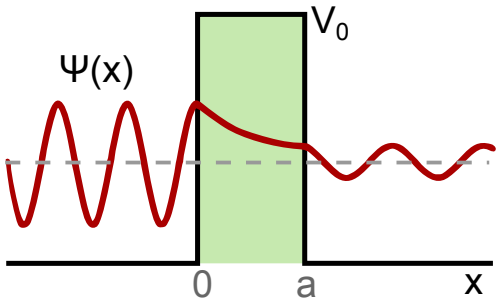

Figure 1.5: Transmitted wave through a rectangular potential barrier, known as quantum tunneling.

1.4.1. The rectangular potential barrier

In classical physics, a particle cannot penetrate into or across a potential barrier if its energy is smaller than the potential of the barrier. In quantum mechanics, a particle may tunnel through a barrier it could not overcome clasically with a probability that decays exponentially with the barrier width (Fig.1.5). This is the well known problem of the rectangular potential barrier of width a and height V_0. Considering an incoming wave from the left, the solutions to the wavefunction in each region are:

$$\begin{aligned} \psi_1(x) =& e^{ik_1 x} + re^{-ik_1 x} && x \leq 0 \\ \psi_2(x) =& Ae^{ik_2 x} + Be^{-ik_2 x} && 0 \leq x \leq a \\ \psi_3(x) =& te^{ik_1 x} && a \leq x \end{aligned}$$

where $\kappa_2 = \sqrt{\frac{2m(E-V_0)}{\hbar^2}}$, r denotes the reflected amplitude and t the transmitted. Applying the continuity conditions on the wavefunction and its derivative at $x = 0$ and $x = a$, one obtains the value of the coefficients. The case which we are interested in is when $0 < E < V_0$, which in the case of weak tunneling ($T \ll 1$) yields a transmission probability:

$$T \propto e^{-2\kappa_2 a} \tag{1.9}$$

One may consider the three dimensional problem where a wave traveling mainly in the Z direction encounters a rectangular potential barrier. The

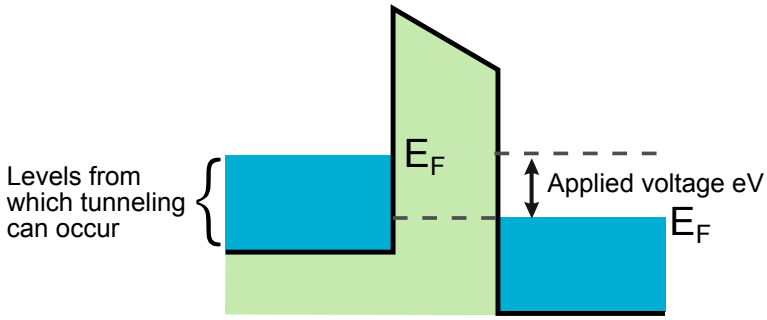

Figure 1.6: Energy diagram for tunneling between two metals separated by vacuum with an applied potential difference V [13].

problem is solved by separation of variables, yielding a plane wave in the X and Y directions and the solution obtained above (let us call it $\Phi(z)$) for the Z direction, i.e.:

$$\Psi\left(x,y,z\right)=\Phi\left(z\right)e^{i(k_x x+k_y y)}$$

In $\Phi(z)$, k is replaced by k_z and, κ and k_z present the following dependence with $\mathbf{k}_{\|}=(k_x,k_y)$:

$$k_z=\sqrt{2m\frac{E}{\hbar^2}-k_{\|}^2}\quad\text{and}\quad\kappa=\sqrt{2m\frac{(V_0-E)}{\hbar^2}-k_{\|}^2}$$

This effect has numerous physical applications: the inversion of the ammonia molecule, the tunnel diode, the Josephson effect, the α-decay of certain nuclei, etc.

Now consider the tunneling occurs between two metals. Observing Fig. 1.6, without a potential difference V and at zero temperature, the tunneling is not possible because the levels on both sides of the barrier are filled. The electric field changes the shape of the barrier, bringing some empty levels in correspondence with the filled ones on the other side of the barrier. Now the tunneling can occur, with the transmission probability calculated above.

The current through a tunnel junction with an applied voltage V may be expressed as:

$$I(V) = \int_{-\infty}^{+\infty} \rho_L(E)\rho_R(E+eV)|M|^2 f(E)(1-f(E+eV))dE \qquad (1.10)$$

where ρ is the density of states of the left (ρ_L) or right (ρ_R) electrode, $|M|^2$ is the transmission probability, $f(E)$ the occupied states of the left electrode and $(1-f(E))$ the unoccupied states of the right electrode.

The Simmons' model[14] gives a very useful and simple approximation to the tunneling current by using a rectangular barrier. The barrier's thickness a and mean energy heigth V_0 of a junction may be obtained by fitting the following equation of the current density to an I-V curve:

$$J(V) = J_0 \left[\left(V_0 - \frac{eV}{2} \right) e^{-A\left(V_0 - \frac{eV}{2}\right)^{\frac{1}{2}}} - \left(V_0 + \frac{eV}{2} \right) e^{-A\left(V_0 + \frac{eV}{2}\right)^{\frac{1}{2}}} \right] \qquad (1.11)$$

where $J_0 = \frac{e}{(2\pi)^2 \hbar a^2}$ and $A = \frac{2a}{\hbar}\sqrt{2m}$.

1.4.2. Jullière's model

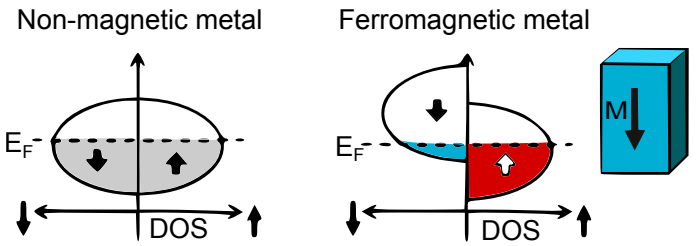

Figure 1.7: Sketch of the exchange split electronic bands of a ferromagnet

The model[15] that Jullière proposed in 1975 (based on the free-electron model) has been extensively used to explain the TMR effect in magnetic tunnel junctions with amorphous barriers. It attributes the difference in resistance

between the magnetic states to the spin polarization of the bands of the ferromagnets and consequently, to spin-dependent electron tunneling. The band structure $E(k)$ of a ferromagnet can be decomposed into two sets of bands, one for majority spin ($\uparrow$ or "spin up"), with spins are parallel to the external magnetic field, and the other for minority spin ($\downarrow$ or "spin down") where the spins are antiparallel. These bands are separated in energy by the magnetic exchange splitting. As can be seen in Fig. 1.7, for a non-magnetic metal, there is the same number of spin up and spin down conduction electrons at the Fermi level. For a ferromagnetic material, due to the magnetic exchange, there is a higher number of conduction electrons with a spin up than a spin down. Then, an electronic extracted from such a material would be partially spin polarized. The **spin polarization** $\mathcal{P}$ of a ferromagnetic material is defined by:

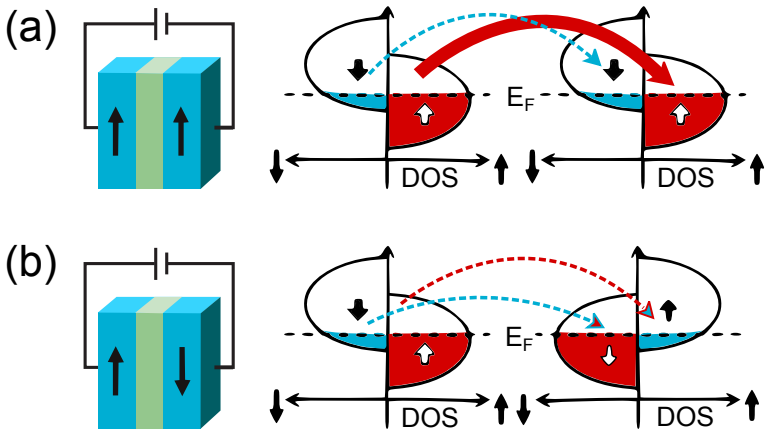

Figure 1.8: Jullière model[15]. The majority electrons easily find available states in the P state (a) while much fewer states are available in the AP state (b).

$$\mathcal{P} = \frac{n_i^{\uparrow} - n_i^{\downarrow}}{n_i^{\uparrow} + n_i^{\downarrow}} \tag{1.12}$$

where $n_{i\sigma}$ is obtained from the spin dependent density of states. A non-magnetic material yields $\mathcal{P} = 0$ while a fully spin-polarized at E_F gives $\mathcal{P} = 1$. If $\mathcal{P}_i$ denotes the polarization of the i^{th} electrode ($i = 1, 2$), then the TMR may expressed as a function of the polarization:

$$TMR = \frac{G_P - G_{AP}}{G_{AP}} = \frac{\left(n_1^{\uparrow}n_2^{\uparrow} + n_1^{\downarrow}n_2^{\downarrow}\right) - \left(n_1^{\uparrow}n_2^{\downarrow} + n_1^{\downarrow}n_2^{\uparrow}\right)}{n_1^{\uparrow}n_2^{\downarrow} + n_1^{\downarrow}n_2^{\uparrow}} = \\ = \frac{2\mathcal{P}_1\mathcal{P}_2}{1 - \mathcal{P}_1\mathcal{P}_2} \tag{1.13}$$

In order for this model to be valid, the tunnel barrier should be thick enough so the wavefunctions experience only a very small overlap. The Jullière model implies that the TMR depends exclusively on the density of states at the Fermi level of the electrodes, and thus is only valid when a small voltage is applied. It also does not take into account the filtering properties of the barrier or the influence of interface states[16].

All these arguments make the Jullière model mainly valid for MTJs with amorphous barriers such as AlO_x, where the various symmetries of the electron wavefunction can couple with evanescent states in AlO_x and have finite tunneling probabilities[17]. The assumption that the tunneling probabilities are equal for all Block states corresponds symmetry independent or **incoherent tunneling**, for which the tunneling electrons do not have a preferred symmetry in momentum space (discussed in detail in the next paragraph).

1.4.3. Coherent magnetic tunneling

Fe, Ni and Co (and some of their alloys) owe their magnetic properties to unfilled $3d$ orbitals, and Bloch states with different symmetries of wave functions exist in these materials. Bloch states with Δ_1 symmetry (*spd* hybridized states) usually have a large positive spin polarization at the Fermi energy. Bloch states with Δ_5 and Δ_2 symmetry (d states) usually have a much smaller (or even negative) spin polarization at E_F.

Coherent tunneling[17] in this context indicates that a state of a given symmetry tunnels into a state of the same symmetry, that is, $\Delta_1 \rightarrow \Delta_1$, etc. If only Δ_1 states (which are highly spin-polarized) were to tunnel coherently through a barrier, a highly spin-polarized tunneling current would be obtained.

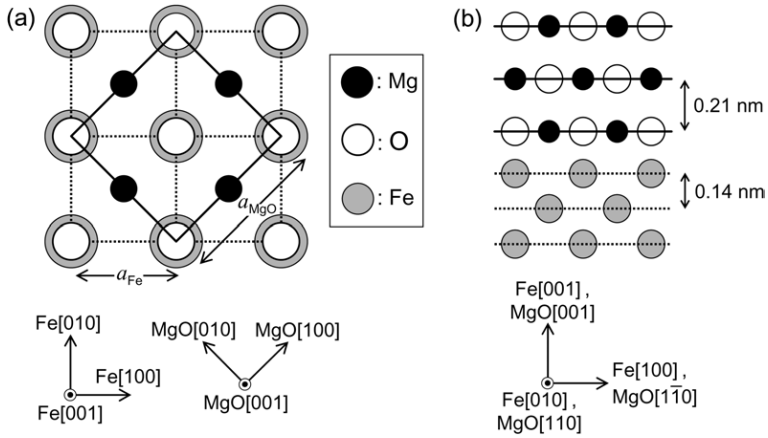

Figure 1.9: Epitaxial growth of Fe on MgO with an almost perfect match. The Fe lattice is rotated by 45° with respect to the MgO lattice[17].

Incidentally, since this spin-polarized state would be forbidden in the AP state, this would result in a high TMR ratio. For this effect to occur, the filtering of the other Bloch states (Δ_2, Δ_5) by the barrier is essential. A schematic view of coherent tunneling is shown in Fig. 1.10.

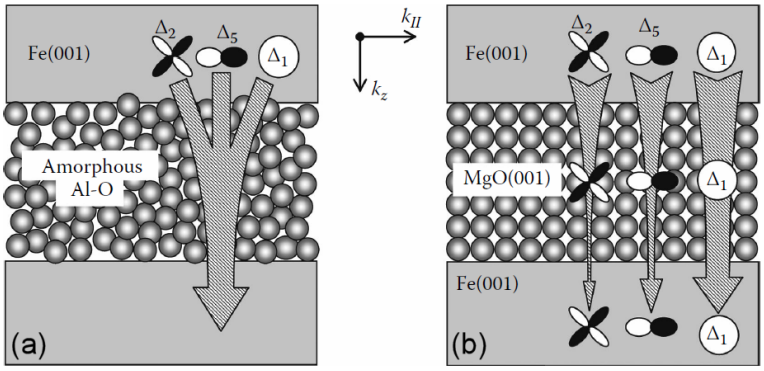

Figure 1.10: Diagram of electron tunneling through (a) amorphous Al-O barrier and (b) crystalline MgO(001) barrier[17].

Crystalline MgO(001) barriers can be epitaxially grown over bcc Fe(001) with a 3% lattice mismatch (see the matching lattices in Fig. 1.9), which is compensated by lattice distortions in the layers and/or by dislocations formed at the

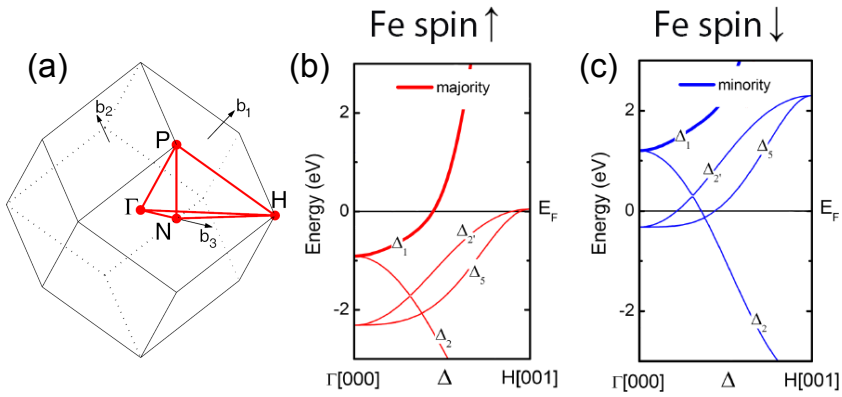

Figure 1.11: (a) Reciprocal space of the bcc Fe lattice, where the Δ direction corresponds to the tunneling direction in real space. Bulk band structure for the (b) majority and (c) minority spin of bcc Fe[17].

interface. Such a high quality interface allows coherent tunneling to take place. Coherent tunneling transport was theoretically predicted for epitaxial Fe(001)/ MgO(001)/ Fe(001) tunnel junctions with crystalline MgO barriers[18,19], and later confirmed experimentally[20,21]. The tunneling probability is highest for $k \parallel = 0$, for which three kinds of tunneling (or evanescent) states exist in the band gap of MgO(001), Δ_1, Δ_2, and Δ_5. These states have specific orbital symmetries, and when the symmetry of the tunneling wave function is conserved, so each Fe Δ_i Bloch state couples with its corresponding MgO Δ_i evanescent state (as illustrated in Fig. 1.10). Due to its symmetry, the MgO Δ_1 evanescent states have the longest decay length, so in the parallel state, the tunneling is dominated by the Fe $\Delta_1 \Leftrightarrow \Delta_1$ MgO $\Leftrightarrow \Delta_1$ Fe electron channel.

The Δ_1 Fe band is fully spin-polarized at the Fermi energy (Fig. 1.11), which makes the conductance in the P state much larger than in the AP state. Therefore, a very large TMR effect is expected, as well as for other FM metals and alloys based on Fe and Co (bcc FeŰCo, bcc CoFeB, and some Heusler alloys)[22].

Chapter 2

Noise in spintronic systems

This chapter describes the main contributions to noise that are observed in spintronic devices, focusing on how noise could be used as a diagnostic tool to obtain information that is inaccessible from *dc* electron transport studies, in magnetic tunnel junctions specifically. In order to understand better the main mechanisms which could contribute to the generation of voltage fluctuations in magnetic tunnel junctions, the physics behind different types of magnetoresistance are briefly mentioned, leading to quantum tunneling through insulating barriers and coherent tunneling through crystalline barriers. Fluctuations up to hundreds of kHz are referred to as"*low frequency noise*" and include thermal, shot, 1/f and random telegraph noise. Noise in the range of GHz is referred to as "*high frequency noise*", and deals with effects such as the thermal ferromagnetic resonance, spin-transfer torque effects or phase noise.

A number of different types of noise may be detected in spintronic devices, and we will now describe the most relevant ones. A schematic representation of the typical features of each contribution to the power spectra is shown in Fig. 2.1.

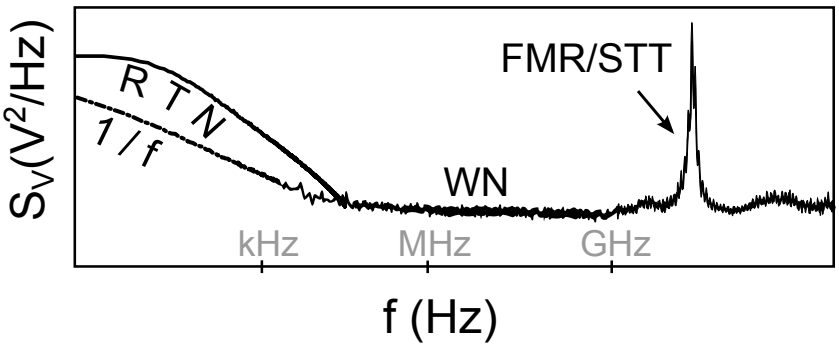

Figure 2.1: Diagram of the main noise contributions in spintronic devices.

2.1. White noise

White noise is a random signal (acoustical, electrical, etc.) with a constant power spectral density. It receives its name from an analogy of white light, which contains light of all visible frequencies. There are two components of white noise in spintronic systems: thermal and shot noise.

2.1.1. Thermal noise

Thermal or Johnson-Nyquist noise was discovered in 1928 by John B. Johnson at Bell Labs[23], who described his results to his co-worker Harry Nyquist who produced a theory explaining the observation[6]. The thermal noise of a conductor depends on its resistance and temperature. It is one of the contributions to "white noise" (independent of frequency), and it is due to the random motion of electrical charge carriers caused by thermal agitation. This noise is the manifestation of the fluctuation-dissipation theorem[5] which relates thermodynamically the dissipation in a dynamic system (resistance), determined through a non-equilibrium property, with the fluctuations in that system. The spectral density S_V of the voltage due to thermal noise is given by:

$$S_V = 4k_B T R \tag{2.1}$$

where k_B is Boltzmann's constant, T is the temperature and R is the electrical resistance of the device under study. Measuring thermal noise can be used to calibrate our experimental setups quite straightforwardly (see Chapter 3).

2.1.2. Shot noise

In statistics, the *Poisson distribution* expresses the probability of a number of events occurring in a fixed intervale of time (or space) if the events occur with a known average rate (or mean), and are independent of the time elapsed since the last event. This distribution was first introduced by Siméon Denis Poisson (1781Ű1840) and its first practical application was carried out by Ladislaus Bortkiewicz in 1898 when he investigated the number of Prussian soldiers accidentally killed by horse kicks. A varied number of processes obey Poisson statistics, from the emission of electrons in a vacuum tube to the photons gathered per pixel in a CCD camera, or the number of molecules found in a small volume at some time.

A discrete random variable X is said to have a Poisson distribution with a mean $\lambda > 0$, if the probability of having k events in a given interval $P(X = k)$ for $k = 0, 1, 2, \ldots$ is given by:

$$f(k;\lambda) = P(X = k) = \frac{\lambda^k e^{-\lambda}}{k!} \tag{2.2}$$

When the average number of events ocurring in the fixed interval of time or space becomes very large, i.e. , $\lambda \to \infty$, the Poisson distribution is equivalent to the Gaussian distribution, as seen in Fig. 2.2.

In electronic devices, shot noise is due to the discreteness of the electrical current. It was first detected by Schottky in 1918 in a vacuum tube, where electrons are emitted by the cathode following a Poisson probability distribution, and received by the anode after a time of flight. In this kind of random process, the mean squared fluctuation of the number of emission events equals the average count of emission events. Thus, the spectral density of the current fluctuations in a vacuum tube is given by Schottky's formula $S = 2eI$, where

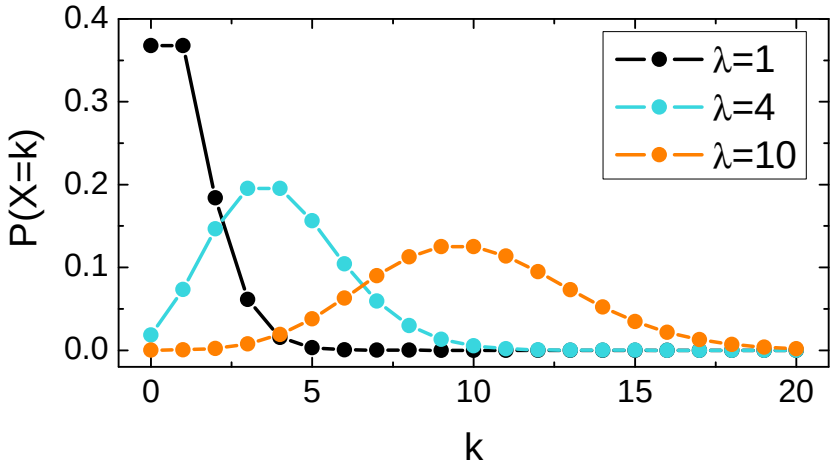

Figure 2.2: Poisson distribution for different values of λ.

e is the charge of the electron and I the average current. The value $2eI$ is referred to as Poissonian of full shot noise. Shot noise presents a frequency independent spectrum (white noise) up to a certain cut-off frequency, typically in the GHz range. This cut-off frequency is related to the time taken for an electron to travel through the conductor[24].

In mesoscopic devices like point contacts or tunnel junctions, the shot noise comes from the fact that the transmission probability T of an electron tunneling from one lead to another is very small ($T << 1$), which yields an expression for the shot noise such as[25]:

$$S_I = \frac{e^3|V|}{\pi\hbar}\sum_n T_n(1-T_n)$$

where V is the bias voltage, T_n is the transmission probability in the n channel and h is PlanckŠs constant. This equation yields the Poissonian value only in the limit of a low transparency system as, for example, a tunnel junction. Variations in the transparency of the system may lead to sub-Poissonian or, even, super-Poissonian shot noise[25].

The equation corresponding to Poissonian voltage shot noise is:

$$S_V = 2eIR_d^2 \tag{2.3}$$

where R_d is the differential resistance of the device. This equation describes white noise only at $T = 0K$, since for $T > 0$ and $V = 0$ the system would exhibit zero fluctuations at zero bias, which violates the fluctuation-dissipation theorem. The problem is solved by adding thermal noise.

Shot noise and thermal noise are often, and incorrectly, viewed as additive and independent noise sources. This independence has been questioned for a long time and it can be shown that both types of noise have the same explanation if the the electrical conductance is treated as a quantum-mechanical transmission phenomenon[26].

The joint expression for voltage white noise[26] (shot and thermal) for a tunnel junction is:

$$S_V = 2eIR_d^2 \coth\left(\frac{eV}{2k_BT}\right) \tag{2.4}$$

We will derive this equation in the following subsection in an intuitive way.

2.1.3. Unified equation for tunnel junctions

A unified expression for the thermal and shot noise can be *informally* (for a more mathematical derivation see Ref.[25]) derived from the same physical model by using several assumptions from various branches of physics and signal analysis[27].

Consider an ideal tunnel junction J with an insulating gap g (vacuum or dielectric) separating two metal contacts A and B. The junction is connected to an ideal voltage source G which applies a constant bias voltage V.

Let us denote $I(t)$ as the current flowing through the circuit, which is kept at a constant temperature T (isothermal). The current is made up of discrete carriers which have an elementary charge q, referred to as electrons from now on.

Considering the electrons as quantum-mechanical particles, there is a finite probability per unit time P_{AB} (P_{BA} respectively) that an electron (instantaneously) tunnels from A to B (B to A respectively). Quantum mechanics gives us the values of P_{AB} and P_{BA} knowing the nature of the junction.

Suppose the detector of our thought experiment allows us to watch individual electrons tunneling through the barrier, because its sampling time τ is small enough. The bandwidth of the measurements would be:

$$\Delta f = \frac{1}{2\tau} \tag{2.5}$$

Then, we can observe three different events:

1. An electron crosses $A \to B$. Then $I(1) = +q/\tau$, occurring with probability $P_{I(1)} = P_{AB}\tau$.

2. No electrons tunnel, so $I(0) = 0$, occurring with probability $P_{I(0)} = 1 - (P_{AB} + P_{BA})\tau$.

3. An electron crosses $B \to A$. Then $I(-1) = -q/\tau$, occurring with probability $P_{I(-1)} = P_{BA}\tau$.

Since these are all the possible outcomes, the average and mean square values of the current are:

$$\langle I \rangle = \sum_{i=-1}^{1} I(i) p_{I(i)} = q(P_{AB} - P_{BA}) \tag{2.6}$$

$$\langle I^2 \rangle = \sum_{i=-1}^{1} I(i)^2 p_{I(i)} = \frac{q^2}{\tau}(P_{AB} + P_{BA}) \tag{2.7}$$

Let us think of the tunneling event as a transition between two states, having the electron in A or B. So n_A, n_B represent the occupation of the states A and B. If the system is in a steady state, n_A and n_B are constant and the following is true:

$$P_{AB} n_A = P_{BA} n_B \tag{2.8}$$

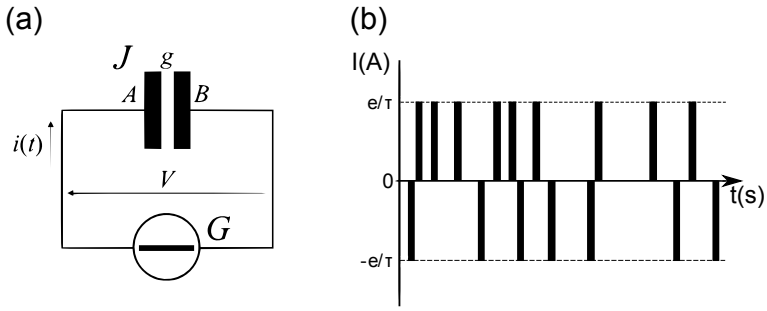

Figure 2.3: (a) The tunnel junction J has contacts A and B separated by a gap g, connected to a source G that supplies a constant voltage V. The current $I(t)$ flows through the junction at temperature T. (b) Three realizations of $\overline{I}$ are observed.

This comes from the *detailed balance* principle[28], which informally states that for kinetic systems which are decomposed into elementary processes, then *"At equilibrium, each elementary process should be equilibrated by its reverse process"*.

The states A and B have energies E_A and E_B, so $E_A - E_B = qV$. Since the occupation numbers satisfy the Boltzmann distribution[29]:

$$\frac{n_A}{n_B} = e^{-\frac{qV}{k_B T}} \tag{2.9}$$

Combining equations 2.8 and 2.9, we arrive at:

$$\frac{P_{BA}}{P_{AB}} = e^{-\frac{qV}{k_B T}}$$

so

$$\langle I \rangle = qP_{AB}(1 - e^{-\frac{qV}{k_B T}})$$
$$\langle I^2 \rangle = \frac{q^2}{\tau} P_{AB}(1 + e^{-\frac{qV}{k_B T}})$$

which combined, along with equation 2.5, yields:

$$\langle I^2 \rangle = 2q\langle I \rangle \frac{1 + e^{-\frac{qV}{k_B T}}}{1 - e^{-\frac{qV}{k_B T}}} \Delta f = 2q\langle I \rangle \coth\left(\frac{qV}{2k_B T}\right) \Delta f$$

Finally, denoting the resistance of the junction by R, the voltage spectral density is:

$$S_V = S_I R^2 = \frac{\langle I^2 \rangle}{\Delta f} = 2q\langle I \rangle R^2 \coth\left(\frac{qV}{2k_B T}\right)$$

If the resistance of the sample presents a non-linear IV, the differential conductance R_d must be used in place of R, as stated by Gupta's theorem[30,31]. The previous equation reduces to the expression for shot noise (Eq. 2.3) or thermal noise (Eq. 2.1), in the limits $T \to 0$ or $V \to 0$.

2.2. 1/f noise

The low-frequency 1/f noise, also referred to as pink noise or flicker noise is a ubiquitous type of noise found in many physical, biological and even economic systems: fluctuations of the sea level, intensity in a music recording, human heart rates or electrical currents in semiconductor devices.

1/f noise was discovered in 1925 by Johnson, in an experiment designed to test Schottky's theory of shot noise in vacuum tubes. After almost a century of research, the origin of 1/f noise in solid state remains unclear and only phenomenological models are used to characterize it.

The noise spectra in spintronic devices (as well as in electronic devices in general or other systems in nature) present a dependence, in some range of frequency, of the form $1/f^{\beta}$, where the exponent β is usually close to 1. This type of noise is referred to as $1/f$ noise, flicker or pink noise. These fluctuations are present in a wide range of different electronic devices, and they are attributed to fluctuations in the conductance. For example, in Si MOSFETs, the resistance of the channel fluctuates due to electron capture into and emission from traps that lie in the oxide layer. In a MOSFET with a large area (above $1\mu m^2$), the 1/f noise appears from a superposition of the effects of a large number of traps with various activation energies and relaxation times[32,33].

A fluctuation which is characterized by a single relaxation time τ is defined by a spectral density which is a Lorentzian function of frequency:

$$S_X(f) = \langle \Delta X^2 \rangle \frac{4\tau}{1+\omega^2\tau^2}$$

Let us now consider that the kinetics of the fluctuating quantity $X(t)$ may be described as a superposition of several relaxation processes with different relaxation times (or even a continuous distribution of relaxation times), schematically represented in Fig. 2.4. Then the spectral density of of such a process is given by averaging the Lorentzian spectral density of a this distribution with a weight function $p_X(\tau)$ which contains the number of subsystems with relaxation time τ and the corresponding variance of fluctuations. The spectral density is then given by:

$$S_X(f) = \int_0^\infty d\tau p_X(\tau) \frac{4\tau}{1+\omega^2\tau^2} \tag{2.10}$$

The spectral density has the form $S_X(f) \propto 1/f$ at some interval of frequency if $p_X(\tau) \propto 1/\tau$. Du Pré[34] and Van der Ziel[35] proposed that the fluctuations are a result of the superposition of activation processes with different relaxation times, with $\tau = \tau_0 e^{-(E/k_B T)}$, where E is the activation energy. Then, if the distribution in activation energies $F_X(E)$ is chosen to be constant, the distribution of relaxation times $p_X(\tau)$ has the required form, since:

$$p_X(\tau)d\tau = F_X(E)dE \Rightarrow p_X(\tau) = F_X(E)/(d\tau/dE) = k_B T F_X(E)/\tau$$

and if $F_X(E) = const.$, $p_X(\tau) \propto 1/\tau$.

The most widely used phenomenological description of 1/f noise is the one proposed by Hooge[36]. This model describes the 1/f noise in terms of the variation of the density of charge carriers, which is proportional to the dimensionless Hooge parameter α. The Hooge parameter allows comparing the $1/f$ noise power in different devices, and is given by:

$$S_V = \frac{\alpha V^2}{\Omega f^\beta} \tag{2.11}$$

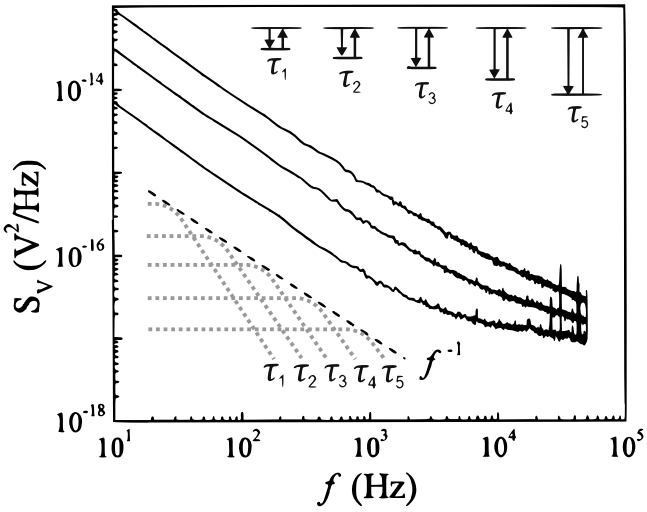

Figure 2.4: Sketch of 1/f noise as a sum of defects with different relaxation times.

where V is the applied DC voltage and Ω the volume or lateral size of the conductive region. In the case of tunnel junctions, the noise power is normalized by the cross-sectional area A of the junction, so the Hooge parameter typically has dimensions of μm^2.

$$S_V = \frac{\alpha V^2}{A f^\beta} \tag{2.12}$$

The exponent β varies between 0.9 and 1.4, and variations from this range are usually due to additional noise contributions, such as random telegraph noise[37] or generation-recombination processes[33].

1/f fluctuations appear in practically all electronic devices and are associated with low frequency fluctuations in resistance. Spintronic devices, like GMR or TMR systems are influenced by defects in their structure which give rise to 1/f type fluctuations. Besides, due to the link between magnetic order and conductivity in spintronic devices, these may exhibit an additional $1/f$ noise source. This term is directly related to the magnetization noise that can be described using the fluctuation-dissipation theorem.

2.2.1. Thermal magnetic fluctuations

As was described in the introduction, there exist a relation between energy dissipated by a system and the fluctuations of a certain generalized force.

In ferromagnetic systems, the energy losses can be described by the complex susceptibility $\chi(\omega) = \chi'(\omega) + i\chi''(\omega)$. This quantity is dependent on frequency and its real and imaginary parts are described as the in-phase and out-phase, respectively, response of the magnetization to a small AC magnetic field. By using this quantity the thermal fluctuations of the magnetization ($S_M(\omega)$) can be expressed[38] as:

$$S_M(\omega) = \Omega \frac{4k_B T}{\omega} \chi''(\omega) \tag{2.13}$$

where Ω is the volume of the ferromagnetic body. The observation of this noise in a ferromagnet was reported at low frequencies in Refs.[38,39]. The obtained power spectrum is consistent with ferromagnetic losses independent of frequency, thus the fluctuations exhibit $1/f$ noise.

2.2.2. Magnetic noise in spintronics

We have already mentioned that in magnetoresistive devices, due to the link between magnetization and resistivity, a magnetic noise from the electrodes can be detected in resistance fluctuations. This relationship was first reported in a multilayer structures which exhibited GMR, in Ref.[40]. In this work, the detected $1/f$ noise is accurately predicted from a fluctuation-dissipation relation using the imaginary (or out-of phase) susceptibility of the system, and it was found that the fluctuations in resistance where proportional to the magnetization noise and the derivative $dR(H)/dH$, see Fig 2.5. It can also be seen in Fig. 2.5 that at H=0 Oe the $1/f$ noise predicted by the fluctuation-dissipation theorem underestimates the resistance noise actually observed. This failure of the fluctuation-dissipation theorem is, in fact, expected as in this field region the main noise contribution is the domain wall dynamics, as long as domain walls are out of thermodynamic equilibrium. This out of equilibrium noise

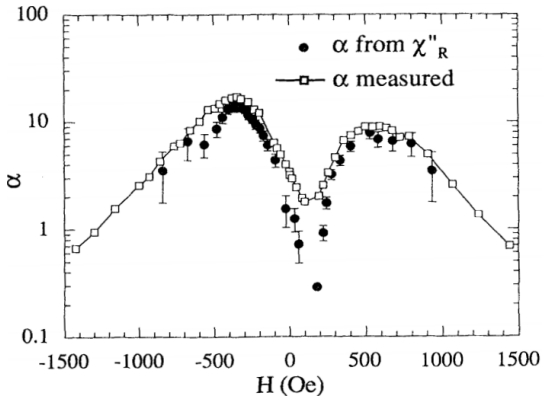

Figure 2.5: Hooge parameter obtained from the resistance noise measurements and the AC susceptibility. Adapted from Ref.[40].

is called Barkhausen noise and has been observed in other spintronic devices as magnetic tunnel junctions in Ref.[41]. Indeed this kind of noise is not $1/f$ noise but rather $1/f^2$ noise, that is consistent with random walk dynamics and avalanches, as is expected in domain wall dynamics which may contribute to noise in the small field range.

The equilibrium noise is exhibited by every spintronic system, e.g. magnetic tunnel junctions, limits the use of GMR or TMR systems in magnetic field sensing and high frequency applications. In general, the design of sensors using crossed anisotropy[42] or easy axis biasing[43] drives the Barkhausen noise negligible. However the presence of this kind of noise and its proportionality to the sensitivity (dR/dH) is a big drawback for using them in general applications.

2.3. Random telegraph noise

Random telegraph noise (RTN) is a type of electronic noise characterized by a time-dependent signal where step-like transitions between two or more discrete voltage (or current) levels take place at random times, as shown in Fig. 2.6(a). RTN can be originated by different mechanisms depending on the structure being studied, like random trapping and releasing of charge carriers at

defect sites in bulk semiconductor crystals or local changes in the magnetization of a FM electrode.

The characteristic times of the levels can be obtained from the histogram of the time trace, or by a theoretical fit of the noise spectrum, shown in Fig. 2.6(b). For a two-level RTN, the spectral density is given by the Lorentzian[44]:

$$S_V^{RTN} = \frac{4\Delta V^2}{(\tau_{up} + \tau_{down})} \frac{T^2}{(1 + (2\pi T f)^2)} \tag{2.14}$$

with $T = (1/\tau_{up} + 1/\tau_{down})^{-1}$, where τ_{up} and τ_{down} are the characteristic dwell times of each level. This equation can be generalized for multilevel RTN.

Analyzing this type of noise may be quite useful for determining different properties, depending on the nature of the fluctuations. If the RTN is due to charge trapping/detrapping, for example in oxide traps in MOSFETS[45], then properties like the trap depth may be extracted from the dependence of $ln(\tau_{up}/\tau_{down})$ with the voltage. An Arrhenius-type dependence is supposed for each characteristic time, and so one obtains:

$$ln(\tau_{up}/\tau_{down}) = K - \frac{q}{k_B T}\left(\frac{x_T}{t}V + \dots\right)$$

where K is a constant, x_T the traph depth, t the oxide thickness and V the applied voltage. Other terms which depend on the temperature may be added to estimate surface potentials, etc.

The resistance fluctuations may also have a magnetic origin, for example, due to the occurrence of magnetization fluctuations in the electrodes of a magnetic tunnel junction. In this case, the fluctuating magnetic moment may be calculated from the dependence of $ln(\tau_{up}/\tau_{down})$ with the applied magnetic field. Again using an Arrhenius law for each characteristic time, one arrives at[44]:

$$ln(\tau_{up}/\tau_{down}) = K + \frac{2\Delta m}{k_B T} H \tag{2.15}$$

where K is a constant, Δm is the fluctuating magnetic moment and H the applied magnetic field.

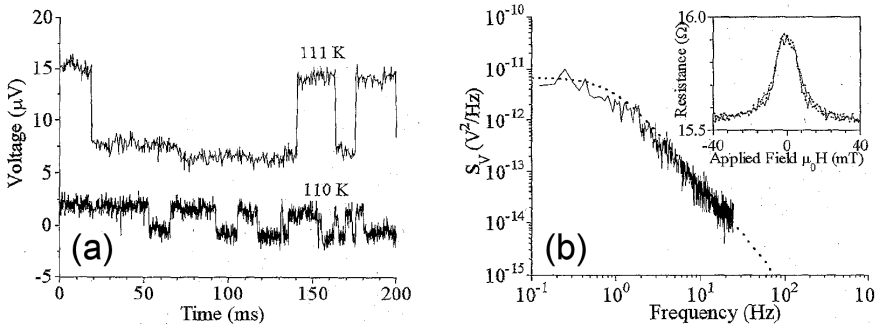

Figure 2.6: Typical RTN (a) time trace with step-like fluctuations and (b) a Lorentzian noise spectrum, fit with equation 2.14 calculated from the up and down lifetimes. Adapted from Ref.[44].

2.4. High frequency noise in spintronics

The introduction chapter deals mainly with low frequency noise, since most MTJs studied in this thesis have a lateral size larger than a micron.

If the lateral size of MTJs is reduced below 1 μm (as the MTJs in Chapter 4) several new effects may be observed. First of all, due to the "inverse magnetoresistance" effect, large currents can be used to change the magnetic state of these small MTJs. Moreover, the influence of the magnetization dynamics on high frequency noise becomes an important factor[46]. Therefore it is worth dedicating a few lines to high frequency noise in spintronic devices. In equilibrium, the magnetization of a ferromagnet aligns with an effective field H_{eff}. The effective field corresponds to the combination of the externally applied magnetic field and the demagnetizing field of the ferromagnetic material under study. When a magnetic configuration is away from equilibrium, the magnetization precesses around the instantaneous local effective field. The Landau-Lifshitz-Gilbert (LLG) equation (equation 2.16) describes the time evolution of the magnetization as due to: the precession around H_{eff} (first term), dissipation (second term) and the influence of spin torque (third term), which opposes the dissipation. The spin torque term in the LLG equation was proposed by Slonzewski in Ref.[47], which describes the torque exerted on the magnetization by a spin-polarized current.

$$\dot{\mathbf{M}} = -\gamma \mathbf{M} \times \mathbf{H_{eff}} + \frac{\alpha}{M_s} \mathbf{M} \times \dot{\mathbf{M}} + \gamma \frac{a_j(\theta)}{M_s} \mathbf{M} \times (\mathbf{M} \times \mathbf{P}) \tag{2.16}$$

where γ is the gyromagnetic ratio, α the Gilbert damping parameter, M_s the saturation magnetization, $\mathbf{P}$ a unit vector in the direction of the current polarization and $a_j(\theta)$ is proportional to the current density J[48]. The different terms are schematically shown in Fig. 2.7.

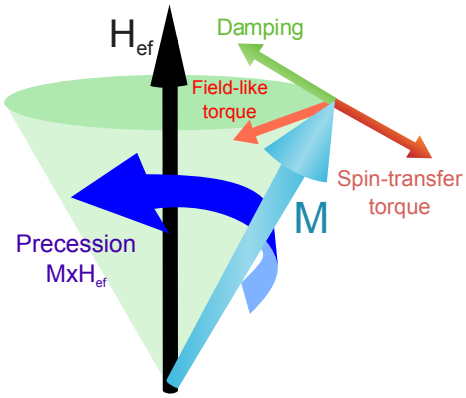

Figure 2.7: Sketch of the different contributions to the LLG equation. Adapted from Ref.[49].

Then, we see that we can alter the magnetization of a ferromagnetic component of a spintronic device of small size either by applying an external field or by running a spin-polarized current through it. With a high enough spin polarized current density, it is even possible to invert the magnetization of the material. So if we carry out noise measurements at high frequency (in the range of several GHz), thermal ferromagnetic resonances and spin torque effects could be observed.

2.4.1. Thermal ferromagnetic resonance (T-FMR)

A ferromagnetic resonance (FMR) is the precession of the magnetic moment of a ferromagnetic material about an externally applied magnetic field[50]. The precession of the magnetization may be excited by applying a transverse rf field.

The microwave energy is strongly absorbed from the source when its frequency is equal to the magnetization's precessional frequency. FMR techniques are extensively used to extract the magnetic properties of materials such as the effective magnetization M_{eff}, the damping coefficient α, the gyromagnetic ratio γ in the metal, etc.

Thermal excitation may cause the spins in a ferromagnetic layer to deviate from equilibrium, and initiate a damped gyromagnetic motion[51]. As a result, a ferromagnetic resonance in the material is excited. It is worth noting that this random thermal field only performs the role of exciting the material's resonating spin waves. If a nanoscale magnetic device, such as a magnetic tunnel junction, is biased by a small dc current (under the value for spin-torque-induced dynamics), the resulting high frequency, voltage noise spectrum presents an FMR peak due to the thermal excitation[52].

Determining the dependence of the thermally excited FMR (T-FMR) with field and bias may give information on such mechanisms as spin-torque driven magnetic switching in nanoscale magnetic tunnel junctions. Also, the noise contribution originating from T-FMR is referred to as mag-noise, and it could present the ultimate limitation on the signal-to-noise ratio in hard drive read heads. This threatens the miniaturization of read heads for ultrahigh area recording density applications.[53]

2.4.2. Spin-transfer torque

As mentioned earlier, a high density, spin-polarized current can exert a torque on the magnetization of a magnetic layer. Typically, the critical current density in magnetic tunnel junctions is around 10^7 A/cm^2 [48], although values as low as 10^6 A/cm^2 have been achieved[54]. This technique could be used as an efficient, fast and reliable way of writing data bits in magnetic random access memories (MRAM)[55]. It would also make the devices simpler (there would be no moving parts), smaller and more energy efficient.

These effects have been extensively studied in magnetic tunnel junctions[48]. A transition from T-FMR to a spin-torque induced steady state, or even a reversal of the magnetization of the free layer may occur for some critical value of current I_c, which can be inferred from the bias dependence of the resonance

frequency, obtained from high-frequency noise measurements[56]. It is typically observed that the frequency and width of the resonance peaks changes little at small currents, but decreases dramatically when $|I| \geq |I_c|$. The decrease is accompanied by a sudden increase in output power, which makes the spin torque effect in MTJs interesting for creating a new generation of microwave oscillators, as seen in Fig. 2.8.

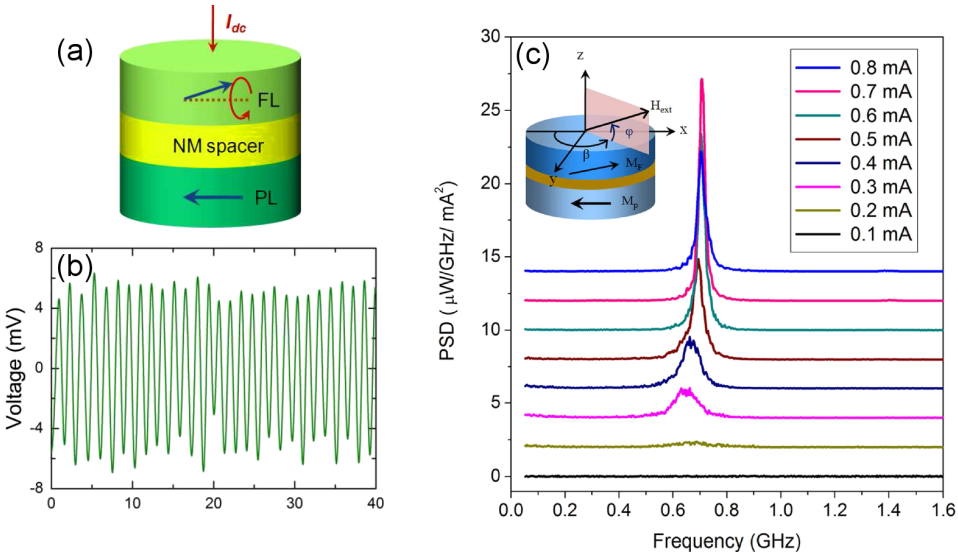

Figure 2.8: MTJs used as high-frequency oscillators (adapted from Ref.[57]). (a) The fixed layer, which acts as a spin polarizer (PL) and excites a steady state precession of the magnetization in the free layer (FL) (b) Voltage oscillations produced by the oscillations of the free layer in the nanopillar sample, in response to the spin transfer torque from a 0.8 mA current. (c) Microwave emission spectra measured in a STNO magnetic tunnel junction.

2.4.3. Phase noise

Phase noise is also another important factor limiting the applications of nanosized devices as microwave oscillators. As we have argued above, a sinusoidal voltage (microwave emission) may be obtained from spin-torque oscillators[57]. In this signal, both the amplitude and the total phase have small

fluctuating contributions. The high-frequency spectrum of the voltage signal presents a peak with some linewidth. The phase fluctuations (which indicate how well the oscillator maintains the oscillations without phase-breaking) and the non-linear coupling between the phase and amplitude both contribute to the linewidth. Both these contributions are of great importance to understand the linewidth broadening and to optimize the quality of the devices. A useful alternative to measuring the spectra of the voltage fluctuations is to obtain the time trace of the oscillations (e.g. using a one shot oscilloscope). With this time trace, the Hilbert transform of the signal can be calculated, separating the contributions of amplitude and phase noise[58]. The fluctuations of each contribution may now be studied using the Fourier transform. The work in Ref.[59] applies this method to characterize the phase and amplitude noise of MgO based magnetic tunnel junctions which are used as high frequency oscillators.

2.5. Noise in single barrier magnetic tunnel junctions

2.5.1. Shot noise in single barrier magnetic tunnel junctions

In this section, we will present a summary of some of the most relevant studies which have been carried out in magnetic tunnel junctions with a single tunnel barrier. We will first deal with Al_2O_3 barriers (historically the first type of barriers used for MTJs) and then move on to the revolutionary implementation MgO barriers.

2.5.1.1. AlO_x barriers

Single barrier MTJs with AlO_x barriers were the first of these devices in which a large tunneling magnetoresistance was observed at room temperature[60–62]. Since AlO_x usually grows amorphously, the electrode/barrier interfaces are far from ideal and have structural defects.

The work of Nowak et al.[63] was one of the earliest studies of SN in magnetoelectronic devices. The authors observe "full" SN ($F = 1$) in $CoFe/Al_2O_3/CoFe$

MTJs in both the parallel (P) and antiparallel (AP) magnetic states.

One of the earliest studies regarding SN was presented by Jiang et al.[64], where the observation of full shot noise($F \approx 1$) in MTJs in the AP state was reported. Later, the same group[65] measured a strong suppression (down to $F \approx 0.45$) of the SN in magnetic tunnel junctions, which was not understood. The junctions with the smallest resistance present a supressed Fano factor (below 0.5 for some MTJs), which along with the reduced resistance and the appearance of random telegraph noise, point to an inhomogeneous current flow and thus a defective barrier. Still, the suppression of shot noise under the Poissonian value was not well understood.

An interesting work regarding sub-Poissonian shot noise was presented in Ref.[66]. Measurements made on low-resistance (less than 100 Ω) MTJs (possibly designed to be used in read heads) showed results which were not consistent with the resistance of the samples examined. The measurements yielded shot noise that was lower than expected, and which pointed to the existence of parallel paths of conduction, pinholes. An electrical model of the sample is proposed where the tunnel junction has an ideal resistance R_T which produces thermal noise when unbiased and shot noise when biased and each pinhole is described as a parallel resistance R_P which exhibits thermal noise only. Through this simple model, the authors are able to account for the decrease of the shot noise as well as the tunneling magnetoresistance, correlating it with the low resistance-area products of the junctions. The model suggests that there exists a relation between the existence (or not) of pinholes and the TMR and shot noise values. Also, shot noise clearly comes up as an outstanding quality test for junction barriers.

Guerrero et al.[67] reported the first detailed study (experiment and model) of shot noise in single barrier magnetic tunnel junctions, which varied with the barrier conditions and the magnetic state. This study contains an investigation of shot noise in $Co(80\mathring{A})/Al_2O_3(14\mathring{A})/Py(100\mathring{A})$ MTJs. The experimental results showed that Cr impurities seem to be localised near one of electrodes. Therefefore, a shot noise reduction down to $F = 0.66$ occurs for non-doped junction, as shown in Fig. 2.9, indicating homogeneously distributed defects (according to theoretical predictions[68]). Also, they found that the Fano factor depended on the magnetic configuration, being enhanced in the AP state. A

model was proposed where sequential tunneling takes place through nonmagnetic and paramagnetic impurity levels in the barrier.

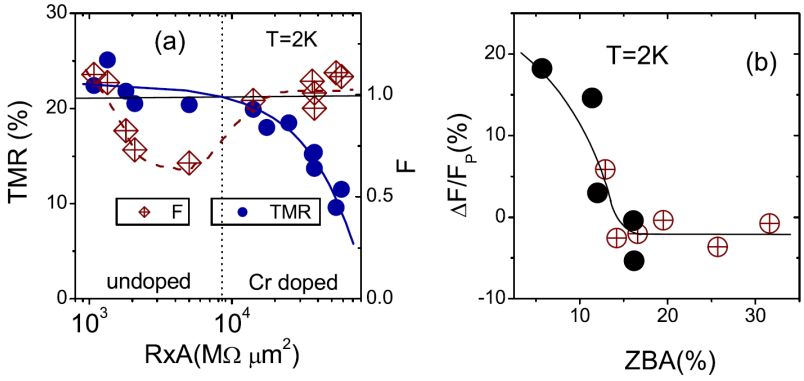

Figure 2.9: (a) Dependence of the TMR and F (for the P state) on the resistance area product (R × A). Solid horizontal line marks $F = 1$. Vertical dashed line separates the Cr-free and Cr-doped regions. (b) Dependence of the relative variation of F with alignment $\Delta F/F_P(\%) = 100(F_{AP} - F_P)/F_P$ on the relative strength of the ZBA. Solid symbols point to the undoped samples. The lines are guides for the eye.

The authors from Ref.[69] report the observation of enhanced spin-dependent shot noise in magnetic tunnel barriers, suggesting transport through localized states within the barrier. The article discusses enhanced shot noise in nonmagnetic tunnel barriers due to two interacting localized states[70] and explains a classical model that can be used to calculate the Fano factor for arbitrary tunnel barriers.

To summarize, amorphous AlO_x present localized states due to impurities, which allows the electrons to tunnel sequentially. This yields a shot noise which is at or below the Poissonian level.

2.5.1.2. *MgO* barriers

The TMR record at room temperature in Al_2O_3[71] was set at 70% (Fig.2.10(a)). A TEM image of the cross-section of a tunnel junction with an AlO_x[72] is shown in 2.10(b), presenting considerable interface roughness. Having the highest

possible, room temperature, TMR is quite desirable for technological purposes. The scientific community was very excited when crystalline MgO barriers were suggested as an effective spin filter[18,19]. Soon after, the ambient TMR record was improved up to 220%[20,21], finally reaching an impressive 604%[73] (Fig. 2.11(a)).

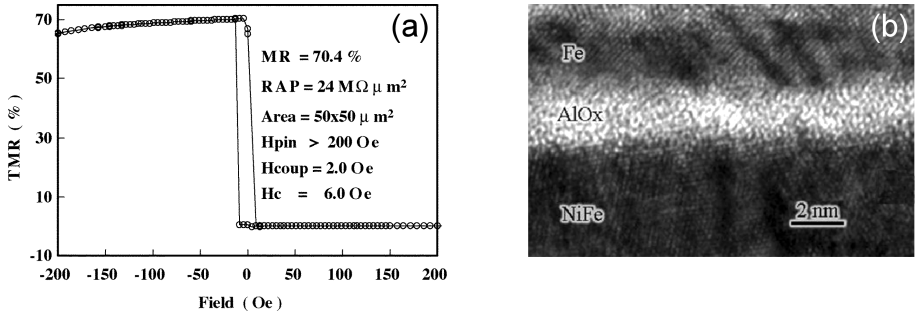

Figure 2.10: (a) TMR record at room temperature for AlO_x barriers (b) TEM image of the cross-section of a Fe/AlO_x/Fe junction. Adapted from Ref.[71].

As can be seen in Fig. 2.11(b), epitaxially grown Fe/MgO/Fe tunnel junctions present a very good interface between the different layers[74]. The first study of shot noise in tunnel junctions with MgO barriers was presented by Guerrero et al.[75]. The junctions showed 185% TMR at room temperature, quite interesting for applications, and 300% at 4 K (see Fig. 2.12). The layer structure of the epitaxial junctions was Fe(100)/FeŰC/MgO(100)/Fe(100). Shot noise as a function of the magnetic state was measured at 10K and up to 1 V, and it presented a Poissonian character (direct tunneling) in both P and AP states. This demonstrated that a pure spin-dependent direct tunneling mechanism was governing the transport, giving the final evidence of the high structural quality of MgO barriers.

Full shot noise in $CoFeB/MgO/CoFeB$ tunnel junctions, with 1.5nm thick barriers was also corroborated down to very low bias ($\pm 5mV$)[76]. Shot noise in the Schottky limit was obtained for both magnetic states (P and AP states), a sign of the absence of electron correlations in the low bias regime. The authors present an interesting work, since they are able to fit the equation of white noise (thermal plus shot noise) to the data at several low temperatures (between 3

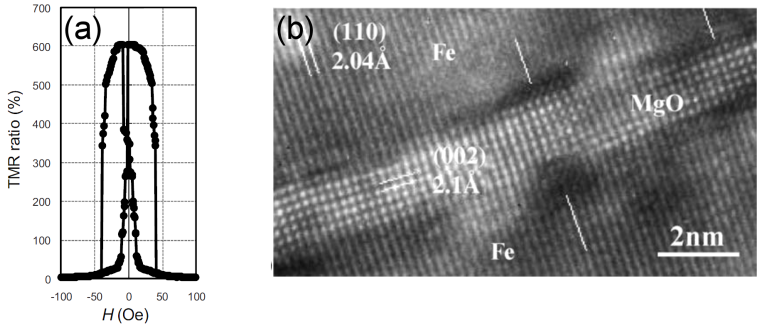

Figure 2.11: (a) TMR record at room temperature for MgO barriers. (b) TEM image of the cross-section of a Fe/MgO/Fe junction. Adapted from Ref.[73].

and 20 K).

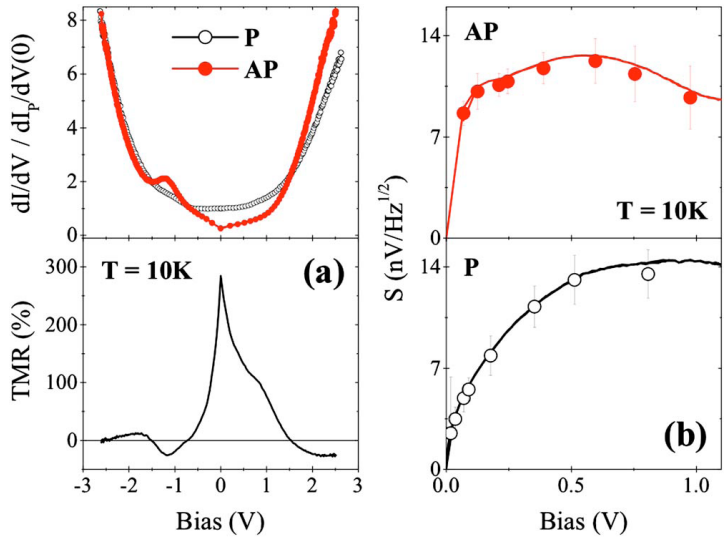

Figure 2.12: (a) Dynamic conductivities at 10 K (top panel) and the related TMR (V) (bottom panel). (b) Shot noise measurements in P and AP states measured at 10 K in bias when the electrons are injected from the top toward the bottom MTJ electrode (negative voltage)[75].

Contrary to what happens in amorphous in Al_2O_3 barriers, crystalline MgO-based MTJs present interfaces which are presumed to be almost free from

defects, giving rise to localized states. The authors from the previous work fabricated junctions with a much thinner barrier (1.05 nm), with high TMR ratios (over 200% at 3K) and an almost Poissonian shot noise[77], as can be seen in Fig. 2.13. The Fano factor in the antiparallel state is found to be quite close to 1, but the parallel state presents $F = 0.91 \pm 0.01$. These values are found not to depend on either temperature or magnetic field. Since the junctions present a hight TMR ratio and $F = 1$ in the AP state, then the barrier does not seem to have interfacial defects, even though it is quite thin. The authors argue that the sub-Poissonian statistics detected in the P configuration are due to a coherent transport of a Δ_1 state in the low bias regime, since this state is filtered out in the AP configuration.

A theoretical first-principles work describing this slight supression of the Fano factor for very thin barriers was presented in Ref.[78], which reproduces the experimental results from the work discussed above[77]. The authors compute the shot noise in ballistic and Fe/MgO/Fe tunnel junctions with different barrier thicknesses, and account for the decrease in shot noise by adding disorder at the Fe/MgO interface. The addition of oxygen vacancies as interface defects is the most favourable energetically. Their inclusion in the calculation of a tunnel junction with a barrier thickness of 5 atomic layers (1.05 nm, as in[77]) brings the calculated TMR ratio from 3580% (concordant with theoretical predictions) to around 250%, which agrees quite well with experimental results. The calculations for this barrier thickness yield a suppression of the Fano factor which depends on the magnetic state, $F_P = 0.87$ and $F_{AP} = 0.98$ which is quite close to the experimental values $F_P = 0.91$ and $F_{AP} = 0.98$. The authors[78] also predict an onset of resonant tunneling in the antiparallel configuration at some threshold bias.

2.5.2. 1/f noise in single barrier magnetic tunnel junctions

The first studies of the dependence of $1/f$ with the applied magnetic field in magnetic tunnel junctions were carried out in systems with AlO_x barriers[63,79–81]. $1/f$ noise experiences a very strong magnetic contribution at the transition between the P and AP states, due to fluctuations arising from the re-

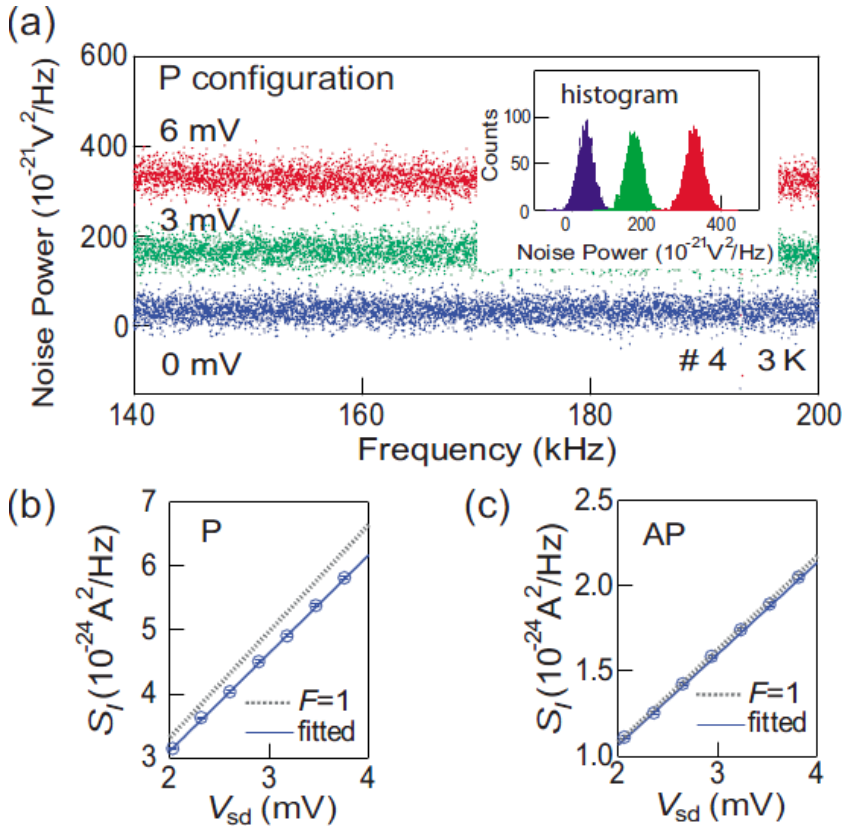

Figure 2.13: (a) Measured spectra in the P state for voltages of 0, 3, and 6 mV at 3 K. The inset shows the histograms of each spectrum between 140 and 180 kHz. (b) Estimated current shot noise (open dots) for the P state. The solid line is the fitted curve, while the dashed line shows the curve corresponding to F=1. (c) Same graph for the AP state. Adapted from Ref.[77].

orentation of the free layer's magnetization[64]. In these conditions, the spectral density of the fluctuations in resistance $S_R(f)$ are expressed as a function of fluctuations in magnetization $S_M(f)$ by the fluctuation-dissipation relation[40]:

$$S_R(f) = \left(\frac{\partial R}{\partial m}\right)^2 S_M(f) \tag{2.17}$$

where m is the magnetic moment and R is the resistance. The expression for $S_M(f)$ corresponds to equation 2.13.

Then, suppposing that χ'' is a constant in a FM system[40], and supposing a that $S_R(f)$ depends on f as shown in equation 2.11 (Hooge model), we can integrate equation 2.17 between f_{min} and f_{max}:

$$\frac{\partial R}{\partial H} = \frac{2m\mu_0}{k_B T \Delta R} \frac{R^2}{A} ln\left(\frac{f_{max}}{f_{min}}\right) \alpha \tag{2.18}$$

so close to the P-AP transition, the 1/f noise is mainly due to magnetic fluctuations and α is proportional to $\partial R/\partial H$.

The use of crystalline barriers, like MgO, improves the structural quality of the junctions, and in general they present much lower normalized noise than for amorphous barriers[82]. MgO barriers also offer an increase (around threefold) in TMR without additional low frequency noise[83]. Crystalline barriers also influence the tunneling transport due to spin filtering, as was seen in subsection 1.4.3. Indeed, the first studies of low frequency noise in MTJs with MgO(111) barriers showed that the noise depends quite strongly with the magnetic state. In Ref.[84,85], our group found an increase in the normalized low frequency noise (Hooge parameter) in the AP state for such junctions. This effect could be due to the difference in stress acting on the barrier depending on the magnetic field, referred to as *magnetostriction*. This difference in normalized noise between the magnetic states was further confirmed to exist in MTJs with MgO(100) barriers[82], where record low normalized 1/f noise values were obtained.

As mentioned in subsection 1.4.3 (and shown in Fig. 1.9), there exists a 3% lattice mismatch between Fe and MgO. Alloying Fe with V changes its lattice parameter, so the interface mismatch between the Fe electrode and the MgO barrier can be reduced. This improvement was found to increase the TMR ratio and suppress the nonmagnetic (P state) and magnetic (AP state) 1/f noise, in juctions with FeV bottom electrodes[86].

The work done in our group in Ref.[87] suggests that doping MTJs with light elements could be advantageous. Carbon doping of epitaxial MTJs decreases the 1/f noise, but also improves the robustness of MTJs, since it seems that Carbon suppresses Fe-O interdiffusion and relaxes the MgO barrier.

Annealing can also have a big influence on the transport of magnetic tunnel junctions. The study in Ref.[88] presents double-barrier MgO magnetic tunnel

junctions with CoFeB electrodes. These type of junctions are described in detail in section 2.6. The junctions show TMR ratios of more than 100% at room temperature, but the TMR presents a highly asymmetric dependence with the voltage. The authors decrease this asymmetry by increasing the annealing temperature, finding that T= 300 °C is the optimal value. The temperature is determined by looking for the maximal TMR ratios in the junctions, as well as a minimal asymmetry with the voltage.

The same authors presented a later work, where the influence of annealing in CoFeB/MgO/CoFeB magnetic tunnel junctions was investigated[89]. The junctions present an impressive TMR up to 235% and the noise is measured for different degrees of crystallization and CoFeB/MgO interface quality depending on the annealing temperature. An extremely low 1/ f noise, compared to Al_2O_3 junctions, is found although it seems to be independent with the annealing temperature. The authors argue that the origin of the low frequency noise is attributed to localized charge traps within the MgO barriers.

The authors from Refs.[90–92] present several studies with the growth charecterization of CoFeB/MgO/CoFeB MTJs and the dependence of 1/f noise with the annealing temperature. The global conclusions extracted from them are: *(a)* the annealing time required for the TMR and noise to reach its maximum and minimum value respectively, depends on the annealing temperature, shorter at higher annealing temperatures, and *(b)* the noise is attributed to oxygen vacancy defects in the MgO tunnel barrier, and thermal annealing reduces this disorder and the number of defects with levels near the Fermi energy of the electrodes.

2.5.3. Low frequency noise in submicron MTJs

Reducing the area of magnetic tunnel junctions may be a good approach for obtaining spin-torque based devices, since the current needed to obtain the necessary current density for STT effects can be notably decreased. The main problem is that decreasing the area of the devices also increases their resistance since $R \propto 1/A$. So the decrease in area must be compensated with thinner tunnel barriers, since the resistance escales exponentially with the barrier thickness. When the lateral size of the junction falls below the μm, matters

turn technologically difficult, since the barriers must be made thinner than $1nm$ to keep the resistance in the hundreds of Ω. The majority of noise studies in junctions of such size deal with high frequency dynamics, with their application as microwave oscillators in mind.

Our group presented electron transport and RTN measurements in submicron MTJs, in particular, with dimensions close to the transition to the single domain regime[93]. These junctions revealed the presence of single magnetic inhomogeneities in the soft and hard layers, appearing as a two-state RTN. It was found that the RTN fluctuations and the related resistance steps of the AP state were due to domain wall motion and magnetic inhomogeneities. These are asymmetrically influenced by the current, which can be used to displace the domain walls in the soft layer by the spin torque effect using relatively low current densities.

2.6. Noise in double-barrier magnetic tunnel junctions

2.6.1. TMR and shot noise in double-barrier magnetic tunnel junctions

A double-barrier magnetic tunnel junction (DMTJ) is a spintronic device composed of three ferromagnetic layers separated between each other by tunneling barriers. One would think that such devices could have enormous TMR ratios, since two tunnel barriers come into play and contribute to the resistance of the antiparallel ($\uparrow\downarrow\uparrow$) state. What is found instead is that the TMR values obtained at low temperatures barely reach 200%[94], quite far from the 604%[73] record in single barrier junctions mentioned above. This could be due to spin-relaxation in the central electrode, so the current loses some spin polarization and the TMR values observed are not as high as initially expected.

It has been shown that these structures may find application in electronic and spintronic devices as, for example, memory cells in MRAMs[95] or as spin-current diode[96]. One may also go further and think about these junctions as data bits who could store twice as much information as a normal MTJ since

they can show 4 distinct magnetic states[97].

The growth and characterization of sputter-grown DMTJs with MgO barriers and $Co_{40}Fe_{40}B_{20}$ ferromagnetic electrodes is presented in Ref.[98]. The conductance at each magnetic state, and thus the TMR are observed to have an asymmetric bias voltage dependence withouth after growth and annealing at low temperature. The authors show that the TMR asymmetry decreases when the junctions are annealed at higher and higher temperatures. The structural improvement is shown in Fig. 2.14. The bias dependence becomes almost symmetric after annealing at 350 °C. A maximum TMR ratio of 120% is obtained for the DMTJs, and its somewhat low value is attributed to an amorphous middle CoFeB layer, which does not crystallize after annealing.

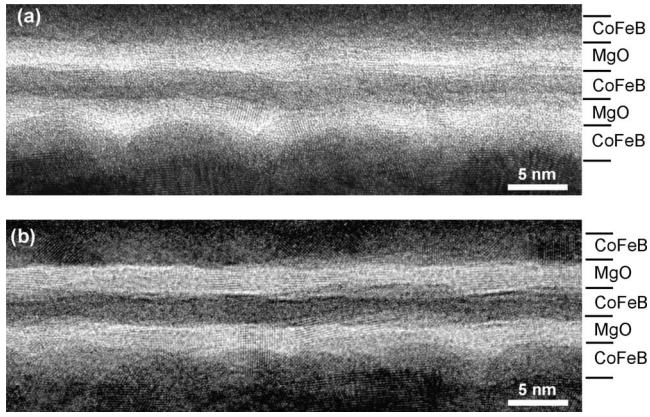

Figure 2.14: Electron micrographs from the barrier region of DMTJs (a) as deposited and (b) after annealing at 350 °C[98].

A theory of shot noise in double-barrier magnetic tunnel junctions, with a normal metal central electrode (FM-NM-FM), was developed in Ref.[99]. The authors study the case of elastic and inelastic regimes, in the case of diffusive (high electron scattering) and ballistic (negligible electron scattering) junctions. The Fano factor is calculated as a function of the angle between the magnetization of the electrodes (i.e. the magnetic state), at different values of spin polarization. Spin-flip processes are disregarded, which is justified if the central electrode is thinner than the spin-flip scattering length. Spin-flip scattering in the normal metal electrode is expected to make the angular dependence of

the Fano factor quantitatively weaker, since the effective polarization and mixing conductance are reduced. In the case of ballistic junctions with a large polarization, the Fano factor sharply drops from 1 to 0 when the junction approaches the antiparallel state. Diffusive junctions, on the other hand, present much lower Fano factors ($F = 1/3$ for a diffusive, single barrier junction) which depends non-monotonically with the angle.

The work in Ref.[100] considers the dependence of the TMR as a function of the central electrode's thickness in FM-NM-FM DMTJs. At certain thicknesses of the middle electrode, periodic oscillations of the TMR may be observed which are related to quantum-well states formed in this electrode[101] and to resonant tunneling through the whole structure. The authors present a theoretical study of coherent tunneling in a FM-NM-FM system within the free-electron approximation. The TMR, which depends on the relative orientation of the magnetic moments of the ferromagnetic electrodes, shows an oscillatory behavior with pronounced peaks as a function of the central electrode's thickness. These oscillations are related to the resonant tunneling through the whole system.

Evidence of tunneling through quantum well states in the middle free electrode was found by our group[102]. Oscillations in resistance were observed at room temperature in both magnetic configurations and for both bias polarities. The quantum well states were observed due to a specific feature of junctions: they experienced a *soft* breakdown due to a nitrogen doping of the barriers. Quantum well states are also observed in nitrogen-free DMTJs in Chapter 5.

A model describing the spin-dependent current and TMR in an all ferromagnetic DMTJ (FM-NM-FM-NM-FM) is presented in Ref.[103]. The theory is based on the two-band model and quasiclassical equations in order to describe the transport phenomena in the ferromagnetic metals. The TMR is studied for the resonance (through quantum well states) and nonresonance tunneling regimes. In the case of non-resonant tunneling, the DMTJs are modeled in two different ways: as a single system presenting coherent (ballistic transport with no scattering) or as two single barrier MTJs connected in series, presenting a consecutive tunneling system. By the use of both these models, including a barrier asymmetry the authors are able to reproduce the asymmetric TMR curves with the voltage which are observed in experiments[98].

2.6.2. 1/f noise in double-barrier magnetic tunnel junctions

Although there have been several reports on the fabrication and characterization of DMTJs only, few of these deal with low frequency noise in this type of junctions.

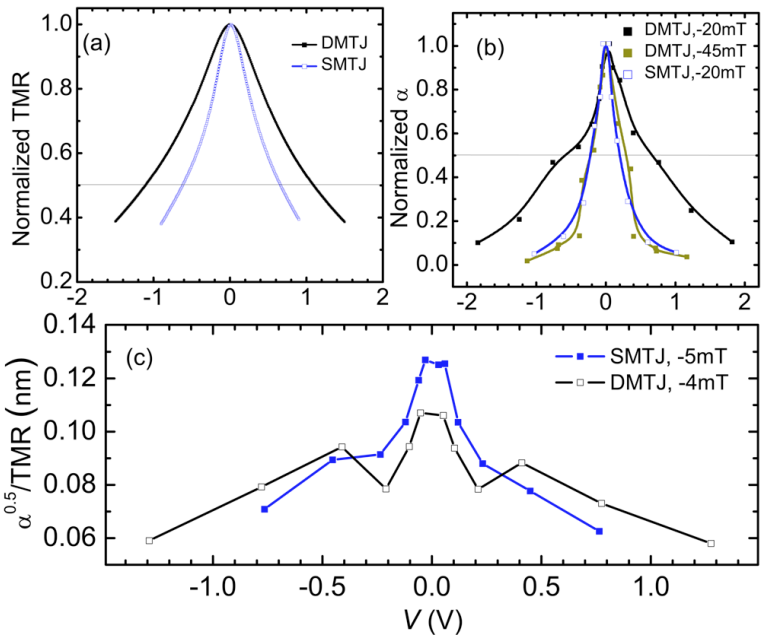

Figure 2.15: The bias dependence of (a) TMR, (b) the noise magnitude parameter in the antiparallel state and (a) the $\alpha^{1/2}$/TMR value during free layer switching for an SMTJ and a DMTJ with symmetric MgO layers. Figure from [104].

Ref. [104] presents a comparison of low frequency noise between sputtered CoFeB/MgO DMTJs and single MTJs with high TMR ratios. From a practical point of view, DMTJs could be expected to show a reduced 1/f noise if the tunneling is not coherent. The junctions were annealed at temperatures between 250-375 °C and have sizes of 20×20Ű50×150 μm^2. The authors find that while the normalized noise is slightly lower for DMTJs in the P state ($\alpha \sim 10^{-10} \mu m^2$), α in the AP state for DMTJs decays slowly with the voltage compared to that

single MTJs, as is shown in Fig. 2.15 (a), (b). The authors argue that the bias dependence of the TMR and α points to the DMTJs behaving like two single MTJs in series, since there is also no sign of coherent/resonant tunneling. Fig. 2.15(c) presents $\alpha^{1/2}$/TMR (which is proportional to the field detection capability of MTJs) as a function of the voltage for a DMTJ and a simple MTJ. The results indicate that for a low bias operation, the DMTJs could be used as more sensitive detectors than single barrier MTJs. In summary, double barrier tunnel junctions have been sucessfully fabricated on numerous reports, but although there exist several theoretical descriptions of the tunnel through this type of devices, there is yet no systematic investigation of the transport mechanisms in them, and particularly of shot noise.

2.7. Charge and spin transport in organic materials

Organic materials present some advantages over inorganic ones, like the ability to chemically adjust the electronic functionality, mechanical flexibility, the capacity to form self-assembled layers, etc. These properties are used daily to produce cheap electronic devices which have large areas where the organic components are involved. The day when scaled-down electronics are made from single molecules still lays in the future, since significant technical problems still need to be figured out.

We will briefly go over the history of organic electronics, and then we will introduce the *young* field of organic spintronics, in which the advantages of organic materials have started being applied to build spintronic devices. We note that this thesis mainly concentrates on the tunneling and hopping regimes and therefore quantum transport through molecules in the high transmittance regime[105] is outside of our scope.

2.7.1. Organic electronics

The world of electronics is currently dominated by Si/SiO_2 metal-oxide, semiconductor field-effect transistors or MOSFETs. The main mechanism be-

hind MOSFETs is the inversion layer that is formed between the drain and source of the transistor by using gate voltages. The ability to change the carrier density in semiconductors by doping and electrical gating is a crucial tool in electronics. General interest in organic semiconductors emerged because of their promising characteristics, and materials such as polymers or small molecules are used in everyday technology as OLEDs, OFETs, photovoltaic cells, etc. Historically, the first studies on organic semiconductors were aimed at improving the conductance of organic polymers. The discovery of high conductivity in oxidized, iodine-doped polyacetylene in 1977 earned Heeger, MacDiarmid and Shirakawa the Nobel Prize in Chemistry in 2000. Films grown with organic polymers are considerably rough, presenting strands reminiscent of spaghetti, which limits their carrier mobility typically to around $0.1 cm^2(Vs)^{-1}$.

Films with a smoother interface may be obtained by using small molecules, which increases the carrier mobility. Pentacene, for example, is the most widely used molecule for the fabrication of organic thin film transistors (OTFTs), setting the mobility record at $6 cm^2(Vs)^{-1}$. Control of the carrier density by doping organic semiconductors is not straightforward, due to their low purity. Therefore, the thin-film-transistor geometry is preferred for organic transistors (Fig. 2.16(a)) rather than that of the MOSFET. In an OTFT, a conducting channel is capacitively induced at the interface between the dielectric and the organic material. Thus the carriers are injected into the organic channel from metallic electrodes, as opposed to the case of MOSFETs, where the charge carriers come from the dopants.

The interface between the inorganic and organic layers is also quite crucial for organic electronics and spintronics. The microfabrication processes used for establishing an electrical contact with the organic components usually damage them considerably. Since the injection and detection of spins takes place at the interfaces between the ferromagnetic electrodes and spacer layers, obtaining high-quality interfaces between organic and inorganic components is of fundamental and practical interest.

Since the interface between the semiconductor and the dielectric (which separates the semiconductor from the gating contact) is of major concern for the efficiency of the transistors, they have been greatly improved by the use of self-assembled monolayers (or SAMs) of small organic molecules such as Alq_3

or the oligomer all-thiophene (T_6), shown in Fig. 2.16(b) and (c).

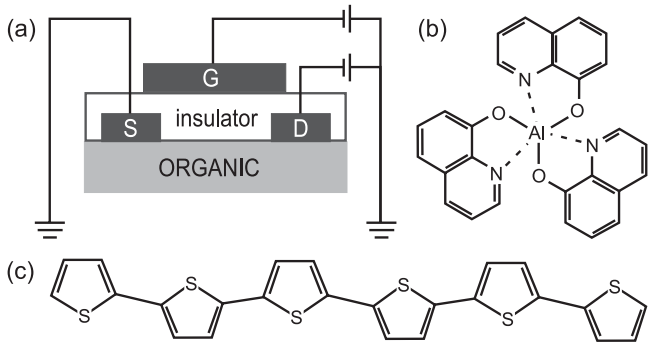

Figure 2.16: (a) Sketch of an organic thin-film transistor. The gate (G) electrode induces a conducting channel and it is separated from the organic film by an insulator. The current through the organic material is injected and collected by source (S) and drain (D) contacts. Structure of the (b) Alq_3 molecule and (c) the T_6 oligomer[106].

As in the case of inorganic electronics, high purity, single crystal organic semiconductors may be grown from molecules such as rubrene and pentacene with reproducible electronic properties. They can be obtained by physical vapour transport (PVT) or despositing them from a solution. Organic single crystals (OSCs) do not present grain boundaries, so they have a minimal number of charge traps. These properties make them ideal materials to test the fundamental electronic properties of organic materials as well as the limitations of OFETs. Recent studies report an increase of the room-temperature mobility in rubrene and pentacene[107].

2.7.2. Electron transport in organic materials

The injection of charge and electronic transport in organic materials is currently not well understood. Two major mechanisms for electronic transport are found in bulk organic materials: **band transport** and **hopping**.

Band-like transport may only occur at low temperatures in organic systems with a high structural order, such as the organic single crystals mentioned earlier. In order for the band transport to take place, the carrier mean free path

must be higher than the separation between molecules. The conduction and valence bands emerge from the overlap of the HOMO and LUMO levels respectively[108].

The **hopping** mechanism is typically found in disordered structures (like the polymer films described earlier), which present a much smaller mobility than for band-like transport. The name *hopping* comes from the fact that the transport results from the charge carriers "hopping" between the localized states of the molecules. It strongly depends on the temperature, electric field, charge traps and the carrier concentration[109].

In organic materials, the definition of n or p-type materials differs from that in the inorganic case. In the organic context, a material is considered n-type if it is easier to inject electrons than holes, or p-type if the opposite is true[110]. Although p-type organic conductors are the most common, there have been reports of n-type organic semiconductors, as well as of ambipolar organic materials, which show p-type and n-type conduction depending on the gate voltage applied. Then, hole transport seems to be the preferred the type of conduction in organic materials, which is explained by the fact that electrons are more easily trapped at the organic/dielectric interfaces than holes.

The transport through a single molecule is quite different from the the transport though a bulk organic material, since it may be affected by Coulomb or quantum confinement effects at low temperatures similarly to quantum dots[111]. The simplest model considers the transport through only one molecular level. In the model, the current flows when the voltage applied between the metallic leads causes the molecular level to be between the Fermi levels of the two leads[112].

Many other models have been developed for the estimation the transport through organic molecules, although the most used is the non-equilibrium Green's function method[113]. Molecular spin valves (an organic molecule sandwhiched between two FM contacts) may be described by some of these models, which consider spin-polarized tranport and predict highly spin-dependent signals[114]. As we present in Chapter 7, a model describing experimentally observed superpoissonian shot noise implies inroducing at least two or more interface levels near and below the Fermi energy.

2.7.3. Organic spintronics

Organic spintronics arises from the combination of organic electronics and spintronics, and is an emerging area of research where spin-polarized currents are mediated by organic materials. Organic materials offer inexpensive, light, flexible, chemically active, and bottom-up fabricated electronics.

As inorganic electronics have shown, taking advantage of the charge and spin of the electron (as opposed to only its charge), allows the construction of spintronic devices which are non-volatile electronics for logic, data storage (MRAM) or communications (for example, STNOs). These devices should also be faster and more power-efficient, due to the fact that the energies of spin dynamics are appreciably lower than for handling charges.

Organic materials are specially attractive for spintronic applications because they present quite long spin relaxation times τ_s, which have been found to be in the range of $10^{-7}/10^{-5}$ s, i.e. orders of magnitude longer than $\sim 10^{-10}$ s found in metals. The spin relaxation time determines the time scale during which the electron does not lose its spin polarization.

The spin relaxation time is given by $\frac{1}{\tau_s} = \frac{1}{t_{\uparrow\downarrow}} + \frac{1}{t_{\downarrow\uparrow}}$, where $t_{\uparrow\downarrow}$ and $t_{\downarrow\uparrow}$ correspond to the average spin flip time from up-spin to down-spin, and vice versa. The length over which the electron maintains its spin polarization is known as the spin relaxation length l_s. In the case of a non-magnetic metal, l_s is related to the spin relaxation time by $l_s = \sqrt{\frac{\tau_s}{4e^2 N(E_F)\rho}}$ where $N(E_F)$ is the density of states at the Fermi level and ρ the resistivity of the metal. Then, if a material is intended to be used as a spacer in a spin valve, the thickness L of the spacer layer should be considerably smaller than the spin relaxation lenghth $L \ll l_s$, for the spin to retain its memory when tunneling between FM electrodes. So longer spin relataxion times could translate into larger MR ratios in hybrid structures.

The longer spin relaxation times found in organic materials may come from the fact that both the spin-orbit coupling and hyperfine interactions are weak in these materials. The previous interactions are the main cause of spin relaxation in inorganic spintronics, and they are absent in organic systems because they are mainly composed of light elements.

Spin-polarized carriers have been injected into organic semiconductors, from

ferromagnetic elements such as gadolinium. The investigation of such a system has been carried out in organic LEDs (OLEDs) with the intention of generating a luminescence dependent on the magnetic field[115,116]. Research on magnetic field effects in OLED devices started in 2003 when Kalinowski et al. discovered that the resistance and the light output of OLEDs could be modified by applying external magnetic fields[115]. This phenomenon was named by "organic magnetoresistance" or OMR effect, particularly interesting since the OLED devices studied did not contain any ferromagnetic materials.

2.7.3.1. Organic spin valves

Organic materials have also been succesfully used in the fabrication of spin valves. The first succesful experimental work regarding the injection of spins into an organic semiconductor was presented by Dediu et al[117]. Lateral spin valves, composed of two LSMO electrodes were used to inject a spin-polarized current in a T_6 channel of width ranging from 70 to 500 nm. Since the coercive field of both electrodes is the same (and there is no AP state), a negative MR of 30% is achieved when the electrodes' magnetization changes from parallel (high field) to a random orientation (low field). The spin relaxation length is estimated to be roughly 200 nm, which leads to a spin relaxation time $\tau_s \sim 1\mu s$ (using $10^{-4} cm^2 (Vs)^{-1}$ as the mobility of T_6).

Perpendicular spin valves (Fig. 2.17(a)) with a structure LSMO/Alq_3/Co presenting P and AP states were fabricated by Xiong et al[118]. Depositing Co as the top electrode creates pinholes and the Co penetrates up to 100 nm into the organic layer (Fig. 2.17(b)). Even though the Co/Alq_3 interface is not well defined, the authors find an MR of -40% at 11 K (Fig. 2.17(d)). The negative sign of the MR is attributed to the negative spin-polarization of the d-band in Co. The authors estimate the spin relaxation length to be $l_s = 45$ nm, using an adjusted Julliére model[118].

Organic spin valves showing GMR have been fabricated using varied organic spacers, based on small molecules, like pentacene, rubrene, or the C_{60} fullerene, π-conjugated polymers like P3HT (poly(3-hexyl thiophene)) or P3OT (poly(3-octylthiophene)), etc. In fact, GMR at room temperature was obtained for spin valve devices consisting of LSMO/P3HT/Co[119] and LSMO/P3OT/LSMO[120].

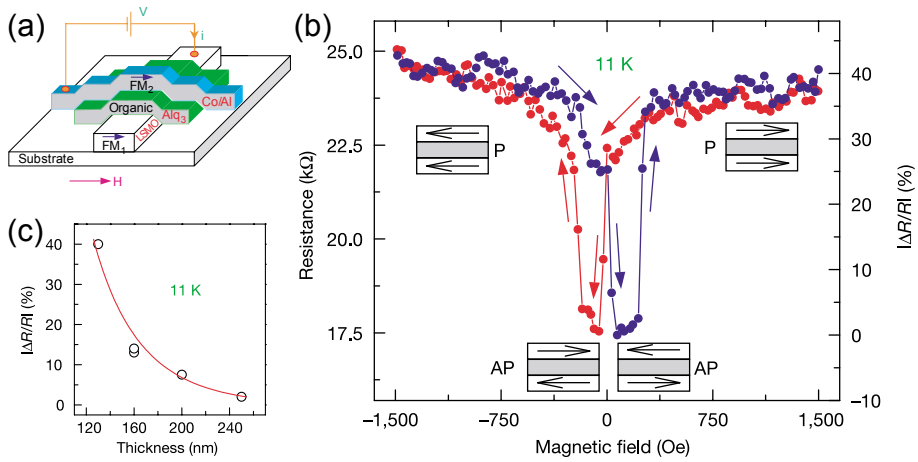

Figure 2.17: (a) Schematic representation of a spin valve device consisting on two FM electrodes and an organic semiconductor spacer. (b) GMR loop of a LSMO (100 nm)/Alq_3 (130 nm)/Co (3.5 nm) spin-valve device measured at 11 K. (c) GMR value of a series of LSMO/Alq_3/Co devices with different Alq_3 thickness. Adapted from[118].

The interface between the FM electrodes and the organic spacer was found to improve if a thin buffer barrier is grown between the electrode and the spacer[121]. In this work, an AlO_x seed layer is included between the Co electrode and an Alq_3 layer in a vertical LSMO/Alq_3/Co device. The authors also prove that optmizing the LSMO interface, a room temperature GMR of -0.15% can be obtained. The GMR vanishes at 325 K, which corresponds to the loss of magnetization of the LSMO layer.

Positive GMR ratios have also been obtained in Alq_3 spin valves[122]. The authors report GMR values of 9% at 80 K and of 1% at 290 K, in Fe/Alq_3/Co devices with an organic layer of 46 nm. The GMR value decreases when the thickness of the Alq_3 is increased. A spin relaxation length of 43 nm at 80 K is estimated. The larger GMR values are found to correlate to sharper Co/Alq_3 interface and a magnetically dead layer at the Fe/Alq_3 interface, which seemingly acts as a tunnel barrier.

The organic−based magnet V[TCNE]$_x$ (where TCNE: tetracyanoethylene), which has a Curie temperature of 400 K, has been used to fabricate an all-

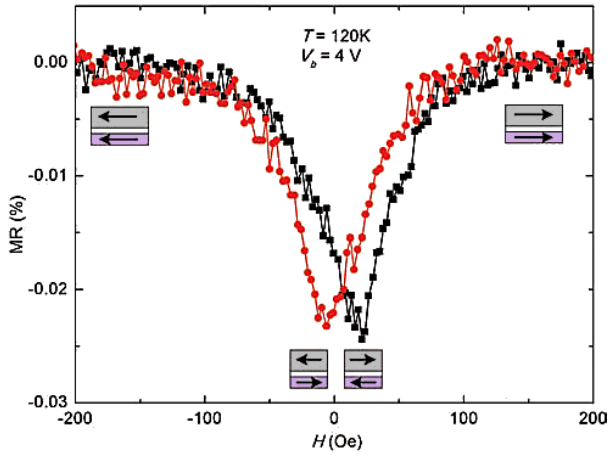

Figure 2.18: Magnetoresistance curve measured at 120 K of an all-organic spin valve[123].

organic spin valve with a structure V[TCNE]$_x$/Rubrene/V[TCNE]$_x$[123]. The organic FM was grown by chemical vapor deposition at 40 K in order to suppress the diffusion of the FM into the organic spacer. A maximum MR of 0.04% at low temperature was obtained (see Fig. 2.18), probably due to the low spin polarization of the organic ferromagnet.

2.7.3.2. Organic magnetic tunnel junctions

If the organic semiconductors are grown thin enough, they can act as tunneling barriers. Spin-dependent tunneling at room temperature was demonstrated in a Co/Alq$_3$/Py structure[124] with Alq$_3$ thicknesses from 1 to 4 nm, as shown in Fig. 2.19. The authors measure a maximal TMR of 6% at room temperature. The influence of interfacial states on the spin relaxation was decreased by including an AlO_x buffer layer between the Co and Alq$_3$ layers.

Xu et al.[125] also obtained organic MTJs with LSMO and Co electrodes and Alq$_3$ or tetraphenyl porphyrin (TPP) as the tunneling barrier. Relatively thick (around 20 nm) but apparently non-uniform tunnel barriers were grown, and the tunneling seemed to take place through areas a few nm thick. A TMR of -15% was found for both types of barriers at 80 K, vanishing at room

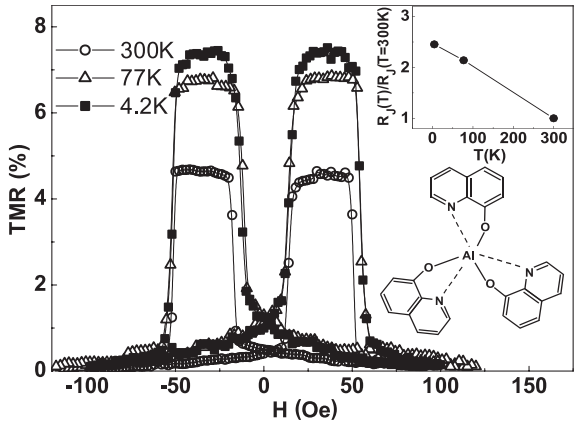

Figure 2.19: Adapted from[124]. TMR at 10 mV bias for an 8 nm Co(0.6 nm)/Al_2O_3(1.6 nm)/ Alq_3(10 nm)/Py junction. The inset shows the temperature dependence of the junction resistance.

temperature.

Room temperature TMR values of around 12% were observed by Szulczewski et al.[126] in CoFeB/MgO/Alq_3/Co devices with values around 12% at room temperature for Alq_3 thicknesses between 2-8 nm. Granular systems of Co nanoparticles in a P3HT matrix have also shown MR values of of 3% for 17 vol % Co at 10 K[127] Finally, TMR values of the order of 300% have been obtained in nanosized LSMO/Alq_3/Co tunnel junctions, where the top contact is created by an AFM tip[128].

2.7.3.3. Single-molecule devices and self-assembled monolayers

Molecular monolayers have already started being used for the miniaturization of electronic devices, a process which is leading to the use of single molecules. The properties of single-molecule devices are still mainly unexplored, but there exist a few important studies.

The concept of molecular electronics dates back to 1974, when the idea of a molecular rectifier was first introduced[129], but the first experimental result measuring the conductance of a single molecule was not obtained until 1997[130]. The main problem in single-molecule electronics is establishing an electrical

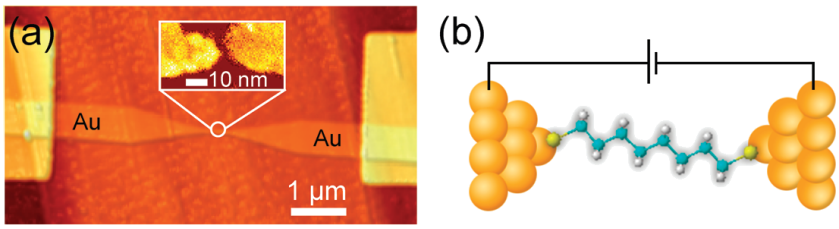

Figure 2.20: (a) Atomic force microscopy image of a Au wire where a nanogap is broken by electromigration. (b) A schematic of a final device incorporating a 1,8-octanedithiol molecule into the nanogap.[131]

contact between the metal and the electrodes, which should only separated by about 1 nm if single molecules are to be contacted at both ends. Some of the techniques used to contact single molecules are: mechanical break junctions, nanopores, electromigration, conducting probe atomic force microscopy, etc[105]. An organic molecule imaged by AFM is shown in Fig. 2.20.

The Kondo effect was observed by Pasupathy et al. in single C_{60} molecules contacted by Ni electrodes[132,133]. Features of the Kondo effect could be seen in the dependence of the conductance with the magnetic field and temperature, and TMR values of -38% and -80% were obtained. Tunnel junctions in which barrier consists on a self assembled molecular layer were reported by Petta et al.[134]. The device, with a SAM of octanedithiol (100-400 molecules) sandwiched between Ni electrodes, was fabricated in the nanometer-scale in the nanopore geometry[135,136]. Negative and positive MR up to 16% were obtained at 4.2 K and for low bias. The junctions presented telegraph noise, which could be due to defects in the molecular barrier and could explain the low TMR values.

To conclude, understanding the mecanisms of electron (hole) transport through molecular barriers in the tunneling or hopping regimes remains one of the key challenges for the young and growing field of molecular spintronics. We expect that the shot noise results from Chapter 7 will shed some light on this problem.

Chapter 3

Experimental methods

In this chapter we will describe the different experimental techniques that have been used to carry out the measurements. We will also enumerate the main contributions that have been added to the set-ups and describe the brand new methods implemented during the course of this thesis. A discussion on how the analysis of data has been improved is also presented.

3.1. Introduction to the experimental techniques

The techniques presented here, as mentioned in the introduction, have been built with the aim of measuring and analyzing voltage fluctuations in magnetic tunnel junctions, either at room temperature or in cryogenic conditions. The existing set-ups were described in detail in the PhD theses of the previous students of the group[137,138].

During the realization of this thesis, these experimental set-ups have been improved, modified and/or extended to accomodate for the wide variety of samples studied. Also, a high-frequency noise measurement setup has been built. The importance of automatizing as much as possible the measurements has also been stressed, in order to maximize the use of both time and resources. The following sections will illustrate each of these experimental designs in detail,

pointing out their improvements or modifications.

A great deal of effort has gone into data analysis as well, with the intent of extracting more precise estimations of the parameter of interest for each particular measurement (Hooge factor, RTN constants, Fano factor, etc.). A brief overview of the development of the tools for the analysis of data will be shown.

3.2. Modeling the low frequency set-up

In the first chapter we *formally* described random signals from a mathematical point of view, and we presented the main concepts needed from time series analysis. We will now describe the circuit used to measure noise voltage in magnetic tunnel junctions, which we employ both for room temperature and cryogenic conditions.

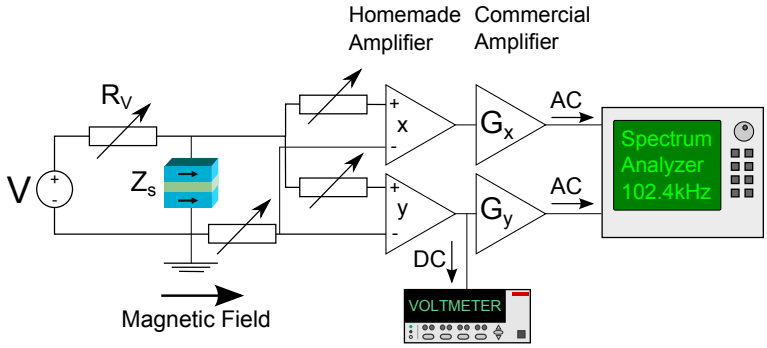

Figure 3.1: Diagram of the low frequency measurement circuit.

The main idea of the experiment is to place the sample in the midst of a controllable external magnetic field and contact the tunnel junction (ideally 4 terminal) so a current runs through it and the voltage is read. The set-up for low frequency should register both the voltage drop on the sample as well as the spectral density of the voltage fluctuations as a function of the external field and the current (or bias). In the room temperature set-up, the DC bias is supplied by a Keithley 6221, low noise current source, and the voltage is measured with a Keithley 2182 nanovoltmeter. In the cryogenic system, the DC bias is provided

by batteries in series with a variable resistor (for noise measurements) or by a Keithley 220 current source (for I-V curves). The voltage is measured by a Data Translation DT330 data acquisition board (or DAC).

A diagram of the experimental circuit is shown in 3.1. The signal (DC + fluctuations) is first duplicated and amplified by two nearly identical homemade preamplifiers. The voltage is registered by a a data acquisition card (DAC) from one of the channels. Each channel, denoted by X and Y, is then amplified a second time by Stanford Research SR560 commercial amplifiers, which filter out the DC part of the signal. These amplifiers also include a band-pass filter which can be varied between f=0 Hz and f=1 MHz. Both channels containing a preamplified and filtered signal are sent to a Stanford Research SR780 spectrum analyzer which has a bandwidth up to 102.6 kHz.

Since both channels of the signal are amplified nearly identically but independently of one another, both channels contain the sample noise signal δV_{R_S} amplified by the same gain, plus a random noise δV_{preamp} due to the detection circuit. The noise due to the electronics of the system is of the same magnitude for both channels, but the noise of one channel is uncorrelated (independent) from the noise in the other channel.

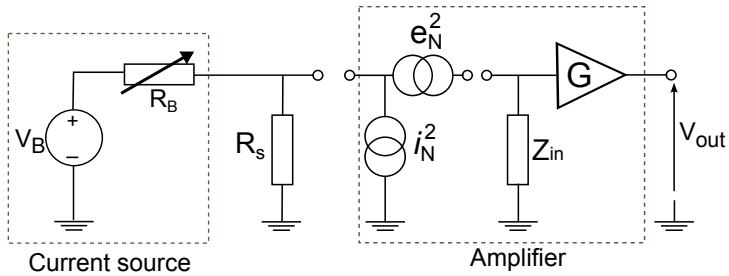

Figure 3.2: Model of the noise sources from the amplifying circuit.

Let us model the noise contribution of the amplifying circuit. We consider the voltage and current noise of the preamplifying stage only, since the signal reaches the second amplifying stage with enough amplitude so that the noise from the second amplifiers may be disregarded. The preamplifier is considered to have a voltage e_N^2 and current noise i_N^2 source, so $\delta V_{preamp} = e_N^2 + i_N^2 R_S^2$, where R_S is the sample resistance. We will also neglect the noise contribution

from the current source, since for noise measurements we have used batteries. Thus, the circuit is modeled as shown in Fig. 3.2, where (from left to right): the current source is shown as a battery in series with a variable resistor, in series with the sample under study (R_S), and the preamplifier, which has voltage and current noise sources and an input impedance Z_{in} and finally G represents an ideal and noiseless amplifier, containing both the preamplier and commercial amplifiers gain.

If we consider the preamplifiers from both X and Y channels to have the same i_N^2, the total fluctuations reaching the spectrum analyzer will be:

$$S_V = e_{N_X}^2 + e_{N_Y}^2 + \delta V_{R_S} + 2i_N^2 R_S^2 \tag{3.1}$$

The details of how this result is derived may be found in Ref.[137]. By using a cross-correlation technique (explained in the next subsection) we may neglect the voltage noise contributions from the preamplifiers. Then, we can see that the only unwanted fluctuations correspond to the current noise of the preamplifiers. So we should choose a preamplifier with the lowest current noise possible. Our homemade preamplifiers employ the INA111 chip, which presents the following characteristics: $e_N = 10nV/\sqrt{Hz}$ and $i_N = 0.8 \times 10^{-3} pA/\sqrt{Hz}$. The current noise of this operational amplifier is 3 orders of magnitude lower than for other widely used chips, such as the INA217 and the INA114.

3.2.1. Cross-correlation

As was mentioned above, the voltage noise from the preamplifiers may be eliminated by the *cross-correlation tecnique*. The spectrum analyzer calculates the cross-spectrum (or cross-correlation spectrum) of the two signals $X(t)$, $Y(t)$.

If we are dealing with complex-valued functions, the correlation function changes to:

$$R_{XY}(\tau) = \lim_{T\to\infty} \frac{1}{2T} \int_{-T}^{T} X^*(t) Y(t+\tau) dt \tag{3.2}$$

This is known as the cross-correlation function of two complex-valued, time-dependent variables. Taking the conjugate of $X(t)$ ensures that aligned peaks (or aligned troughs) with imaginary components will contribute positively to the integral.

Each of the two channels mentioned above contains the signal of interest $V_R(t)$ and the voltage noise of its preamplifier, i.e. $X(t) = V_R(t) + X_{preamp}(t)$ and $Y(t) = V_R(t) + Y_{preamp}(t)$. $X_{preamp}(t)$ is independent (or uncorrelated) from $Y_{preamp}(t)$, so using 3.2:

$$R_{XY}(\tau) = \lim_{T\to\infty} \frac{1}{2T} \int_{-T}^{T} (V_R(t) + X_{Preamp}(t))^* (V_R(t+\tau) + Y_{Preamp}(t+\tau)) dt =$$

$$\lim_{T\to\infty} \frac{1}{2T} \Big(\int_{-T}^{T} V_R^*(t) V_R(t+\tau) + \cancelto{0}{\int_{-T}^{T} V_R^*(t) X_{preamp}(t+\tau)} +$$

$$\cancelto{0}{\int_{-T}^{T} X_{preamp}^*(t) V_R(t+\tau)} + \cancelto{0}{\int_{-T}^{T} X_{preamp}^*(t) Y_{preamp}(t+\tau)} \Big)$$

we see that the only term that survives is the term involving $V_R^*(t)V_R(t+\tau)$. We now have all the tools needed to obtain the voltage fluctuations of a magnetic tunnel junction without any influence from electronic circuits.

The spectrum analyzer used in the experiments obtains the cross-spectrum, which is given by:

$$\mathcal{F}\{R_{XY}\} = \mathcal{F}\{X(t)\}^* \cdot \mathcal{F}\{Y(t)\} \tag{3.3}$$

Good spectra are obtained after averaging many cross-correlation spectra at each voltage. This procedure reduces the variance of our measurement by $1/N$ (the deviation as $1/\sqrt{N}$), with N the number of averages. The number of averages is chosen so obtaining one averaged spectrum does not take "too long", as the time T for taking one average is given by the Δf and f_{max} settings of the spectrum analyzer (see subsection 1.2.2).

A nice and simple way to check the correct calibration of the setup is by measuring the thermal noise of a resistor. We typically use this measurement

to obtain the gain values of our homemade pre-amplifiers, although it can also be used as a lab activity by undergraduate or graduate Physics students to estimate the value of Boltzmann's constant. Fig. 3.3 shows how a good estimate of k_B can be obtained from the slope of S_V *vs.* RT for just a few resistors.

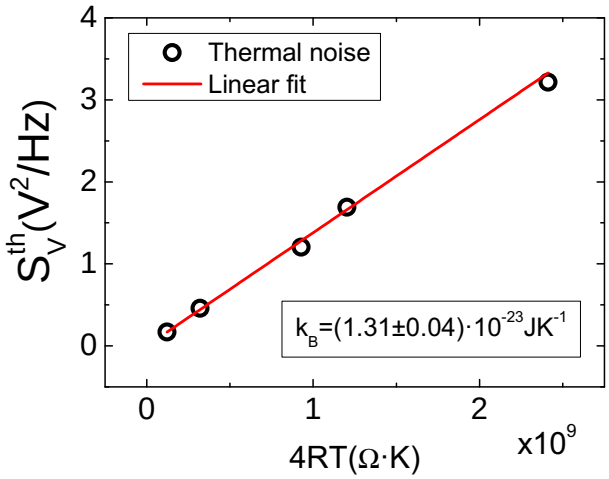

Figure 3.3: Estimation of k_B from the thermal noise of several resistors at room temperature.

3.3. Cryogenic low frequency noise measurements

Our cryogenic set-up consists on a Janis cryostat, which has an outer liquid nitrogen jacket, and an inner liquid ^{4}He reservoir. A ^{3}He (closed-circuit) insert which allows us to cool samples in a vacuum down to $T = 0.3K$.

The basic principle of the ^{3}He cryostat is to condense ^{3}He gas by bringing it in thermal contact with a pumped ^{4}He reservoir, referred to as a 1 K pot. Once the ^{3}He has condensed, temperatures below 0.3 K are achieved by reducing the vapor pressure on top of the liquid ^{3}He reservoir, in our case, by an active carbon cryopump. The cryostat and all its components are shown in Fig. 3.4.

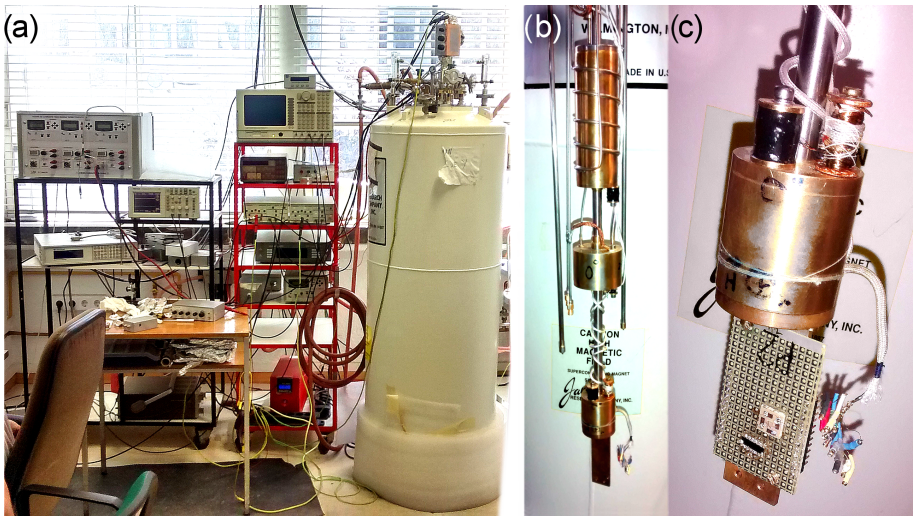

Figure 3.4: (a) Cryogenic system for low frequency noise measurements. (b) ^{3}He insert, where the active carbon cryopump, 1K pot, liquid ^{3}He pot and sample mount can be seen. (c) Mounted samples. The colored pins connect the junctions to the measurement circuit.

An external magnetic field may be applied to the samples in any direction of space by a 3D superconducting magnet, composed of a single coil for the Z-axis and two Helmholtz coils for the X and Y axes. The coils have been calibrated at $T = 4.2K$ (submerged in liquid ^{4}He). The X, Y and Z axes can produce magnetic fields up to B =1 T, 1 T and 3.5 T, respectively. The 3D magnet and the calibration of each axis is shown in Fig. 3.5 (a) and (b).

The sample is mounted on a sample holder, and contacted to lateral gold pins by gold wires and indium. Each tunnel junction has four contacts, two for voltage and two for current. The sample holder is fixed onto our ^{3}He insert (Fig. 3.4(c)), and each pin is contacted by manganin wires which connect the junction to the preamplifier, located atop the cryostat. The voltage connections are doubled (two manganin wires) because the signal is duplicated, as we mentioned above. Manganin is used because of its bad thermal conductivity. Our preamplifier allows us to switch between three different junctions, so for every cool-down of the cryostat, three junctions are contacted. The measuring circuit is the one described in the previous section.

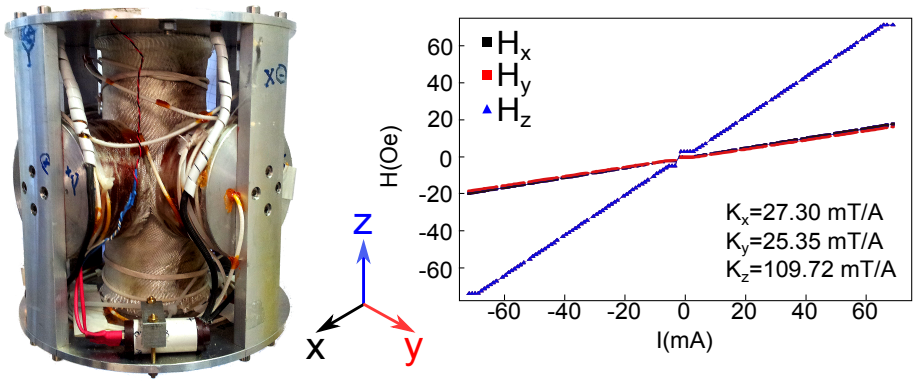

Figure 3.5: Photo of the 3D magnet and the H vs I calibration of each of the superconducting coils.

Our homemade current source is composed by a battery (or batteries in series, depending on the voltage needed), connected in series to variable resistors R_V. By reducing or increasing the total resistance in series with the batteries, the current through the circuit may be modified. Part of the variable resistance may be changed by a step-motor, R_{Motor}, which is controlled by Labview, so for every experiment we can vary the voltage between a maximum and minimum voltage. The spectrum analyzer, voltage reading, magnetic field and the current (between a maximum and minimum value) are all controlled by Labview, so long runs of measurements are automatically recorded.

3.3.1. Superconducting shunt and programmable triple current source

An important modification to the system, carried out during the course of this thesis, is is the addition of a **superconducting shunt** to the coil (or coils) of each axis of the magnet. The superconducting shunt consists on a superconducting wire which is surrounded by a heater. The function of the heater is to maintain the shunt in a normal conducting state when desired.

The shunt is connected to each magnet coil as shown in Fig. 3.6. If one wishes to vary the current in the magnet by the use of the current source, the shunt is kept in the normal state so the current goes through the coil, since it

is the electrical path of lowest resistance.

Superconducting currents in a superconducting loop may practically last indefinetely, depending on the dissipation of the circuit (bad contacts, solder points between different materials, etc). This is what occurs when the heater of the shunt is turned off. Whichever current the source was outputting at the moment the shunt becomes superconducting is trapped inside the superconducting loop. Thus, we are able to maintain a magnetic field while having the current source turned off. This is very useful for noise measurements, because the current source of the magnet introduces undesired effects in our signal of interest when the magnetic field used is higher than 0.1 T.

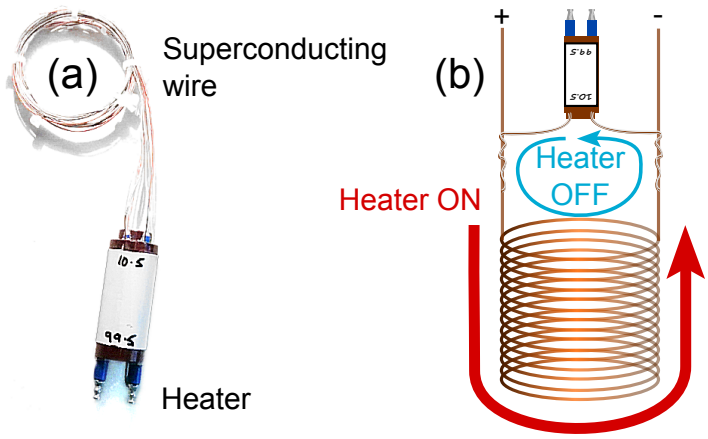

Figure 3.6: (a) Photo of one of the superconducting shunts used. (b) Diagram of the use of a superconducting shunt. When the heater is ON, the shunt is in the normal state and the current source provides the current for the coil. When the heater is OFF, the shunt is superconducting and a superconducting current is trapped.

To install each of the shunts, the superconducting coils had to be de-soldered from the copper wires which transmit the current from the source, and enough superconducting wire from the coil had to be carefully sanded down to remove the insulating varnish on it. The shunt was then coiled around the exposed coil wire, and the soldering joints re-done.

In order to control the heater of each shunt, and to have a better and uni-

fied control of the set of coils which compose the magnet, the technical support service (SegainvexUAM) of our university built a triple, **programmable current source**, shown in Fig. 3.7. The magnetic field desired may be expressed in spherical coordinates, and the progam will calculate how much current is needed from each source.

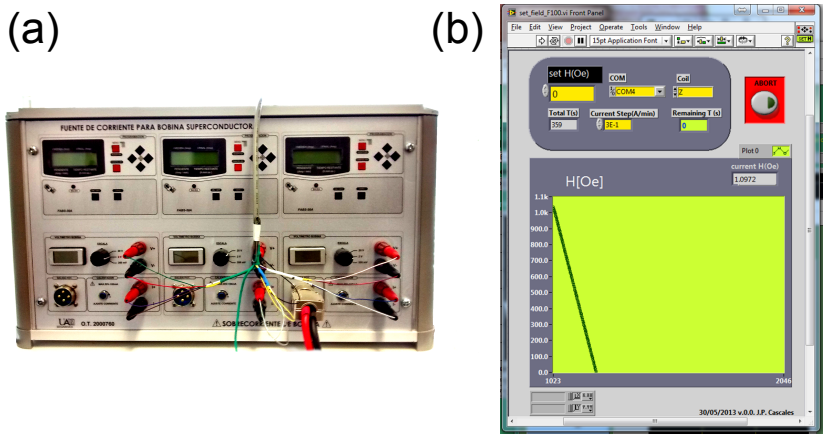

Figure 3.7: (a) Photo of the programmable current source (b) Labview window of the program controlling the current source.

3.4. Room temperature low frequency noise measurements

The room temperature set-up consists on an identical amplifying circuit as the one described above, although the way of contacting the junctions had to be modified with respect to the low temperature setup. In order for the system to serve for high and low frequency measurements, the contacts of the tunnel junctions are connected to our measurement circuit by microwave probes made by *Picoprobe* which serve as appropriate waveguides for the propagation of GHz signals. The sample is placed in the spacing between the iron core of an electromagnet. The contacted sample and the electromagnet can be seen in 3.8.

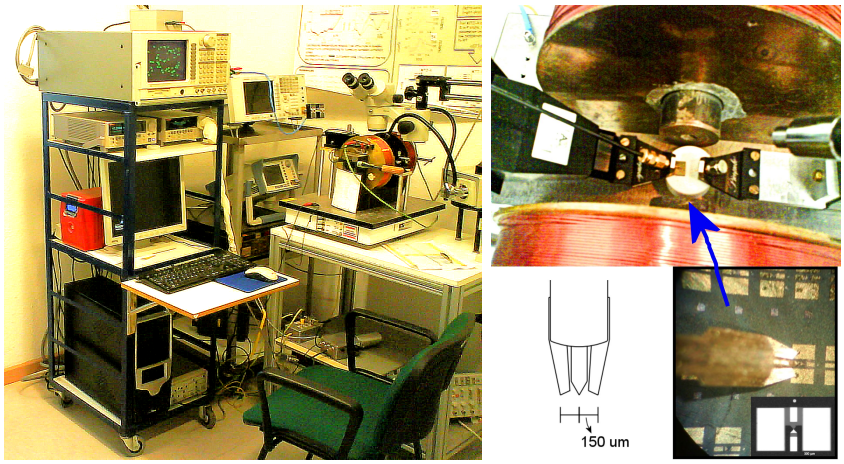

Figure 3.8: Room temperature low frequency set-up.

3.5. Room temperature high frequency noise measurements

A new experimental system has been created to carry out high frequency noise measurements with the use of an Agilent Technologies EXA signal analyzer. This high-frequency analyzer has a bandwidth from 9 kHz to 26.5 GHz, so thermally excited FMR and STT effects (see section 2.4) can be detected since they occur in the GHz range. In practice, we set the span of the analyzer to 18 GHz. The external magnetic field is varied using the electromagnet from the previous room temperature set-up, and the samples are contacted by the use of a *Picoprobe* waveguide.

An important part of the setup is the *bias tee* (Fig. 3.9), a three-port network which can either be used to separate the DC and AC parts of an incoming signal, or to join a DC and an AC signal into a single output. The three ports are: a low frequency port (LFP), a high frequency port (HFP), and a mixed signal port (MSP).

A diagram of the measurement circuit can be seen in Fig. 3.9. The measurement consists of the following steps: a DC current I, provided by a Keithley 6221 current source, is sent through the LFP, out the MSP, into the tunnel junction under study. The reflected signal, containing both the DC voltage

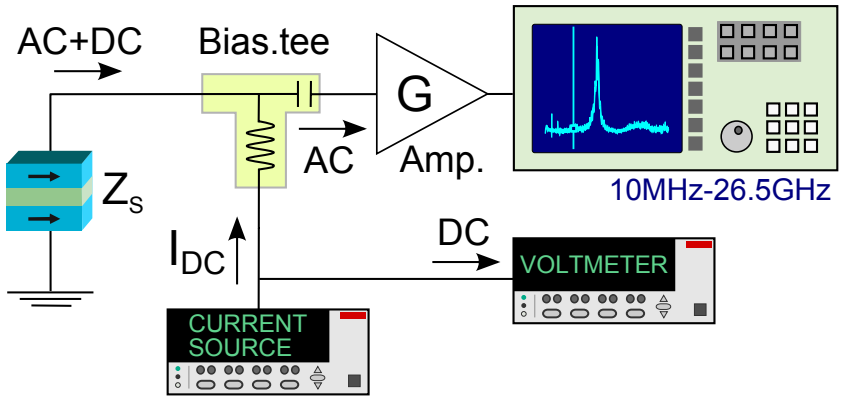

Figure 3.9: Room temperature high frequency set-up.

falling on the MTJ plus the AC voltage fluctuations (T-FMR, STT, etc), goes back into the MSP. The DC voltage out the LFP is measured with a Keithley 2182 nanovoltmeter. The high frequency AC signal coming out of the HFP is amplified by a Miteq AVG6 amplifier, and then input into the spectrum analyzer.

3.6. Calibration of the high frequency set-up

We will now proceed to explain the calibration method used to extract the effect of the circuit (its *transfer function*) on our signal of interest.

This calibration is based on the very detailed work presented in Ref.[139]. The calibration has been done in several steps, modeling each component or group of components of the circuit in an appropriate way. The circuit is modeled as shown in Fig. 3.10.

3.6.1. Bias tee, amplifier and spectrum analyzer

We will group the bias tee, amplifier and spectrum analyzer (SA) together in our calibration. Let us consider that this group may be described as a two-port network (or quadripole), with input impedance Z_{in}, gain G and output impedance Z_{out}.

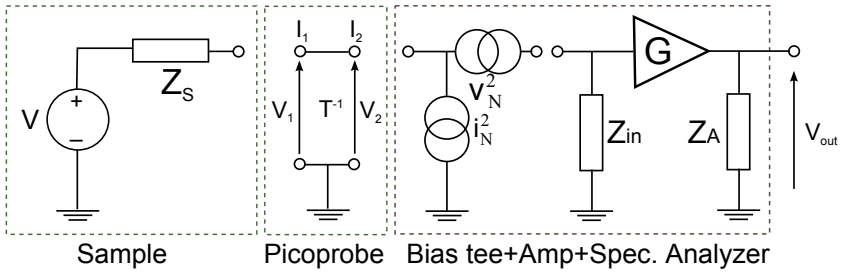

Figure 3.10: Model of the room temperature high frequency set-up.

If there are no noise sources in the circuit and v_s is the voltage falling on the sample, we have a voltage divider followed by the amplification of the signal. So if we connect a sample Z_s, the measured voltage v_m is given by:

$$v_m = G\frac{Z_{in}}{Z_s + Z_{in}}v_s$$

We will consider that the analyzer produces two independent, voltage and current noise sources v_n and i_n), so adding them:

$$v_m = G\frac{Z_{in}}{Z_s + Z_{in}}(v_s + v_n + Z_s i_n)$$

The spectrum analyzer obtains $\overline{|v_m|^2}$ over the bandwidth Δf (section 1.2.2). Since our signal is complex in principle, we have:

$$\overline{|v_m|^2} = G^2|\frac{Z_{in}}{Z_s + Z_{in}}|^2(\overline{|v_s|^2} + \overline{|v_n|^2} + \overline{|Z_s i_n|^2} + Z_s^*\overline{i_n^* v_n} + Z_s\overline{i_n v_n^*})$$

Since $Z_{in} = 50\Omega$, we can obtain the gain G, as a function of frequency ω, which can be done by measuring two different v_s and keeping Z_s constant.

A vector network analyzer (VNA) is used for this purpose. The VNA keeps Z_s at 50Ω, while outputting different voltages. Since in the VNA we can only select the output power, we have to measure the output power directly from the VNA to the SA, where we obtain v_{s_i} with $i = 1, 2$.

We then connect our bias tee and the amplifier between the VNA and the SA and measure the voltage for the same two output values of power, i.e. v_{m_i}.

We then have two equations with G, so subtracting one from the other, we can get (as a function of ω):

$$G^2 = \left|\frac{Z_s + Z_{in}}{Z_{in}}\right|^2 \frac{|v_{m_2}|^2 - |v_{m_1}|^2}{|v_{s_1}|^2 - |v_{s_1}|^2}$$

3.6.2. Picoprobe

The probe circuit can also be treated as a quadripole. A quadripole is an electrical circuit or device with two pairs of terminals connected together internally by an electrical network. Two terminals constitute a port if they satisfy the port condition: the same current must enter and leave a port.

There is more than one way of describing a quadripole (through its impedance matrix, scattering matrix, etc). We use the **transmission matrix**, much more convenient for our case.

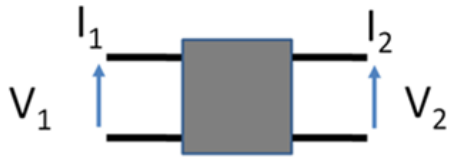

Figure 3.11: Sketch of a two-port network or *quadripole*.

The transmission matrix $\mathbf{T}$ relates the input voltage and current V_1, I_1 to the output current and voltage V_2, I_2 (shown in Fig. 3.11) as follows:

$$\begin{pmatrix} V_1 \\ I_1 \end{pmatrix} = \begin{pmatrix} A & B \\ C & D \end{pmatrix} \begin{pmatrix} V_2 \\ I_2 \end{pmatrix}$$

This matrix is unitary, that is:

$$AD - BC = 1$$

We need to determine these coefficients as a function of ω. This description is equivalent to the previous one, so:

$$Z_{in} = V_1/I_1,\ G = V_2/V_1,\ Z_l = V_2/I_2$$

which can be expressed in terms of the matrix coefficients

$$Z_{in} = \frac{Z_l A + B}{Z_l C + D}$$

$$G = \frac{Z_l}{Z_l A + B}$$

So, we can measure Z_{in} of the quadripole, which corresponds to measuring the impedance of the system in reflection, $Z_r(\omega)$.

$$Z_r(\omega) = \frac{Z_l(\omega) A + B}{Z_l(\omega) C + D}$$

If we do it for three different Z_l, we will have a system of four equations (three from the different Z_L's and the unitary condition for $\mathbf{T}$) with four unknowns, so all the coefficients can be obtained.

We use a capacity (OPEN), an inductance (SHORT) and a 50 Ω load as our three different impedances. The different impedances are contacted with the probe, and found on a calibration substrate specially intended for this purpose. In the OPEN case, capacitive effects are the most relevant, while in the remaining two, inductive effects are the ones that dominate. The values for the capacity or inductance of the impedances are given by the manufacturer.

Then, our system of equations is:

$$Z_O(\omega) = \frac{A + jC_0\omega B}{C + jC_0\omega D}$$

$$Z_S(\omega) = \frac{jL_s\omega A + B}{jL_s\omega C + D}$$

$$Z_L(\omega) = \frac{jL_{50}\omega A + B}{jL_{50}\omega C + D}$$

$$AD - BC = 1$$

These coefficients give the transmission matrix in the direction of propagation opposite of the one we need. Our final result is the inverse matrix of $\mathbf{T}$, T^{-1}, with coefficients a, b, c and d, where:

$$a = D, b = -B, c = -C, d = A$$

3.6.3. Calibration of the samples

Since magnetic tunnel junctions are essentially a capacitor in the shape of a nanopillar, capacitive and inductive effects appear in the signal from the sample itself. Removing the filtering effect of the sample from the measurements is referred to as $de-embedding$, and the magnetic tunnel junctions can be modeled by the circuit shown in Fig. 3.12 (a) (see Ref.[139]). The tunnel junction used in this graph is one of the nanopillars of sizes under 100 nm discussed in Chapter 4. Using the VNA, we can obtain the real (resistive) and imaginary (capacitive and inductive) parts of the impedance Z_s of the junctions as a function of frequency. From these graphs, we can extract the R, L, C and r values of each junction.

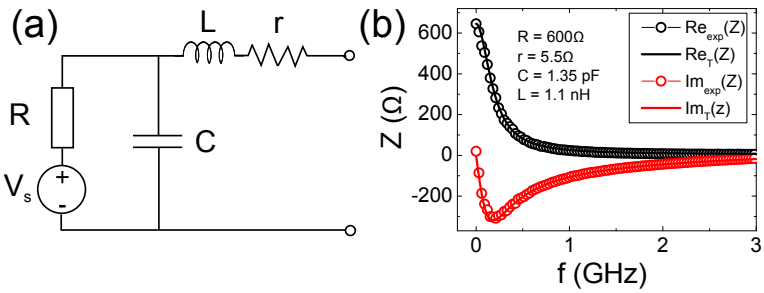

Figure 3.12: (a) Modeling of the samples[139]. (b) Extraction of the sample parameters from the impedance vs frequency graph.

3.6.4. Complete transfer function

Considering the sample as a voltage noise source v_s in series with the sample impedance Z_s, we can connect the different parts of our model (Fig. 3.10) and obtain the global transfer function.

$$v_s = Z_s I_1 + V_1$$

$$V_2 = I_2 Z_{in}$$

$$v_m = G V_2$$

Using the transmission matrix, we can relate:

$$V_1 = aV_2 + bI_2$$

$$I_1 = cV_2 + dI_2$$

and knowing that:

$$v_s = (1 + j\omega RC)V_1 + [R + (1 + j\omega RC)(r + j\omega L)]I_2$$

we obtain the relation between the measured spectral density $S_{v_m}(\omega)$ and the spectral density of the sample's fluctuations $S_{v_s}(\omega)$ by:

$$S_{v_m}(\omega) = G^2 \frac{|Z_{in}|^2}{|\theta(\omega)|^2} S_{v_s}(\omega) \tag{3.4}$$

where

$$\theta(\omega) = (1 + j\omega RC)(aZ_{in} + b) + [R + (1 + j\omega RC)(r + j\omega L)](cZ_{in} + d)$$

Thus, the transfer function relates $S_{v_m}(\omega) = |H(\omega)|^2 S_{v_s}(\omega)$. The modulus squared of the transfer function for the junction from Fig. 3.12 (b) is plotted in Fig. 3.13.

The periodic modulation of the curves (or *ripple*) seen in the high frequency measurements is caused by standing waves generated from the reflection of the GHz signals in bends of the circuit wires, or when a connection between two components is not impedance-matched. The period of the modulation corresponds to the length of the wire where the standing wave appears. The *ripple* may be removed from the graphs with a simple Fourier transform filter.

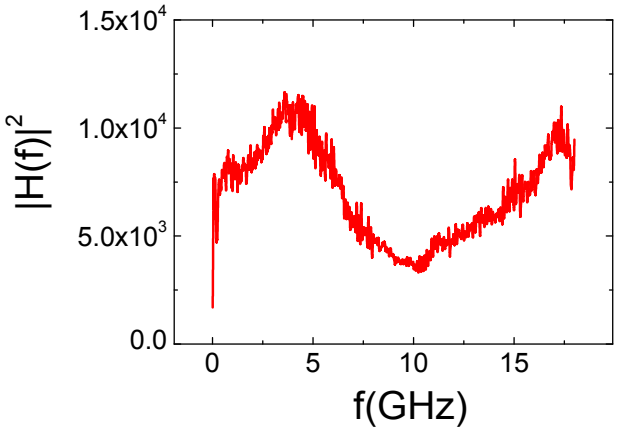

Figure 3.13: Modulus squared of the transfer function for the sample in Fig. 3.12.

3.7. Data analysis

In relation to low frequency noise, we have carried out an extensive work regarding the analysis of the data. The main goal was to improve the relative error of the estimated parameters extracted from the spectra or time series, as well as converting the analysis of the data to a semi−automatic and reliable process.

We have written MATLAB programs which incorporate fixed criteria, and only require a minimum input by the researcher. Regardless of the good functioning of the programs, the analysis, curve fittings, etc, are always supervised should strange results arise. The improvements in data analysis have focused on estimating the parameters of 1/f noise, shot noise and random telegraph noise.

3.7.1. 1/f noise analysis

For spectra presenting 1/f noise (equation 2.11), we have

$$S_V(f) = \frac{\alpha V^2}{A f^\beta} \Rightarrow log\left(S_V(f)\right) = log\left(\frac{\alpha V^2}{A}\right) - \beta log(f)$$

so if we perform the linear fit $y(x) = mx+n$ to the logarithm of the spectrum (with $x = f$), $\alpha = Ae^n/V^2$ and $\beta = -m$. Each parameter is obtained with its standard deviation.

The range of frequencies $[f_{min}, f_{max}]$ for which the fit is carried out is determined before running the program. Also, the band-pass filter of the SR560 amplifiers is undone by dividing the spectra by the filter's transfer function. For this, the high-pass and low-pass cutoff frequencies must be indicated as well. Unwanted peaks sometimes appear in the spectra which come from the power grid (50Hz and its multiples), and they are also automatically removed. An example of a successful fitting is shown in Fig. 3.14. The analyzed spectra usually contain a dominant 1/f contribution from the sample for a bias above 10 mV, while the measurement lines and current source contribute negligibly.

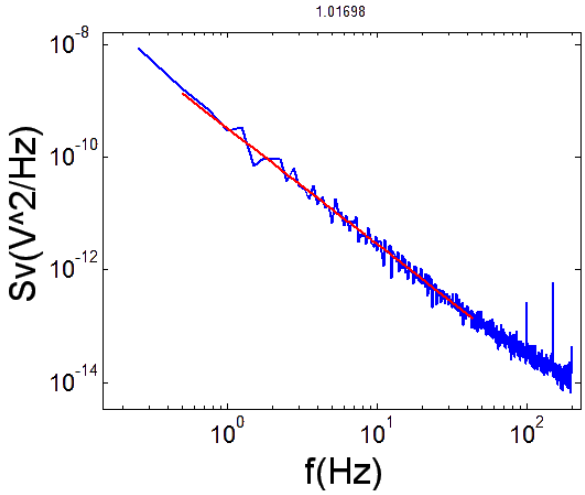

Figure 3.14: Fit of equation 2.11 to a spectrum presenting 1/f noise.

3.7.2. Shot noise analysis

For spectra presenting a frequency independent region (i.e. flat), we have two different options for extracting the value of shot noise.

If the spectrum is 1/f-like at first, and is frequency independent at higher frequencies, we can consider describing it by:

$$S_V(f) = \frac{\alpha V^2}{A f^\beta} + S_V^{white}(f) \tag{3.5}$$

where S_V^{white} corresponds to the white noise (shot noise, thermal noise and noise from the amplifiers). If we fix $\beta = 1$, a fit of the type $y(x) = a/x + b$ yields $\alpha = aA/V^2$ and b is equal to the white noise value. The minimum and maximum frequency between which the fit is carried out is defined at the start. The result of such a fitting is shown in Fig. 3.15 (a).

Another alternative is to calculate the histogram of the spectrum. Since the flat part of the spectrum oscillates around the value corresponding to the white noise amplitude, the result of the histogram is a Gaussian curve centered at S_V^{white}. By fitting the histogram with $y(x) = Ae^{-\frac{(x-x_0)^2}{\sigma^2}}$, the white noise amplitude is given by x_0 and its standard deviation by σ. A typical fit of this sort is presented in Fig. 3.15 (b).

When the temperature is low enough (T=0.3 K) so $eV \ll k_B T$, then the white noise obtained corresponds to the shot noise from the sample, plus some electronic noise from the experimental setup. Supposing this noise remains constant with the applied bias, we extrapolate the value of noise from the electronics from shot noise measurements. The shot noise must scale linearly with the voltage (eq. 2.3), and must be zero at zero bias. So the noise from the electronics is estimated as the offset which must be subtracted from the mesurements so the shot noise is zero at zero bias. For higher temperatures, also the thermal noise is subtracted from the measurements to extract the shot noise using equations 2.3 and 2.4.

3.7.3. Random telegraph noise analysis

Two different methods of analyzing random telegraph noise have been developed.

3.7.3.1. Using the time series and spectrum.

This is the most usual method found in the literature to obtain the time constants of the process. Our program saves two files, for the time series and

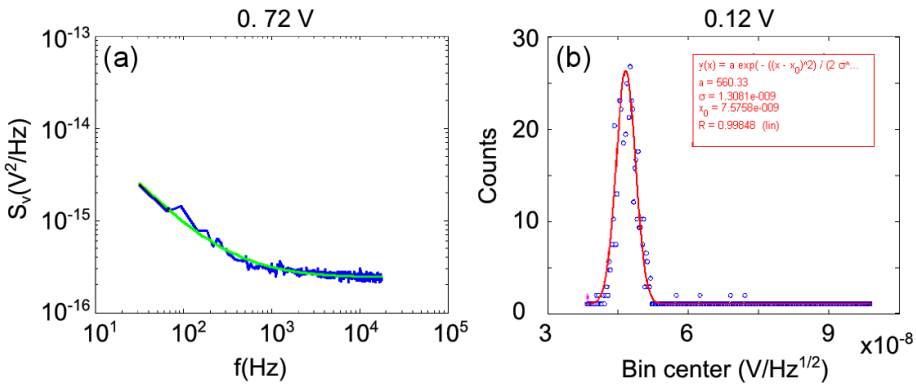

Figure 3.15: Fit of (a) equation 3.5 to a spectrum presenting 1/f and shot noise or (b) a Gaussian to the histogram of a spectrum presenting shot noise.

the spectrum, at each value of the parameter that is being varied (current, voltage or magnetic field).

If we are studying 2-state RTN, the histogram of a time series will have two gaussians, centered around the voltage values of each state. We calculate the value of each timeseries, and fit two Gaussian peaks to it. The difference in voltage ΔV between the levels is estimated from the difference between the center of the peaks $\Delta V = x_0^{up} - x_0^{down}$. Then, using equation 2.14, we can fit the spectrum by $y(x) = \frac{AT^2}{1+(2\pi Tx)^2}$ where $A = \frac{4\Delta V^2}{(\tau_{up}+\tau_{down})}$ and $T^{-1} = 1/\tau_{up} + 1/\tau_{down}$. Thus, we have two equations, and since we know ΔV from the time series, only two unknowns, τ_{up} and τ_{down}. The program discards bad fits by checking the χ^2 value of the fit. An example of a good fit is shown in Fig. 3.16.

3.7.3.2. Using only the time series.

The time constants of the RTN process may be obtained only using the time series if a sufficiently large number of up-down, and down-up transitions are recorded. This way, fitting the spectrum with the theoretical curve is not necessary. The time constant τ_{up} may be estimated by the total time the time trace is in the *up* state, divided by the number of *up* terraces in the trace, which is equivalent to calculating the average of the duration of the *up* terraces. The same applies for τ_{down}. We have:

3. Experimental methods

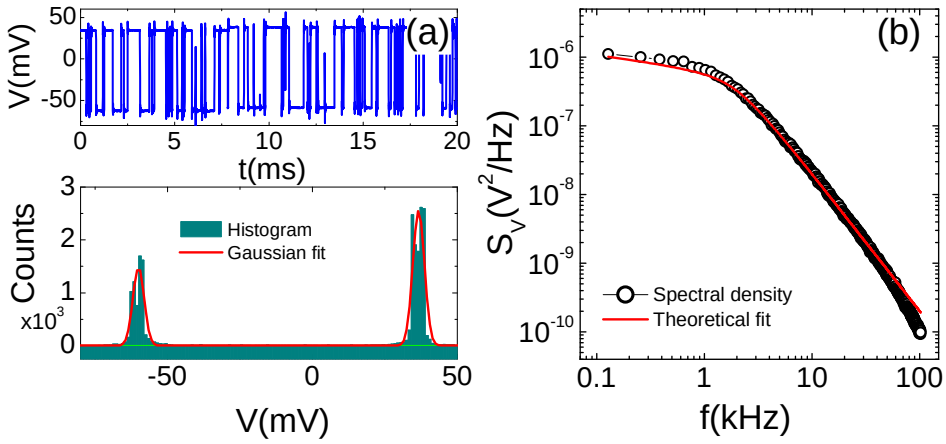

Figure 3.16: Fit of (a) two Gaussian peaks to the histogram of the time series and (b) the theoretical RTN equation to its respective equation.

$$\langle \tau_{up} \rangle = \frac{\sum_{i=1}^{N_{up}} t_i^{up}}{N_{up}}$$

$$\langle \tau_{down} \rangle = \frac{\sum_{i=1}^{N_{down}} t_i^{down}}{N_{down}}$$

Our program first calculates the histogram of the time series, makes sure there are two Gaussian peaks (2 state RTN), calculates the number of transitions, and finally gives an estimate for τ_{up} and τ_{down}.

Chapter 4

Spin-torque effects and noise in MTJs of sizes under 100nm

4.1. Introduction and motivation

In this Chapter, we present a comparative room temperature study of spin-torque and low frequency noise in MTJs of lateral size under 100 nm. We show that two types of spin torque related effects are detected: (i) current-induced switching is observed from TMR measurements and (ii) the influence of spin torque transfer effects on the magnetization dynamics. Although this thesis deals mainly with low temperature, low frequency noise measurements in MTJs of lateral size above a micron, this Chapter presents a combination of room temperature low (LF) and high frequency (HF) noise measurements in sub-100nm MTJs. Through low frequency noise measurements, the fluctuating magnetic moment involved in the current switching process is estimated for MTJs with external fields applied along the hard axis direction. These results are supported by micromagnetic simulations. Furthemore, the obtained 1/f noise presents features which indicate that traces of the magnetization dynamics are detected at low frequencies. The study of noise and the dynamics of the magnetization in sub-100 nm MTJs at low temperatures presents an important experimental challenge.

4.1.1. Spin transfer torque effects in nanoscale MTJs

To help readers, we begin with a bibliographical introduction on spin-torque effects observed in MTJs to serve as context. As we mentioned in Section 2.4, oscillations known as a ferromagnetic resonance arise from the precessional motion of the magnetization of a ferromagnetic material when an external magnetic field is applied in the presence of microwave pump field perpendicular to it. Since magnetic tunnel junctions are composed of ferromagnetic electrodes, it is possible to detect such resonance peaks if the spectra up to a few tens of GHz of their voltage fluctuations are measured.

Oscillations of the magnetization in magnetic tunnel junctions, specially of very small lateral size, could be driven in a different way. The fact that a spin-polarized electrical current flowing non-collinearly to the local magnetization, can apply a large torque to a ferromagnet, through the direct transfer of spin angular momentum[47], offers the possibility of manipulating magnetic elements in devices without the use of magnetic fields. Certain oscillatory magnetic modes, unreachable with magnetic fields alone, may be achieved by driving nanomagnets by spin polarized currents. As we have already mentioned (Section 2.4), the difference in the spin direction of a spin-polarized current and the magnetization of a ferromagnetic layer may change the spin direction of outgoing electrons with respect to incident electrons, and the difference in spin polarization can apply a torque on the ferromagnet. This is schematically shown in Fig. 4.1, and is referred to as the spin-transfer torque effect.

The spin transfer torque effect was independently predicted in 1996 by Slonczewski[47] and Berger[140]. They argued that a current flowing perpendicular to the plane in a magnetic multilayer structure could generate a strong enough spin transfer torque to reorient the magnetization of one of the FM layers. These studies sparked interest in the ST effect, and in 1998 the first measurements of current-induced resistance changes in magnetic multilayer devices were reported[141,142]. Spin torque induced magnetization reversal in lithographically patterned devices were observed shortly after[143,144].

In the regime where the current density applied to the MTJ is low, the resulting *damped oscillatory modes* are due to the external applied magnetic field and thermal fluctuations, referred to as thermal FMR (T-FMR). This

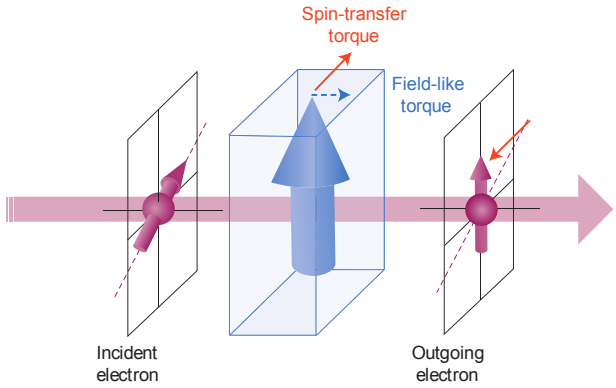

Figure 4.1: Illustration of the current-induced torque of a spin-polarized current on a ferromagnet. Adapted from Ref.[49]

effect is typically observed for applied current densities below $J \simeq 10^7 A/cm^2$[48]. The effective damping can be cancelled altogether by the spin torque from a d.c. current at some critical value of the current density J_C. This results in an auto-oscillation of the magnetization which is often referred to as a steady state precession.

The study of spin torque effects in magnetic tunnel junctions is not only of fundamental interest but has a huge technological importance as well. The ability to switch the magnetization of a FM layer with only current could pave the way for new, smaller and faster data storage devices. Using MTJs as data bits could be quite useful since their magnetic state may be switched only by current. Making the MTJs smaller would not only increase the storage density of the devices, it would reduce the amount of current needed to "write" each data bit, since the current density is inversely proportional to the area of the junction. When electrons flow from the free to the pinned electrode, the AP state is favored (and the P state is destabilized) for in-plane MTJs . Conversely, the flow of electrons from the pinned to the free electrode stabilizes the P state. Also, simple magnetic, multilayer structures may act as nanoscale oscillators, converting electrical d.c. energy into high-frequency magnetic oscillations which could be used as microwave sources and resonators. Although several studies show that a more effective ST effect could be reached with perpendicular magnetization[145,146], in this Chapter (as in the rest of the the-

sis) we will focus our discussion on magnetic tunnel junctions with **in-plane magnetization**.

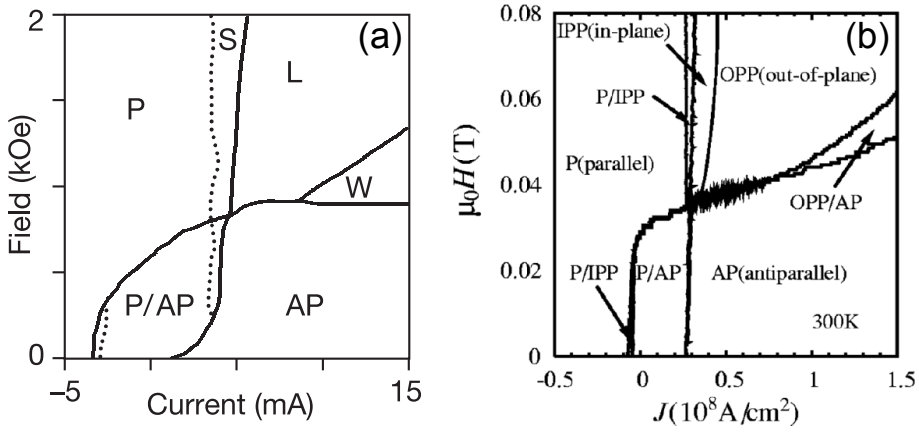

Figure 4.2: Switching phase diagram constructed from (a) experimental measurements of room-temperature current switching in a Co/Cu/Co spin valve[147] and (b) from the numerical integration of the LLG equation with the Slonczewski term, including thermal fluctuations at T=300 K[148].

A phase diagram of the magnetic state (P or AP) of MTJs as a function of the applied current (or voltage) and external magnetic field may be constructed from experimental magnetoresistance curves, which gives information about the critical switching currents and switching fields. Several authors have reported both experimental[147] and theoretical[148] studies of such diagrams, which show promise for the application of spin transfer based devices. One of the first experimental results of such phase diagrams, by Kiselev et al.[147], confirmed the spin transfer torque mechanism as an effective way to switch FM layers with currents in spin valves. Spin valves present a few disadvantages with respect to MTJs, as they present lower resistance and MR ratios. Fig. 4.2(a) presents a experimental current switching phase diagram obtained at room temperature by Kiselev et al.[147], for Co/Cu/Co spin valves of elliptical cross-sections (130x70nm^2). In this graph, positive current I denotes the flow of electrons from the free to the fixed layer. As is shown, the state diagram is constructed from the resistance *vs*. field curves, which indicate at which currents or fields a change in the magnetic configuration occurs. The authors extract the depen-

dence of the modes of the multilayer structure as a function of the current and external field. At low current, the field dependence of the observed oscillations correspond to small-angle precession and can be described by the Kittel formulas[50]. The zones in Fig. 4.2(a) labelled with S and L indicate *small* and *large* angle precession, respectively. Macrospin simulations reproducing the previous experiment can be found in Ref.[148]. The model captures the essential features of the experiment when thermal fluctuations are included, as can be seen in Fig. 4.2(b).

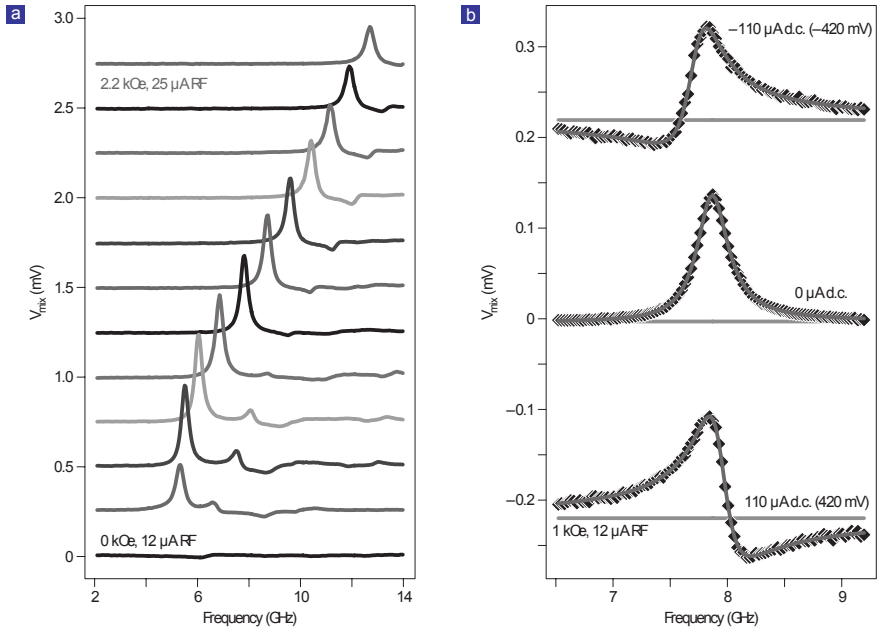

Figure 4.3: ST-FMR spectra at room temperature for: (a) I =0 for in plane magnetic fields spaced by 0.2 kOe. I_{RF} ranges from 12 μA at low field (high resistance) to 25 μA at high field. (b) Primary ST-FMR peaks at H = 1000 Oe and $I_{RF} \sim 12\mu$A for different d.c. biases. Symbols are data; lines are lorentzian fits. Adapted from Ref.[149]

The first quantitative measurements of the direction and magnitude of the spin-transfer torque effect in magnetic tunnel junctions were carried out by Sankey et al.[149] and Kubota et al.[150]. In the work by Sankey et al.[149], the authors measure the bias and angular dependence of the spin-transfer torque

in CoFeB/MgO/CoFeB MTJs by using spin-transfer-driven ferromagnetic resonance (ST-FMR) technique[151]. The ST-FMR technique consists on biasing the sample with both a direct current I_{DC} and a microwave-frequency current I_{RF} through a bias-tee, and then sweeping the RF frequency. The spin-transfer torque from I_{RF} may excite resonant magnetic dynamics, which causes the resistance to oscillate at the driving frequency, and the resonant voltage response is measured by a lock-in. The fitting of the main ST-FMR peak by an equation derived from a macrospin model gives information on the magnitude and direction of the torque. The authors find that the torque lies in plane at low currents, while an out of plane component is found for higher bias. Fig. 4.3 shows (a) how the frequency of the resonance peak varies with the magnetic field and (b) how the line-shape resonance peak at a fixed field changes with the bias.

The work by Kubota et. al[150] used the spin-torque diode effect[152] to estimate the charactersitics of the spin-transfer torque in MgO-based MTJs. The spin-torque diode effect in an MTJ consists on the application of a small radio-frequency alternating current to a nanoscale MTJ, which can generate a measurable d.c. voltage across the device when the frequency is resonant with the spin oscillations that arise from the spin-torque effect. The authors study the spin-transfer torque for biases beyond the critical switching current. They estimate a considerable perpendicular torque at high biases, although the values found for the in-plane torques differ from Ref.[149]. This could point to the importance of the perpendicular component of the torque for inverting magnetization by current.

A rather complete study of the oscillation modes present in nanoscale MTJs was carried out by Helmer et al.[153]. In this article, the authors study the field dependence of the mode frequency of thermally excited spin waves (T-FMR) in MgO-based, rectangular nanopillar MTJs of lateral sizes between 60x100nm and 105x190nm. The experimental results are backed by calculations based on the diagonalization of the dynamical matrix of a system of three coupled, spatially confined magnetic layers. The result is presented in Fig. 4.4, where the calculated dependence of the oscillation modes with the external field is shown for fields applied along the (a) easy and (b) hard axis of magnetization. Modes originating from the free layer or the synthetic antiferromagnet are identified,

as each category presents a characteristic shape. This result is important and we will use it to identify the oscillation modes observed in our samples further on.

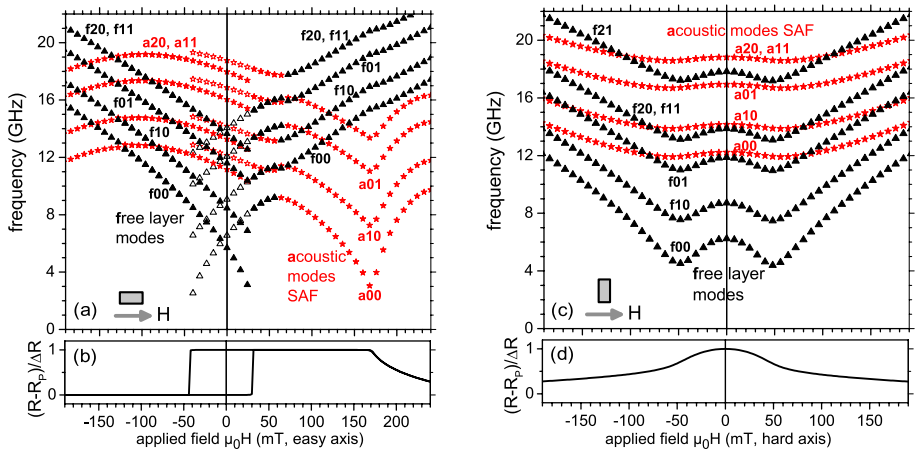

Figure 4.4: Calculated mode frequencies versus magnetic field along (a) easy axis and (c) hard axis for a rectangular nanopillar. (b) and (d) show the corresponding calculated hysteresis loops. Adapted from Ref.[153]

4.1.2. Transition from T-FMR to a steady state precession

The next step towards making a practical use STT effects was presented in parallel theoretical[154,155] and experimental studies[156]. The transition from the T-FMR regime to an in-plane, steady state precession (SSP) state is studied in CoFe/Cu/CoFe/NiFe spin valves of nanoscale size ($50\text{x}100\text{nm}^2$)[156]. The transition is identified from the sudden decrease in the frequency and linewidth Δf accompanied by an increase output power P of the emitted microwaves on the applied current (Fig. 4.5(a)). Petit et al.[157] found the influence of spin-torque on HF fluctuations in nanoscale CoFe/ Al_2O_3/ CoFe/ NiFe magnetic tunnel junctions. The authors study the dependence of the frequency, linewidth and oscillation amplitude for current densities below the critical value for spin torque. They find that the magnetic fluctuations are either reduced or enhanced

by the d.c. current bias depending on its polarity.

Further work on this effect was presented by Houssameddine et al.[56] *on the same type of samples as we deal with in this Chapter*, which are described in the following Section. The authors study the transition from T-FMR to a steady-state precession in nanoscale MgO tunnel junctions. They find that the devices presenting the clearest transition to the steady state (steep decrease in frequency, narrower linewidths, high increase in output power) exhibit low resistance and TMR ratios of around 30%. The transition for high (HTMR) and low (LTMR) resistance junctions is shown in Fig. 4.5(d) and (e). The authors consider the LTMR samples to have nonuniform tunnel barriers (when the MgO thickness is reduced below 1 nm), so localized high-current densities could potentially create nonhomogeneous excitation modes.

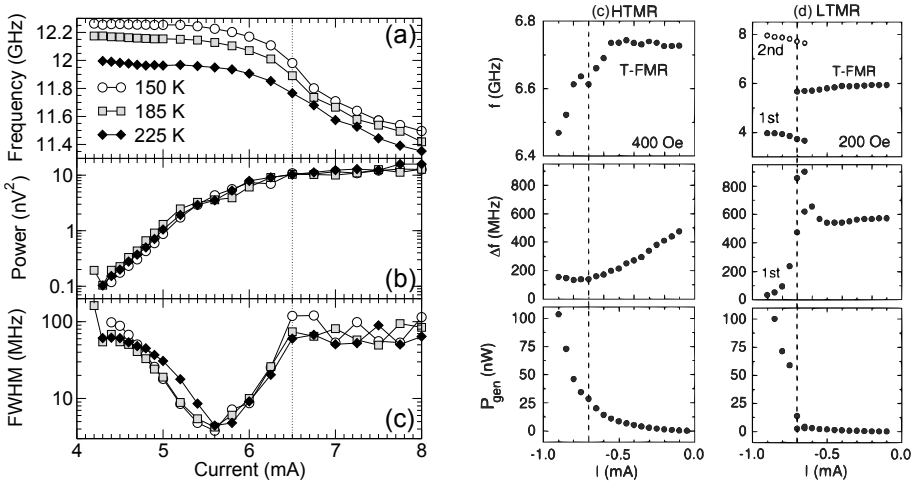

Figure 4.5: (a) Frequency, (b) power, and (c) linewidth of the fundamental mode as a function of applied current in sputtered CoFe/Cu/CoFe/NiFe spin valves. Adapted from Ref.[156]. Frequency, linewidth, and integrated power vs current I for (d) the high resistance and (e) low resistance nanoscale MgO MTJs. Adapted from Ref.[56]

In a later publication, Houssamedine et al. investigated the details of the transition from T-FMR to a SSP by time-domain measurements of the magnetization oscillations in LTMR samples[158,159]. This study presents an important result: the steady state regime identified in Ref.[56] from the analysis of

frequency-domain results is actually divided into two regimes. These regimes occur in HTMR and LTMR devices alike, as discussed in Ref.[159], but the transition to the SSP presents a higher and sharper change as the samples tend to the LTMR type. Fig. 4.6 presents (a) f and (b) Δf as a function of the current for a LTMR device with a TMR of 50%[159]. The first corresponds to currents $|I| > |I_c|$, where I_c is the current which onsets the decrease in frequency, linewidth and increase in microwave power. This regime presents *intermittent* steady state oscillations which decay every few ns ("turn" off and on) (Fig. 4.6(c),(e)) and which present slightly different oscillation frequencies each time. These changes in frequency are responsible for the magnitude of the linewidth of the resonance peak. The second regime corresponds to $|I| > |I_c^*| > |I_c|$, where I_c^* is a second critical current above which the SSP does not decay (Fig. 4.6(d),(f)). In this regime, the frequency fluctuations (phase noise) yield a linewidth of the order of 25 MHz. The linewidth of a time segment during which the frequency remains constant is of 1.4 MHz.

Returning to pseudo pinholes (or "hotspots") and barrier inhomogeneities, these defects are naturally present in magnetic tunnel junctions with ultrathin barriers[160], but they can also be created artificially by a soft breakdown[102]. The presence of pseudo pinholes was suggested to qualitatively modify the magnetoresistance[161] and the magnetization reversal mechanisms in MTJs, even in the absence of ST effects[162,163]. Although shot noise could be used to characterize ultrathin barriers in sub-100nm MTJs, it has not been extensively studied, as they present higher 1/f noise amplitudes. The study by Zhong et al.[164] of shot noise in MgO based MTJs with areas $10^{-2}\mu\text{cm}^2$ reveals Poissonian statistics with barriers 0.95 nm thick.

There has also been some controversy with respect to ST in MTJs with pinholes. While numerical calculations for a single[165] or for multiple hotspots[166], point to a decrease of the threshold ST current in comparison with nonbroken MTJs, Finocchio et al.[167] predict an increase of the minimum current to excite microwave dynamics in junctions with pinholes. Thus, the realization that nonhomogeneous barriers create local, high current densities could constitute an important step forward in the application of these devices as components of data storage technology.

In this Chapter, we will present a comparative study of high and low fre-

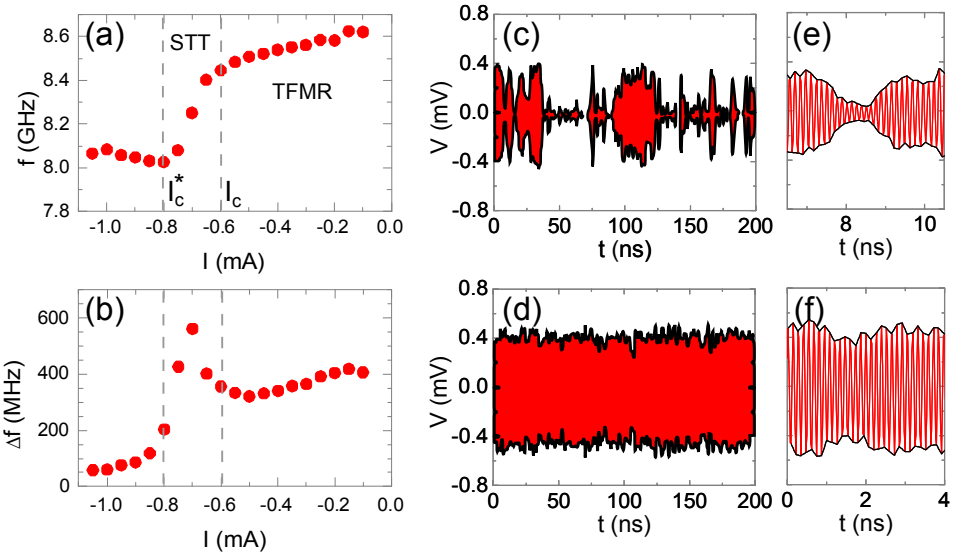

Figure 4.6: Current dependence of the emission frequency in a LTMR (50%) devices presenting a decrease in (a) frequency and (b) linewidth with the current at I_c, which become constant at I_c^*. Adapted from Ref.[159]. 200 ns segment of the full time trace (gain corrected) for (c) $|I_c| < |I| < |I_c^*|$ and (d) $|I| > |I_c^*|$. 4 ns zoom revealing the high frequency oscillations for (e) $|I_c| < |I| < |I_c^*|$ and (f) $|I| > |I_c^*|$. Adapted from Ref.[158].

quency noise in elliptical MTJs of lateral dimensions under 100 nm, which exhibit spin transfer torque effects which could be enhanced due to reduced barriers. The experimental setups for HF and LF noise measurements were described in Chapter 3. An external magnetic field is applied in both the hard and easy axis (HA or EA) of magnetization. The high frequency spectra in the GHz range present peaks corresponding to the FMR modes of the multilayered structures, so the effect of the spin-polarized current on the oscillation modes can be estimated. We will show that we can indirectly obtain information about the current-switching phenomena and the changes in the oscillation modes with the current by the combined study of TMR and LF noise measurements. The analysis of these HF results will be compared with data obtained from LF measurements, ideally in the same sample and under the same conditions, in order to determine whether the spin-torque driven effects discussed above can

be detected (or not) in LF noise measurements. *1/f noise around the transition of a damped oscillation to a steady state precession has been observed*[168] *and calculated*[169] *in previous studies, but to our best knowledge it has not been analyzed systematically.* Possibly, the most complete study of 1/f noise and spin torque effects is the work done by Eklund et al.[170], in which the the 1/f noise up to 150 MHz and the white noise up to 25 GHz is measured in nano-contact spin valves. The dependence of the 1/f and white noise is found to be related to the linewidth of the oscillation. The oscillation linewidth in such devices has been found to be due to the phase noise originated from the nonlinearity of the oscillation frequency (i.e. the frequency depends on the oscillation amplitude)[171].

In this context, our LF measurements should constitute a better quantification of the stochastic hopping and the role of the thermal noise at the transition between the T-FMR to SSP transition in the kHz range. This realization could be immensely useful, as the experimental setup for noise measurements in the kHz range is technically simpler than for high frequency signals (MHz-GHz), as it requires standard BNC connections, cheaper electronics, etc. Obtaining both low and high frequency data in one single MTJ was often difficult, as switching from one setup to another involves electrically disconnecting the MTJs, which frequently resulted in a partial or full degradation of the sample. We will present the more significant and illustrative results.

Both easy and hard axis measurements present current magnetization reversal effects. The hard axis data present current switching effects from the P to the AP state (negative currents) while the measurements with field along the easy axis promote the P state (positive currents) by shifting the coercive field to lower values. The current-switching effects observed in our nanoscale MTJs are reproduced by micromagnetic simulations of an MTJ with a reduced barrier (or pseudo-pinhole).

4.2. Sample characteristics

The fabrication of the junctions was carried out by Dr. Jordan Katine at Hitachi Global Storage Technologies, and were supplied to our group through a collaboration project with the group of Dr. Ursula Ebels at SPINTEC, in

CEA Grenoble (France).

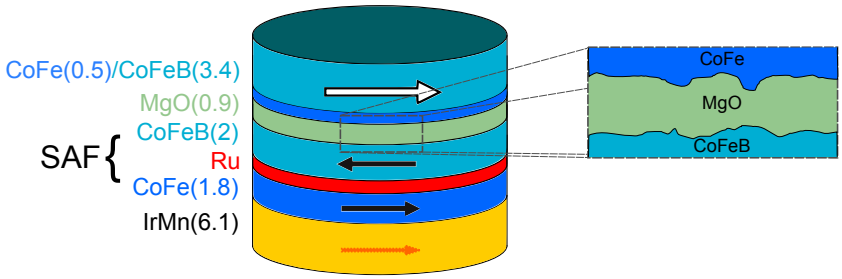

Figure 4.7: Diagram of the elliptical nanopillar layer structure, presenting a non-homogeneous 0.9 nm thick MgO barrier.

As is shown in Fig. 4.7, the multilayer nanopillars have the following structure:

IrMn(6.1)/CoFeB(1.8)/Ru/ CoFe(2)/MgO(0.9nm)/CoFe(0.5)/CoFeB(3.4)

where the numbers indicate the thickness of the layer in nm. The pinned layer consists of two ferromagnetic layers which are antiferromagnetically (AF) coupled through a thin ruthenium layer. This structure is referred to as a *synthetic antiferromagnet* or SAF. An antiferromagnetic IrMn layer, exchange-coupled to the lower ferromagnetic layer, is added to rigidify the synthetic AF. The MgO barrier is deposited by sputtering and the free layer consists of a bi-layer of CoFe/CoFeB. The measured nanopillar devices have elliptical cross-sections of different sizes, with the minor and major axes ranging from 40×80 to 65×130 (in nm), and a nominal RA product of 1.5 $\Omega\mu m^2$. The easy axis (EA) direction is parallel to the pinned layer's magnetization and it coincides with the major axis of the ellipse, while the in-plane hard axis (HA) is perpendicular, but still in-plane, to the easy axis. The devices are embedded in impedance matched RF coplanar waveguides for electrical contacting using special RF probes. *In our measurements, positive voltage means that electrons flow from the pinned to the free electrode, promoting the P state. Negative voltage favors the AP state.*

The wafer contains MTJs contacted with waveguides in two different configurations: reflection and transmission. For the reflection configuration, only one

probe is needed to contact the MTJs, while two are needed in the transmission mode. The wafer also includes other types of waveguides for the calibration of the measurements: a short with 50 Ω of impedance, a transmission line and a capacitance (or open waveguide). Figure 4.8 shows a photograph of the wafer, where we identify reflection and transmission MTJs and the line and short waveguides.

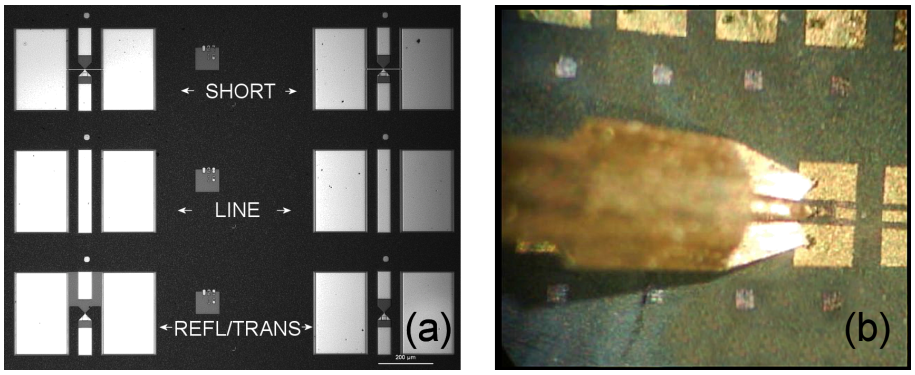

Figure 4.8: (a) Image of the substrate, containing short and line type waveguides, as well as transmission and reflection MTJs. (b) View through the microscope of a reflection MTJ contacted with our RF probe.

Previous measurements on devices of this kind[56,158,159] have shown that the devices fall into two different groups: samples with high resistance and TMR ratios around 90% (labeled HTMR) and samples with low resistance and TMR ratios around 30-60% (labeled LTMR), as shown in Fig. 4.9. The authors report that repetead high-current measurements on HTMR devices may gradually turn them into LTMR devices. These LTMR devices seem to be stable against high-current measurements, and the authors speculate that the difference between sample types could be due to localized reductions in the tunneling barrier[56].

Let us now discuss the characteristics of the samples measured in our experiments. Indeed, the statistics of our MTJs reveal a mean TMR value of around 60% and an average RA product of 1.8 $\Omega\mu m^2$ (in agreement with the nominal value of 1.5 $\Omega\mu m^2$). Fig. 4.10 presents a histogram with the obtained TMR values, clearly showing two (or three) distinct groups of low and

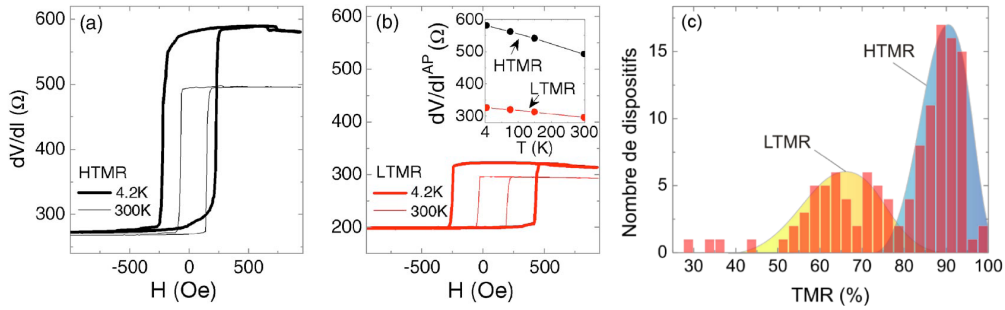

Figure 4.9: Field-dependent transfer curves for (a) HTMR and (b) LTMR elliptical devices at 4.2 and 300 K. The inset in (b) shows the evolution of the AP-state dV/dI with temperature for both types of devices[56]. (c) TMR distribution of the measured samples, presenting two different types of junctions (LTMR and HTMR)[159].

high TMR junctions, which corresponds quite well to what was reported in Ref.[159] (Fig. 4.9(c)). A considerable amount of MTJs were only measured with field applied along the hard axis. We have estimated the easy axis TMR value of these samples from their hard axis TMR ratio and the expression $TMR(HA) = TMR(EA)(1 - cos\theta)/(2 + \chi(1 + cos\theta))$[172], with $\chi = 2$.

MTJs with ultra-low RA are interesting for practical devices (STT-MRAM, STO, read head in hard disk drives). For junctions with low MgO thicknesses (and low RA products, correspondingly), there exists a correlation between the TMR ratio and the MgO thickness[20]. A decrease in TMR is experienced when the thickness of the MgO barrier is reduced, due to local inhomogeneities (or pseudo-pinholes) in the MgO barrier. Obtaining MTJs with low RA products and high TMR ratios, for which homogeneous barriers are needed, is a real engineering challenge. The STT effect requires high current densities, and since MgO barriers only withstand a certain amount of voltage, having a low RA allows high currents to flow through the MTJ without causing the breakdown of the barrier[173]. *Therefore, we will focus on LTMR MTJ devices with reduced MgO barriers as they are perfect candidates to study magnetization dynamics and spin torque effects in their magnetic layers.*

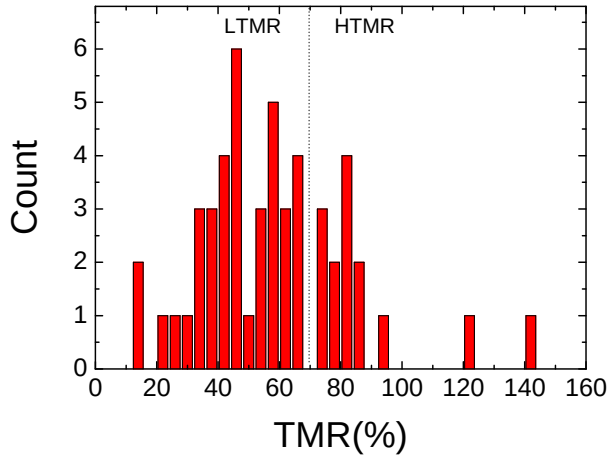

Figure 4.10: Histogram of the TMR values of the measured samples. The graph shows the samples are distributed into groups of high and low TMR samples.

4.3. External field along the easy axis of magnetization

When the external field is directed along the easy axis of magnetization (long axis of the ellipse), we can observe a step-like transition in resistance, from the AP (positive fields) to the P state (negative fields). As an example, we show high and low frequency noise measurements carried out in the same 40x80nm^2 sample.

The first effect that was noticed in these samples was a shift in the coercive field with the current, shown in the TMR graphs in Fig. 4.11(a). The TMR curves were obtained by sweeping the field positive to negative values . Only *half* a hysteresis cycle is shown to observe the change in coercive field. A full TMR cycle taken at low bias (2 mV) is shown in the inset of Fig. 4.11(a). As can be seen in Fig. 4.11(b), the coercive field H_C is stable for negative currents, for which electrons flow from the free to the pinned layer, favoring the AP state. For positive currents (electrons flow from the pinned to the free layer), the coercive field shifts to lower values (favoring the P state) with a somewhat linear dependence. Results from both high and low frequency

measurements are plotted in the graph.

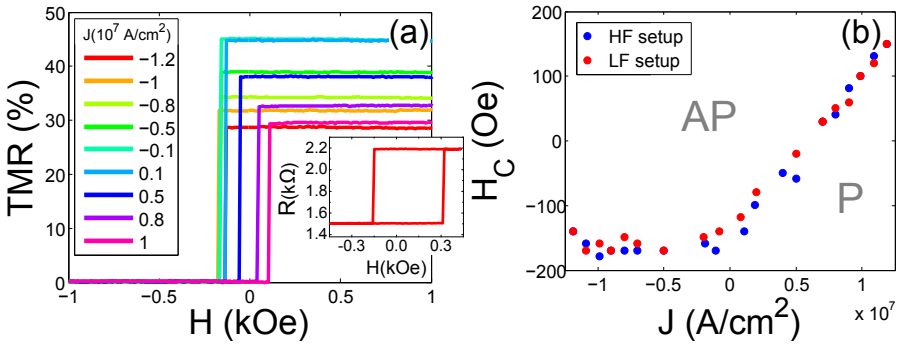

Figure 4.11: 40x80nm^2 MTJ biased along the easy axis direction. (a) TMR curves at different applied currents. The coercive field of the MTJ changes with increasing positive current. The inset shows a full TMR cycle at (b) Change in the coercive field with the applied current from HF and LF noise measurements.

The dependence of H_C on the current points to spin-torque related effects, as the self-field induced by the current is considerably lower than the shift of the coercive field. The self field generated by the current is estimated by $H_{self} = \frac{Jr}{2}$. This expression is obtained from Ampere's law, where J is the current density and r the radius of the disk. Since we are dealing with elliptical disks, we use $r = \sqrt{a^2 b^2}$ with $a = 40$ nm and $b = 80$ nm the ellipse's semi-axes. The self field obtained for the highest current is $H_{self} \simeq 17Oe$, while the change in H_C is $\Delta H = H_C(I = 300\mu A) - H_C(I = 0) \simeq 320Oe$, much too high to be explained by the self field.

A typical high frequency noise spectrum presents resonance peaks centered around a frequency f_{res}, with linewidths Δf. An example of such a spectrum is shown in Fig. 4.12. We have studied the evolution of these resonance modes with both an external magnetic field and a d.c. current I. The resonance peaks may be characterized by their f_{res}, Δf and output power P of the microwave emission. We calculate the power from $V^2_{output}/50\Omega$, where V_{output} is the sum of the areas under each resonance peak and 50Ω is the load on the input of the spectrum analyzer.

We have constructed surface plots at constant current, with the high frequency spectra taken at different applied external fields, so the evolution of the

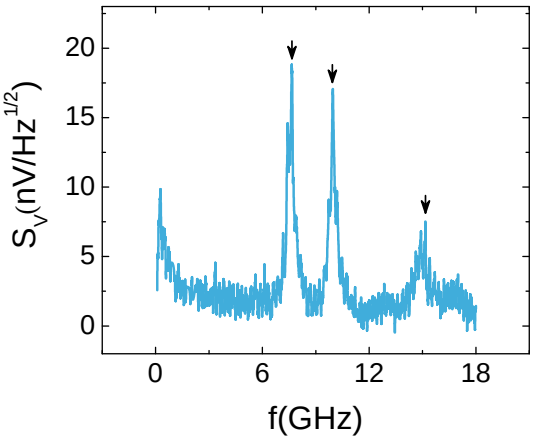

Figure 4.12: High frequency spectrum in the P state (H=-250 Oe) for $J = -1.2 \cdot 10^7 A/cm^2$ of a 40x80nm elliptical MTJ. The spectrum reveals 3 different oscillation modes.

modes with the current can be detected. Some charactersitic plots are shown in Fig. 4.13. For positive currents, the P state is stabilized and the AP state is stabilized, and vice versa for negative currents. This fact is reflected in Fig. 4.13, as the modes observed have higher amplitudes in the AP state for positive currents, and in the P state for negative currents.

Six clear modes are detected, which come from oscillations of the free layer (labeled F0, F1, ...) and the SAF structure (A0, A1 and A3). The free layer modes are V-shaped, while the modes not showing a minimum at low fields correspond to SAF modes[153] (see Fig. 4.4(a)). The SAF modes should present a minimum at the high field required for the spin-flop of the SAF, but our applied fields are not high enough. The F0 mode typically corresponds to excitations localized near the edges of the layer[153]. The F2 mode only appears in the state which is excited (P or AP), depending on the polarity of the current. A possible fourth free layer mode, F3, is labeled, although it appears very tenuous and is only present in one graph ($J = +1.2 \cdot 10^7 A/cm^2$). Several other samples revealed similar oscillation modes.

We have carried out an analysis of the F0 and F1 modes (as they have the highest amplitudes) as was discussed in Ref.[56]. The analysis of these results

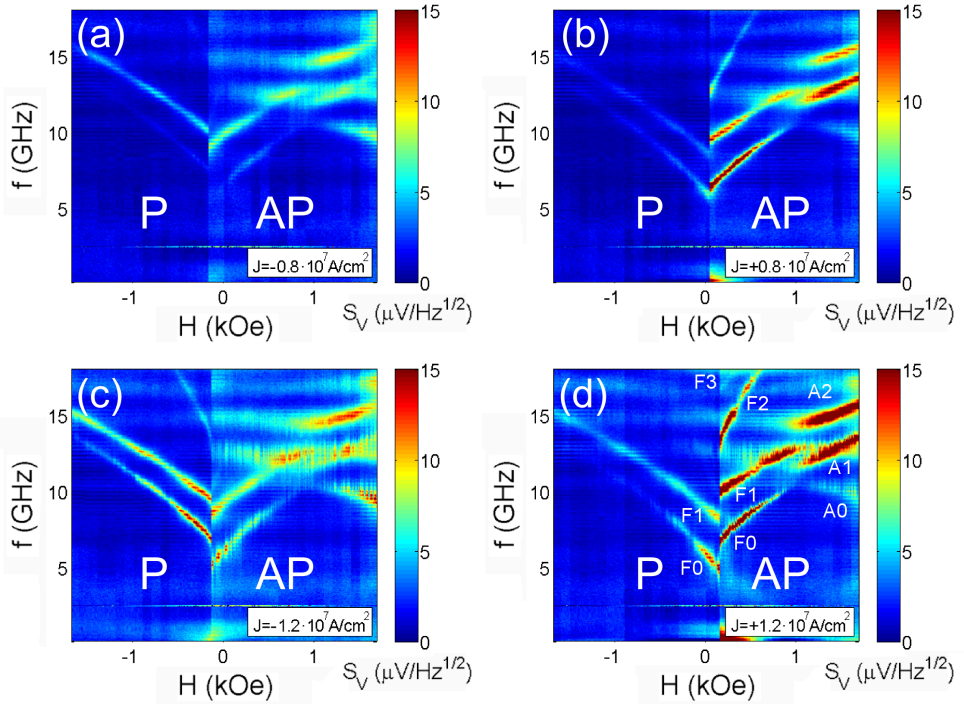

Figure 4.13: 3D plots at $J = \pm 0.8 \cdot 10^7, \pm 1.2 \cdot 10^7$ A/cm^2 constructed with the high frequency spectra, presenting several oscillation modes of the FM layers.

reveals that for *negative currrents*, a decrease in frequency is observed for the first and second modes in the P state, starting at $J \sim -10^7 A/cm^2$. Under the same conditions, the AP state data presents the same dependence as the P state, but the features are not as clear. The change of the oscillation frequency, linewidth and output voltage of the F0 and F1 modes for H=-350 Oe (P state) is shown in Fig. 4.15(a)-(c). The microwave power contains the contributions of both F0 and F1 modes. As can be seen, the decrease in frequency and linewidth and the increase of output power corresponds to the behavior reported in Ref.[56] (shown in Fig. 4.5(b)). In fact, the decrease of the frequency with the current in our sample with a zero bias TMR around 45% closely matches the transition shown in Fig. 4.6(a) of a LTMR device with TMR=50%. The minimum linewidth Δf obtained for the F0 mode is 500 MHz, much higher than what is observed in the steady state in Ref.[158](∼25 MHz). Therefore, although there

are not many current points, *we conclude that our highest negative current takes our sample to the intermittent SSP regime*[158] discussed above. For positive currents such a transition is not found, although the emitted microwave power does increase with the current (the amplitude of the modes increases).

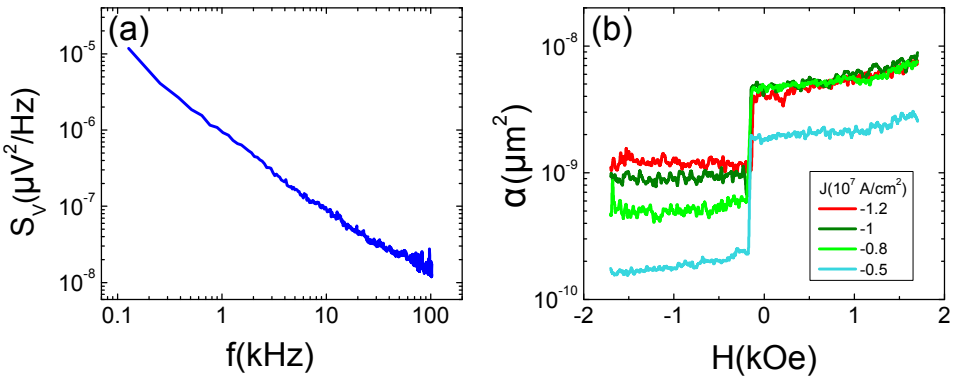

Figure 4.14: (a) 1/f spectra of the 40x80nm MTJ in the P state (H=-250 Oe) for $J = -1.2 \cdot 10^7 A/cm^2$. (b) Dependence of the Hooge parameter on the external field for several current density values.

As was mentioned, low frequency noise measurements were also carried out in *the same sample*, using the same current and magnetic field values. A typical 1/f spectrum is shown in Fig. 4.14(a). Fig. 4.14(b) plots the dependence of the Hooge parameter α on the magnetic field, for several currents. The Hooge parameter remains somewhat constant for each magnetic state. The analysis of the 1/f noise data as a function of the current density reveals the signature of effects observed in the HF results. As is shown in Fig. 4.15(a), the Hooge parameter α in the P state (averaged between -500 and -1700 Oe, $\langle \alpha_P \rangle$) monotonically increases with the applied current for current densities below $\pm 10^7 A/cm^2$. Then, only for negative currents, the normalized noise reaches a maximum and starts decreasing for around $J = -10^7 A/cm^2$. Comparing with the high frequency results on the same graph, it seems that the fact that GHz modes exhibit increasingly higher amplitudes for $|J| < 10^7 A/cm^2$ also increases the 1/f fluctuations[170] down to the kHz range. Further, the onset of the transition from T-FMR to SSP is also detected at low frequencies as the 1/f fluctuations diminish at the start of the transition.

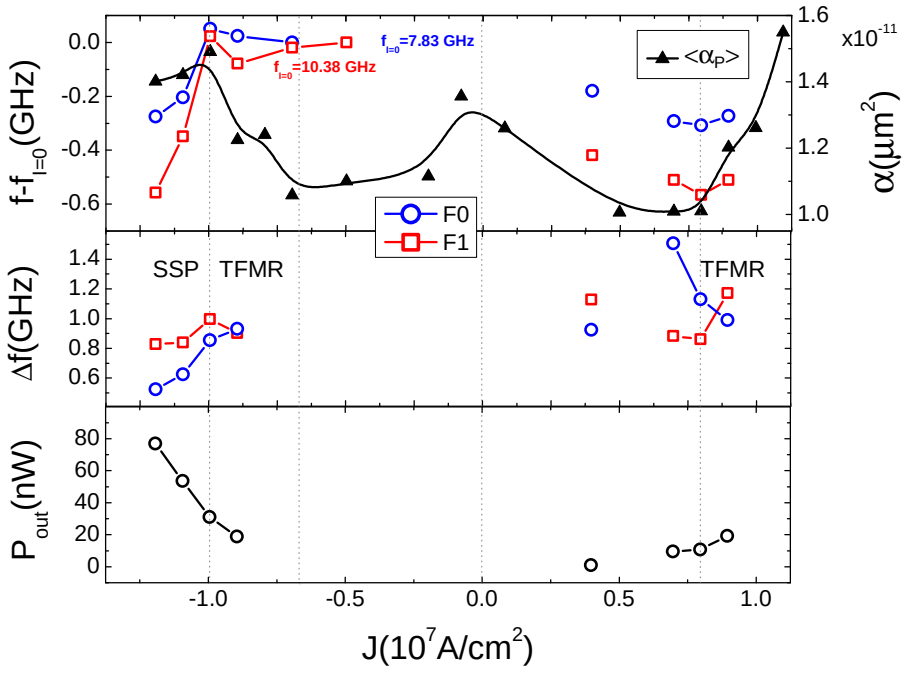

Figure 4.15: High and low frequency noise measurements in the P state of a 40x80nm^2 MTJ. Dependence of the modes' (a) frequency, (b) linewidth and (c) microwave power (of F0+F1) on the current density. Fig. (a) also includes the average Hooge parameter in the P state as a function of the current density in the field range between -500 and -1700 Oe.

Therefore, we explain the features in $\langle\alpha_P\rangle$ shown in Fig. 4.15(a) as follows: *(i)* the angle between M_{pinned} and M_{free} is small but non-zero, so both positive currents (exciting the AP and stabilizing the P state) and negative currents (vice versa) increase the amplitude of the oscillations in the magnetic state which is excited for each polarity; *(ii)* the onset of a transition from T-FMR to a steady-state precession regime is detected from HF frequency measurements of the free layer modes in the P state for negative currents; *(iii)* we can detect the transition from 1/f noise measurements in the kHz range, which seem to be sensible to the regime of HF oscillations.

So by comparing our low frequency results with the high frequency data, we can ascertain that we are detecting signs of spin-torque related phenomena

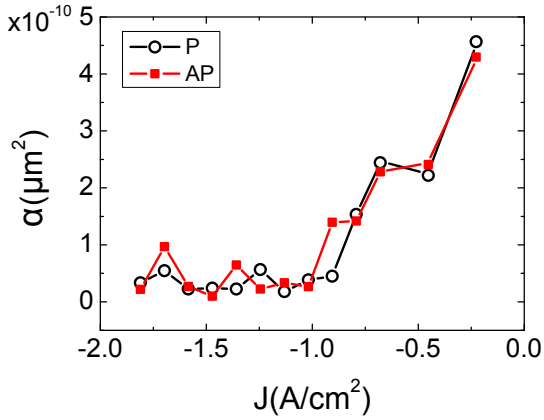

Figure 4.16: Dependence of the Hooge factor with the current density in a HTMR, 45x125 ellipse, with $TMR = 81\%$ and $R = 2.29\Omega\mu m^2$.

in low frequency 1/f measurements. *Further, our low frequency results are sensible to ST-driven effects for even smaller currents than our high frequency measurements.* We remark that qualitatively different low frequency noise was observed in HTMR junctions. These MTJs, expected to have a more uniform, pinhole free barrier, revealed a decrease in the Hooge factor with an increasing applied bias (shown in Fig. 4.16), similarly to what was previously observed for Fe/MgO/Fe MTJs with 2-3 nm thick MgO barriers[82,174,175].

4.4. External field along the hard axis: current-induced magnetization reversal

Next we consider the case of magnetic fields applied along the hard axis of magnetization. The main difference with the easy axis measurements is the fact that the free layer's magnetization does not suddenly switch from an AP to a P alignment with respect to the pinned layer. Instead, the free layer's magnetization rotates from the hard axis (at high fields) until it is parallel to the pinned layer's magnetization (the P state). In this case, current-switching effects due to spin-torque transfer could be observed at low fields.

We will show that we indeed observe STT switching in our low RA junctions,

and that *the analysis of low frequency random telegraph noise effectively evaluates the non-homogeneity of the ultra-thin barrier*[176]. High frequency noise measurements in this configuration are used to conclude that indeed the increase in resistance at low fields corresponds to a change from the P to the AP state.

As was mentioned above, MTJs of sizes under 100nm with low TMR (around 30-40%) and low RA products have been suggested to have localized reductions in the tunneling barrier[56]. We show that the fraction of area where the barrier is reduced may be estimated by analyzing the random telegraph noise (RTN) present in the samples. We find that due to inhomogeneous spin currents, these low TMR MTJs can be switched between the AP and P states using rather low current densities when an external magnetic field is directed along the hard axis. Micromagnetic simulations, with an effective pseudo-pinhole area close to what is estimated from the RTN, support the main experimental observations.

As we have seen, when no external field is applied, the free electrode's magnetization M_f and the pinned electrode's magnetization M_p are aligned parallel (P state). When the field is applied along the hard axis, the highest resistance is reached for fields around 1.5kOe (Fig. 4.17(a)) and M_f is fully aligned with H. Since M_p remains fixed, the angle between M_f and M_p is around 90°. We will refer to this state by AP_{HA}, the hard axis anti-parallel state. Then we have that R(P)<R(AP_{HA})<R(AP).

The TMR curves shown in Fig. 4.17(a) were obtained when the field applied along the HA was swept from a high positive to a high negative value. For positive currents, the sample behaves as expected, and reaches the P state when the field approaches 0. However, for negative currents, when the field is lower than the switching field, i.e. $|H| < H_{switch}$, ST effects overcome the external H and switch the sample to a high resistance state. The resistance of the sample in this state is higher than in the AP_{HA} state, hence we argue that the sample switches to the AP state. Figure 4.17(b) shows a phase diagram of the magnetic state of the sample, dependent on H and the applied current, constructed from TMR curves at different currents. It can be seen that a region appears at some negative critical current density where the sample is switched to the AP state. The same behavior was observed in a considerable amount of devices (of similar or different size). Indeed, Fig. 4.18 shows a similar

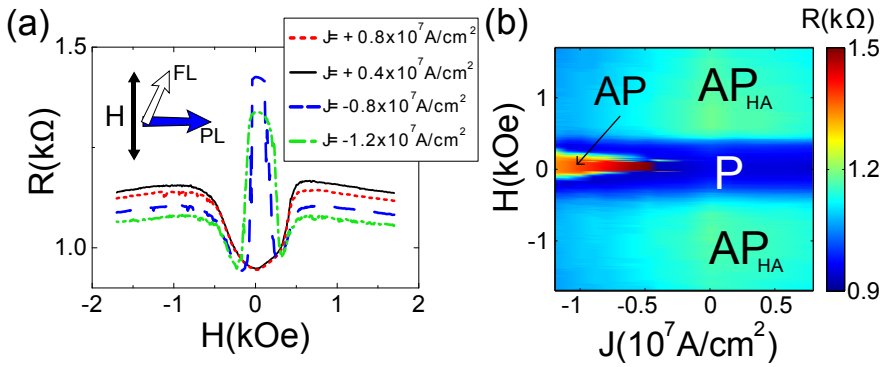

Figure 4.17: 40x80nm^2 sample measured in the LF setup. (a) TMR curves for several currents with H in the hard axis direction. Positive currents show a typical TMR curves, while negative currents show an abrupt increase in resistance at low fields. (b) Phase diagram of the magnetic state of the hard axis sample, constructed from the TMR curves. At low H, the switch to the AP state occurs at around $J = -4 \cdot 10^6$ A/cm^2. Adapted from Cascales et al.[176].

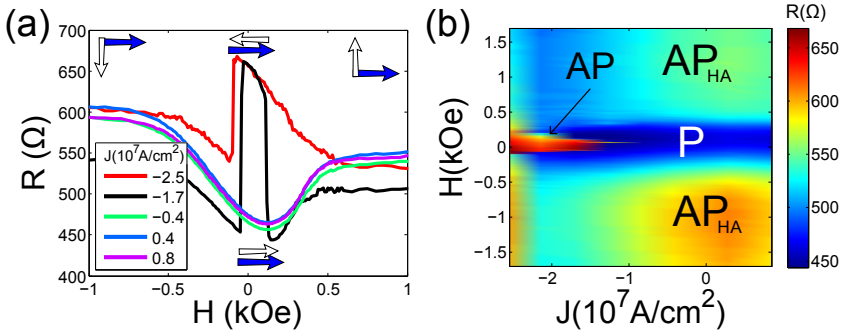

Figure 4.18: 50x100nm^2 sample measured in the HF setup. The (a) TMR curves and (b) phase diagram show a similar switching with the current as those shown in Fig. 4.17, although at a higher current density ($J = -1 \cdot 10^7$ A/cm^2).

dependence of the resistance on the current in a 50x100nm^2 MTJ, measured in the high frequency setup.

Fig. 4.19(a) presents contour plots constructed from the HF spectra at a fixed value of the current of the 50x100nm elliptical MTJ. Four different oscillation modes could be seen, which due to their shape (comparing with results in Fig. 4.4(b)[153]), seem to be two free layer and two SAF modes. A noteworthy feature is that, for fields close to $\pm 300Oe$, the mode's frequency dependence with the field changes from a "red shift" to a "blue shift". Numerical simulations carried out by Finocchio et al.[177] reported that for MTJs biased along the hard axis, there exists a critical field at which the current dependence of the oscillation frequency changes, passing from a Şred shiftŤ (typical of in-plane magnetization) to a Şblue shiftŤ (typical of out-of-plane magnetization). At this critical field, the non-linear phase noise is fully compensated, the minimum of the generation linewidth is observed, and the oscillation frequency is independent of the current. Indeed, it can be seen in 4.19 that the feature, e.g. for positive fields, remains fixed at around 3 GHz for all the current values. Similar features have been observed in several other samples. For example, Fig. 4.19(b) presents a surface plot showing up to 7 different oscillation modes in a 65x130nm elliptical MTJ (this sample did not present a magnetization reversal).

The dependence of the F0 mode with the field is analyzed for both samples and shown in Fig. 4.19(c),(d). The analysis reveals that for hard axis measurements, the samples do not present a transition to steady-state regime as in the easy axis case. A decrease in frequency is observed for positive currents, but the mode's linewidth remains more or less constant with the current density. The microwave power steadily increases with the applied current. Applying an external magnetic field along the hard axis has been reported to exhibit lower resonance frequencies and smaller linewidths compared to the easy axis[178], but we do not find so in our measurements.

Another notable difference between easy and hard axis measurements is the following: *(i)* the current switching occurs for positive currents between the AP/P states in the easy axis case, while *(ii)* the switching takes place between the P/AP states for negative currents in the hard axis. Therefore, it seems that current switching and steady state precession occur for opposite signs of

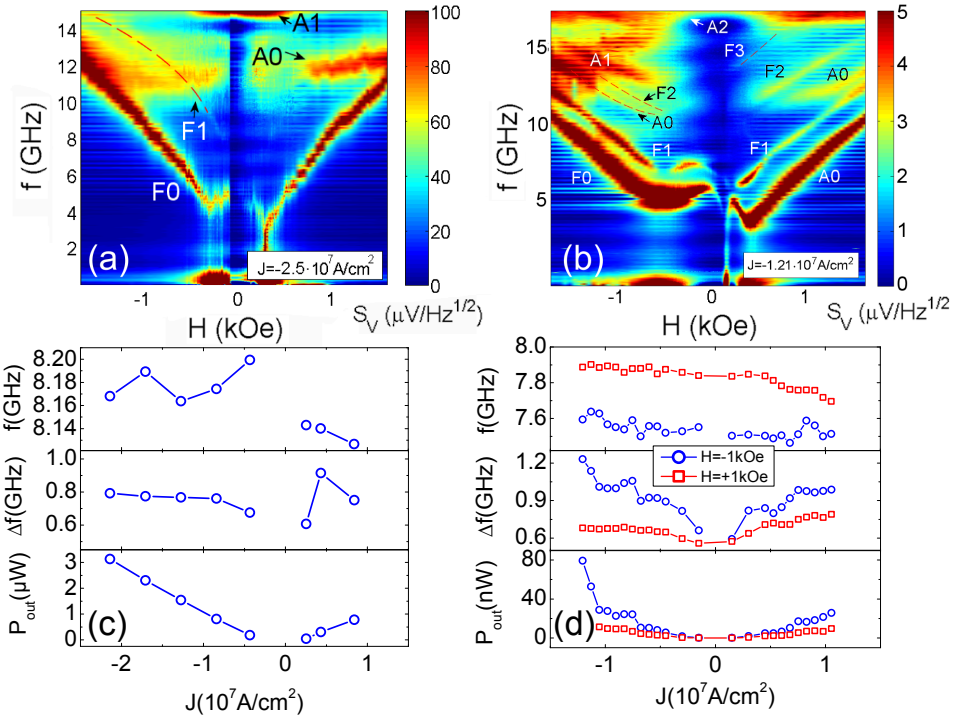

Figure 4.19: Surface plots of high frequency oscillations in MTJs with the field directed along the hard axis. (a) The 50x100nm MTJ from Fig. 4.18 with $J = -2.5 \cdot 10^7$ shows two free layer and two SAF modes. (b) A 65x130nm MTJ with $J = -1.2 \cdot 10^7$ presents up to seven oscillation modes. Study of the frequency, linewidth and microwave power with the current density of the F0 mode in the (c) 50x100nm (for $H = -1kOe$) and (d) 65x130nm (for $H = \pm 1kOe$) samples.

the current, and the sign depends on the direction of the applied field.

Now let us discuss the magnetization reversal effects shown in the TMR graphs. We imagine the switching process as a double well potential, where for $|H| > H_{switch}$, the minimum of energy corresponds to the typical HA TMR configuration and for $|H| < H_{switch}$, the minimum of energy corresponds to the AP state due to ST. In the vicinity of H_{switch} we get a bi-stable situation and thermally activated RTN is detected. The conditions for such a bi-stability should primarily exist in the areas of the soft magnetic electrode which are located close to the pseudo-pinholes, i.e. where the current density is the

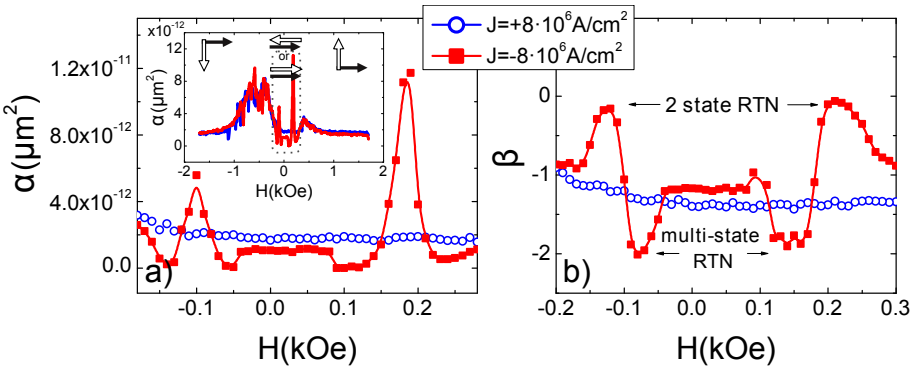

Figure 4.20: Dependence of the (a) Hooge parameter α and the (b) 1/f exponent β on the magnetic field. The curves indicate the range of H which presents 2 state ($\beta \simeq 0$) or multi-state ($\beta \simeq -2$) RTN. The inset in (a) plots α for the whole range of external field.

highest.

We have used the LFN measurements as a tool to quantify the barrier and current inhomogenities in these MTJs with ultra thin barriers. Special attention has been paid to random telegraph noise as a potential source of useful information for estimating the size of the "hot spot" region of the barrier. The spectra in these samples usually present 1/f noise, save for the fields where RTN is present. The field dependence of the Hooge factor α revealed a clear maximum in noise centered around the field value where the resistance switch takes place (Fig. 4.20(a)). Also, the exponent β (see the 1/f noise equation 2.11) approaches 0 for these same field values (Fig. 4.20(b)), i.e. the curve becomes flat and Lorentzian-like. These features clearly identify the range of H which presents RTN.

The characterization of the RTN was then carried out by analyzing the spectra and time-series at these fields, following the method explained in Section 3.7. Figure 4.21 shows typical RTN features in the LTMR samples, where the field is directed along the HA. Fig. 4.21(a) shows typical time series of the voltage fluctuations for magnetic fields in and outside the field range where a strong RTN is detected. The graph corresponding to H=+190 Oe shows well defined step-like jumps between two voltage levels. The amplitude of these

RTN fluctuations is a factor of 10^2 larger than RTN for higher fields. Fig. 4.21(b) shows that for the field values in the range where the magnetization reversal takes place (H=+190 Oe) one observes a Lorentzian-like spectrum, typical of RTN. On the other hand, outside the range (H=+1700 Oe and H=+600 Oe), the spectrum is nearly 1/f. The graphs shown in figures 4.21(a) and (b) correspond to $J = -1.2 \cdot 10^7$ A/cm^2.

For each current, the fluctuating magnetic moment Δm involved in the RTN is estimated in the following way. The fluctuating voltage ΔV is obtained from histogram of the time-series and the spectra are fitted by Equation 2.14, as explained in Section 3.7. Then we calculate $ln(\tau_{up}/\tau_{down})$ with respect to H for each current, and we fit this by the Arrhenius law $ln(\tau_{up}/\tau_{down}) = C + 2\Delta mH/k_BT$ (where C is a constant) as shown in Fig. 4.21(c). Figure 4.21(d) shows the estimation of Δm for different currents, which is found to be around $(2-4) \cdot 10^5$ μB, for both resistance switches (AP-P and P-AP) present in each curve. Similar effects were observed in several other the junctions. Considering the moment per atom in CoFeB to be of 1 μB[179], its lattice parameter a = 0.284 nm, an fcc structure (hence there are 4 μB in a volume of a^3) and if we suppose that the fluctuating moment is only present in the free layer, then we estimate that the volume which corresponds to $\Delta m = 4 \cdot 10^5$ μ_B is 23% of the volume of the free electrode, which fluctuates and generates the RTN[176]. This percentage is obtained from the ratio of the volumes $V_{RTN}/V_{electrode}$ where $V_{RTN} = \Delta m a^3/4\mu_B$ and $V_{electrode} = x \cdot y \cdot z$, where x = 20 nm, y = 40 nm and z = 3.9 nm.

4.4.1. Micromagnetic simulations

We have carried out numerical simulations, with OOMMF[180], of junctions with and without pinholes described by a simple qualitative model in order to account for the observed phenomena[176]. The reduction of the barrier or the presence of a pseudo-pinhole are modeled as a region of area a in the insulating barrier which concentrates the current going through the structure, as schematically shown in Fig. 4.22(b). If J is the current density flowing through the electrodes of area A, then the current density in the pin-hole is $J \cdot A/a$. For negative currents, electrons flow from the free to the pinned layer and

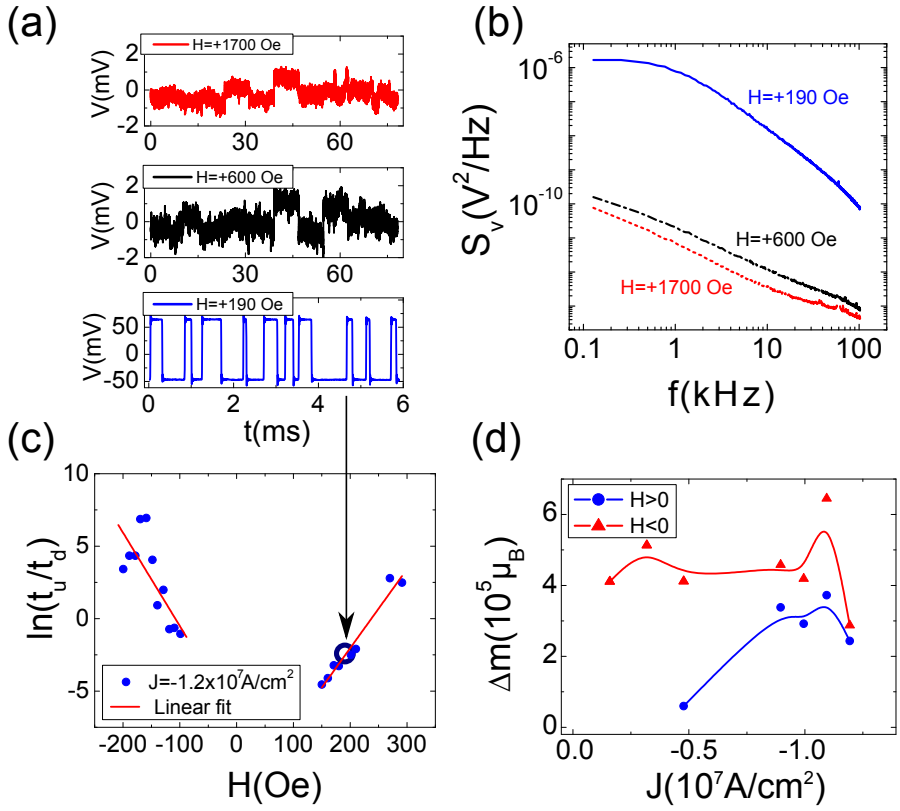

Figure 4.21: (a) Voltage fluctuations for three different applied magnetic fields for $J = -1.2 \cdot 10^7$ A/cm^2. The time-trace of the magnetization reversal (H=+190 Oe) presents RTN fluctuations which are two orders of magnitude higher in amplitude than other values of the field (H=+1700 Oe, H=+600 Oe). (b) Lorentzian-like spectrum typical of RTN at H=+190 Oe and a typical 1/f spectrum for H=+1700 Oe and H=+600 Oe. (c) Linear fit to an Arrhenius-type law of the τ_{up}/τ_{down} ratio. (d) Estimation of the fluctuating moment Δm with respect to the applied current.

this favors an AP alignment of the electrodes' magnetizations. The constants for CoFeB used in the simulations are: spin polarization $P = 0.5$ and saturation magnetization M_s=1150 kA/m. The TMR curves (Fig. 4.22(a),(b)) have been calculated by obtaining the average angle between the free and pinned layer's magnetizations, and using the expression $R(\theta) = R(0) + \Delta R(1 - cos\theta)/(2 +$

$\chi(1 + cos\theta))$[172]. Since H was only applied along the HA in this sample, we have to estimate ΔR. From our data, $TMR(\pi/2) = 23\%$ and $R(0) = 945\ \Omega$, so with $\chi = 0.5$ we obtain that $\Delta R = 0.6R(0)$, i.e. a reasonable $TMR = 60\%$.

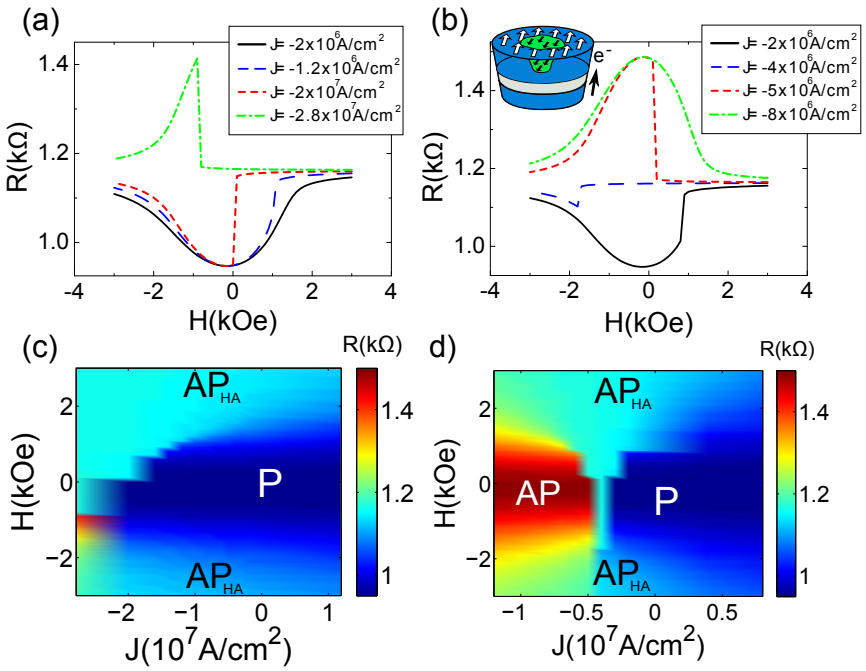

Figure 4.22: (a) Simulated TMR curves for different current values in a junction with a perfect barrier. (b) Simulated TMR curves for different currents with a pin-hole in the barrier. (c) Phase diagram constructed from the TMR curves in (a), where the switching current is found to be $J = -2{\cdot}10^7$ A/cm^2. (d) Phase diagram constructed from the TMR curves in (b), which presents a much lower switching current density, $J = -4 \cdot 10^6$ A/cm^{2}for $A/a = 5.3$. Adapted from Cascales et al.[176].

The results of the simulation (Figure 4.22) closely resemble the experimental results (Fig. 4.17(b)) with the exception of the AP/P switch for negative fields. Our simulations show that a smaller current is necessary to switch the free layer's magnetization if the current through some region of the barrier, where there is a higher effective current density, compared to a perfect junction[176]. Fig. 4.22(a) shows that a perfect barrier needs a much higher current density

to obtain a resistance switch ($J = -2 \cdot 10^7$ A/cm^2) than junctions with local barrier reductions, as seen in Fig. 4.22(b). Figures 4.22(c) and 4.22(d) show a phase diagram constructed from all the TMR curves for an MTJ with (d) and without (c) a pinhole. Indeed, for the ratio $A/a = 5.3$ (for which close to 20% of the insulating surface concentrates current), we obtain a switch to the AP state for low H at precisely $J = -4 \cdot 10^6$ A/cm^2, as can be seen in Figs. 4.17(b) and 4.17(d). If the fluctuating moments are located in the free layer, and strictly above the area a of the pinhole, this corresponds to 20% of the volume of the free layer, which is remarkably close to the 23% mentioned above.

Some disagreement between simulations and experiment could be related to the fact that the simulations are done at zero temperature while the experiments were carried out at 300 K, since it has been demonstrated by simulations that temperature fluctuations facilitate reversal processes[181].

4.5. Discussion and conclusions

We have found that low TMR nanopillar MTJs of sizes under 100nm exhibit spin torque related magnetization dynamics and current-induced magnetization switching. The analysis of the measured high frequency oscillation modes with respect to the current reveals the onset of a steady-state precession regime for negative currents, when the field is applied along the easy axis of magnetization. A comparison of this analysis with 1/f noise results as a function of the current reveals that the changes in magnetization dynamics in the GHz range are reflected in the low frequency noise. *The beginning of the transition to the steady state regime appears as a maximum in the normalized 1/f noise (Hooge parameter).* Although 1/f noise has been observed for such a transtion in previous studies[168,178], a systematic study has not been carried out before.

Regarding the current switching effects, if the MTJs are biased along the easy axis, an AP/P switch is favored for positive currents, while a P/AP transition occurs for negative currents for fields along the hard axis. The analysis of random telegraph noise in samples biased along the hard axis presenting current switching effects allow us to quantify the fluctuating magnetic moment in the free layer. These measurements are supported by micromagnetic simula-

tions, which show that local reductions of the MgO barrier could be responsible for the substantial decrease in critical current needed for spin torque induced magnetization switching. The obtained results should help to define the "current window range" for the potential application of nm sized magnetic tunnel junctions as ultra small field sensors.

The scenarios which could describe the barrier reduction in our MTJs are (a) a reduction of the effective barrier (pseudo-pinhole) which involves direct tunneling or (b) centered or off-center defect states in the barrier which induce sequential tunneling, appearing as electric RTN. The following arguments disprove electric RTN as the main source of the random telegraph noise: RTN of a purely electric origin observed in sub 100 nm MTJs with ultrathin (< 1 nm) MgO tunnel barriers, showed to be field independent[182], and it appears for field values outside the magnetization reversal range as in our experiment (Figs. 4.21(a) and 4.21(b)). Field dependent RTN appears for a range of fields around the magnetization reversal and is two orders of magnitude higher in amplitude than the electric RTN which is detected at higher fields. Moreover, RTN due to domain walls or magnetic inhomogenieties[172] should also be excluded since the lateral dimensions of the MTJs under study are smaller than 100 nm, which is below the typical DW width. In order to evaluate more precisely what the contribution of electric RTN is, shot noise measurements should be carried out. Direct (indirect) tunneling should give Poissonian (sub-Poissonian) shot noise[75,183].

To summarize, HF and LF noise measurements were carried out in MgO based, nanoscale MTJs with reduced barriers exhibiting low TMR ratios. These devices are good candidates for ST switching, as they seem to present lower current threshold barriers. The external magnetic field was applied along the easy and hard axis of magnetization, and different spin-torque driven related effects have been observed. The comparison between HF and LF data reveals that ST related effects can be detected by TMR and low frequency noise measurements. This proves to be a powerful and simple technique to study current-switching phenomena and spin-torque based magnetization dynamics in MTJs.

4. Spin-torque effects and noise in MTJs of sizes under 100nm

Chapter 5

Conductance and shot noise in Double-Barrier MTJs

5.1. Introduction

In this Chapter we present shot noise measurements in double-barrier magnetic tunnel junctions (DMTJs). We find that the shot noise can be controlled by the magnetic state of DMTJs and also differences in thickness, spin between two MgO barriers[183]. The measurements at biases where the influence of QWSs is small are found to be in good agreement with a theoretical model, developed by our collaborators, which takes into account spin relaxation in the central electrode[183–185]. Our findings reveal new perspectives for the magnetic control of SN and also present a novel method to quantify the electron spin relaxation in spintronic devices.

Double-barrier magnetic tunnel junctions are spintronic elements which could, in the future, replace single-barrier junctions as components in hard-disk drives or as magnetic sensors. First of all, single-barrier MTJs are more susceptible to dielectrical breakdown than DMTJs.

DMTJ devices also present a high versatility for controlling their electrical resistance (or TMR). They can present lower shot noise values than single

MTJs, and consequently have better signal-to-noise ratios. As we will show in this chapter, engineering DMTJs with certain barrier and electrode thicknesses gives control over the shot noise value of the device, which can be switched with the different magnetic states.

As it was mentioned in the introductory chapter, MgO-based junctions became important elements of spintronic devices after spin dependent transport was observed in Fe/MgO/Fe magnetic tunnel junctions[20,21]. The use of MgO for an effective spin injection in MTJs has allowed reducing spin relaxation effects which occur because of conductivity mismatch[186,187]. Previous studies regarding spin coherency and shot noise in MTJs revealed that junctions with Al_2O_3 barriers present supressed shot noise values ($0.7 < F < 1$) due to sequential tunneling[67]. Serial arrays of magnetic tunnel junctions also present a supressed SN[188].

On the other hand, MTJs with MgO barriers present full shot noise values ($F = 1$), which is independent of the magnetic state. This was observed in Fe/MgO/Fe MTJs[75]. The study of junctions with ultrathin MgO barriers (less than 1 nm thick), yielded a Fano factor of $F \simeq 0.92$ in the parallel state[77,78].

Double-barrier magnetic tunnel junctions have been fabricated using nanoparticles[189,190] or a continuous magnetic layer as the central electrode[191]. DMTJs present some advantages in comparison with single barrier MTJs, like higher TMR ratios[191,192]. Also, DMTJs present a smaller decrease of the TMR with the applied voltage in comparison with single MTJs. For example, epitaxial DMTJs with room temperature TMR ratios of 140% only show a decrease down to 75% for voltages around 1 V[74]. Having high values of TMR at high voltages is essential for applications.

Incidentally, the dependence of the TMR with the applied bias reveals oscillations induced by quantum well states (QWSs)[102,190]. Another advantage is that spin accumulation in the central layer is expected to notably enhance spin torque[193–196]. Resonant tunneling in DMTJs may have advantages in comparison with standard MTJs due to resonant spin-torque effects[161,195,197]. Also, a current driven magnetization reversal may occur at lower current densities in DMTJs[197].

The control of shot noise has been extensively studied in the area of photonics, and is currently exploited to improve detection methods[198]. The precise

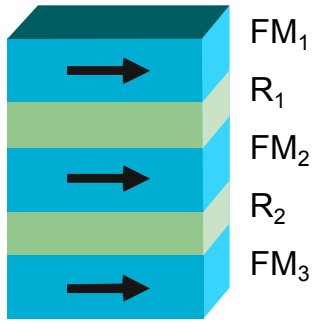

Figure 5.1: Sketch of a DMTJ. The thickness of the barriers determines the resistances R_1, R_2, and the thickness of the FM layers the coercive field of each magnetic electrode.

control of shot noise in spintronics still remains an important and unexplored issue.

Thus, being able to control the spin diffusion and coherency in spin polarized tunneling could be important for the further development and technological application of hybrid magnetic nanostructures [10]. In this thesis we report on the investigation of shot noise in seminal, epitaxial Fe/MgO/Fe/MgO/Fe DMTJs.

5.2. Growth method and junction types

As can be seen in Fig. 5.1, a double barrier tunnel junction consists of three ferromagnetic electrodes, separated by tunnel barriers. The resistance of the DMTJ corresponds to the sum of the resistance of each tunnel barrier, which depends on the thickness of the barrier. If the coercive fields of the FM electrodes are different, then up to four different magnetic states can be obtained in a DMTJ. The different coercive fields are achieved by either growing FM layers of different thickness, or by coupling an FM electrode to an antiferromagnetic layer.

The growth of the junctions was carried out by the group of professors Michel Hehn and Coriolan Tiusan within a collaboration project between the Magnetrans-UAM group and the Institute Jean Lamour, Nancy Universitè

(France). The growth method is described in detail in Ref.[191].

Three different types of DMTJs, with different combinations of electrode and barrier thicknesses, were grown at room temperature by Molecular Beam Epitaxy (MBE)[183]. The junctions were grown on MgO(100) substrates under ultra high vacuum conditions (UHV) at a base pressure of around 10^{-11} mbar. In MBE, the source materials used in the growth are heated in evaporation cells. The sublimation of the source materials creates a gaseous beam of the required substance, which then condenses on a wafer or substrate. The substrate may be heated if necessary, as well as kept continually rotating to obtain a homogeneous growth. The slow deposition rate of the MBE technique allows the films to be grown epitaxially. UHV conditions are necessary for the epitaxial growth to take place in a clean environment with a minimal contamination.

The MgO(100) substrates were annealed at 600 °C for 20 min before the growth in order to remove carbon impurities. The diffusion of the remaining C impurities to the Fe bottom electrode is prevented by growing a 10-15 nm thick MgO buffer layer at 450 °C on the substrate[191]. A control of the growth down to the monolayer level was achieved by monitoring in-situ the intensity oscillations in the reflection high-energy electron diffraction (RHEED) pattern along the [100] direction during the layer-by-layer growth of the MgO barriers. Fig. 5.2 shows such a RHEED pattern of the bottom Fe layer where the MgO buffer layer is (a) absent or (b) present. The sample with an MgO buffer layer does not show the c(2x2) surface reconstruction related to carbon, which is seen in the sample with no buffer layer.

DMTJs with lateral sizes from 10 to 30 μm were patterned by a combination of UV lithography and Ar ion etching, controlled by Auger spectroscopy[191]. The square-shaped pillar is fabricated in the following way. After the deposition of the different layers, the surface of the wafer is cleaned and covered with a photosensitive resin (or resist) (Fig. 5.3(b)). The resist is then exposed to ultraviolet light through a mask with opaque and transparent regions with the desired square-shaped pattern. The chemical properties of the exposed resist change, and such regions are removed with the appropriate solvent. The remaining resin protects the surface underneath from the Ar ions, so only the resin-free surfaces are etched, leaving a square-shaped pillar MTJ. Once the

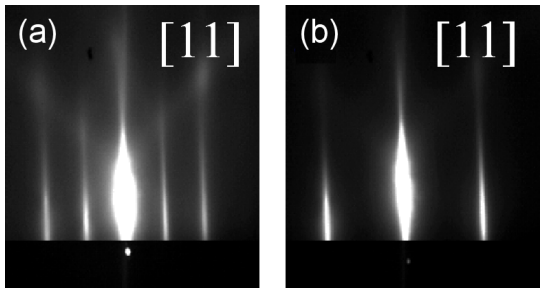

Figure 5.2: RHEED patterns along the [110] crystallographic direction of the Fe bottom layer of samples (a) without or (b) with an MgO seed layer between the substrate and the Fe layer. The buffer layer prevents the diffusion of carbon to the Fe electrode, so evidence of the c(2x2) reconstruction, related to C, is seen in (a) but not in (b). Adapted from Ref.[191].

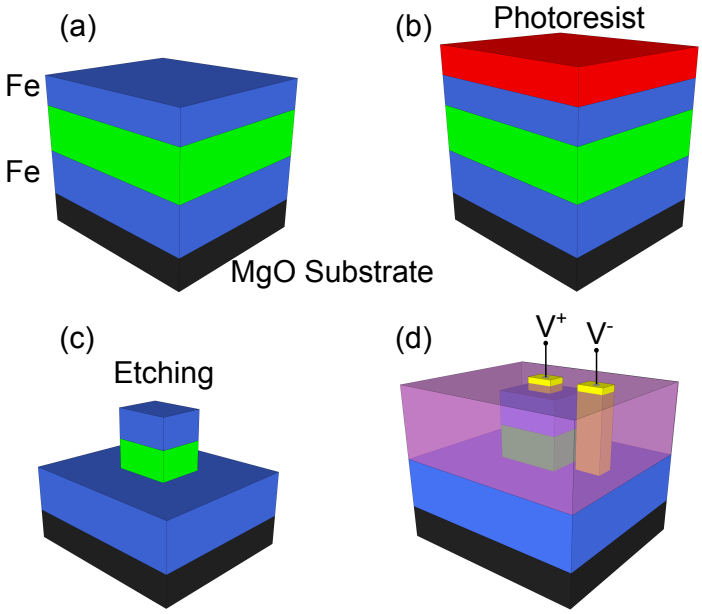

Figure 5.3: Diagram of the photolithography process. (a) Unpatterned sample. (b) Deposition of the resin. (c) Etching of the top electrode and MgO barrier. (d) MTJ pillar with the deposited contact pads. Figure from Ref.[138].

etching reaches the bottom electrode (Fig. 5.3(c)), the bottom electrode is patterned down to the substrate using a different mask following the process

we just described.

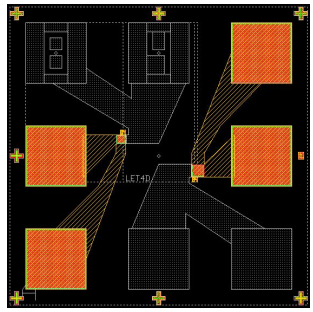

Figure 5.4: Diagram of the contact pads in DMTJs. Figure from Ref.[138].

A silica layer is sputtered over the whole wafer, isolating the top and bottom electrodes to avoid short-circuits. Then, "windows" are opened in the silica onto the top and bottom electrodes by lithography (Fig. 5.3(d)). Finally, aluminum contacts of the type shown in Fig. 5.4 are deposited.

The first type of junctions (DMTJ1) have the structure:

$$\mathrm{MgO//MgO(15)/Fe_1(45)/MgO(11ML)/Fe_2(10)/MgO(3ML)/Fe_3(20)/Au(20)}$$

where numbers in parenthesis are thicknesses in nm, while ML stands for monolayer. These junctions have a strong asymmetry between barriers, as one is considerably thinner than the other. The TMR as a function of the magnetic field is shown in Fig. 5.5(b). In agreement with previous findings[191,192], the antiferromagnetic coupling between two ferromagnetic layers across the thinnest MgO barrier in DMTJ1 results in the presence of two different AP1 ($\uparrow\ \downarrow\uparrow$) and AP1^r ($\downarrow\ \uparrow\downarrow$) states for which the central layer is aligned opposite to the neighboring ones. The difference in resistance between the AP1 and AP1^r states is attributed to the possible influence of domain walls formed in the synthetic antiferromagnet in the latter state. This option is supported by the fact that the normalized 1/f noise observed in the AP1^r, as is shown in Fig. 5.6. The TMR dip in-between corresponds to the AP2 ($\downarrow\ \downarrow\uparrow$) state.

The second and third type of DMTJs, DMTJ2 and DMTJ3, have the following layered structure:

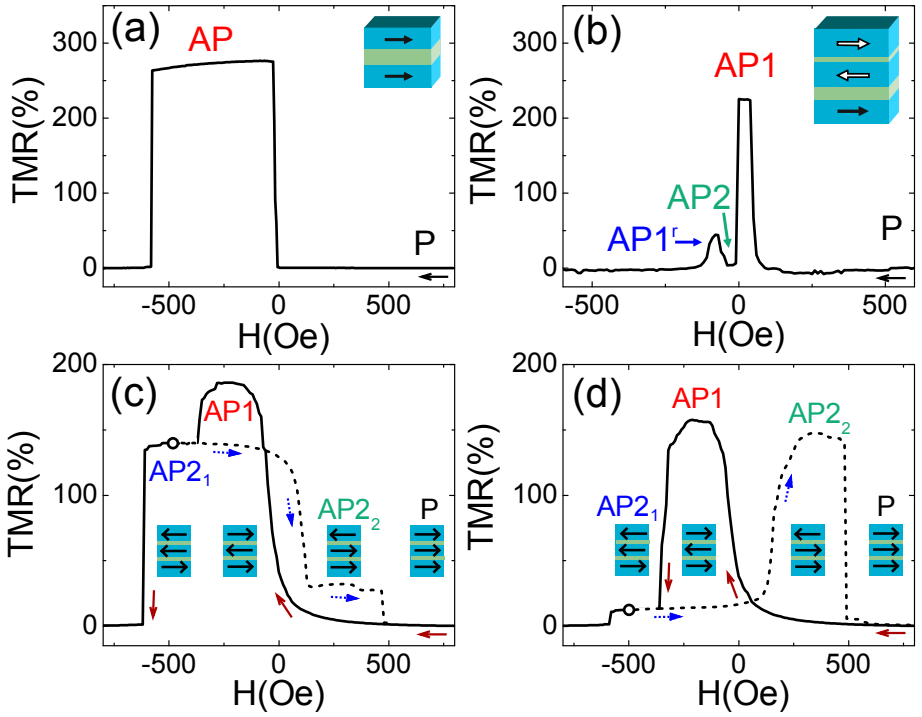

Figure 5.5: TMR curves at T=0.3 K with a field sweep from positive to negative, from Ref.[183]. (a) Single barrier MTJ with an area of 100 μm^2. (b) DMTJ1 with a very thin barrier, resulting in coupled top and central layers. (c) DMTJ2 junctions with a thick barrier 2. The resistance difference between AP1 and $AP2_1$ is higher than between $AP2_1$ and P. (d) TMR in DMTJ3 with a thick barrier 1. This results in a bigger resistance jump from $AP2_1$ to P, than from AP1 to $AP2_1$. The circle in (c) and (d) indicates when the field sweep changes direction in order to obtain the $AP2_2$ state.

MgO//MgO(10)/Cr(42)/Co(10)/Fe_1(5)/MgO(10 or 8ML)/
Fe_2(5)/MgO(9ML)/Fe_3(10)/Co(30)/Au(10)

The wafers for DMTJ2s and DMTJ3s were grown simultaneously. The 2ML difference in thickness of the bottom barrier is controlled by a shutter. The asymmetry between the tunnel barriers in these junctions is much lower than for DMTJ1s because both barriers in these junctions differ only slightly. The barrier asymmetry of DMTJ2 ($R_2 > R_1$) samples is opposite to that of DMTJ3

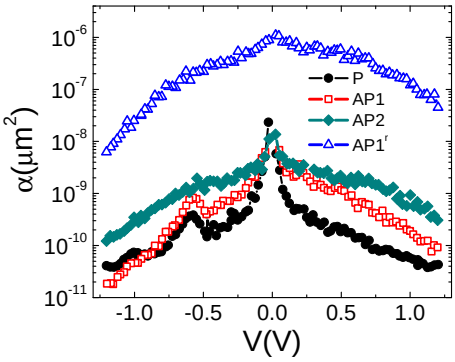

Figure 5.6: Normalized 1/f noise at T=4 K in a DMTJ1 sample in four different magnetic configurations.

($R_1 > R_2$), where the topmost barrier is labelled as number R_1 and the bottom barrier as R_2.

The dependence of the TMR on the magnetic field for DMTJ2 and DMTJ3 samples is shown in Fig. 5.5(c),(d). Both TMR graphs present the features expected from the barrier thicknesses. DMTJ3s show a larger resistance jump between the AP1 (↑↓↑) and $AP2_1$ (↑↓↓) states than between the $AP2_1$ (↑↓↓) and P (↓↓↓) states. DMTJ2 samples show the opposite behavior.

The $AP2_2$ state (↑↑↓) is present in both DMTJ2 and DMTJ3 samples, although reliable shot noise measurements in this state were only obtained for DMTJ3s. Indeed, one can observe in Fig. 5.5(c) and (d), that if the magnetic field sweep is stopped when the sample is in the $AP2_1$ state (↑↓↓), and then the field sweep goes back to positive values, then the central layer is inverted and we obtain the $AP2_2$ state (↑↑↓).

As can be seen, the central Fe layer in DMTJ1 samples has a thickness of 10 nm, while for DMTJs 2 and 3 the thickness is 5 nm. The thinnest continuous Fe layer which could be grown by molecular epitaxy (system at the University Henri Poincarè of Nancy) is of 5 nm. By making the central layer as thick as 10 nm, the Fe layer is guaranteed to be epitaxially flat, which is necessary for the growth of the thin 3 ML MgO top barrier in DMTJ1s. On the other hand, for DMTJ2 and DMTJ3 samples, the central layer is grown as thin as possible so the spin flip processes are minimized.

5.3. Experimental results

Shot noise and transport measurements at low temperatures were carried out in the cryogenic system described in Section 3.3. The main experimental findings show that the shot noise in weakly asymmetric samples (DMTJ2s and DMTJ3s) is supressed below the classic value ($F = 1$). The Fano factor was obtained as explained in Section 3.7. This approximation is justified above 100mV, where $eV/k_BT > 100$. Even though the noise and electron transport measurements were done at 0.3 K and 4 K, the real temperature for the less resistive samples was somewhere below 10 K at the highest biases (around 1 V). This was estimated by comparing the $I-V$ curves measured at 0.3 K, 4 K and 10 K. Measurements at 60 K were also carried out, for which the contribution of thermal noise to the frequency independent part of the noise spectrum was estimated and subtracted.

5.3.1. Control MTJs

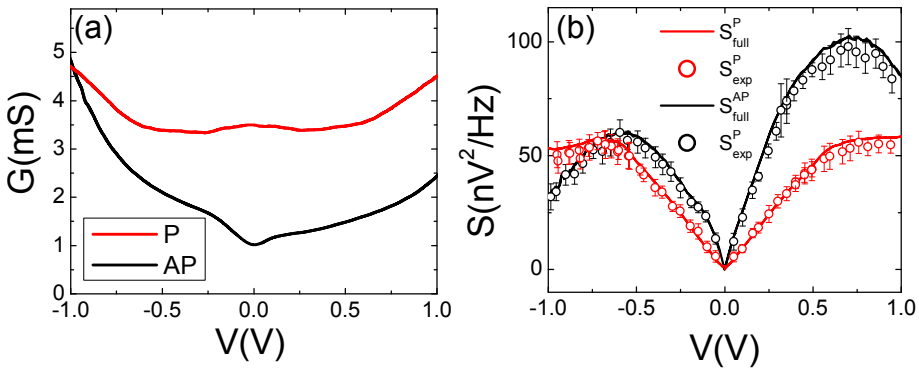

Figure 5.7: (a) Conductance in the P and AP states of a single barrier control MTJ at T=4 K. (b) Experimental (circles) and full (lines) shot noise in the P and AP states on a single barrier MTJ with an area of 100 μm^2. These control measurements yield $F \simeq 1$, suggesting a good structural quality of the junctions. Samples from the study shown in Ref.[75].

The shot noise measurements are compared with control measurements carried out in single-barrier MTJs with the following layer structure: MgO//

MgO(10nm)/Fe(45)/MgO(2.5)/Fe(10)/Co(20)/Pd(10)/Au(10) with the numbers indicating thickness in nm. These junctions were studied in a previous work by our group[75]. The TMR of a 10x10μm^2 MTJ is shown in Fig. 5.5(a). Shot noise measurements carried out at T=4 K in epitaxial MTJs with a single, 2.5nm MgO barrier, present nearly Poissonian statistics ($F \simeq 1$), in agreement with previous results[75]. Fig. 5.7 shows that shot noise measurements in the P and AP states yield the Poissonian value. These single barrier junctions serve as control for the shot noise measurements in the DMTJs. The fact that $F \simeq 1$ in the control MTJs indicates that the epitaxially grown samples are of good structural quality.

5.3.2. Shot noise in DMTJs with high barrier asymmetry

These type of junctions present a signature of QWSs in the central layer in the dependence of the conductance with the applied bias. The oscillations are clearly observed for two of the magnetic states (P and AP2), as shown in Fig. 5.8(a).

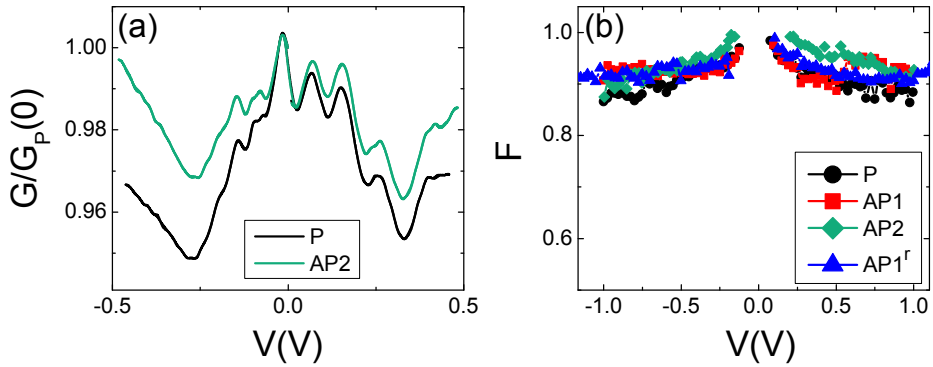

Figure 5.8: (a) Oscillations in conductance for two magnetic states. Each conductance curve is normalized by its value at zero bias. (b) Bias dependence of the normalized shot noise for a DMTJ1 sample. The Fano factor is found to depend weakly on the magnetic state.

The shot noise measurements carried out in DMTJ1 samples revealed that

shot noise in these structures is only weakly suppressed ($F \sim 0.9$) and is nearly independent of the magnetic state. The thicker barrier dominates the transport statistics because of the large difference between barriers. This is evident in the TMR curve (Fig. 5.5(b)), which only deviates from the P state resistance when the central layer's magnetization is opposed to the bottom layer's magnetization.

5.3.3. DMTJs with low barrier asymmetry

In DMTJ2 and DMTJ3 samples, which have a low barrier asymmetry, the slight difference between barriers becomes important and the shot noise measured depends quite strongly on the magnetic state of the DMTJ. Depending on the magnetic state and bias, the Fano factor varies in the range of $F \in (0.5 - 0.9)$. Fig. 5.9 shows shot noise measurements at T=0.3 K in a DMTJ3 sample in all four magnetic states.

The solid curves represent the estimated full SN from the $I-V$ curves while the dots indicate the experimental shot noise obtained from the spectra. As can be seen, the shot noise is sub-poissonian in all four magnetic states. The dependence of the shot noise with the magnetic state can be better appreciated when the normalized shot noise is plotted. Fig. 5.10 presents the Fano factor for (a) a DMTJ2 sample (three magnetic states shown) and (b) the DMTJ3 sample from Fig. 5.9. As can be seen, the asymmetry of the barrier determines the value of the shot noise for each magnetic state. For the DMTJ3 sample ($R_1 > R_2$) we have that $F_P > F_{AP2_2} > F_{AP1} > F_{AP2_1}$ while the order is reversed in DMTJ2s ($R_2 > R_1$). Also, an enhacement of the shot noise occurs at voltages higher than 500 mV for certain values of the energy, as can be seen in Fig. 5.10(b). The relative magnitude of these quasi-periodic anomalies increases with the applied bias and is weakly dependent on the magnetic state, and they seem to originate from resonant tunneling through quantum well states.

The shot noise was also measured at a fixed current, while sweeping the magnetic field in order to achieve all four magnetic states of a DMTJ3 sample[185]. As can be seen in Fig. 5.11, the Fano values match the results carried out at fixed fields while varying the bias. The main disadvantage of this method is

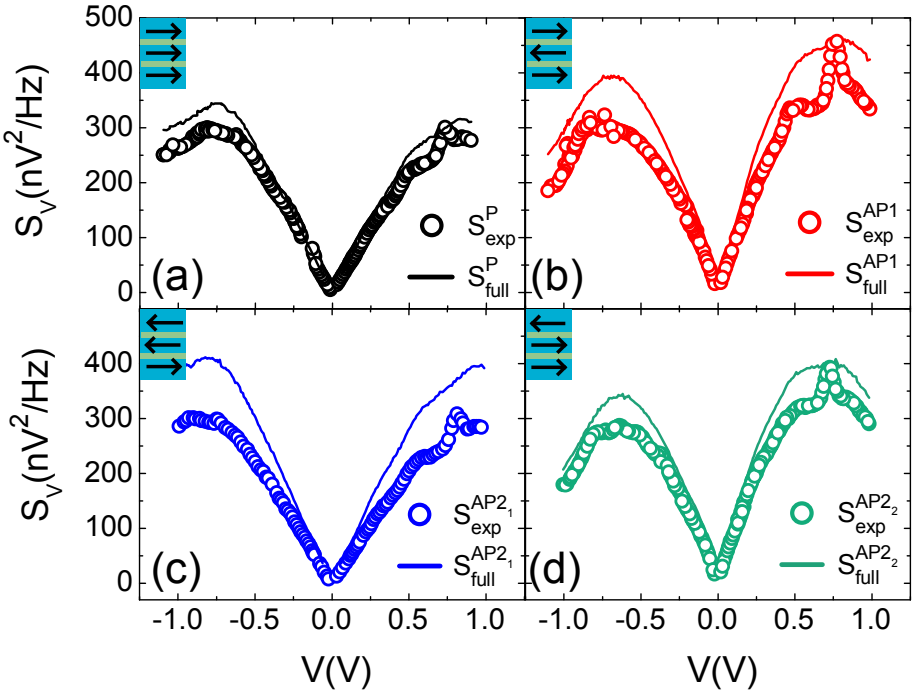

Figure 5.9: (a)-(d) Typical bias dependence of the shot noise for DMTJ2 measured in four different magnetic configurations at T=0.3K. The experimental data (points) is compared to full shot noise (lines)[183].

having control over the applied bias, since the resistance of the junction changes with each magnetic configuration under constant current.

5.3.4. Tunneling through quantum well states in DMTJs

As was discussed in Section 2.6, quantum well states may form in the central electrode of a DMTJ. Evidence of the presence of such states has been detected as oscillations in the conductance of all three types of DMTJs shown here.

The differential conductance, after subtracting the parabolic background G_0, for DMTJ3s is compared with the Fano factor at different temperatures[183] in Fig. 5.12(a),(b). The well defined oscillations of the differential conductance indicate the presence of resonant transmission through QWSs formed in the central Fe_2 layer.

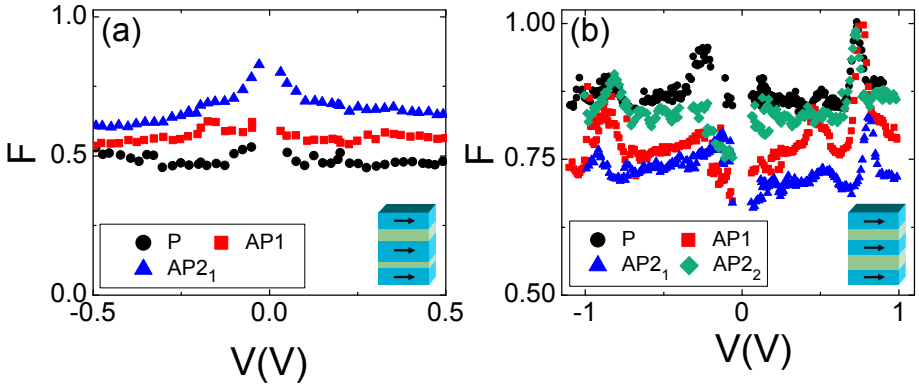

Figure 5.10: Dependence of the Fano factor with the magnetic state as a function of the applied bias for (a) DMTJ2 and (b) DMTJ3 samples[183]. The normalized shot noise is determined by the magnetic configuration of the junction.

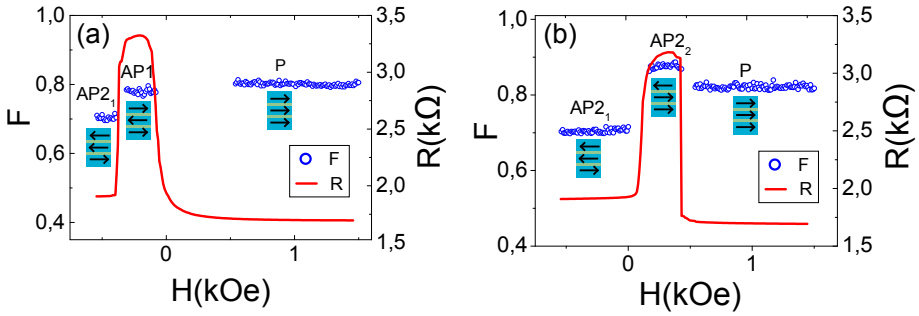

Figure 5.11: Shot noise and resistance at a fixed current during a magnetic field sweep at T=0.3K (a) from positive to negative values and (b) from the AP2$_1$ at negative fields back to positive fields. Data from Ref.[185]

Fig. 5.12(c) compares the conductance oscillations for each type of DMTJ. As can be seen, DMTJ1 samples present more oscillations in the range of energy shown than DMTJ2 or DMTJ3 samples. The appearance of QWSs in the central electrode of a DMTJ can be compared to the finite potential well problem in quantum mechanics. In this simplified situation, the number of bound states increases with the width d of the well as $N \propto d^2$, while the states become more closely spaced in energy. Indeed, the samples with a 10 nm central

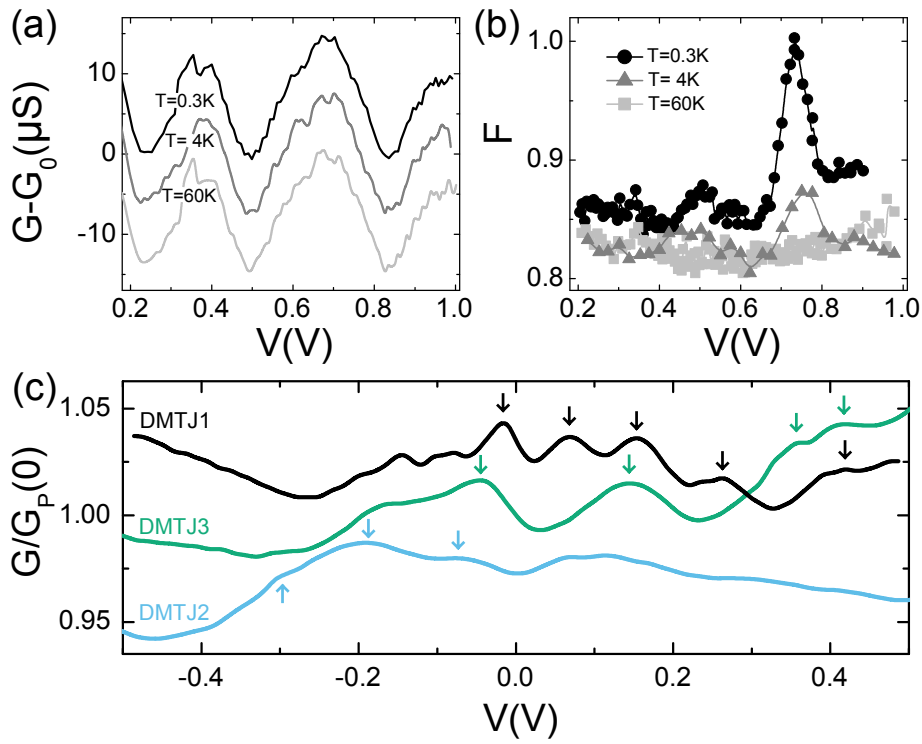

Figure 5.12: (a) Oscillations in the conductance of a DMTJ3, which are not affected by temperature[185]. (b) Shot noise in the P state at 0.3 K, 4K and 60K[185]. The effect of quantum well states is gradually suppressed with increasing temperature. (c) Oscillations in the P state conductance due to QWSs (indicated by arrows)[183]. The oscillations are more pronounced for $V > 0$ in DMTJs 1 and 3, and for $V < 1$ for DMTJ2s. The curves have been offset for better observation.

Fe electrode (DMTJ1s) present a larger number of conductance oscillations than those with a 5 nm thick central layer (DMTJ2s or DMTJ3s) for the same bias range (Fig. 5.12(c)) . Moreover, the QWSs calculated in Ref.[190] for Fe/MgO/Fe/MgO/Fe DMTJs qualitatively agree with the oscillations obtained for our DMTJ3s with 5 nm Fe central layers. QWSs are more pronounced for positive biases (when electrons tunnel from the bottom to the upper electrodes) for DMTJs1,3, and, as could be expected from the barrier asymmetry, are more pronounced for negative bias for DMTJ2s as can be seen in Fig. 5.12(c). Indeed, the voltage distribution across an asymmetric DMTJ shows that QWSs affect

the conductance mainly when electrons tunnel from the contact's Fermi level to the central layer through the thicker barrier[199,200]. A diagram representing this effect is shown in Fig. 5.13. Also, the oscillations in conductance due to QWSs are more significant, in general, in DMTJ1 and DMTJ3 samples. This is explained by the fact that the barrier through which the tunnel to QWSs occurs has a better structural quality for DMTJ1 and DMTJ3 samples (bottom barrier, R_1) than for DMTJ2s (top barrier, R_2).

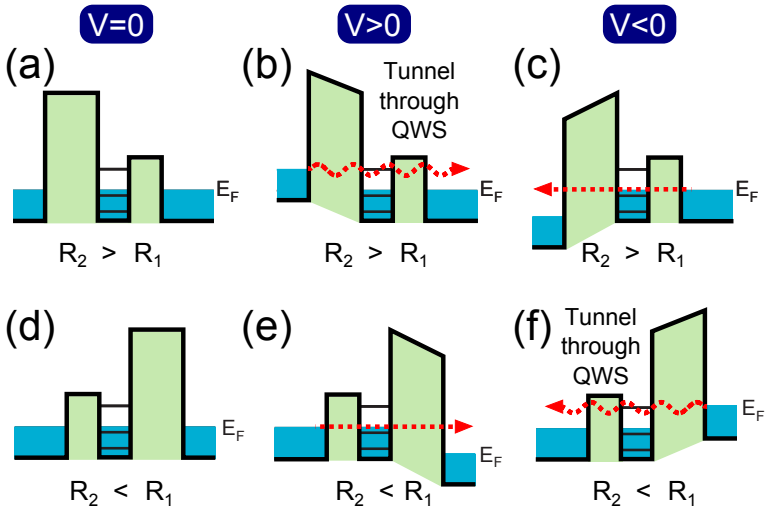

Figure 5.13: Diagram of resonant tunneling through QWSs in a DMTJ structure. DMTJs 1 and 3 correspond to (a),(b),(c) and DMTJ2s to (d),(e) and (f). Adapted from Ref.[200].

Depending on the degree of coherency involved in the transmission through QWSs, SN is expected to show a shallow dip in the Fano factor due to coherent resonant transmission followed by a resonant enhancement in the negative differential conductance regime due to Coulomb interactions[25,201,202]. These anomalies in Fano are more pronounced for DMTJ3s and for positive bias, where QWSs in the conductance are more clearly observed (Fig. 5.10(b)). We also remark that the observed periodic anomalies in the conductance and Fano factor cannot be attributed to Coulomb blockade effects, where the Fano factor has periodic minima decreasing in amplitude with the applied bias[203].

5.4. Theoretical model

The following theoretical model was developed by the groups of Prof. Józef Barnaś (Adam Mickiewicz University) and Prof. Vitalii Dugaev (Rzeszów University of Technology) both in Poland, with the aim of understanding the variation of the Fano factor with the barrier asymmetry and magnetic state of the system. The model is included in Refs.[183,185] along with the results shown above, and explained in detail in Ref.[184].

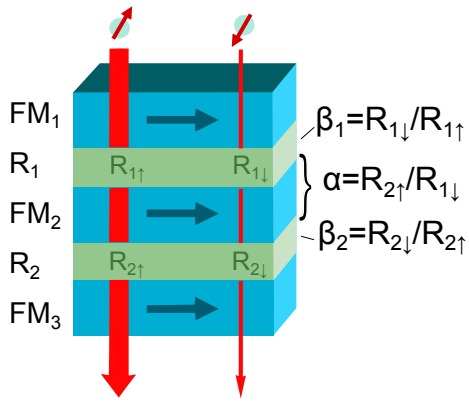

Figure 5.14: Diagram of a DMTJ illustrating the two-current model and the parameters α, β_1 and β_2.

The shot noise through a double barrier junction with ferromagnetic electrodes is calculated using a model of sequential tunneling. In the model, DMTJs are described by the parameters α, β_1 and β_2, as well as the spin relaxation parameter g. These correspond to the asymmetry (α), which takes into account the difference between the barriers, as well as the two spin filtering parameters (β_1 and β_2, one for each barrier). The influence of resonant tunneling is not taken into consideration. The parameters have been evaluated by fitting the experimental Fano factor for all magnetic configurations as well as the TMR ratio, showing a good agreement the experimental observations in the case of strong spin relaxation.

5.4.1. Calculation of shot noise in the absence of spin relaxation

If spin-flip transitions can be disgarded (or are absent), the two spin channels $\sigma = [\uparrow, \downarrow]$ can be considered as fully separated (see Fig. 5.14). The shot noise of each spin channel, S_σ, can be then calculated from the expression for spinless particles[204]:

$$S_\sigma = \frac{R_{1\sigma}^2 S_{1\sigma} + R_{2\sigma}^2 S_{2\sigma}}{R_\sigma^2}, \tag{5.1}$$

where $R_{i\sigma}$ is the resistance of the i-th junction in the spin-σ channel, R_σ is the total resistance of the spin-σ channel, $R_\sigma = R_{1\sigma} + R_{2\sigma}$, and $S_{i\sigma} \simeq \frac{2eV}{R_\sigma}$ (valid if the transmission probability is small for each barrier). V is the external voltage applied to the system, and the index $i = 1, 2$ refers to the two tunnel barriers of the DMTJs: $i = 1$ for the left and $i = 2$ for the right barrier. Including both spin channels when calculating the shot noise S of the double-junction structure one obtains $S = S_\uparrow + S_\downarrow$.

The average value of charge current driven by the voltage V is

$$I = V \frac{R_\uparrow + R_\downarrow}{R_\uparrow R_\downarrow}. \tag{5.2}$$

From Eqs. 5.1 and 5.2, the Fano factor in the absence of spin relaxation is given by:

$$F \equiv \frac{S}{2eI} = \frac{(R_{1\uparrow}^2 + R_{2\uparrow}^2)\, R_\downarrow^3 + (R_{1\downarrow}^2 + R_{2\downarrow}^2)\, R_\uparrow^3}{R_\uparrow^2 R_\downarrow^2 \,(R_\uparrow + R_\downarrow)}. \tag{5.3}$$

In the case of a symmetric structure, $R_{1\sigma} = R_{2\sigma} = R_\sigma/2$, from Eq.(4) one finds $F = 1/2$. In order to describe the numerical results, we introduce the following parameters (see Fig. 5.14):

$$\alpha = R_{2\uparrow}/R_{1\uparrow}, \quad \beta_i = R_{i\downarrow}/R_{i\uparrow}. \tag{5.4}$$

Let us now consider the case of a DMTJ with three ferromagnetic electrodes. The Fano factor in each magnetic configuration can be obtained as a function

of α, β_1 and β_2 by using eqs. 5.3 and 5.4. Using as a reference the resistance of each barrier in the P state, $R^0_{\sigma\uparrow}$, the coefficients take the following values for each state:

P	$R^P_{1\sigma} = R^0_{1\sigma}$	$R^P_{2\sigma} = R^0_{2\sigma}$
AP1	$R^{AP}_{1\sigma} = \sqrt{R^0_{1\uparrow}R^0_{1\downarrow}}$	$R^{AP}_{2\sigma} = \sqrt{R^0_{2\uparrow}R^0_{1\downarrow}}$
$AP2_1$	$R^{AP2_1}_{1\sigma} = R^0_{1\sigma}$	$R^{AP2_1}_{2\sigma} = \sqrt{R^0_{2\uparrow}R^0_{1\downarrow}}$
$AP2_1$	$R^{AP2_2}_{1\sigma} = \sqrt{R^0_{1\uparrow}R^0_{1\downarrow}}$	$R^{AP2_2}_{2\sigma} = R^0_{2\sigma}$

As an example, let us consider the AP1 state, for which the resistance of each junction is highest. The corresponding resistance $R^{AP1}_{i\sigma}$ (for $i = 1, 2$) can be expressed by the resistances in the P configuration as $\sqrt{R^0_{i\uparrow}R^0_{i\downarrow}}$.

5.4.2. Calculation of shot noise in the presence of spin relaxation

The previous model proves to be unsufficient to describe the experimental data, since for example, the Fano in the P state is symmetric with the parameter α while in the experiment that is not the case. Thus, spin relaxation in the central electrode is included in the theory in order to obtain a better comparison.

Therefore, taking the spin relaxation into account, one writes the relevant equation for spin density fluctuations δS_z [184]:

$$\Delta J_z^{(2)} - \Delta J_z^{(1)} = -\frac{\delta S_z}{\tau_s}, \tag{5.5}$$

where $J_z^{(i)}$ is the z-component of spin current in the i-th barrier and τ_s is the spin relaxation time in the central electrode. In the limit of strong spin relaxation, instead of Eq. 5.3 one finds[184]:

$$F = \frac{R_{2\uparrow}R_{2\downarrow}(R_{1\uparrow} + R_{1\downarrow})^2 + R_{1\uparrow}R_{1\downarrow}(R_{2\uparrow} + R_{2\downarrow})^2}{[R_{1\uparrow}R_{1\downarrow}(R_{2\uparrow} + R_{2\downarrow}) + R_{2\uparrow}R_{2\downarrow}(R_{1\uparrow} + R_{1\downarrow})]^2}. \tag{5.6}$$

The Fano factors in all four magnetic configurations can be calculated in the same fashion as the case without spin relaxation. In a general case, the authors take into account the spin fluctuations *via* Eq.5.5. However, the corresponding

formulas are cumbersome and will not be presented here and may be found in Ref.[184]. The key element of the theory is the dependence of the SN on the spin density fluctuations. These fluctuations are described by Eq. 5.5 and depend on the spin relaxation. The spin relaxation is conveniently described by the parameter $g = d/v_F\tau_s$, with d being the thickness of the central layer, and v_F the Fermi velocity.

Since the resistance of each state can be calculated as a function of the parameters, the TMR for one of the AP states (AP1, $AP2_1$ or $AP2_2$) may be defined by:

$$TMR = \left(\frac{R_{AP}}{R_P} - 1\right) \tag{5.7}$$

The maximum TMR occurs in the AP1 configuration, which is given by:

$$TMR_{AP1} = \frac{(\sqrt{\beta_1} + \alpha\sqrt{\beta_2})(1 + \alpha + \beta_1 + \alpha\beta_2)}{2(1+\alpha)(\beta_1 + \alpha\beta_2)} - 1\,. \tag{5.8}$$

By using the experimental Fano values for the magnetic states and the TMR in the AP1 state, we have been able to carry out a comparison between experiment and theory.

5.4.3. Comparison between experiment and theory

As can be seen in Fig. 5.15, the experimental data can be accounted for rather well by tuning the parameters α, β_1, β_2 and the spin relaxation parameter g[183–185]. To compare the theoretical results with the experimental data we have used average Fano values in the range between 0.2 and 0.5 V in order to avoid the possible influence of defect states in the barrier below 200 mV[205] or of QWSs observed above 0.5V. Figures 5.15(a) to (c) show the comparison, at T=0.3 K, of the calculated Fano factors as a function of the asymmetry parameter α with the Fano in the measured magnetic states in a DMTJ1,2 and 3 sample respectively. Fig. 5.15(d) presents the same comparison at T=60 K of the DMTJ3 sample of graph (c). There is a good qualitative and quantitative agreement with the experimental results. The combined TMR and SN provide

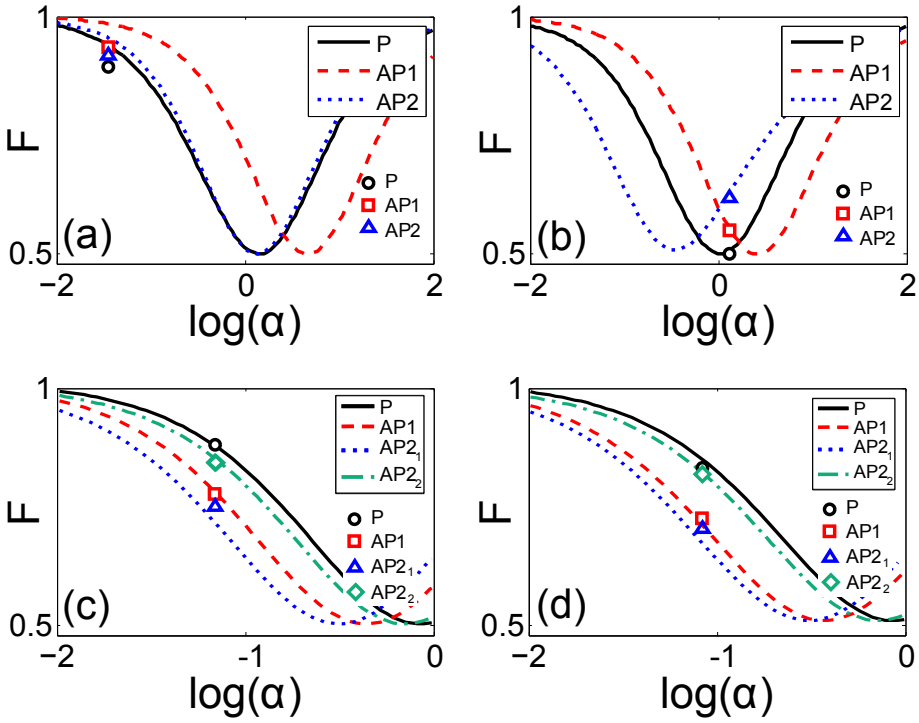

Figure 5.15: Comparison of theory (solid lines) and experiment (points) of the Fano factor measured for three different DMTJs. (a) DMTJ1 at T=0.3 K ($\alpha = 0.035$, $g = 4.9$, $\beta_1 = 42$, $\beta_2 = 2$)[183]. (b) DMTJ2 at T=0.3 K ($\alpha = 1.3$, $g = 0.3$, $\beta_1 = 75$, $\beta_2 = 11$)[183]. DMTJ3 (c) at T=0.3K (g=100, $\alpha = 0.07$, $\beta_1 = 5.7$, $\beta_2 = 27.8$, and (d) T=60K, with $g = 100$, $\alpha = 0.08$, $\beta_1 = 3.5$, $\beta_2 = 28.3$[185].

an evaluation of the three independent parameters α, β_1 and β_2 as well as the spin relaxation g.

Figure 5.16 shows the estimated parameter g and the barrier asymmetry α for our DMTJs at T=0.3 K. It is interesting to note that the best fits to the theory for two measured DMTJ3s (see Fig. 5.15(c)) appear with relatively low g (i.e. large τ_s, estimated to be around 10^{-12}s for $v_F = 10^4$m/s). On the other hand, SN in both measured DMTJ2s is best described with $g \sim 100$[183] (i.e. short τ_s) as seen from Fig. 5.16(a). We relate shorter τ_s in DMTJ2s with an increased density of oblique defects as the epitaxial MgO is grown above

the critical thickness for the plastic relaxation of MgO on Fe[191]. These defects could be "imprinted" on the central electrode, increasing its defectiveness and, in agreement with the Overhauser-Elliott-Yafet model[206], strongly reducing τ_s. The spin relaxation time data estimated from the theoretical fit is plotted along with the results for other materials[207] in Fig. 5.16(b).

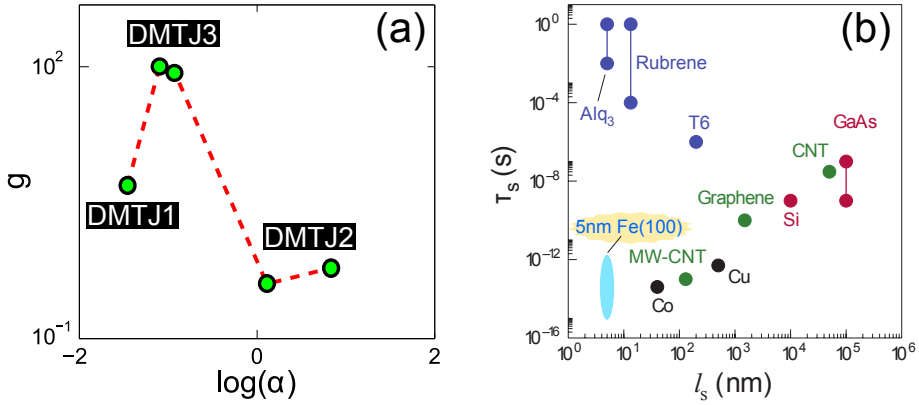

Figure 5.16: (a) Minimum values of the spin relaxation parameter g *vs* α which yield the experimental shot noise and TMR values for all three types of DMTJs. (b) Spin diffusion length l_S as a function of the spin diffusion time τ_S for various spintronics materials, which includes our rough estimation for DMTJ2 and DMTJ3 samples. Adapted from Ref.[207].

We note that the model neglects other possible sources of noise, like $1/f$ and thermal noise. Also, the SN is calculated neglecting spin coherent resonant tunneling. Moreover, the model does not include any deviation of the angle between magnetizations from 0 or π, which may influence the Fano factor[99] or the influence of QWSs, disorder and interfacial states, which may reduce the Fano factor[78]. All these contributions can be responsible for the deviation of the theoretical curves from the experimental points in Fig. 5.15. The strongest deviation in the case of DMTJ1 (Fig. 5.15(a)) could be attributed to the presence of exchange coupling through the thin (3ML) MgO barrier[191,192] and the possible formation of domain walls in the central Fe electrode.

5.5. Conclusions

In conclusion, we have demonstrated that shot noise in Fe/MgO/Fe/MgO/Fe double-barrier magnetic tunnel junctions with a high barrier asymmetry is only weakly suppressed below the Poissonian value ($F \sim 0.9$) and is independent of the magnetic state[183,185]. On the other hand, shot noise in DMTJs with low barrier asymmetry can be effectively reduced below the full shot noise value. Furthermore, the SN value is determined by the relative magnetic configuration of a DMTJ. The corrected Fano factor in these structures is independent of the bias for voltages below 0.5 V. A weak enhancement of shot noise observed at voltages above 0.5 V, supported by oscillations in conductance, indicates the formation of quantum well states in the middle magnetic layer.

The proposed theoretical model[184], based on sequential tunneling through the system and including spin relaxation, successfully accounts for the experimental observations for bias voltages below 0.5 V, where the influence of quantum well states is negligible. The comparison of the model with our experimental data allows obtaining an estimate of the spin relaxation time in the central electrode in the DMTJ.

The work presented in this Chapter could spark several fundamental studies in the area of spintronics. For example, having control over the shot noise in DMTJ devices could be used for the controlled injection of spins between ferromagnets, as well as between FM and other materials. Furthermore, if other materials are used as a central electrode, our work could prove to be a novel method to study the spin relaxation time in different materials using SN measurements.

From a technical point of view, we present a novel method of engineering spintronic devices with the most fundamental noise source in electronics can be controlled and reduced. This scheme could be useful for vertical (e.g. spin current injection in semiconductors through double MgO barriers) or lateral (e.g. quantum dots) electronic structures. DMTJs also seem the preferred option for reducing the intrinsic noise of magnetic field sensors[104], in detriment of serial arrays of MTJs[208] which may experience a higher chance of failure.

Chapter 6

Band edge noise spectroscopy of magnetic tunnel junctions

This Chapter proposes a conceptually new way to gather information on the electron bands of buried metal(semiconductor)/insulator interfaces through the study of the bias dependence of 1/f noise in tunnel junctions with fully epitaxial barriers. In this case, the tunneling probability could be influenced by the relaxation of defect states which determine band edge tails. We demonstrate the validity of this concept by carrying out low frequency noise measurements on $Fe_{1-x}V_x$/MgO/Fe ($0 < x < 0.25$) magnetic tunnel junctions with an improved interface mismatch, thus presenting defect free MgO barriers.
The 1/f noise exhibits clear peaks at specific applied voltages, which are related to the position of the band edges of FeV and therefore indicate that electron tunneling to the band edges of the magnetic electrodes takes place. The change in magnitude of these noise anomalies with the magnetic state allows estimating the degree of spin mixing that takes place between the spin polarized bands at the ferromagnet/insulator interface.
Numerical calculations of the tunneling electron density of states as a function of V doping are in qualitative agreement with the experimental results.

6. Band edge noise spectroscopy of MTJs

6.1. Introduction and motivation

Buried metal (semiconductor)/insulator interfaces are found at the heart of electronics[209]. The current in tunneling devices is determined by the bias, barrier and density of states of the electrodes[17,191]. Electron states not allowed in bulk could become permitted at the surface leading to topological[210,211] or interface resonant states[212]. For metallic structures the scarce knowledge on the interface bands is mainly obtained by indirect methods such as ballistic electron emission spectroscopy[213] or high-resolution X-ray spectroscopy[214]. The possibility of having a reliable and down-scalable in-situ method for investigating interface electron bands remains centrally important[215].

Tunneling magnetoresistance[15,60,61] is extremely sensitive to the band structures of ferromagnet/insulator (FM/I) interfaces[16–21,216–218]. Despite recent attempts to understand the nature of the electron bands which contribute to electron transport in spintronic devices[219–221], the issue remains unsettled. The main tool to characterize interfaces or barriers has been inelastic electron tunneling spectroscopy (IETS)[221–223] analyzing the derivative of the *conductance as a function of bias*. The resulting IETS signals depend on the tunneling density of states (DOS) and inelastic scattering[17,191,224] which could obscure the detection of the band edges in the presence of interface disorder. The bias dependence of *the conductance and its low frequency fluctuations* could be an alternative way to study the interface or electron confinement[225,226] DOS.

As we will discuss in detail below, a commonly accepted phenomenological approach relates the excess low frequency noise (LFN), which often presents $1/f$ dependence, with electrons scattering from defects characterized by a broad distribution of relaxation times with energy[32]. If dominant defect states are located close to the interfaces, they could create interface band edge tails. Therefore, when the tunneling is tuned to some specific band edge in the opposite electrode, the current could acquire an extra LFN due to multiple relaxations originating from defect states contributing to the formation of the band edge tails.

In this Chapter we investigate the bias dependence of conductance and LFN in single barrier tunneling devices in order to determine in-situ the energies of the band edges of the buried interfaces. We unambiguously demonstrate the

validity of the *band edge noise spectroscopy (BENS)* concept by studying seminal Fe/MgO/Fe MTJs with partial doping of the bottom electrode (Fe) with Vanadium (V). Such substitution has been shown to reduce defect states inside the MgO barrier due to improved interface matching between $Fe_{1-x}V_x$ and MgO in $Fe_{1-x}V_xMgO$/Fe MTJs.[86,227,228]. Our numerical simulations confirm that tunneling of band-tail electrons, influenced by spin orbit interactions, are responsible for the observed LFN anomalies.

6.2. Growth and characterization of the samples

The samples presented in this Chapter were grown by the group of Prof. Stephane Andrieu from the Institute Jean Lamour, CNRS-Nancy University within a bilateral collaboration project with our group.

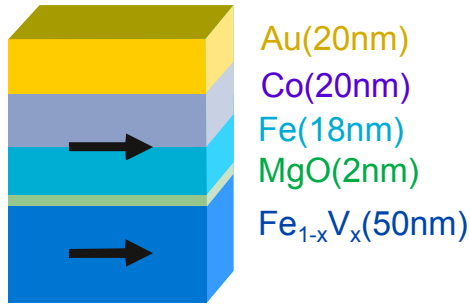

Figure 6.1: Sketch of the sample layer structure.

As can be seen in Figure 6.1, the layer sequence of the studied MTJs is:

$$MgO//Fe_{1-x}V_x(50\ nm)/MgO(2nm)/Fe(18\ nm)/Co(20\ nm)/Au(20nm)$$

The single-crystal multilayers were deposited on MgO(100) substrates by molecular beam epitaxy (MBE) at a typical base pressure of 10×10^{-10} mbar. Before the deposition, the substrates are outgassed at 875 K. A 10nm MgO layer is grown at 725 K in order to prevent the diffusion of residual carbon

to the bottom electrode[229]. The bottom electrode, magnetically the softest, is grown using Fe-V alloys with different concentrations of Vanadium, obtained by Fe and V co-evaporation. The film is then annealed at 825 K for 20 minutes to reduce its roughness. Afterwards, a 2 nm thick MgO barrier is deposited and controlled by reflection high energy electron diffraction (RHEED) intensity oscillations. Then, an 18 nm thick Fe layer is grown over the MgO barrier and annealed for 10 min at 475 K. A 20 nm thick Co is grown over the Fe layer, forming a magnetically harder electrode by the coupling between layers. The layered structure is protected from oxidation by a 20 nm Au film. The MTJs were patterned by UV photolithography (described in Section 5.2) and Ar etching into pillars with square cross sections of lateral size from 10 to 50 μm. Additional details about the fabrication of the samples can be found in Refs.[227,230].

6.3. Experimental results

The setup for low temperature noise measurements was described in Section 3.3. The typical noise power spectra (S_V) in the antiparallel (AP) or parallel (P) states reveal the presence of 1/f noise in the frequency range between 1 and 100 Hz (depending on the sample type), where $S_V(f) \propto 1/f^{\beta}$ (with $0.8 < \beta < 1.5$), as can be seen in Fig. 6.2. The fact that the 1/f noise is only observed up to such low frequencies is indicative of a high structural quality. The bias dependence of the LFN has been determined through the Hooge factor (α) from the phenomenological expression (Equation 2.11) $S_V(f) = \alpha \cdot V^2 A \cdot f$, where V, A and f indicate bias voltage, area of the sample and frequency, respectively. Qualitatively similar results have been obtained by analyzing integrated LFN . Shot noise (SN) was obtained from the frequency independent part of the spectra for temperatures below 10K, as explained in Section 3.7 and demonstrated in Chapters 5 and 7.

We begin by analyzing the electron transport and SN behavior at T=4 K, which is summarized in Fig. 6.3. As can be seen in Fig. 6.3(a), the zero bias TMR as a function of V content shows a maximum value for a Vanadium content of 8%, confirming a reduction of the interface mismatch reported previously at room temperature[86,227,228]. In the same graph, it can be seen that

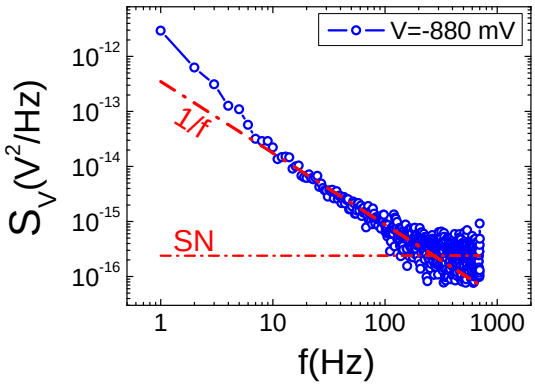

Figure 6.2: Typical low frequency noise spectrum presenting 1/f and shot noise contributions for a sample with a $Fe_{0.75}V_{0.25}$ bottom electrode.

tunneling statistics of these junctions is Poissonian (within the experimental tolerance) presenting an average Fano factor of $F = 1 \pm 0.05$. This indicates that the samples have a very high structural quality and present direct (or very nearly direct) tunneling processes.

Figure 6.3(b) shows the bias dependence of the Hooge factor with the bias in both P and AP states for a Fe/MgO/Fe MTJ used as reference or control sample. An excess LFN is seen for biases below 200 mV, where FeO[205] and Fe/MgO[191] interface defect states have been predicted to influence the conductance. For the MTJ with a non-optimized Fe/MgO interface one observes a strong suppression of LFN with bias with weak anomalies in α around 0.5 V (indicated by arrows in the graph).

The doping of Fe with V improves the interface mismatch and decreases the Fe/MgO interface defect states density[86,227,228], which allows the implementation of the BENS method. Figure 6.4(a) shows the dependence of the shot noise and the Hooge factor α with the applied bias, for $Fe_{0.96}V_{0.04}$/MgO/Fe MTJs. The shot noise analysis yields a Fano factor close to one, indicating that direct tunneling takes place in the bias range under study (Fig. 6.4(a)). In contrast to what is observed for the reference sample (Fig. 6.3), the LFN shows a clear enhancement (factor of 2) of conductance fluctuations around ± 0.6 V. Yet a stronger enhancement of the LFN close to 0.6 V is observed in the AP configuration. Along with the enhacement of 1/f noise, as can be

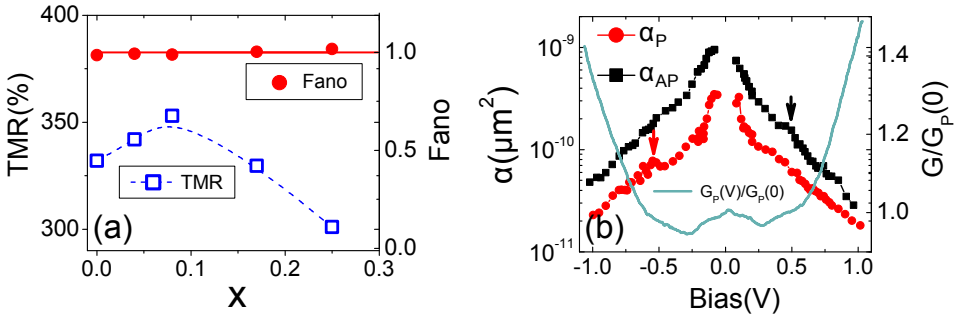

Figure 6.3: (a) Dependence of the zero bias TMR and the Fano factor at $T = 4$ K as a function of V content. (b) Bias dependence, at $T = 4$ K, of the dynamic conductance in the P state, and the Hooge factor α for both P and AP states for Fe/MgO/Fe junctions. Arrows indicate weak peaks.

seen in Fig. 6.4(b), the dynamic conductance in the P state shows an upturn around 0.6 V. The upturn is much clearer in the P state, so the AP state not shown for simplicity. Numerical calculations of the tunneling electron DOS indicate that the upturn in conductance and the noise enhancement could be related with the opening of a new transmission channel when the Fermi level of one magnetic electrode crosses one of the band edges of the other magnetic electrode, indicated by arrows in Fig. 6.4(b). Details of the calculations are discussed further on.

Even clearer signs of the band edges in LFN are seen when the V content reaches 8%, for which the lowest background LFN and the maximum TMR (Fig. 6.3) are achieved. Figure 6.5 shows the dependence of α with the applied bias in $Fe_{0.92}V_{0.08}$/ MgO/ Fe MTJs were the optimum relation between two competing effects is reached: (i) the relaxation of the FM/I interface and (ii) a non-essential suppression of the magnetization and the induced Fe-V structural disorder[86,227,228].

We have found that the $Fe_{0.92}V_{0.08}$/MgO/Fe MTJs show clear anomalies in the Hooge factor for biases around 1 V and around 0.6 V for the P state only, as shown in Fig. 6.5(a),(b). Fig. 6.5(d) demonstrates how the anomaly in the P state around 0.6 V gradually disappears with temperature, probably due to thermal excitations.

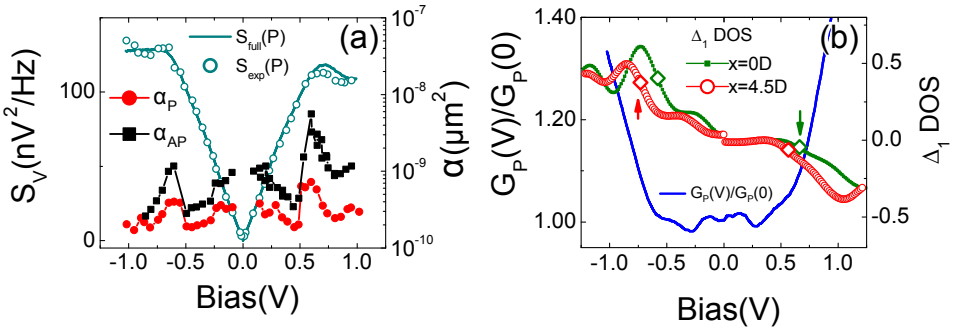

Figure 6.4: (a) Bias dependence at $T = 4\ K$ of the Hooge factor and SN for Fe $_{0.96}$ V$_{0.04}$ /MgO/Fe MTJ. (b) Dependence of the conductance with the applied voltage at $T = 4\ K$ combined with the calculated Δ_1 DOS as a function of energy with respect to E_F. Inflection points (open dots) indicate Δ_1 DOS band edges for 4% Vanadium for $V < 0$ and pure Fe (x=0) for $V > 0$.

Qualitatively similar effects were seen for $Fe_{0.83}V_{0.17}$/ MgO/ Fe and $Fe_{0.75}V_{0.25}$/ MgO/ Fe MTJs with the latter being the most robust to electrical breakdown (standing up to 2.5 V). In the high V content range, the LFN is strongly influenced by random telegraph noise at positive biases around 1 V, reflecting a stronger asymmetry in interface defect states previously visualized with scanning electron microscopy for $Fe_{0.8}V_{0.2}$/MgO/Fe MTJs[228].

6.3.1. BENS method and phenomenological 1/f model

Let us now explain the peaks observed in 1/f noise with the concept of *band edge noise spectroscopy* (BENS) which is qualitatively sketched in Fig. 6.6(a). If the tunneling through the barrier is coherent, the main source of LFN is conductance fluctuations due to atomic defects affecting Δ_1 and Δ_5 interface states. The resulting localized states close to the band edges[231] could contribute, as reported for bulk semiconductors[232,233], to the enhanced LFN. The key new feature of the *BENS* is the versatility in displacing the Fermi level (E_F in Fig. 6.6(a)) of the ejector electrode with respect to the different band edges (or mobility edge, E_C in Fig. 6.6(a)) by simply varying the applied bias. The right panel shows how the conductance and its derivatives are expected to

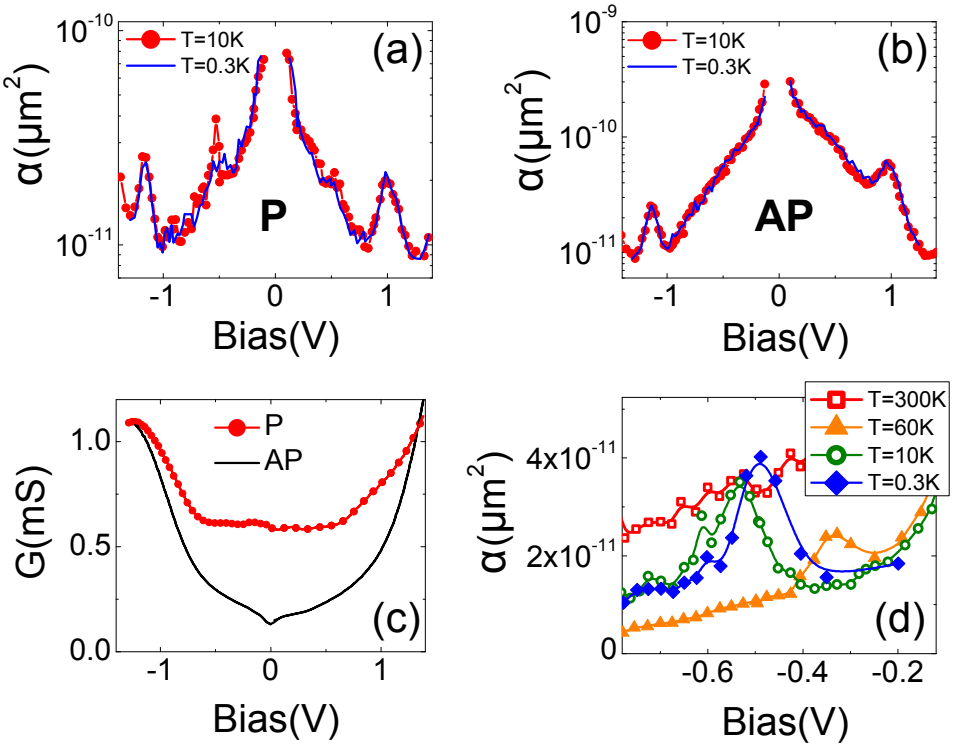

Figure 6.5: Bias dependence at $T = 4\ K$ of the Hooge coefficient for the (a) P state and (b) AP state in $Fe_{0.92}\ V_{0.08}$ /MgO/Fe MTJs. (c) Bias dependence at $T = 4\ K$ of the dynamic conductance for the P and AP state. (d) Low frequency noise peaks gradually disappear with increasing temperature.

change when a new electron channel with a band edge opens at E_F. In order to clearly detect inelastic relaxation through IETS, some well defined defect states should relax energy through coupling to a well-defined set of phonon energies.

A simplified physical picture explaining the variation of LFN when tunneling to three different energies $E_{1,2,3}$ around E_C (Fig. 6.6(a) and Fig. 6.7(a)) is as follows. When electrons tunnel to energies $E_1 > E_C$, their relaxation time is fast due to the delocalized character of the band states near E_1 with a correspondingly small contribution to LFN. For tunneling to electron states $E_3 < E_C$ the LFN is also expected to be small due to low probability of these tunneling events. However, when electrons tunnel to the energies $E_2 \lesssim E_C$,

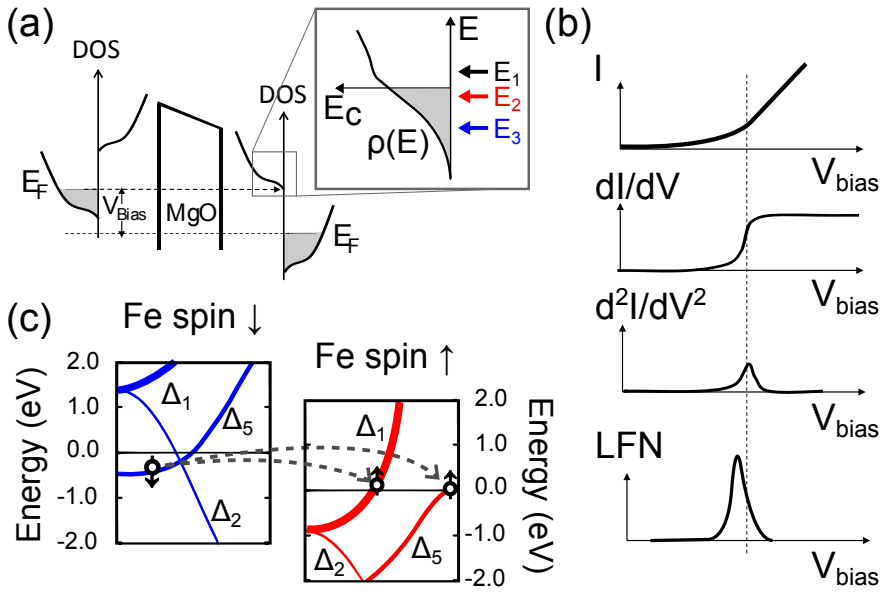

Figure 6.6: (a) Sketch of the principle behind BENS, presented for the AP state, where E_C corresponds to the mobility edge. (b) The energies of these defect states can be inferred from the IV curve of the sample, and its first (dynamic conductance) and second (IETS) derivatives, but they are detected in a much clearer way though low frequency measurements.(c) Sketch of a band edge (Δ_1, Δ_5) contribution to the tunneling at $\sim -1.2V$.

the tunneling current could be affected by multiple trapping-type relaxations originating from shallow defect states contributing to the formation of the band edge tails. We estimate that the LFN peak width is roughly determined by the energy difference between the mobility edge and the bottom of the band tail.

A commonly accepted phenomenological model (already discussed in Section 2.2) attributes the occurrence of 1/f noise to the scattering of electrons from defects, where each of these defects is characterized by a certain relaxation time τ. The total $1/f$ noise is described as the sum of the contribution of multiple defects presenting a broad distribution of relaxation times with energy[32]. If the dominating defect states are located close to the interfaces, they may modify the edges of interface bands, creating tails. Defect states with different relaxation times are sketched in Fig. 6.7(a). These defects create a band edge

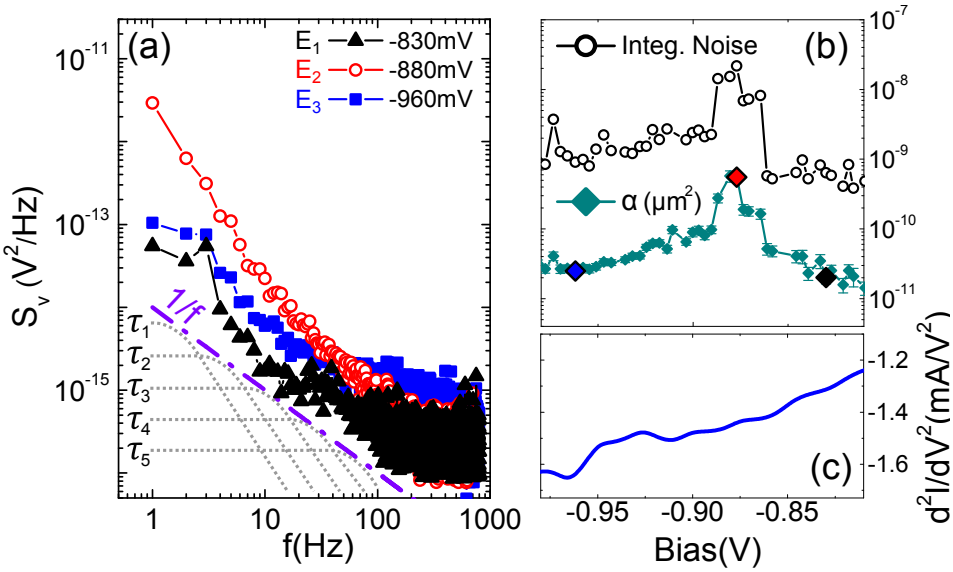

Figure 6.7: (a) Spectra at T=0.3K corresponding to the three energy states from a junction with 25% Vanadium in the P state, with a maximum 1/f noise at the expected band edge energy. (b) The peak is clear in the dependence bias of the Hooge factor as well as of the integrated noise (normalized by the voltage squared, and therefore, adimensional). (c) The noise peak is not reflected in the IETS curve.

tail, as shown in Fig. 6.6(b). The sum of the Lorentzian-type spectra from the relaxation of each defect state, characterized by τ_i, all contribute to the total $1/f$ noise.

The following arguments accompanied by rough experimental noise power spectra explain the nature of the LFN anomalies found in our tunnel junctions with different Vanadium concentrations. If the Fermi levels of the ferromagnetic leads are adjusted (by applying a bias) so the Fermi level of one electrode aligns with a certain band edge from the other electrode (as shown in Fig. 6.6(c) of the manuscript), an extra LFN may appear due to multiple relaxations which originate from the defect states which create the band edge tails. These band edge tails contain localized states below a mobility edge E_c (Fig. 6.7(b)). When electrons tunnel to energies above E_c, ($E_1 > E_c$) their relaxation time is fast because of the delocalized character of these band states and their contribution

to the LFN is small (in the frequency window where conductance fluctuations are experimentally measured). The low frequency noise is also expected to be small when tunneling to electron states much below the mobility edge ($E_3 < E_c$), which corresponds to a small density of states due to the low probability of these events taking place. However, when electrons tunnel to energies in the proximity or just below the mobility edge ($E_1 \lesssim E_c$), the tunneling current may be affected by the defect states which form the band edge tails, and provide an excess contribution to the low frequency noise. Spectra for these three situations are presented in Fig. 6.7(a). Note that due to their high barrier and interface quality, our single crystalline magnetic tunnel junctions show mostly flat spectra (shot noise) above 100 Hz even at high bias ($\sim 1\ V$)

The LFN peak width is roughly determined by the energy difference between the mobility edge and bottom of the band tail. The band tail width by itself could be determined by the influence of the different type of defect states (O, Mg, Fe, vacancies or interface steps) on the position of the energy bands. Previous numerical calculations[205] evaluated energies of O and Mg defects states inside an MgO barrier to be below 150 mV .

In order to demonstrate that the position of the observed LFN anomalies depends only weakly on the method of analysis, Fig. 6.7(b) compares the dependence of α and the integrated LFN noise (which is adimensional because it is normalized by the square of the bias) with the bias in the P state, at $T = 0.3\ K$, of a tunnel junction with 25% Vanadium. Both methods provide qualitatively similar results.

As can be seen in Fig. 6.7(c), the noise peak is not reflected in the IETS curve. We believe that the random interface potential and the absence of well-defined defect states smear out the IETS signals. Tunneling to the band tail weakly influences IETS reflecting only the derivative of the DOS close to E_C. On the other hand, much stronger changes in LFN vs. bias are seen due to a strong change of excited defect relaxation times[233] when tunneling close to E_C, activating an excess of the low frequency conductance fluctuations. Therefore, interface defect states dominate the LFN, and not the derivative of the conductance (Fig. 6.7(c)). We argue that the LFN mainly originates from disorder/defects close to the FM/I interface because: (i) the tunnel through the barrier is direct (Fig. 6.3); (ii) the metallic nature of the electrodes, with

resistance a few thousand times below the barrier resistance, ensures that electric signals and their fluctuations mainly come from regions in the barrier and interfaces; (iii) by analyzing LFN at higher biases we avoid the direct resonant excitation of localized FeO or O interface defect levels predicted below 200 mV[205].

In the MTJs under study, electron tunneling mainly occurs between polarized bands with different Bloch state $\Delta_{1,5}$ symmetries spin filtered by the MgO barrier[18–21,216,217]. This allows a rough estimation of the interband mixing at the interface by analyzing variation of *BENS* response with relative alignment of the electrodes. Let us discuss qualitatively the reasons why *BENS* could provide LFN peaks both in the P and AP states (Figs. 6.4,6.5). For simplicity, we shall use the majority and minority Fe electron bands tunneling in Fe/MgO/Fe junctions (Fig. 6.6(c)). When the MTJ is in the AP state, then in accordance with *BENS* arguments $\Delta_{5\uparrow} \Rightarrow \Delta_{5\downarrow}$ and $\Delta_{1\uparrow} \Rightarrow \Delta_{1\downarrow}$ band edge tunneling could provide a peak in the low frequency noise of the AP state at different biases from 0.4 to 1.3 V if conductance fluctuations originate from elastic scattering events. Experimentally, however, we observe LFN peaks in the P state as well (Fig. 6.4(a)), which we link with the presence of spin-orbit coupling induced $\Delta_{1(\uparrow\downarrow)} \Longleftrightarrow \Delta_{5(\downarrow\uparrow)}$ interband mixing at the Fe/MgO interface[234]. Indeed, large lateral momentum transfer and interband scattering could be dominant only close to the interfaces[22]. Within such scenario, the relation between amplitudes of the peaks LFN(P)/LFN(AP) provides an evaluation of the degree of interband mixing between majority $\Delta_{1\uparrow}$ band and the minority $\Delta_{5\downarrow}$ of roughly 0.2-0.3.

6.4. Numerical calculations

In order to examine quantitatively the applicability of our model, numerical calculations have been carried out by the group of Professor Mairbek Chshiev from the Université Joseph Fourier in Grenoble (France). The simulation consists of $ab-initio$ calculations of $\sqrt{2} \times \sqrt{2}$ unit cell of $Fe_{1-x}V_x$ /MgO (x=0, 0.045, 0.091, 0.182) with a 5 monolayers (ML) of MgO and 11 ML of $Fe_{1-x}V_x$. The first-principles calculations are based on density functional theory (DFT) as implemented in the Vienna *ab initio* simulation package

(VASP)[235–237] within the framework of the projector augmented wave (PAW) potentials[238,239] to describe electron-ion interaction and generalized gradient approximation (GGA)[240] for exchange-correlation interactions. A 13×13×3 K-point mesh was used in our calculations. A plane wave energy cut-off equal to 500 eV for all calculations was used and is found to be sufficient for our system

The TMR is calculated from the numerical calculations using the Jullière model[15], as shown in Fig. 6.8. A maximum value is reached for 9% of V, which is quite similar to the experimentally observed 8% value.

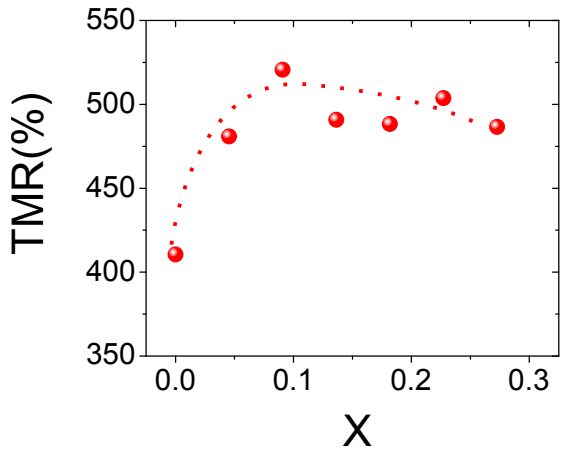

Figure 6.8: Dependence of the calculated TMR values as a function of the Vanadium content. The symbols correspond to the estimated TMR values and the dotted line is a guide for the eye.

Fig. 6.9 compares the experimentally observed LFN anomalies in the P state (open dots) with the band edge positions (closed dots) estimated from inflection points in the DOS simulations for the majority and minority Δ_1 and Δ_5 states of $Fe_{1-x}V_x$/MgO (x=0, 0.045, 0.091, 0.182) structures (as indicated by arrows in the Fig. 6.4(b)). We have also indicated by horizontal dotted lines the estimated positions of the band edges of the Fe/MgO structure.

A reasonable agreement between simulations and the experiment is observed, especially for the Vanadium content between ($0.04 < x < 0.17$) with reduced lattice mismatch, the lowest background LFN and the highest TMR.

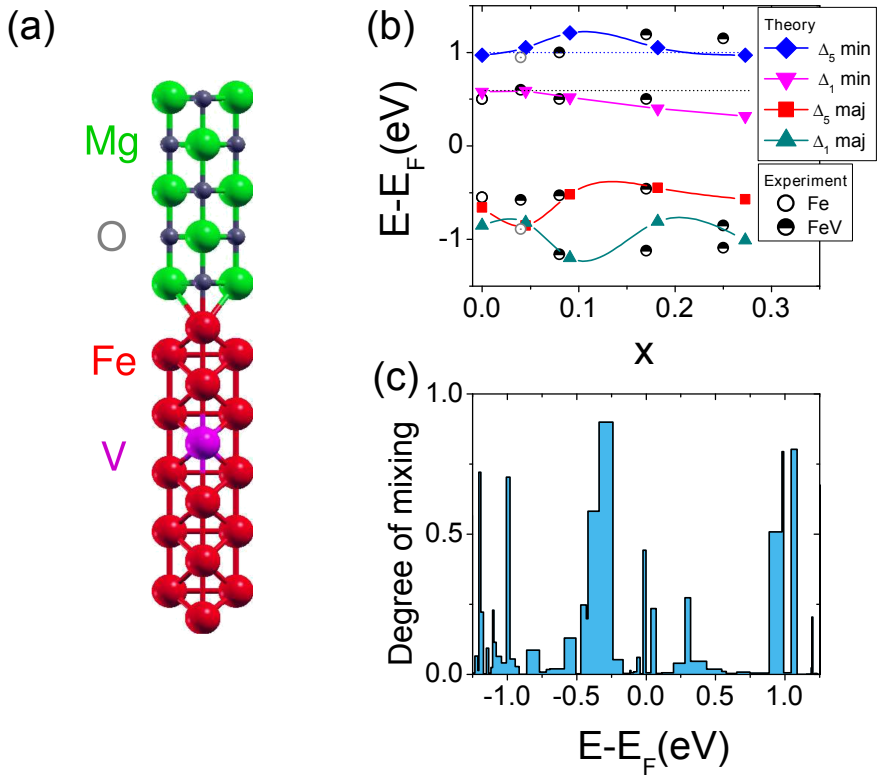

Figure 6.9: (a) Schematic of the calculated crystalline structure for a $\sqrt{2} \times \sqrt{2}$ unit cell of $(Fe_{1-x}V_x)_{11}/MgO_5$. (b) Calculated changes in the energies of the band edges in $Fe_{1-x}V_x$ compared to the experimental data of low frequency noise anomalies for the P state. Fully open experimental points indicate a weak peak (increase of noise in less than 10%). (c) Calculated degree of mixing between Δ_1 and Δ_5 interface Bloch state character in $(Fe_{1-x}V_x)_{11}/MgO_5$ for x=0.091.

A few factors could contribute to some difference between experimental results and calculations. First of all, calculations do not consider the presence of dislocation induced mismatch as well as the structural disorder difference between bottom and top interfaces[228]. On the experimental side, measurements on MTJs with the least Vanadium were done below 1 V due to their vulnerability, making them difficult to compare with the calculation results above 1 V.

Finally, in order to understand the influence of spin mixing at the interface,

we have also analyzed the Bloch state character of the interfacial Fe atom in the presence of SOI as a function of the energy difference to E_F. Fig. 6.9(c) presents this analysis for Δ_1 and Δ_5 interface states in $Fe_{0.909}V_{0.091}$/MgO structure, mainly participating in the electron tunneling through MgO. When the degree of mixing at certain energy is equal to zero, it means that there is no mixing between different Δ channels and there is only one Δ Bloch state character that dominates the tunneling at this energy tunneling. The channel mixing is more pronounced at biases around $-(0.4-0.5)\ V$ and not above $\pm 1V$, i.e. close to the intervals where LFN anomalies of different magnitude were observed in both magnetic states (Fig. 6.9(c)). We believe that $\Delta_{5\uparrow} \Rightarrow \Delta_{5\downarrow}$ and $\Delta_{1\uparrow} \Rightarrow \Delta_{5\downarrow}$ mixing could be due to surface induced band crossings and explains the appearance of peaks in LFN both in the P and AP states.

6.5. Conclusions

In conclusion, the concept of band edge noise spectroscopy has been introduced in this Chapter. This method allows investigating the energies of electron band edges of the materials in a wide class of tunneling devices by the analysis of low frequency noise as a function of the applied bias. We have successfully tracked the band edge energies of the FM electrodes in epitaxial FeV/MgO/Fe magnetic tunnel junctions with different degrees of V doping. The dependence of the *BENS* on the relative magnetic alignment of the electrodes allows us to estimate the importance of interband hybridization and spin flips at the FM/I interfaces. Numerical calculations based on density functional theory of spin-polarized density of states have been carried out in collaboration with Prof. Mairbek Chshiev's, and present a good qualitative agreement with our experimental results. Given the crucial importance of buried interfaces in solid-state devices, the clear need to understand their electronic structure, and the limited options available, development of this novel methods our work presents a substantial advance in the field of characterizing buried interfaces.

6. Band edge noise spectroscopy of MTJs

Chapter 7

Direct and sequential tunneling regimes through organic barriers

7.1. Introduction

In this Chapter, we investigate conductance and shot noise in magnetic tunnel junctions with organic barriers. The aim is to compare two different types of samples have been measured: *(i)* magnetic tunnel junctions with PTCDA tunnel barriers between 1.2 and 5 nm thick and *(ii)* spin valves with thick (200nm) Alq_3 barriers.
Our organic magnetic tunnel junctions (O-MTJs) with PTCDA barriers present magnetoresistance ratios between 10% and 40%, and they systematically exhibit superpoissonian shot noise which additionally depends on the magnetic configuration of the device[241]. Our observations are accounted for qualitatively within a model based on spin dependent electron tunneling through an interacting two-level (or multi-level) system. On the other hand, the spin valves with thick Alq_3 barriers present subpoissonian shot noise which depends on the temperature, indicative of variable range hopping.

As was presented in Section 2.7, the use of organic molecules has introduced revolutionary ways of creating new spintronic devices in the past few years. Or-

ganic elements used as components in electronic devices have some advantages over inorganic materials, since their electronic properties can be tuned chemically, they are mechanically flexible or they can form self-assembled layers. Organic spintronics may lead to unique devices with interesting properties, as for example organic light emitting diodes (OLEDs) which present magnetically controlled luminescence[242]. Exploring the unique properties of the organic world to improve and create new functionalities in spin related optics, electronics and memory elements has attractted considerable attention in the past decade[114,117,118,124,243–245]. Despite the extensive research carried out in organic materials, the statistics of tunneling electrons through organic barriers remains mostly unexplored. For example, $1/f$ noise measurements have been used to determine device quality[246], or transport features in graphene-based devices (including one or several layers)[247]. In another study, the $1/f$ noise and DC leakage measurements were used as a diagnostic tool for OLED reliability in a production line[248]. Current $1/f$ noise measurements have been also used to identify individually contacted organic molecules[249,250].

Section 2.7 also discussed several reports of magnetoresistance effects in organic spin valves and magnetic tunnel junctions in which the thickness of the organic spacers range between a few tens of nm up to a few hundred nm, exceeding by far the tunneling regime. Constructing MTJs with organic barriers is experimentally demanding, as the organic layers need to be continuous and have thicknesses of a few nm. Only a handful of studies of O-MTJs with thin organic barriers, presenting room temperature TMR have been carried out[124,126,251].

There exists a great controversy regarding the magnetoresistance effects observed in spin valve devices containing organic semiconductor layers (such as Alq_3) of thicknesses around 100-200 nm. Some authors associate the observed MR effects to spin injection and transport in the organic layer, while others propose that tunneling takes place through locally thin regions of the layer. The literature also suggests an additional point for disagreement, as studies present both positive[122] and negative[117] MR ratios.

Several explanations for the physical origin of the MR sign in junctions with Alq_3 have been proposed. Barraud et al.[128] studied nanoindentation-based LSMO/Alq_3/Co junctions. In this study, the authors aim to explain

the fact that both negative[121] and positive[252] MR is observed for large area junctions with thick organic spacers. The authors suggest that the formation of spin-hybridization-induced polarized states in the first molecular layer at the electrode interface completely changes the magnetoresistance of organic spin valves. A conclusion is reached that the sign of the MR at small measurement voltages is determined by the sign of the product of the polarization of the different FM/OSC interfaces, i.e. $P(Alq_3/Co)$ and $P(LSMO/Alq_3)$. Another interpretation of the origin of the MR devices with thick organic spacers is given by Wang et al.[253]. The authors study a semi-spin valve device with only one FM electrode with Alq_3 spacers. They find that the electrical conductivity of the organic film at room temperature is affected by the stray fields of the domains present in a magnetically unsaturated ferromagnet. The "fringe" fields from the ferromagnet provide a local magnetic field that changes the electronic transport properties through the hyperfine field, showing that the MR effects in the device originate from electrical transport through the inhomogeneous stray fields from the ferromagnet.

In this chapter we will compare the different statistics in the transport through thin PTCDA layers in the tunneling regime (1.2-5 nm) or thick (200 nm) Alq_3 spacers in the sequential tunneling regime, with the hope of shedding light on the mechanisms which govern the transport through them. Our results show qualitatively different electron tunneling statistics when the organic spacer in these devices is in the tunneling regime or well above it. The results regarding OMTJs with PTCDA spacers have been published in Ref.[241].

From the point of view of technological applications, the key limiting factor for the operation for any spintronic device is its signal to noise ratio. Therefore, the investigation of noise sources in organic tunnel junctions and spin valves is of fundamental and technological interest, as the noise ultimately determines their practical applications. As we discussed in Chapter 2, shot noise (SN) measurements have been used systematically to characterize the electronic transport mechanisms in inorganic spintronics[67,75–77,79,89,175,254]. The precise knowledge of shot noise can provide valuable information on electron correlations near the interfaces with organic barriers, especially in the regime of direct tunneling. In fact, the role of interfaces remains one of the central issues in organic spintronics[255].

7. Direct and sequential tunneling regimes through organic barriers

The normalized shot noise or Fano factor in MTJs with inorganic barriers has been reported to be equal to unity[67,75] for high-quality barriers (direct tunneling) or less than unity[63] for non-homogeneous barriers (sequential tunneling). The Fano factor in our O-MTJs with PTCDA barriers varies between 1.5 and 2, which points to spin dependent bunching taking place when electrons directly tunnel through the barrier. Our main findings are explained in terms of a model which includes tunneling through a two level (or multilevel) system, originated from interfacial bonds of the PTCDA molecules. Our results suggest that interfaces play an important role in the control of shot noise when tunneling through organic barriers. The normalized shot noise values in our devices with thick Alq_3 layers is clearly suppressed below the poissonian value, indicating that the tunneling processes are sequential, with the number of "jumps" depending on the temperature.

7.2. Organic magnetic tunnel junctions in the electron tunneling regime

7.2.1. Sample growth

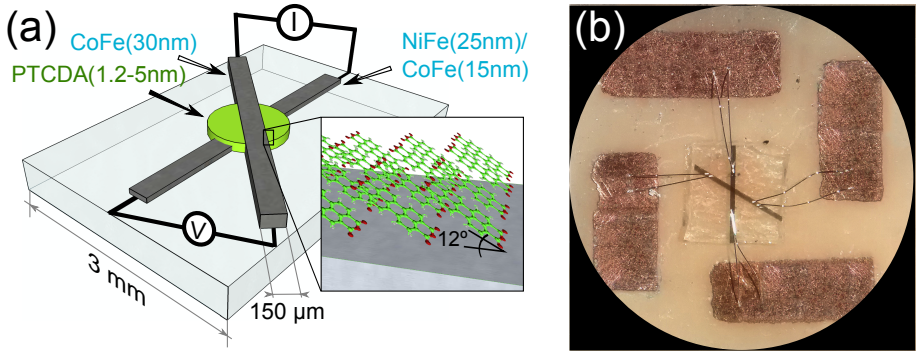

Figure 7.1: (a) Diagram of the sample structure. (b) View through the microscope of a sample on a glass substrate contacted to Cu pads.

The growth of the junctions was carried out by Dr. Jhen-Yong Hong within a collaboration project between the Magnetrans-UAM group and the group of

7.2 Organic magnetic tunnel junctions in the electron tunneling regime

Prof. Minn-Tsong Lin from the National Taiwan University (Taipei, Taiwan). The layer sequence in the PTCDA organic MTJs studied is:

NiFe(25nm)/CoFe(15nm)/Al_xO(0.6nm)/PTCDA(1.2-5nm)/Al_xO(0.6nm)/CoFe(30nm)

The structure was deposited onto a glass substrate, and the junctions were prepared in a high-vacuum environment with a base pressure lower than 10^{-8} mbar. The metallic layers were deposited by sputtering with an Ar working pressure of 5×10^{-3}mbar. Organic semiconductor (OSC) PTCDA layers were grown by thermal evaporation at 10^{-8} mbar, with a deposition rate of 0.1 nm/s. Thin AlO_x layers were grown between the PTCDA layer and both ferromagnetic layers by partially oxidizing Al in oxygen plasma for 5 s. Figure 7.1(a) presents a schematic view of the investigated O-MTJs. As can be seen, the ferromagnetic electrodes are deposited as lines of width of 150 μm. The free layer is a NiFe/CoFe line, parallel to which the external magnetic field is applied. The pinned layer is made of CoFe, and it forms an angle of 45° with the free layer, which results in the pinned layer having a higher effective coercive field than the free layer. The glass substrate is then glued onto a circuit board and the electrodes of the sample are wire-bonded to millimeter sized Cu pads, as shown in Figure 7.1(b). The circuit board is mounted on our sample holder, and the Cu pads are connected to our measurement circuit with gold wires.

Previous studies on this kind of samples revealed a TMR of 12% at room temperature, and an exponential dependence of the resistance with the PTCDA film thickness[251], indicative of quantum tunneling. The recent work by Hong et al.[256] presents the characterization of the OSC/FM interfaces in these samples through XPS measurements. The junctions exhibit room temperature, MR ratios of around 12% when the partially oxidized alumina buffer layer is included between the OSC and the FM layers. The authors conclude that the PTCDA molecules lie essentially flat regardless of the layer they are deposited onto (AlO_x/Co or Co). A tilt angle of $12° \pm 3°$ (see Fig. 7.1(a)) is estimated for the average stacking orientation of the molecules with respect to the contact plane (either AlO_x or Co). The C 1s and O 1s core-level XPS spectra indicate that a hybridized layer is formed at the OSC/FM interface. *The addition of a thin AlO_x buffer layer prevents the electronic interaction (hybridized layer)*

between the Co and PTCDA layers, preserving an effective spin injection into the organic PTCDA spacer thanks to which an MR response is observed.

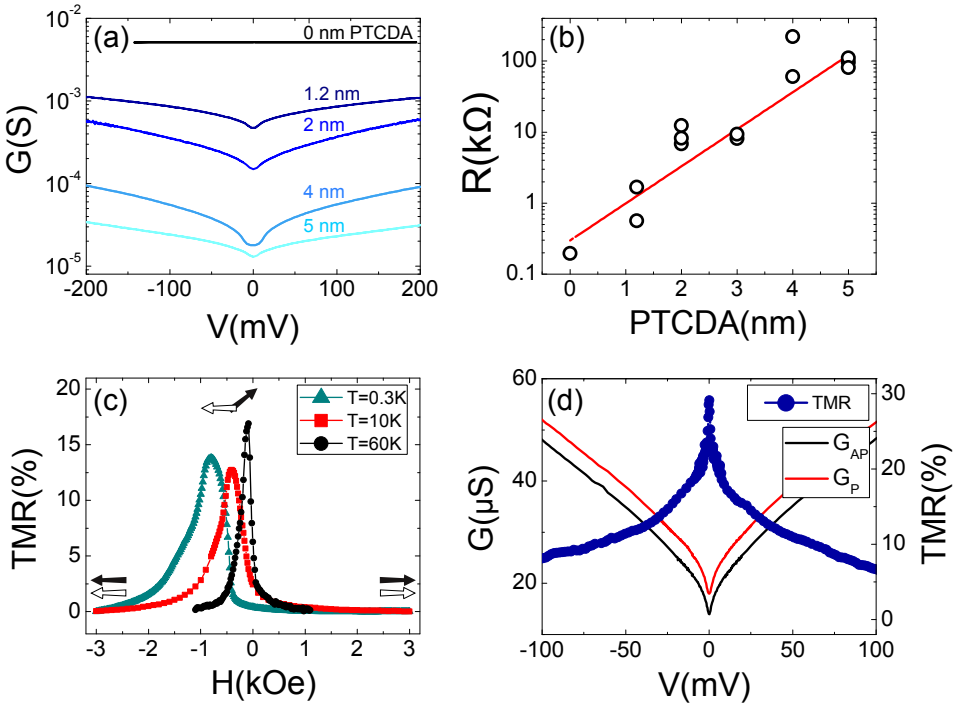

Figure 7.2: (a) Bias dependence of the differential conductance of the studied O-MTJs as a function of the PTCDA thickness. (b) Experimental dependence of the resistance on the PTCDA thickness. (c) TMR curves at different temperatures for a sample with 2nm of PTCDA. (d) Dependence of the TMR and differential conductance on the bias voltage in the P and AP states for a 4nm PTCDA O-MTJ. Figure from Ref.[241].

The conductance in our O-MTJ samples decreases exponentially with the barrier thickness. As can be seen in Fig. 7.2(a), when only the AlO_x buffer layer is grown (no PTCDA) the behaviour of the junction is metallic-like, since its resistance decreases when the temperature is lowered, while the opposite is true in general for junctions with PTCDA. As was mentioned in Section 2.7, adding an AlO_x buffer layer improves the interface between the FM electrodes and the organic layer[121]. Figure 7.2(b) plots, for all the measured samples, the exponential increase of the resistance with the PTCDA thickness. This

indicates that the insulating PTCDA layer indeed acts as a barrier in the single step tunneling regime[257]. Figure 7.2(c) shows tunneling magnetoresistance (TMR) curves for three different temperatures of a 2nm PTCDA O-MTJ, where the parallel (P) and antiparallel (AP) magnetic alignment of the electrodes are indicated by arrows. The TMR decreases with the applied bias, and is reduced considerably when the bias reaches 100 mV (see Fig. 7.2(d)). Figure 7.2(d) also shows the differential conductance in the P and AP states as a function of the bias voltage at T=0.3 K for a 4nm PTCDA O-MTJ.

To provide further proof that direct tunneling takes place, we have compared the temperature dependence of the resistance in our samples with one-dimensional ($G(T) \propto e^{-AT^{-1/2}}$) and variable range ($G(T) \propto e^{-AT^{-1/4}}$) hopping models[258], as is done in Refs.[259,260]. A is a constant related to the bulk-related inverse localization radius. Figure 7.3 presents a fit of both models to the temperature dependence of the resistance of a 2nm PTCDA O-MTJ. We have plotted $log(G(T) - G(T = 0.3K))$ (or $log(\Delta G)$) as a function of $1/T^{1/2}$ or $1/T^{1/4}$. If the data obey any of the laws, the graphs should present linear dependence of $log(\Delta G)$ for some interval of temperature. We indeed find a linear behaviour in both Figs. 7.3(a) and (b) between room temperature and 20 K. As can be seen, the variable hopping model presents a better agreement with our results. Therefore, from the dependence of the conductance with the temperature we conclude that a three-dimensional hopping transport may take place at high temperatures for around 30% of the tunneling electrons. For temperatures below 20K the transport turns into direct tunneling.

We found that the magnetic tunnel junctions with PTCDA barriers were more robust than conventional inorganic MTJs, and typically did not experience dielectrical breakdown as readily. Out of 14 samples studied, only 3 have degraded during multiple bias sweeps up to 500 mV.

7.2.2. Superpoissonian shot noise

Shot noise and transport measurements at low temperatures were carried out in the cryogenic system described in Section 3.3. The main experimental findings systematically show that the shot noise in O-MTJs is enhanced above the classic value ($F = 1$). The Fano factor was obtained as explained in Section

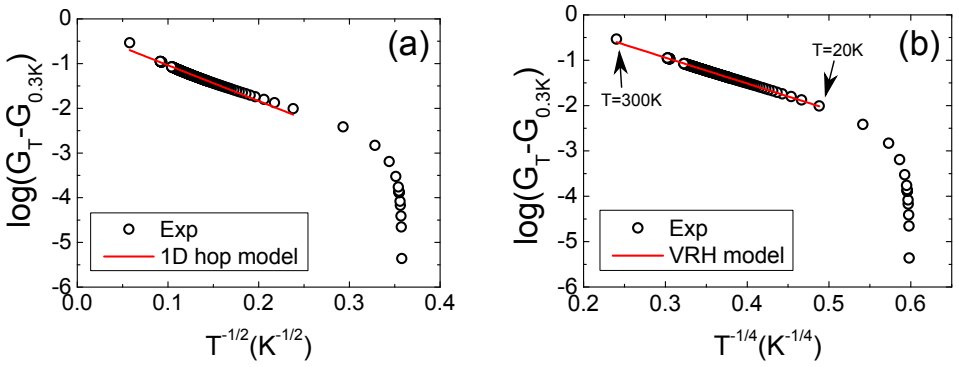

Figure 7.3: Comparison between the dependence of the resistance with the temperature in a 2nm PTCDA O-MTJ and a (a) one-dimensional and a (b) variable range hopping model. Figure from Ref.[241].

3.7.

Let us denote the Poissonian value of shot noise by S_{full} and the experimental shot noise obtained from the spectra by S_{exp}. The experimental SN and S_{full}, and the Fano factor at $T = 0.3K$ for the 2 nm PTCDA junction from Fig. 7.2(c) are shown in Figs. 7.4(a) and (b) for the P and AP states. The dependence of S_{exp} and S_{full} (Fig. 7.4(c)) and the Fano factor (Fig. 7.4(d)) with the bias is also shown for another sample with a 5 nm thick PTCDA barrier. *As can be seen, the Fano factor ranges from $F = 1$ at low voltages to $F \simeq 2$ at higher voltages*[241]*. All the O-MTJ samples measured displayed a qualitatively similar variation of the Fano factor with the bias voltage.* The shot noise could be obtained for voltages up to a few tens of mV only. The maximum voltage for which the shot noise is measured corresponds to the energy at which the $1/f$ noise becomes dominant and obscures the frequency independent part of the noise spectrum. Even though the spectra could be obtained up to 100 kHz, filtering due to the capacitance of the samples (dependent on the PTCDA thickness) allowed shot noise measurements only between 1-10 kHz. The appearance of $1/f$ noise restricted SN measurements in all the studied samples, especially in the AP state.

Figure 7.5(a) presents the average saturation value of the Fano factor in the P state of the samples for which frequency-independent spectra. Figure

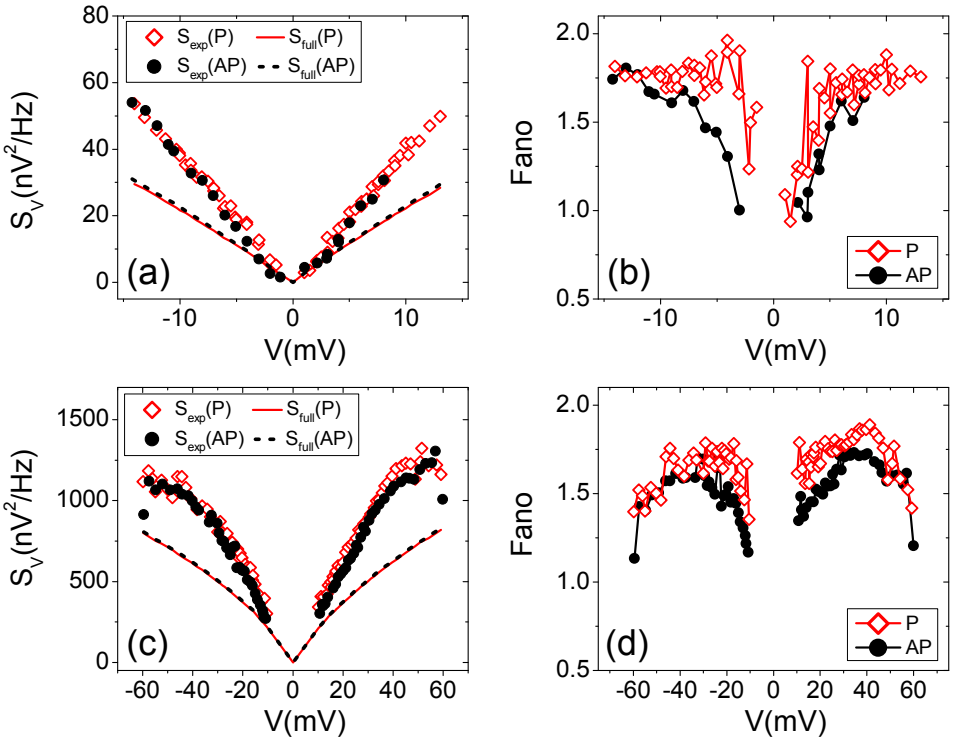

Figure 7.4: Voltage dependence of the noise at T=0.3 K in the P and AP states of the (a) experimental (dots) and expected full shot noise (lines). (b) Fano factor for a 2 nm PTCDA O-MJT. (c) and (d) present similar results for a 5 nm PTCDA O-MJT. Figure from Ref.[241].

7.5(b) also shows the variation of TMR with the PTCDA thickness. Control junctions, with only a 1.2nm AlO_x layer and no PTCDA show TMR values below 1%, and a metallic-like electron transport. (Fig. 7.2(a)). This points to diffusive electron transport, for which the theory[25] predicts the Fano factor equal to 1/3, which agrees quite well with Fig. 7.5(a). Therefore, the control measurements prove that the super-poissonian SN observed in the samples is due to the PTCDA barriers. Our O-MTJs with PTCDA between 1.2 and 5 nm show relatively high TMR and super-poissonian tunneling statistics with the Fano factor approaching 2, which is indicative of co-tunneling or tunneling with bunching. Eight O-MTJs of different barrier thicknesses, from three sample sets, have shown qualitatively similar SN values (Fig. 7.5(a)).

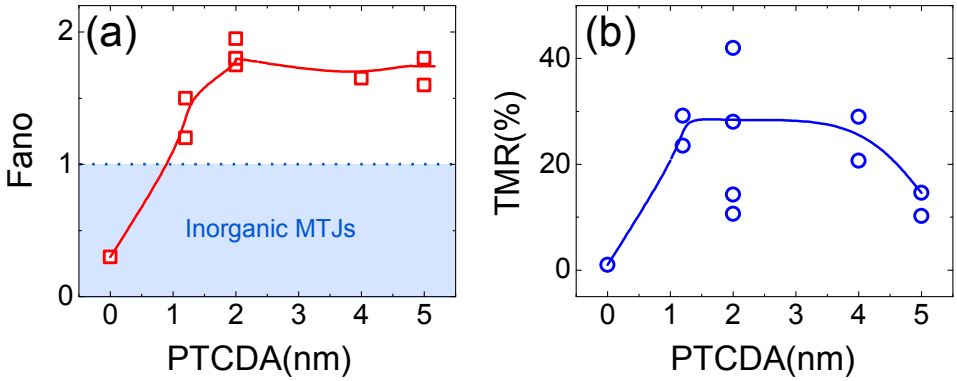

Figure 7.5: (a) Dependence of the maximum Fano factor in the P state on the PTCDA thickness at T=0.3 K. The shadowed region corresponds to the range of Fano values for MTJs with inorganic barriers. (b) Zero bias TMR at *vs.* PTCDA thickness at T=0.3 K. Figure from Ref.[241].

7.2.3. Model and discussion of the results

A number of electron tunneling mechanisms (Kondo effect[261], co-tunneling[262,263], and others[264,265]) are capable of producing super-poissonian shot noise. However, they are mostly relevant for small quantum dots. The observed SN has been accounted for in terms of the approach developed by Belzig[266], extended to include spin dependent transport.

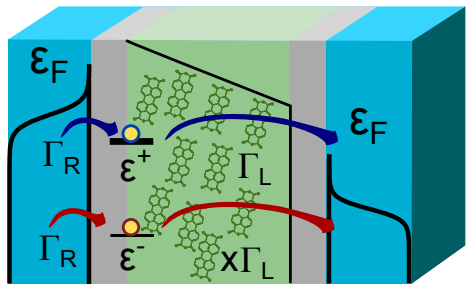

Figure 7.6: (a) Sketch of the theoretical two-level model. Electrons tunnel from one lead to another via two energy levels, leading to super-poissonian shot noise.

The following theoretical model has been developed by collaborating with

the groups of Prof. Jozef Barnaś from and Prof. Vitalii Dugaev. We show below that the observed SN could be accounted for in terms of the approach developed by Belzig[266]. The corresponding model is based on tunneling through a two-level system (or multi-level system in a more general case), with remarkably different tunneling rates through the two levels. A diagram presenting the main features of the model is shown in Fig. 7.6. Physically, the origin of these two levels with different couplings could be bonding and antibonding interface states. Thus, one level is either below the Fermi level of the drain electrode or it is weakly coupled to the electrodes, while the second level is in the tunneling window (between the Fermi levels of the source and drain electrodes) and is strongly coupled to the electrodes. Essentially, *the new feature of the model is the assumption that the coupling of the molecular level to the electrodes is spin dependent.*

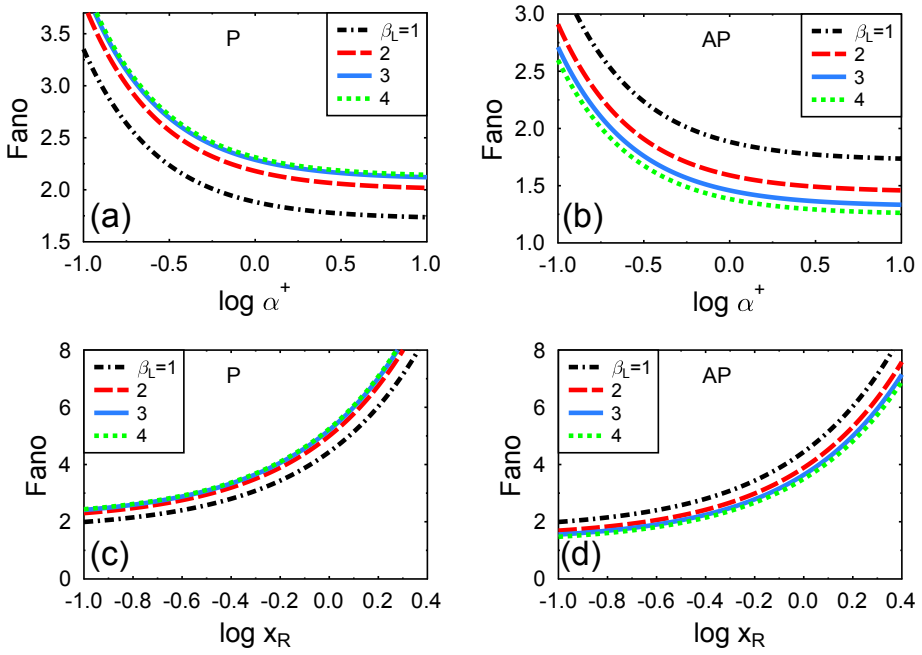

Figure 7.7: Fano factor in the P (a) and AP (b) configurations as a function of α^+ for $x_R = 0.3$, $\alpha^- = 0.2$, $\beta_R = 4$, and indicated values of β_L. The Fano factor in the P (c) and AP (d) configuration as a function of the parameter x_R for $\alpha^+ = \alpha^- = 1$, $x_L = 1$, $\beta_R = 4$, and indicated values of β_L.

7. Direct and sequential tunneling regimes through organic barriers

To describe the transport through the two-level system, the authors use the relevant master equation (expressed in matrix form) to find the probability that the molecule is occupied the upper or lower energy states. The rates in the matrix are parameterized by the bare tunneling rates $\Gamma^{\pm}_{L\sigma}$ and $\Gamma^{\pm}_{R\sigma}$ to the upper (+) and lower (−) level from left (L) and right (R), which capture the basic features of the assumed model and level positions. The temperature-dependent factor x corresponds to the tunneling from the lower level to thermally activated holes, and we assume that $x \ll 1$. Following Refs.[266,267], the noise and Fano factor are calculated using the full counting statistics method.

The following factors are introduced the factors: $\alpha^{\pm} = \Gamma^{\pm}_{R\uparrow}/\Gamma^{\pm}_{L\uparrow}$ to describe left-right asymmetry, $\beta_{L(R)} = \Gamma^{\pm}_{L(R)\uparrow}/\Gamma^{\pm}_{L(R)\downarrow}$ to describe spin asymmetry on the left and right sides (note this spin asymmetry is equal for both levels), and $x_{L(R)} = \Gamma^{+}_{L(R)\uparrow}/\Gamma^{-}_{L(R)\uparrow}$ to account for asymmetry in the bare tunneling to the two levels. In the limit of independent of spin tunneling rates, $\Gamma^{\pm}_{L\uparrow} = \Gamma^{\pm}_{L\downarrow} = \Gamma_L$ and $\Gamma^{\pm}_{R\uparrow} = \Gamma^{\pm}_{R\downarrow} = \Gamma_R$, one obtains the result of Belzig, $F = 3$. In a general case, the Fano factor depends on the parameters introduced above. The dependence of F on α^{+} for P and AP configurations is shown in Figures 7.7(a) and (b), respectively, for $\beta_R = 4$ and indicated values of β_L. Note, the Fano factor is super-poissonian, but it can vary in a relatively broad range, roughly from $F \approx 1.5$ to $F \approx 3.5$ for the assumed parameters. The dependence of the Fano factor on x_R is presented in Figures 7.7(c) and (d) for the P and AP states, for $x_L = 1$, $\beta_R = 4$ and β_L. The Fano factor strongly increases with increasing x_R and decreases when x_R becomes small, although it remains larger than 1. This is because at small values of x_R, the role of the parameter x becomes reduced.

The generating function $S(\chi)$ (a sort of partition function) can be presented as a sum of independent Poissonian processes transferring ne charge[266]. This means that the occurrence of a process with large n during one cycle is possible because tunneling to the left lead from the lower level is strongly suppressed by the temperature factor (small x) or small coupling of this level to the leads. *In other words, several electrons can be quickly transferred through the upper level till the cycle is stopped by an electron at the lower level. This leads to a super-Poissonian process, and to a Fano larger than 1.* The description can be generalized to a multilevel system.

For appropriate parameters one can find a reasonable agreement with the

experiment (Figure 7.8(b),(c)). The fit of the experimental data to the theory is done in the following way. With the experimental Fano factor in the P and AP states (obtained when the Fano factors in Fig. 7.4 saturate), and the TMR ratio of each tunnel junction, we have three conditions and three unknown parameters. We have fixed x_R, which is related to the parameter x, at $x_R = 0.3$ which seems to give the best agreement between theory and experiment. Also, we assume the spin asymmetry is the same for tunneling right and left, we set $\beta_L = \beta_R = \beta$. Thus, we have three parameters to determine from a fit between experiment and theory: α^+, α^- and β.

The parameters chosen are those that make all three functions F(P), F(AP) and TMR the closest to the experimental value. The graphs in Fig. 4 show the experimental points of F(P), F(AP) and TMR compared to the theoretical curve. For simplicity, all parameters except β were fixed in order to show a line plot and not a more complicated graph (surface plot, etc). The obtained parameters are presented in Table 7.1.

PTCDA(nm)	F_P	F_{AP}	TMR(%)	α^+	α^-	β
2nm	1.75±0.1	1.41± 0.2	29.1	0.49	0.33	2.11
2nm	1.92±0.04	1.9± 0.05	9.3	0.77	1.01	1.53
5nm	1.8±0.05	1.71± 0.03	10.2	0.92	1.01	1.57

Table 7.1: Fitting parameters obtained for the samples in Fig. 2 (a),(b) and (c) respectively.

Since the tunneling probabilities are different for spin up and down electrons, the factor F also depends on the magnetic (P and AP) configuration, which agrees with the experimental Fano and TMR values. The most important property of the model (Fig. 4(a)) is a strong asymmetry in tunneling rates through the two levels, leading to super-poissonian noise.

In Fig. 7.8 we show (a) the Fano factor and (b) the TMR in the P and AP states as a function of the parameter β, which describes the spin asymmetry in tunneling rates. The solid and dashed lines are the theoretical results, while the points correspond to the experimental data. Note, for each sample the TMR and Fano factors have been fitted with the same parameter β, which justifies validity of the approach.

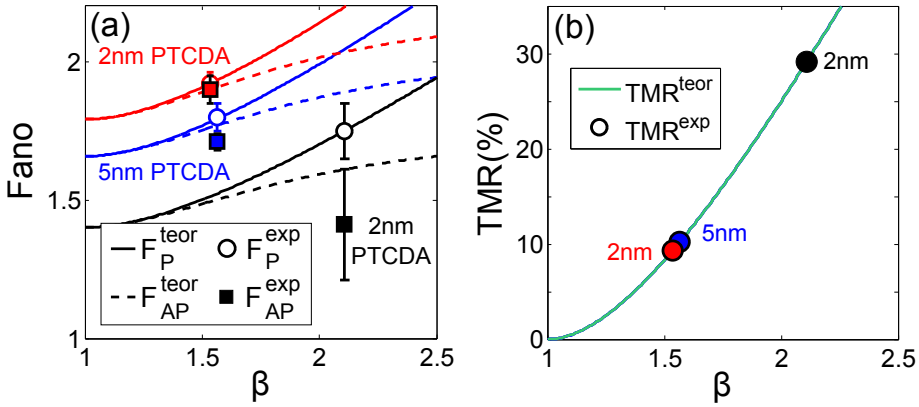

Figure 7.8: Fit of the theory to experimental values of the (a) Fano factor and (b) the TMR for the samples with 2 and 5 nm of PTCDA. The Fano points are obtained from the average saturation value in the Fano factor *vs.* bias plots, and the error bars indicate the dispersion of the average. Figure from Ref.[241].

Therefore, the model essentially accounts, qualitatively, for the experimental data (Figs. 7.4 and 7.5). In real junctions, we have a large number of molecular chains, which slightly differ from one another. Moreover, they interact with the thin AlO_x buffer layers. All this can lead to some splitting of the levels and may result in tunneling through a quasi-continuum band (multilevel system).

Physically, the two or more levels with different couplings, which are responsible for the observed superpoissonian shot noise, can have its origin in localized states arising from interfacial bonds between the PTCDA molecules and the AlO_x buffer layers. The following arguments suggest that the localized states in the model have an interfacial nature: (*i*) the exponential dependence of the tunneling resistance on PTCDA thickness (Fig. 7.2(a)) including the metallic character of the conductance when only the AlO_x buffer layer is present (see Fig. 7.2(a)); (*ii*) a lateral size of the junctions larger than a micron, for which the influence of Coulomb blockade is minimized. The physical origin of the interfacial states could be a charge neutrality level[268], or gap states[269], which appear due to the alignment of the energy levels at metal/organic interfaces[270]. The bias dependence of the interfacial density of states could explain

the suppression of the Fano factor at large voltages (Fig. 7.4(d)).

7.3. Sequential tunneling through thick organic layers

As we discussed earlier, there are a number of open questions concerning the MR responses detected in spin valve devices with organic semiconductor spacers of thicknesses well above the tunneling regime. In the previous section we concluded (thanks to shot noise measurements) that direct tunneling can take place through thin (1.2-5 nm) organic tunnel barriers, which influence the tunneling statistics so these O-MTJs present superpoissonian shot noise.

We will now go above the tunneling regime by considering the shot noise of organic spin valve devices with 200 nm thick, Alq_3 organic spacers. The study of the tunneling statistics in these devices, through shot noise measurements, will hopefully solve some of the standing questions about electronic transport mechanisms which take place in thick organic layers.

7.3.1. Growth and sample characteristics

The growth of the junctions was carried out by the group of Dr. Valentin A. Dediu from the Institute for Nanostructured Materials CNR in Bologna, which has ample experience in the growth of organic spintronic devices[117,121].

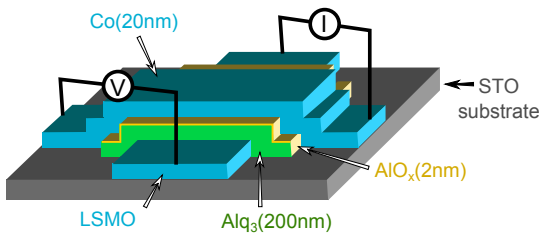

Figure 7.9: Diagram of the layered structure of an Alq_3 device.

The layer sequence of the organic spin valves with Alq_3 is:

$$La_{0.7}Sr_{0.3}MnO_3(20nm)/Alq_3(200nm)/Al_2O_3(2nm)/Co(20nm)$$

7. Direct and sequential tunneling regimes through organic barriers

The junctions with Alq_3 barriers were grown by the following procedure[271]. The bottom ferromagnetic electrode of the devices is a 20 nm thick, 1×5 mm^2 strip of $La_{0.7}Sr_{0.3}MnO_3$ (LSMO). This film is grown on a matching $SrTiO_3$ (STO) 5×10 mm^2 substrate grown by pulsed plasma deposition (PPD) in a $4 \cdot 10^{-2}$ mbar oxygen atmosphere, with the substrate kept at 880 °C. The sample is then exposed to air and moved to the organic semiconductor (OSC) deposition chamber (base pressure $2 \cdot 10^{-8}$ mbar). Before depositing the OSC layer, the is heated to 250 °C for 20 min to recover its surface properties. Afterwards, an Alq_3 layer 200 nm thick is evaporated on top of the LSMO at a rate of 0.05 $\mathring{A}/s$ at room temperature. The sample is exposed to air yet again and taken back to the PPD chamber where a 2 nm thick AlO_x tunnel barrier is deposited at an oxygen pressure of $2.5 \cdot 10^{-2}$. Lastly, the sample is exposed to air and moved to a metal deposition chamber, where a 20 nm thick Co strip is evaporated with an electron gun at a $5 \cdot 10^{-8}$ mbar base pressure.

A previous work on these junctions, carried out by Dr. Dediu's group, studied MR effects in devices with 250 nm thick Alq_3 layers, at temperatures between 100 K and 300 K[271]. The best result yielded an MR of 22% at -0.1 V and 100 K (see Fig. 7.10(a)). The authors also found that the magnetoresistance quickly decreased when the voltage was increased up to 1 V. What is perphas more surprising is the discovery of an electrical hysteresis cycle of the resistance of the sample (see Fig. 7.10(b)). The authors find that they can switch the device to a low or high resistance state increasing the voltage to a maximum positive or negative value. The MR response in the high resistance state is found to dissappear.

We began the characterization of the samples close to 100 K. Fig. 7.11(a) presents the first MR curve measured, at T=92 K. The curve does not present the clear transitions from earlier results, and it was found that the sample was in an intermediate (between low and high) resistance state, since high resistance proved to be around 30 kΩ. Figure 7.11(b) plots the first electrical hysteresis cycle tried on the sample in (a). As can be seen, the sample resistance of the sample is changed from low resistance (lower branch) to a high resistance (upper branch).

In the process of extracting shot noise results, the device was cooled down to 4 K to eliminate the influence of charge traps (appearing as random telegraph

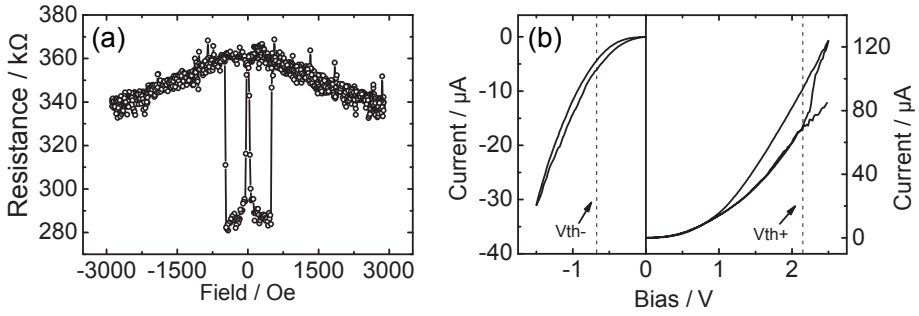

Figure 7.10: (a) MR curve of an organic spin valve with a 250 nm thick Alq_3 spacer. b) IÚV curve at 100 K showing the electrical hysteresis of the same device as in (a). Adapted from Ref.[271].

fluctuations). It was found that the critical current values needed for switching the resistance of the spin valves became increasingly higher as the temperature dropped (see Figure 7.11(b)). The MR response was also lost and not recovered afterwards, although the resistance of the sample did not degrade. Losing the MR effect at low temperatures supports the MR origin presented by Wang et al.[253] since: (*ii*) the resistance of the sample did not degrade, hence the loss of the MR response cannot be attributed to dielectrical breakdown; (*ii*) decreasing the temperature makes the ferromagnetic electrode magnetically harder, changing the size and coercive field of the magnetic domains.

7.3.2. Suppressed shot noise in the variable-range hopping regime

Let us now discuss the shot noise results obtained for our Alq_3 based spin valves. We have found that these samples with thick molecular barriers present a different type of electronic transport, as is apparent from the analysis of the Fano factor and conductance at different temperatures.

Fig.7.12(a) presents our main findings regarding shot noise in these organic spin valve devices. As can be seen, the normalized shot noise or Fano factor is subpoissonian and independent of the voltage, but is heavily influenced by the temperature. A lower temperature yields a higher Fano factor, which could mean that the transport is dominated by variable range hopping. The fact that

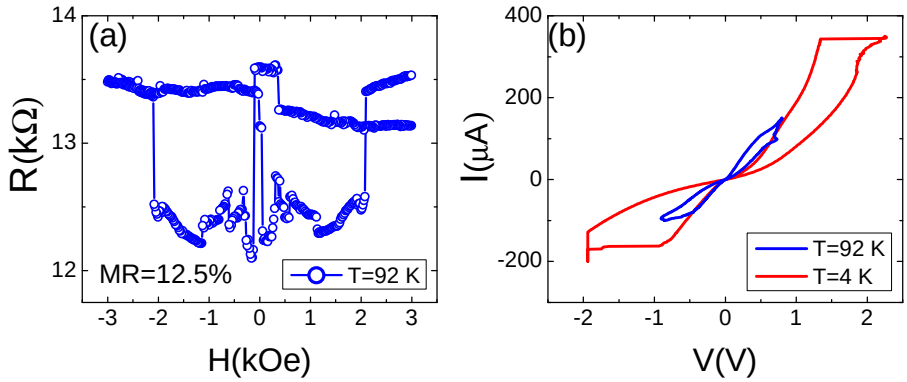

Figure 7.11: (a) MR curve of an organic spin valve with a 200 nm thick Alq_3 spacer. b) IŰV curve at 92 K and 4 K showing the electrical hysteresis of the device in (a). The switch becomes increasingly difficult as the temperature is lowered below 10K.

the shot noise is subpoissonian shows that multi-step tunneling takes place and the strong influence of the temperature agrees with the variable range hopping hypothesis, since a increase in Fano when the temperature is lowered points to an increase in the characteristic hopping length. Indeed, we show that in Fig. 7.12(b) the dependence of the conductance (minus $\sigma_{T\to 0}$) with $1/\sqrt{T}$ of a sample with a 200nm thick Alq_3 barrier, obeys the variable range hopping law $\sigma = \sigma_0 exp(-(T_0/T)^{\frac{1}{d+1}})$ for d=1 (one dimension). A diagram illustrating the temperature-dependent, multistep hopping is shown in Fig. 7.12(c).

Therefore, we conclude that the temperature dependence of the shot noise and conductance in O-MTJs with thick Alq_3 barriers (Fig.7.12) has signatures of Mott variable range hopping (VRH)[272]. It has been previously found that sequential (multistep) tunneling decreases the shot noise below poissonian values[273]. When an electron conduction through the barrier occurs by a VRH process, it has been predicted that the expected Fano F=L_0/L is not universal, with L_0 being some characteristic scaling length and L the length of the sample (which is the barrier thickness here)[273]. In the random hopping network the characterstic length L_0 represents a typical distance between the most resistive hops. If we consider L_0 to be hopping length[273] $L_0 \approx r_c \sim (\frac{1}{T})^{\frac{1}{1+d}}$, with d being the dimensionality. The Fano factor increases about 7-10 fold when the

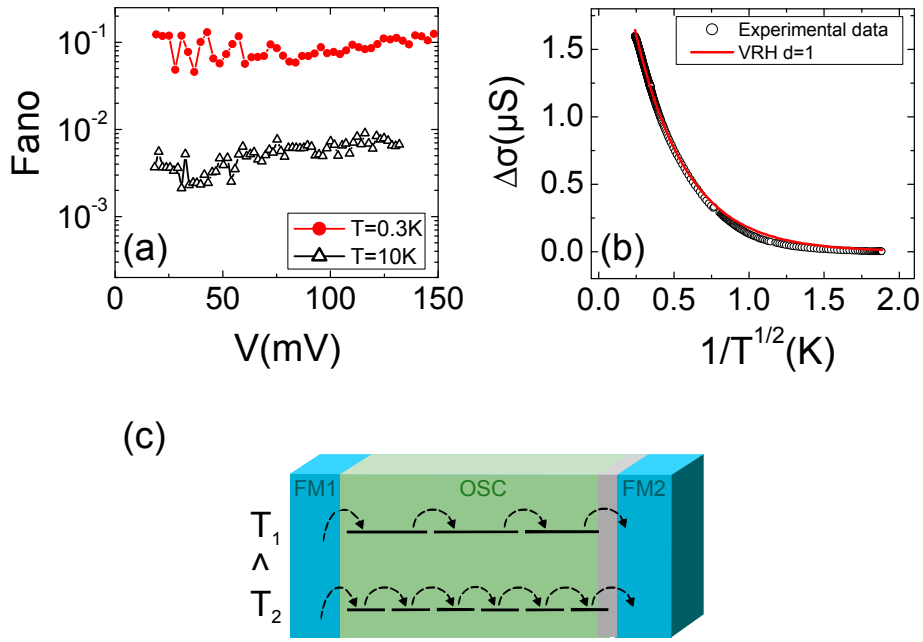

Figure 7.12: (a) The Fano factor is independent of the voltage but it decreases when the temperature is lowered. The noise is always subpoissonian ($F < 1$). (b) Dependence of the conductance with $1/\sqrt{T}$ of a sample with a 200nm thick Alq_3 barrier, fit by a variable range hopping law for d=1. (c) Schematic representation of temperature-dependent, multistep hopping through the organic barrier.

temperature decreases from 10 K to 0.3 K (Fig.7.12(a)), which points to a quasi one-dimensional VRH transport through the Alq_3 barrier at low temperatures.

7.4. Conclusions

In *conclusion*, we have investigated conductance and shot noise in magnetic tunnel junctions with organic barriers of thicknesses in two different cases: *(i)* within the tunneling regime (PTCDA barriers) and *(ii)* spin valves with organic spacers well above tunneling thicknesses (Alq_3 barriers). Organic magnetic tunnel junctions with PTCDA barriers present magnetoresistance ratios between 10% and 40%. The tunneling statistics through thin PTCDA barriers have proven to be superpoissonian, and the devices systematically present

Fano values between 1.5 and 2[241]. The superpoissonian shot noise is likely due to localized states originated from interfacial bonds of the PTCDA molecules. The experimental results are qualitatively explained by a model based on spin dependent electron tunneling through an interacting two-level system.

For a technological application, the shot noise could be reduced or controlled, for instance, by the growth of double-barrier[183] O-MTJs. Challenges for further work include extending the bias range where the shot noise could be investigated and comparing the role of the organic layers in the superpoissonian SN by the study of O-MTJs with different organic layers.

We have also addressed the long-standing, question of what the type of transport takes place through thick, organic semiconductor spacers in organic spin valves. Our spin valves with thick Alq_3 barriers present subpoissonian shot noise which depends on the temperature, which is indicative of variable range hopping. This means that the transport through these thick, organic barriers is most likely sequential tunneling, where the electrons experience a number of jumps while crossing the organic layer. The hopping length depends on the temperature, so the electrons need fewer jumps to traverse the organic spacer as the temperature is decreased.

Further studies should include samples grown in the same conditions, with different thicknesses of Alq_3, with the aim of finding a dependence of the Fano factor with the spacer thickness at a fixed temperature. This would provide additional proof that variable range hopping is the mechanism behind the transport in organic spin valves with spacers above the tunneling regime.

Chapter 8

Transport and noise in topological insulator/ferromagnet tunnel junctions

TOPOLOGICAL insulators are a novel kind of materials which are insulating in the bulk but conducting on the surface (or edge, for a 2D material). The robust surface states arise from the topology of the band structure of the material, and present a spin-polarization which is locked to the momentum. These properties make topological insulator materials interesting for spintronic applications, either as memory bits or processors. Up until now, topological insulators have been mostly studied by external characterization techniques (ARPES, STM, etc.). Electronic transport measurements through these films have also been carried out, although if their special properties are to be taken advantage of for electronic applications, their surface states should remain stable when different kind of materials are placed in contact with them. In this Chapter, we present the fabrication of tunnel junctions with a topological insulator electrode, and their characterization by electronic transport and noise measurements. This could constitute a huge step forward in the application of topological insulators as well as give information on the stability of the surface states when the materials are placed in contact with insulating, metalic or ferromagnetic materials.

8. Transport and noise in TI/FM tunnel junctions

8.1. Introduction and motivation

Let us first review the history behind *topological insulators*. As is illustratively mentioned in Ref.[274], "electrical insulators are usually appreciated for their ability to do nothing". Insulating materials trap or restrict the motion of free charges, which is useful in all kinds of applications. Insulators have an energy gap which separates the conductance and the valence bands (see Fig. 8.1(a)), so they are electrically inert because a considerable amount of energy is needed to transfer an electron from one band to another. The key idea is that electrons in an insulator can be thought to occupy localized orbitals. With this in mind, having a bulk energy gap may not mean that the material is insulating as a whole, as was found in the discovery of the Quantum Hall Effect[275] (QHE). In the QHE an energy gap appears because the electrons are localized in closed circular orbits, so the bulk of the material is insulator-like. However, at low temperature and high magnetic fields these orbits are quantized (Landau levels) and the material is not insulating at the edge, allowing motion of charge through edge states. This is intuitively explained because near the edges, the electron orbits get interrupted by the surface and the electrons tend to get bounced back into the material, and the electrons follow a motion of a series of semicircles along the edges (as shown in Fig. 8.1(b)). The edge states allow the charge to flow in one direction only, which is completely determined by the magnetic field. Because of this, these states are insensitive to scattering from impurities resulting in the exact quantization of the Hall resistance.

Even though both insulators and QHE materials have a bulk energy gap, the difference between them is a matter of topology[276]. All materials can be classified by an integer index number (a topological invariant) known as the Chern invariant. This index is constructed from the bulk electronic wave functions, in a similar way as the genus (g which counts the holes in solid bodies) is calculated in geometric topology. Regular insulators and QHE materials have different index numbers and belong to a different topological class, much the same way a sphere ($g = 0$) is topologically different from a donut ($g = 1$).

The addition of the spin-orbit interaction may give a QHE type of behavior in the absence of an external field, and this electronic phase is referred to

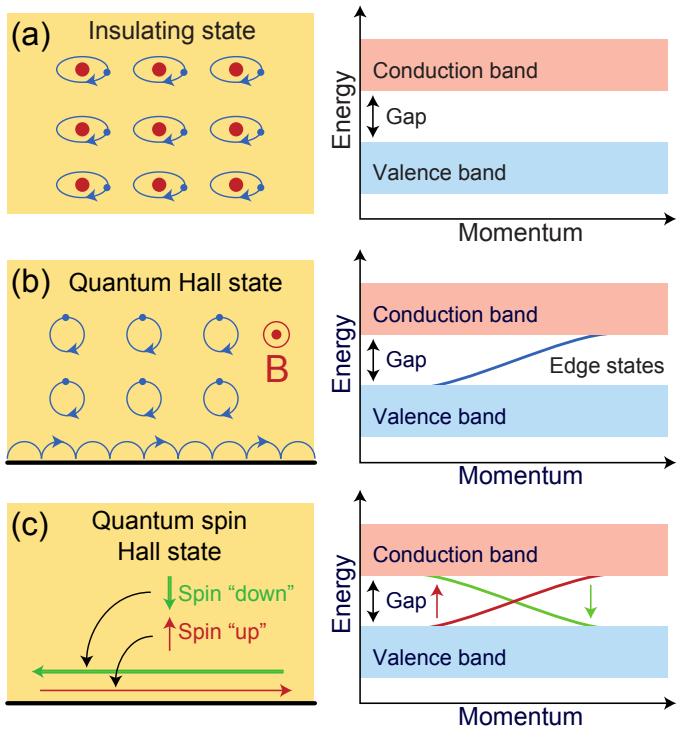

Figure 8.1: (a) Insulators present localized electrons and an energy gap between the valence band and the conduction band. (b) A 2D quantum Hall state in a strong magnetic field has an insulating bulk energy gap but allows a one-dimensional, one-way, edge electrical conduction. (c) The quantum spin Hall state or 2D topological insulator at zero magnetic field also has a bulk energy gap but allows conduction in spin-filtered edge states. Adapted from Ref.[274].

as a *topological insulator* (see Fig. 8.1(c)). A topological insulator (TI) is a material which is insulating in bulk but presents spin-dependent conducting edge or surface states which are protected by time-reversal symmetry. Having time-reversal symmetry, means that the system or process has to look the same if the flow of time is reversed.

The idea of a TI first came up when a 2D system conserving time-reversal symmetry and presenting the Quantum Spin Hall Effect (QSHE) was predicted[277]. This was followed by the prediction of 3D TIs[278]. A 2D TI is therefore analogous to a QSHE system. At the same time, the QSHE was

collaboratively predicted and detected in HgTe/CdTe quantum wells[279]. However, the experimental *boom* occurred with the prediction of Bi-based TIs[280] and their posterior experimental realization[281]. Bi_2Se_3 and Bi_2Te_3, in particular, became the prototypical TI materials that were studied most heavily. In these materials, an inversion between the conduction band and valence band occurs at the Γ point due to a strong spin-orbit interaction, which is responsible for them being in a TI phase.

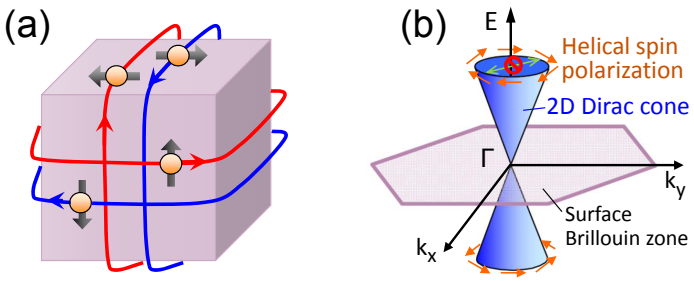

Figure 8.2: (a) Schematic real-space picture of the surface state of a 3D TI. (b) Energy dispersion of the 2D Dirac, which due to the helical spin polarization, back scattering from k to -k is prohibited. Adapted from Ref.[282].

A 2D or 3D TI presents edge or surface states which are spin-polarized in-plane, and locked at right angles to the carrier momentum, so that electrons with spin-up/down propagate in opposite directions (Fig. 8.1(c) and Fig. 8.2(a)). This spin-locking makes electron spin easy to manipulate, possibly even without the use of any magnetic fields[283]. The edge or surface states of a 3D topological insulator consist of an odd number of massless Dirac cones, with a single cone in the simplest case (see Fig. 8.2(b)). Since time-reversal flips the sign of spins 1/2, running time backwards leaves the system unchanged (each spin current still moves in the same direction) and time-reversal symmetry is conserved.

The experimental verification of the band structure of topological materials has been carried out with the use of angle-resolved photoemission spectroscopy (ARPES). This technique allows obtaining energy-momentum graphs of band dispersion, and having a probing depth of under a few nm, it is ideal for probing surface states.

The first TI surface states were observed in BiSb[284], which was followed by the observation of the surface states of Bi_2Se_3[281], which presented an excellent agreement between theory and experiment. Also, the use of spin-ARPES has allowed the determination of the spin dependence of the topological surface states[285] (see Fig. 8.3).

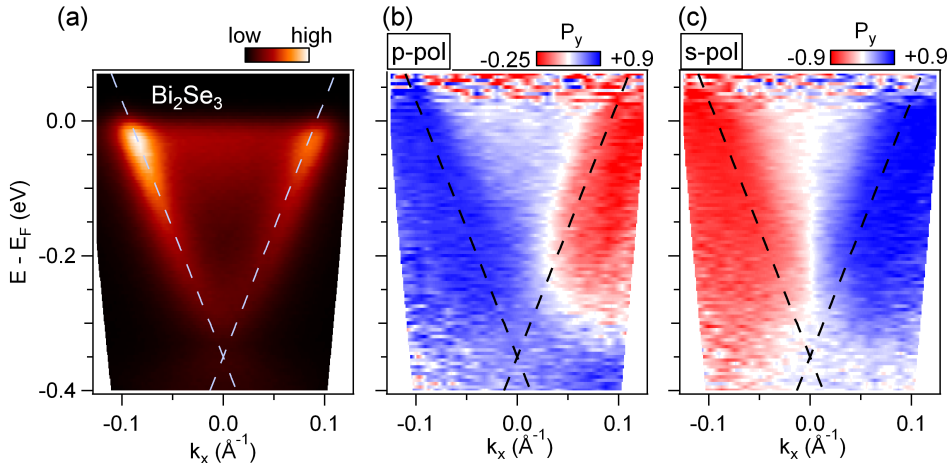

Figure 8.3: (a) Spin-integrated ARPES intensity map of Bi_2Se_3. (b),(c) Corresponding spin polarization maps taken with p and s-polarized light, respectively. Adapted from Ref.[285].

The topological insulators under discussion in this Chapter are Bi_2Te_3 and Bi_2Se_3. These materials present the crystal structure shown in Fig. 8.4. One monolayer of the crystal is composed of five alternating layers of Bi and Te or Se, referred to as a *quintuple layer* (1 QL$\simeq$ 1 nm). If thin films of such materials are grown epitaxially, ideally the film can be grown down to one quintuple layer. It has been shown that TI films of BiSb, Bi_2Se_3, Bi_2Te_3 and Sb_2Te_3 are 3D TIs down to thicknesses of 5QL below which they become 2D TIs[286,287].

We will study tunnel junctions with a TI bottom electrode of thickness well into the 3D TI range: 10 and 20 QL. The TI materials used will be Bi_2Te_3

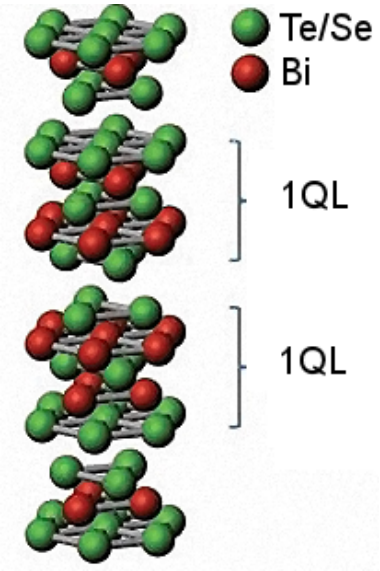

Figure 8.4: Quintuple layer sandwhich structure of Bi_2Te_3 and Bi_2Se_3 crystals. Adapted from Ref.[288]

for the 10 QL junctions and Bi_2Se_3 when the film is 20 QL thick. In Bi_2Te_3, the Dirac point of the surface states is buried in the valence band, and the Fermi energy lies within the conduction band. The band structure for a 5 QL thick Bi_2Te_3 layer obtained by ARPES[289] is shown in Fig. 8.5(a). The band structure of Bi_2Se_3 is similar, the Fermi energy also lies within the conductance band but the Dirac point is in the middle of the insulating gap at around 160 mV. The band structure for 20 QL of Bi_2Se_3[290] can be seen in Fig. 8.5(b)

The band structure of topological insulators may also be probed by *scanning tunneling microscopy* or STM. It is amusing that tunneling conductance measurements on Bi_2Te_3 and Bi_2Se_3 films showing TI surface states were measured before the notion of topological insulators ever came to be[291]. As can be seen in Fig. 8.6(a),(b) the conductance of both materials presents changes in slope of the conductance at energies related to the band structure (entering or leaving bands or surface states). A similar result was obtained years later once TIs were identified, on Bi_2Te_3 films, which shows similar behavior[292] (Fig. 8.6(c),(d)).

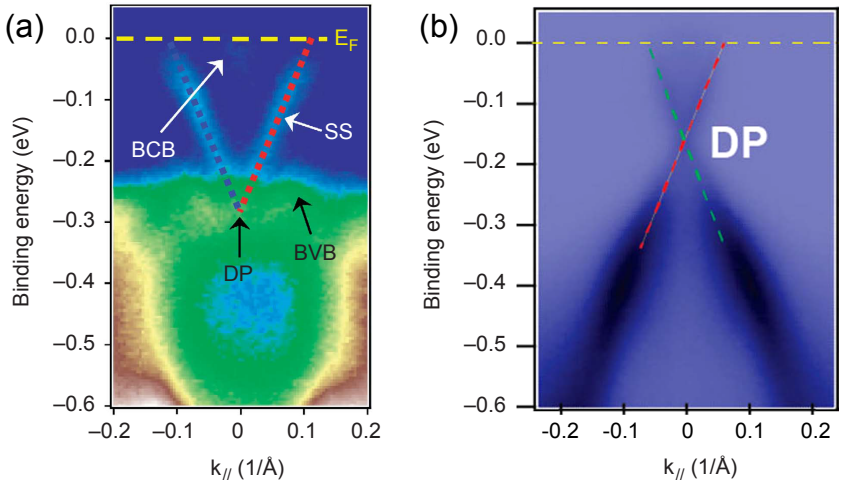

Figure 8.5: ARPES energy dispersion plot of (a) 5 QL Bi_2Te_3[289] and (b) 20 QL Bi_2Se_3[289] topological insulator films.

In Ref.[293], *pn* junctions have been fabricated using a $p-type$ topological insulator $(Bi_{1-x}Sb_x)_2Te_3$ and an $n-type$ conventional semiconductor InP. The conductance of these devices shows features correspondent to the band structure of the TI, and present an interesting alternative to growing TI tunnel junctions. The spin-momentum locking in a Bi_2Se_3 has also been probed by transport measurements[283], from the voltage that appears on ferromagnetic contacts separated from the TI by a tunnel barrier. The voltage is determined by the direction and magnitude of the charge current, found to scale inversely with the TI film thickness, and its sign is that expected from spin-momentum locking. This work constitutes the first use of spin-locking of a TI on a spintronic device. A theoretical approach of a similar system was discussed in Ref.[294].

In this Chapter we aim to show the sucessful construction of tunnel junctions with a topological insulator electrode. *Therefore, our main motivation is to obtain information about the band strucure of TIs by investigating both electron transport and low frequency noise.* The characterization of the density of states of different TI electrodes could be quite straightforwardly obtained with electronic transport and noise measurements, compared to ARPES or STM measurements. The obtained knowledge could greatly advance the practical

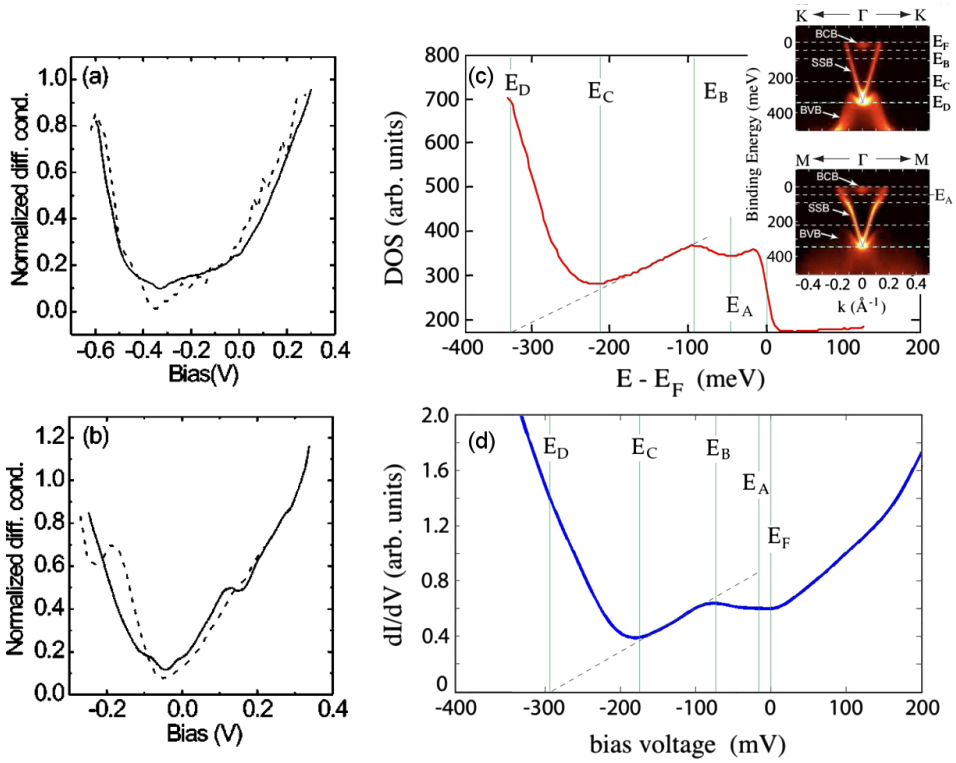

Figure 8.6: Tunneling differential conductance curves from Ref.[291] of (a) of Bi_2Se_3, acquired directly with a lock-in detection technique at a temperature of 4.2 K. (b) Same for Bi_2Te_3. Comparison of the obtained (c) DOS from ARPES and (d) the tunneling differential conductance (which is proportional to the DOS) in similar Bi_2Te_3 samples[292].

implementation of topological insulators as components in data storage well as give information on the stability of the surface states when the materials are placed in contact with insulating, metalic or ferromagnetic materials.

8.2. Growth and sample characteristics

The growth of the samples was carried out in Dr. Jaghadeesh Moodera's group, at Francis Bitter Magnet Laboratory at MIT (Cambdrige, USA) during two short stays (summers of 2013 and 2014) of the author of this thesis under the FPI programme of the Spanish MINECO. Several working junctions were

produced in under two months of attempts, with the experience of the group's postdocs: Cui-Zu Chang, Bin Li, Peng Wei and Ferhat Katmiss.

The Bi_2Te_3 and Bi_2Se_3 films were grown by Dr. Chang and Dr. Katmiss, respectively. The barrier and top electrode were fabricated by Dr. Li and Dr. Wei. Several recipes were tried, with different electrode and barrier thicknesses. The most sucessful attempt of the Bi_2Te_3 samples (summer of 2013) had the layer structure:

Si(111)//Bi_2Te_3(10QL)/Al_2O_3(5nm)+AlO_x(0.8nm)/Co(100nm)/Al_2O_3(3.8nm)

The low success rate for obtaining working junctions was explained by the roughness of the surface over which the tunnel barrier is grown (TI+capping layer). In order to improve the TI/barrier interface, the TI was changed to Bi_2Se_3, two additional measures were proposed to reduce the roughness: (*i*) using sapphire substrates and (*ii*) growing a thicker film of the TI. The Bi_2Se_3 samples fabricated during the summer of 2014 consist on:

Sapphire//Bi_2Te_3(10QL)/Al_2O_3(5nm)+AlO_x(0.7nm)/Co(100nm)/Al_2O_3(3.8nm)

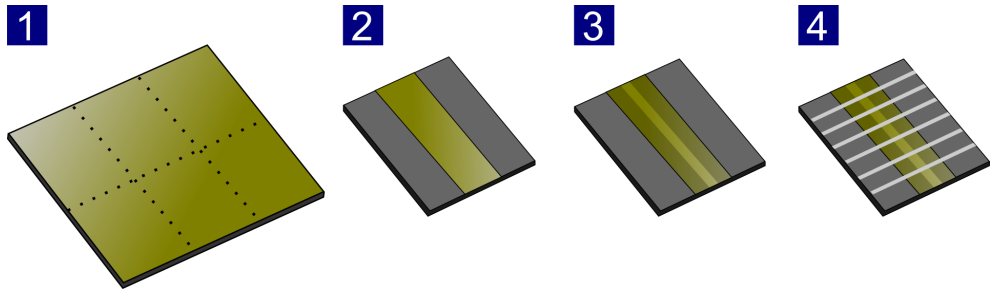

Figure 8.7: Steps for the growth: (1) MBE deposition of the TI film. (2) Partial ion milling of the TI previous to the *long strip* definition. (3) Definition of the TI long strip and deposition of an Al_2O_3 tunnel barrier. (4) Deposition of the Co cross-strips.

The growth procedure consisted on on several steps, which are shown in Fig. 8.7:

1. The TI film was deposited by MBE under UHV conditions ($P_{base} \sim 5 \cdot 10^{-10}$ torr) by two cryogenic pumps. Typically, Bi, Se and Te are evaporated from Knudsen cells. The substrate temperature is varied depending on the recipe, and is an important factor in the growth. Before exposing the TI film to air, a sputtered, 5 nm thick, capping layer of AlO_x to protect it.

2. Partial ion milling with an Ar beam of the TI film to obtain a rough *long strip*, which will serve as the bottom electrode of the junctions. The etching is carried out in 30 s intervals allowing 15 s of time for the material to cool in-between. Depending on the material, different total etching times are required.

3. The sample is then loaded into a different growth chamber, where three different layers are grown by thermal evaporation with their respective shadow-mask. First of all, a narrower TI long strip is defined by growing a 6 nm thick Al_2O_3 layer around the area which will conduct the electrical current. Afterwards, the tunnel barrier layer is fabricated by plasma-oxidizing during 30 s a 0.7/0.8 nm Al layer.

4. In the same chamber, a 10 nm Co cross-strip or top electrode is deposited. Two additional layers are evaporated as protection: a 3 nm Al_2O_3 and a 0.8 nm Al layer which oxidizes naturally. The estimated junction area is of 0.0032 cm^2.

8.3. Transport and low frequency noise measurements

We will now present the obtained experimental results on electronic transport and low frequency noise. Some initial transport measurements were carried out in Dr. Moodera's laboratory at cryogenic temperatures, to determine whether the growth had been sucessful. Several sample sets were then brought back to our group to study their transport and low frequency noise properties at low temperature. The measurements were carried out in the setup described

in Section 3.3, and the 1/f and shot noise were analyzed as explained in Section 3.7.

8.3.1. $Bi_2Te_3/Al_2O_3/Co$ tunnel junctions

As mentioned above, preliminary low temperature, transport measurements were carried out on some of the samples in this set at MIT. The junction which showed the most promising result is shown in Fig. 8.8, where (a) presents an IV curve on a 1.5 kΩ sample and (b) a differential conductance *vs.* bias curve of the same junction at 1 K. The IV curve in Fig. 8.8(a) is compared to the Brinkman model equation[295], which describes asymmetrical tunneling conductance. As can be seen, the agreement between the experimental data and the theoretical equation is quite good, and the fit yields an effective tunneling barrier thickness of around 1.6 nm. From the layer sequence of these samples, we see that there should be 5.8 nm of tunnel barrier material between the TI and Co. The effective barrier thickness of 1.6 nm points out the fact that the TI+capping surface must be quite rough, and explains why a considerable amount of junctions appear shorted (ruled out from further investigation). In Fig. 8.8(b), we see that for negative voltage, which corresponds to electrons tunneling from the TI to the Co, there are changes in the conductance which are similar to what is shown in Fig. 8.6, in particular to graph (d). The fact that our conductance curve resembles an STM result makes us guess that due to the roughness of the film, the transport is carried out through a hot-spot or localized small region with an effective barrier of 1.6 nm. As mentioned in Ref.[292], the tunneling conductance reflects the DOS at the Γ point of the TI. As can be seen in Fig. 8.8(b), we can see features in the conductance which are related to the band structure of Bi_2Te_3. The features could correspond to the energy when the cross-section of the Dirac cone becomes a warped hexagon[292] (E_{SSB}), a linear region which could correspond to transport through the surface state, and E_{VB} which could indicate reaching the valence band. Carrying out a linear fit of the supposed surface state region allows us to extrapolate an estimated energy value for the Dirac point (DP) of around 280 mV, which agrees with previous results[289,292].

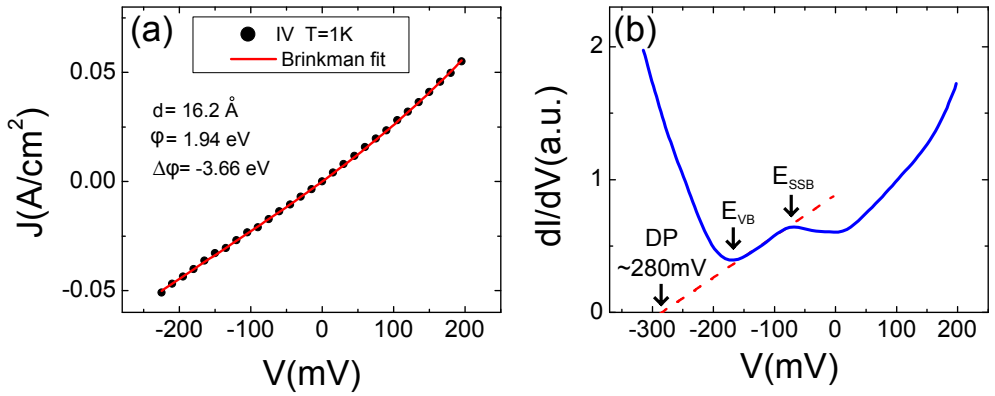

Figure 8.8: Transport measurements on a Bi_2Te_3 tunnel junction at T=1 K. (a) IV curve with a Brinkman model fit, which yields an effective barrier thickness of 1.6 nm. (b) Differential conductance of the sample sample at room temperature and 1 K.

Further measurements at our laboratory in Madrid were carried out on a 1.8 kΩ sample. As is shown in Fig. 8.9(a), an IV curve of the junction at T=0.3 K presents a good agreement with the Brinkman model[295], which yields an effective tunnel barrier of around 1.5 nm (similar to the previous sample). The conductance presents a parabolic conductance (tunnel junction-like behavior) with changes in slope at energies related to features in the DOS of the TI. The overall shape of the conductance did not change with the temperature (up to 90 K), as shown in Fig. 8.9(b), except for a zero-bias anomaly peak which was accentuated with decreasing temperature (Fig. 8.10(a)). Again, negative bias corresponds to electrons tunneling from the TI to the Co. As can be seen, several slope changes in the conductance occur at energies close to interesting energy values of the band structure of the TI. The features could correspond to E_{CB} leaving the conductance band, E_{SSB} the surface states become a warped hexagon in k-space, and finally E_{VB} entering the valence band. The features of the conductance remain up to 90 K, which could mean that the surface states are robust at least up to this temperature.

Shot noise measurements were carried out in this sample for low range of voltages. Due to the roughness of the TI/barrier interface, 1/f and random telegraph noise obscures the frequency independent part of the spectrum, so shot

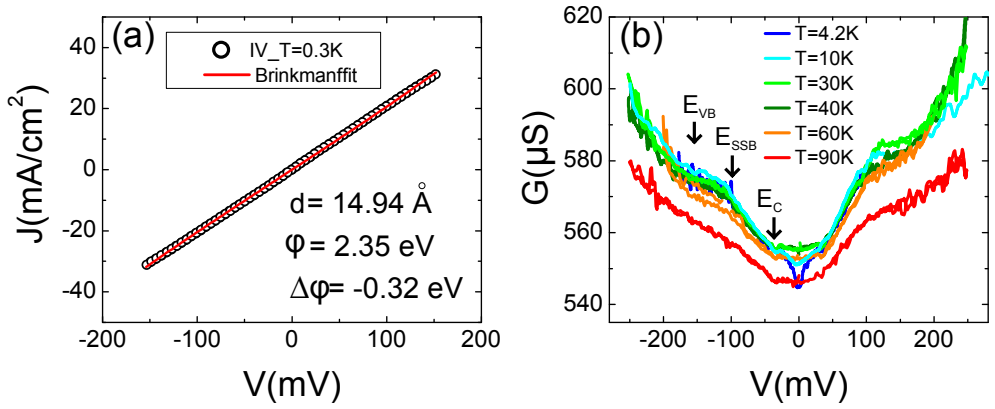

Figure 8.9: (a) IV and (b) differential conductance of a Bi_2Te_3 tunnel junction at low temperatures. The IV curve is compared to the Brinkman model. The effect of the temperature on the conductance appears as a change in the zero-bias anomaly, and changes in slope reflect the DOS of the TI.

noise could only be extracted up to ±20 mV. As can be seen in Fig. 8.10(b), at 40 K the shot noise is sub-poissonian, pointing to sequential tunneling taking place through the barrier which is consistent with having a non-homogeneous, rough interface and a sequential tunneling process. As the temperature is lowered, the shot noise increases. Since the resistance of the junction increased as it was cooled down (around 4% from 10K to 3K), the insulating behaviour may increase in the effective tunneling barrier causing the tunneling to become more direct (less probable sequential tunneling). Therefore, the more direct tunneling transport improves and the shot noise becomes less sub-poissonian. The fact that shot noise becomes superpoissonian ($Fano > 1$) at some small voltage range has yet to be understood. However, it is worth noting that the appearance when the temperature is lowered of superpoissonian shot noise seems to be correlated with the zero bias anomaly (ZBA) seen in the conductance (Fig. 8.10(a)). One could speculate on the influence of some correlation (Kondo or spin flip type) on both the ZBA and shot noise. In fact, we observed that the resistance of the junction increased around 4% between 10K and 3K, consistent with the Kondo effect (see Fig. 8.10(c)). Furthemore, the increase in resistance of the ZBA is linear when plotted *vs.* log(T), as seen in the inset of Fig. 8.10(a). The appearance of superpoissonian shot noise when the

temperature is decreased could therefore be tied to the Kondo contribution[261].

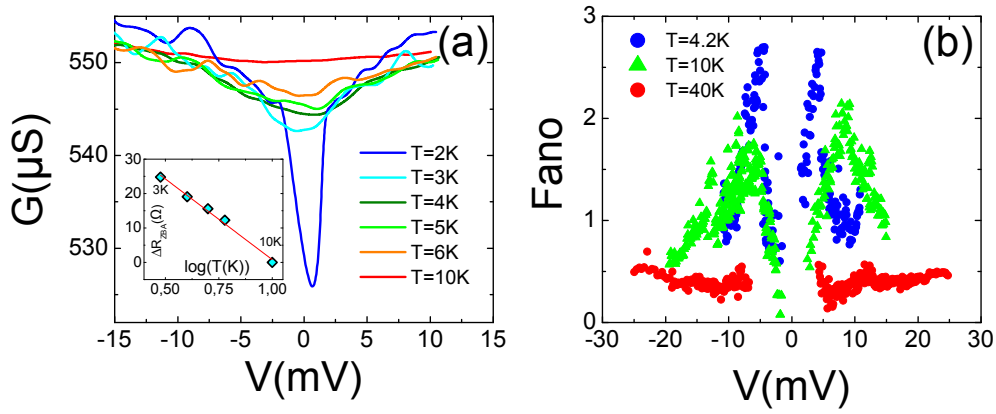

Figure 8.10: Bias dependence at different temperatures of the (a) zero-bias anomaly and the (b) shot noise for the junction in Fig. 8.9. The inset in (a) shows the resistance increase of the ZBA is linear when plotted *vs.* log(T), consistent with a Kondo-type effect.

On the other hand, the analysis of 1/f noise yields interesting results which could be interpreted using band edge spectropy method[296]. As is shown in Fig. 8.11, the Hooge parameter α presents minima and maxima at certain values of energy, which are compared to the ARPES results for Bi_2Te_3[289] as well as the changes in conductance from Fig. 8.9(b). The increase in 1/f noise usually corresponds to some excess of random telegraph noise, which appears when charging (electron trapping) effects take place in the barrier (or its interface, see Chapter 2). The fact that the features in 1/f noise occur at energies which could be related to the band structure of the TI may indicate that the opening or closing of transport channels (entering or leaving the different bands) influences the voltage fluctuations. This has been discussed in Chapter 6 where the concept of *band-edge spectroscopy*[296] was presented. The features in 1/f noise, labeled by numbers in Fig. 8.11, compare to the band structure of Bi_2Te_3 as follows: (1) may correspond to E_CB, (2) and (3) could be related to E_{SSB} when the surface state becomes warped and (4) points to an increase in fluctuations at E_{VB} related to the valence band. The temperature dependence of

one peaks (2) and (3) was tracked when we let the sample warm up from LHe[4] temperatures. As can be seen from both the conductance (Fig. 8.10(b)) and the normalized 1/f noise, the band-related features gradually dissappear when the temperature is increased. However, the position of both peaks, specially the one around -120 mV and labeled as E_{SSB} in Fig. 8.9(b), does not shift in energy when the temperature increases. This may provide an argument that (2) and (3) are related to the surface states, which have been reported to be thermally stable[297].

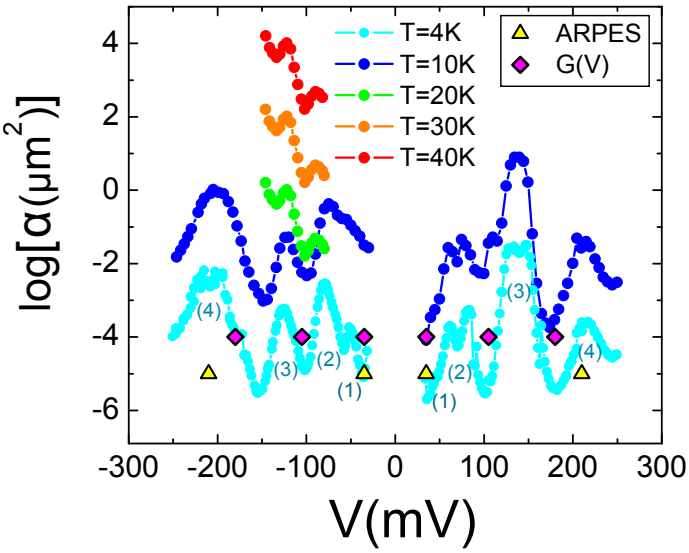

Figure 8.11: Dependence of the 1/f noise in the Bi_2Te_3 junction for different temperatures, compared to the ARPES band structure of the TI[289] and conductance features. The curves have been offset for convenience.

An external magnetic field was also applied along the direction of the Co strips, in order to look for a dependence similar to what was reported in Ref. [283]. Even though evidence of transport through the TI surface states is found, we did not observed a magnetoresistive response, which could indicate a loss of spin polarization through the amorphous Al_2O_3 barrier before reaching the Co contact.

8.3.2. $Bi_2Se_3/Al_2O_3/Co$ tunnel junctions

Let us now discuss the results obtained on two of the junctions with a thicker, 20 QL Bi_2Se_3 electrode. Similarly as the Bi_2Te_3 samples, these junctions do not show any magnetoresistive response. As can be seen from Figures 8.12(a),(c), the Brinkman fit of the IV curves of the two junctions at T=10 K yields results which are similar to what was obtained for Bi_2Te_3 samples. An effective barrier of around 1.7 nm is obtained for both barriers, which again points to a somewhat rough, TI/barrier interface, since the nominal barrier is 5.7 nm. The conductance graphs in Figs. 8.12(b), (d) is parabolic-like but does not present such sharp slope changes like the previous samples. Also, charging effects are detected, giving slightly different results each measurement, as can be seen by observing the difference in the forward (increasing current) and backward (decreasing current) branches of the IV.

Conductance measurements at T=1 K on other junctions from the set were carried out at MIT, and present a more similar scenario to the Bi_2Te_3 samples. As can be seen in Fig. 8.13(a), the conductance curves of all three junctions present slight slope changes indicated by arrows, which compare favourably to features in the ARPES band structure of Bi_2Se_3 (Fig. 8.5(b)). A ZBA anomaly can also be seen for samples #3 and #4, consistent with the Bi_2Te_3 samples. The dependence of the resistance with the temperature was studied for sample #1 (see 8.13(b)), and also presents a Kondo like dependence at low temperatures.

Extracting shot noise results from the junctions in Fig. 8.12 proved unviable since the 1/f noise and random telegraph noise completely covered the frequency independent contribution. 1/f results, shown in Fig. 8.14 for two different samples at T=10 K, presented similar features to what was obtained for previous samples. The noise peaks appear at energies which can be compared to the band structure of Bi_2Se_3. The ARPES energies for Bi_2Se_3 (Fig. 8.5(b)) of the Dirac point and the beginning of the valence band are plotted along with the 1/f data, as well as the inflection points of the conductance of samples #2 and #3 from Fig. 8.13. Therefore, let us comment on the 1/f features: (1) may

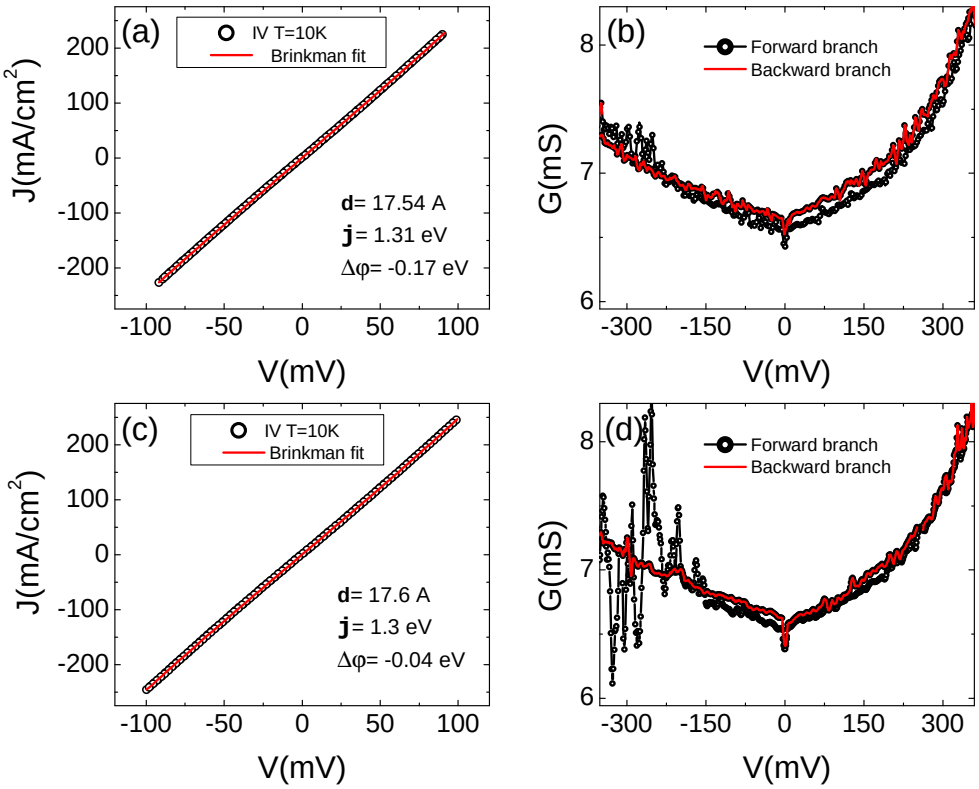

Figure 8.12: (a) IV and (b) differential conductance of a Bi_2Se_3 tunnel junction at T=10 K. The IV curve is compared to the Brinkman model. The conductance curves presents charging effects and is not reproducible in the back and forth branches of the IV.

correspond either to the conductance band edge, or (1) and (2) may be both due to the surface states as in the previous samples. (3) appears at a similar energy to the Dirac point (marked by red arrows), specially in sample #1. (4) may indicate the beginning of the valence band. The temperature dependence of the features could not be studied as before, since the junctions experience dielectrical breakdown.

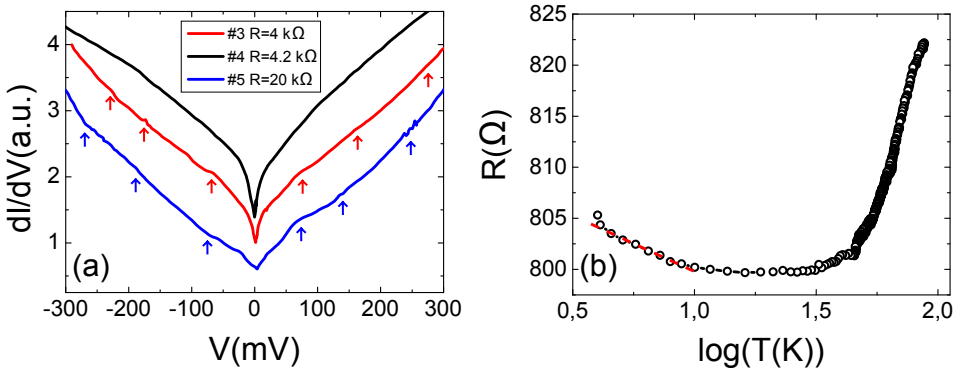

Figure 8.13: (a) Conductance measurements at T=1 K on three different $Bi_2Te_3/AlO_x/Co$ tunnel junctions. Samples #4 and #5 present conductance features at specific energies. (b) R *vs.* log(T) for sample #1, showing a Kondo like behaviour at around 10 K.

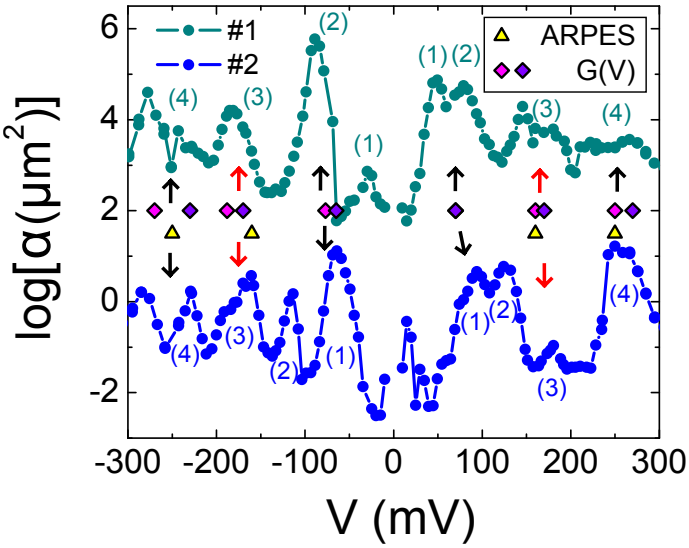

Figure 8.14: Dependence of the 1/f noise of two Bi_2Se_3 junctions at T=10K. ARPES band features of Bi_2Se_3 and inflection points of the conductance of samples #2 and #3 from Fig. 8.13 are also shown. The arrows indicate peaks which could be related to band features of the TI. Peak (3), marked with red arrows, could be consistent with the energy of the Dirac point in 20 QL Bi_2Se_3 [290]. The curves have been offset for convenience.

8.4. Conclusions

In this Chapter we have reported about the sucessful fabrication of tunnel junctions with a topological insulator bottom electrode, of which the author of this Thesis participated during two short stays at Dr. Moodera's group at MIT within the FPI programme (Spanish MINECO). Topological insulators are currently a *hot topic* of research in the branch of spintronics, because they present robust, spin-polarized surface (or edge) states which could give rise to low power electronics. The characterization of the properties of these materials has so far mainly been carried out by ARPES or other cumbersome external techniques.

We have demonstrated that features related to the band structure of these materials in contact with ferromagnetic layers through an Al_2O_3 barrier could be experimenatlly detected through electronic transport measurements, as well as through low frequency noise measurements. Since no lithography and only shadow-masks were used in the growth procedure, we conclude that under the right conditions, TI films can be electrically contacted and included into electronical devices quite straightforwardly. Obtaining reliable, topological insulator tunnel junctions could simplify the study of the properties of such materials as well as pave the way for the manipulation of their spin-polarized properties for technological purposes. Future measurements will deal with TI films in the 2D limit, with the aim of exploiting the spin polarized edge states for spintronic applications. Also, crystalline barriers such as MgO could improve the interface, and allow the probing of the spin-filtered surface states.

8. Transport and noise in TI/FM tunnel junctions

General conclusions

To conclude, this thesis has reported on electron transport and voltage fluctuation *voltage noise*) measurements in magnetic tunnel junctions of varied configurations and materials relevant for several branches of research in spintronics. The measurements were carried out at cryogenic and room temperatures, for two ranges of frequency: low (up to 100 kHz) and high (up to 18 GHz) frequency.

The existing cryogenic set-up has been improved and almost fully automatized, with modifications such as the inclusion of superconducting shunts in the 3D magnet. A new, room-temperature, noise measurement setup in the GHz range has also been built. New data analysis procedures have been programmed to improve the estimated quantitites. The main experimental results and conclusiones in this manuscript are:

1. In MTJs of sizes under 100 nm, which are promising basic elements of magnetic random accesss memories, we have ***(i)*** detected and characterized spin-transfer torque related effects through studies of low frequency noise. ***(ii)*** We have also estimated the fluctuating magnetic moment, due to barrier inhomogeneities which is involved in current-induced spin torque switching effects. This estimation indicates that around 20% of the soft electrode may contribute to the formation of a magnetic inhomogeneity which in its turn triggers spin torque switching as confirmed by micromagnetic simulations. Finally, we have ***(iii)*** correlated changes in the dynamics of the magnetization of the ferromagnetic electrodes from high frequency measurements to features in the low frequency 1/f noise measurements.

2. We have carried out the first detailed investigation of shot noise in double barrier magnetic tunnel junctions, with a variable assymetry between barriers. We have found that ***(i)*** shot noise in Fe/MgO/Fe/MgO/Fe double-barrier

magnetic tunnel junctions, with slightly different barriers, is subpoissonian and determined by the magnetic configuration of the device. ***(ii)*** We have detected the presence of quantum well states in the middle magnetic layer as oscillations in the conductance and enhanced shot noise values at certain voltages. ***(iii)*** The comparison of our data with a theoretical model based on sequential tunneling allows us to estimate the spin relaxation time in the central electrode of the junctions.

3. The method of *band edge noise spectroscopy* has been proposed, which may be used for determining the energies of electron band edges of the buried interfaces present in tunneling devices. ***(i)*** We have successfully estimated the band edge energies of the ferromagnetic electrodes in epitaxial FeV/MgO/Fe magnetic tunnel junctions with different degrees of V doping by the analysis of their low frequency noise as a function of the applied bias. The 1/f noise exhibits clear peaks at specific applied voltages, which are related to the position of the band edges of FeV. ***(ii)*** A comparison of the results with numerical calculations of the tunneling electron density of states as a function of V doping shown in qualitative agreement with the experiment.

4. The investigation of the conductance and shot noise in magnetic tunnel junctions with organic barriers has been studied in spin valve devices within the tunneling regime (PTCDA barriers) and with organic spacers of thickness well above it (Alq3 barriers). ***(i)*** Our organic magnetic tunnel junctions with PTCDA barriers systematically exhibit superpoissonian tunneling statistics with Fano values between 1.5 and 2, likely due to localized states originated from interfacial bonds of the PTCDA molecules. ***(ii)*** These results are qualitatively accounted for within a model based on spin dependent electron tunneling with statistics controlled by an interacting two-level system. ***(iii)*** The longstanding question regarding the type of transport taking place through thick, organic semiconductor spacers has also been addressed. The shot noise in spin valves with thick Alq3 barriers has been found to be subpoissonian and dependent on the temperature, consistent with variable range hopping.

5. Finally, we report on the sucessful fabrication of tunnel junctions with topological insulator bottom electrodes at Dr. Moodera's laboratory at the Massachussetts Institute of Technology. The author of this Thesis participated in the growth during two short stays at Dr. Moodera's group. Preliminary

conductance and noise measurements at low temperature reveal features related to the band structure of the topological insulators.

8. General conclusions/Conclusiones generales

Conclusiones generales

En conclusión, en esta tesis se han estudiado el transporte electrónico y las fluctuaciones del voltaje (*ruido en voltaje*) en uniones túnel magnéticas de configuraciones y materiales variados, relevantes para varias ramas del ámbito de la espintrónica. Las medidas se han llevado a cabo a temperatura ambiente y a bajas temperaturas (de hasta 0.3 K), para dos rangos de frecuencia: baja frecuencia (hasta 100 kHz) y alta frecuencia (hasta 18 GHz).

El sistema criogénico de medida se ha mejorado y automatizado prácticamente en su totalidad. Por ejemplo, se han incluido interruptores superconductores (*superconducting shunt*) en nuestras bobinas superconductoras. También se ha construido un nuevo sistema de medida de ruido a temperatura ambiente, en el rango de los GHz. Se ha mejorado el procedimiento de análisis de datos mediante el uso de nuevas rutinas de cálculo, con el fin de aumentar la precisión de las variables físicas estimadas. Los resultados experimentales más relevantes que se han obtenido durante el curso de esta tesis son:

1. En uniones túnel magnéticas de tamaño inferior a los 100 nm, se han ***(i)*** detectado y caracterizado cambios en la dinámica de la imanación, a frecuencias de GHz, de los electrodos ferromagnéticos causados por efectos de transferencia de espín. ***(ii)*** El aumento del ruido 1/f a baja frecuencia para ciertos valores de la corriente ha sido relacionado con los cambios en la dinámica de la imanación observados en las medidas a alta frecuencia. ***(iii)*** Además, se ha estimado el momento magnético involucrado en el cambio de estado resistivo inducido por corrientes a partir de la medida y el análisis del ruido telegráfico en muestras que presentan barreras inhomogeneas. Esta estimación indica que alrededor del 20 % del electrodo libre puede contribuir a la formación de una inhomogeneidad magnética que desencadena un cambio resistivo por *spin torque*, que a su vez

ha sido confirmado mediante simulaciones micromagnéticas .

2. El primer estudio detallado del ruido de disparo ha sido llevado a cabo en uniones túnel de doble barrera, con una asimetría variable entre barreras. Se ha encontrado que ***(i)*** en nuestras uniones túnel con barrera doble (con la estructura Fe/MgO/Fe/MgO/Fe) fabricadas epitaxialmente y con barreras ligeramente asimétricas, el ruido de disparo es subpoissoniano y está determinado por la configuración magnética del dispositivo. ***(ii)*** Además, la influencia de estados de pozo cuántico presentes en el electrodo central ha sido detectada en forma de oscilaciones en la conductancia y un aumento del ruido de disparo a ciertos valores del voltaje. ***(iii)*** Los datos experimentales han sido comparados con un modelo teórico basado en el túnel secuencial, que ha permitido estimar el tiempo de relajación de espín en el electrodo central.

3. Se ha propuesto el concepto de *band edge noise spectroscopy*, como un método para determinar las energías de los bordes de las bandas electrónicas de interfases "enterradas" de los dispositivos túnel. ***(i)*** Se han estudiado uniones túnel magnéticas con la estructura FeV/MgO/Fe y diferentes grados de dopaje de vanadio, en las cuales se han estimado con éxito las energías del borde de las bandas de los electrodos ferromagnéticos de dichos dispositivos mediante el análisis del ruido de baja frecuencia en función del voltaje aplicado. El ruido 1/f ha presentado picos claros para ciertos valores del voltaje aplicado, correspondientes con las energias de borde de la estructura de bandas de la aleación FeV. ***(ii)*** Se han comparado, con buen acuerdo cualitativo, los resultados experimentales con cálculos numéricos de la densidad de estados del hierro en función del dopaje con vanadio.

4. La conductancia y el ruido de disparo han sido estudiados en uniones túnel con barreras orgánicas delgadas dentro del régimen de túnel (barreras de PTCDA) y con espaciadores orgánicos de espesor muy por encima de él (barreras de Alq3). ***(i)*** Las uniones túnel magnéticas orgánicas con barreras de PTCDA han mostrado sistemáticamente ruido de disparo superpoissoniano, con valores del factor de Fano entre 1,5 y 2, debido muy probablemente a estados localizados originados por enlaces interfaciales de las moléculas PTCDA. ***(ii)*** Estos resultados se han justificado cualitativamente mediante un modelo teórico basado en el túnel electrónico dependiente del espín de un sistema cuya estadística viene dada por dos niveles interactuantes. ***(iii)*** También se ha abor-

dado la cuestión del tipo de transporte electrónico que tiene lugar a través de espaciadores semiconductores orgánicos de grosores de cientos de nanómetros. Se ha encontrado que el ruido de disparo en las válvulas de espín con barreras de Alq3 gruesas es subpoissoniano y depende de la temperatura. Estas propiedades son consistentes con el régimen de túnel secuencial denominado *variable range hopping*.

5. Por último, se ha detallado la fabricación con éxito de uniones túnel que incluyen un electrodo de aislante topológico, llevada a cabo en el laboratorio del Dr. Moodera en el Massachussetts Institute of Technology. El autor de esta tesis participó en el crecimiento de los dispositivos durante dos estancias cortas en el grupo del Dr. Moodera. Las medidas preliminares de conductancia y ruido a baja temperatura muestran características relacionadas con la estructura de bandas de los aislantes topológicos.

8. General conclusions/Conclusiones generales

Bibliography

[1] D. L. Graham, H. A. Ferreira, and P. P. Freitas, TRENDS in Biotechnology **22**, 455 (2004).

[2] P. Freitas, F. Cardoso, V. Martins, S. Martins, J. Loureiro, J. Amaral, R. Chaves, S. Cardoso, L. Fonseca, A. Sebastião, *et al.*, Lab on a Chip **12**, 546 (2012).

[3] L. Fu, Z. X. Cao, S. Hemour, K. Wu, D. Houssameddine, W. Lu, S. Pistorius, Y. S. Gui, and C.-M. Hu, Applied Physics Letters **101**, 232406 (2012).

[4] R. Brown and D. Mazey, or Annals of Chemistry, Mathematics, Astronomy, Natural History and General Science **4**, 161 (1828).

[5] H. B. Callen and T. A. Welton, Phys. Rev. **83**, 34 (1951).

[6] H. Nyquist, Phys. Rev. **32**, 110 (1928).

[7] G. Durin, P. Falferi, M. Cerdonio, G. A. Prodi, and S. Vitale, Journal of Applied Physics **73**, 5363 (1993).

[8] W. Thomson, Proc. Roy. Soc. London **8**, 546 (1857).

[9] G. Binasch, P. Grünberg, F. Saurenbach, and W. Zinn, Phys. Rev. B **39**, 4828 (1989).

[10] M. Baibich, J. Broto, A. Fert, F. Van Dau, F. Petroff, P. Etienne, G. Creuzet, A. Friederich, and J. Chazelas, Phys. Rev. Lett. **61**, 2472 (1988).

[11] A. Cebollada, J. Martnez, J. Gallego, J. de Miguel, R. Miranda, S. Ferrer, F. Batallán, G. Fillion, and J. Rebouillat, Phys. Rev. B **39**, 9726 (1989).

[12] D. Herranz, R. Guerrero, R. Villar, F. G. Aliev, A. C. Swaving, R. A. Duine, C. van Haesendonck, and I. Vavra, Phys. Rev. B **79**, 134423 (2009).

[13] S. Gasiorowicz, *Quantum Physics* (John Wiley & Sons, 2003).

[14] J. G. Simmons, Journal of Applied Physics **34**, 1793 (1963).

[15] M. Julliere, Physics Letters A **54**, 225 (1975).

[16] J. M. De Teresa, A. Barthélémy, A. Fert, J. P. Contour, F. Montaigne, and P. Seneor, Science **286**, 507 (1999).

[17] S. Yuasa and D. D. Djayaprawira, Journal of Physics D: Applied Physics **40**, R337 (2007).

[18] W. H. Butler, X.-G. Zhang, T. C. Schulthess, and J. M. MacLaren, Phys. Rev. B **63**, 054416 (2001).

[19] J. Mathon and A. Umerski, Phys. Rev. B **63**, 220403 (2001).

[20] S. Yuasa, T. Nagahama, A. Fukushima, Y. Suzuki, and K. Ando, Nature Materials **3**, 868 (2004).

[21] S. S. P. Parkin, C. Kaiser, A. Panchula, P. M. Rice, B. Hughes, M. Samant, and S.-H. Yang, Nature Materials **3**, 862 (2004).

[22] E. Tsymbal and I. Zutic, *Handbook of Spin Transport and Magnetism* (Taylor & Francis, 2011).

[23] J. B. Johnson, Phys. Rev. **32**, 97 (1928).

[24] R. J. Schoelkopf, P. J. Burke, A. A. Kozhevnikov, D. E. Prober, and M. J. Rooks, Phys. Rev. Lett. **78**, 3370 (1997).

[25] Y. Blanter and M. Büttiker, Physics Reports **336**, 1 (2000).

[26] R. Landauer, Phys. Rev. B **47**, 16427 (1993).

[27] L. Callegaro, American Journal of Physics **74**, 438 (2006).

[28] S. MacEachern, *Kendall's Advanced Theory Of Statistics. Vol 2B: Bayesian Inference. Anthony O'Hagan, Edward Arnold, London, 1994. No. of pages: 330. Price: č35. ISBN: 0-340-52922-9*, Vol. 16 (John Wiley and Sons, 1997) p. 1907.

[29] C. E. Carroll, *Statistical physics, Vol. 5: course of theoretical physics, : L.D. Landau and E.M. Lifshitz, 2nd rev. ed. 484 pages, New York, London, Pergamon Press, 1969.*, Vol. 291 (Elsevier Science, 1971) p. 406.

[30] M. Gupta, Phys. Rev. A **18**, 2725 (1978).

[31] M. Gupta, Proceedings of the IEEE **70**, 788 (1982).

[32] P. Dutta and P. M. Horn, Rev. Mod. Phys. **53**, 497 (1981).

[33] S. Kogan, *Electronic Noise and Fluctuations in Solids* (Cambridge University Press, 1996).

[34] F. Du Pré, Physical Review **78**, 615 (1950).

[35] A. V. D. Ziel, Physica **16**, 359 (1950).

[36] F. N. Hooge, T. G. M. Kleinpenning, and L. K. J. Vandamme, Reports on Progress in Physics **44**, 479 (1981).

[37] K. S. Ralls and R. A. Buhrman, Phys. Rev. Lett. **60**, 2434 (1988).

[38] G. A. Prodi, S. Vitale, M. Cerdonio, and P. Falferi, Journal of Applied Physics **66**, 5984 (1989).

[39] S. Vitale, R. Tommasini, M. Cerdonio, M. Bonaldi, A. Cavalleri, and G. Durin, Journal of Applied Physics **72**, 4820 (1992).

[40] H. T. Hardner, M. B. Weissman, M. B. Salamon, and S. S. P. Parkin, Phys. Rev. B **48**, 16156 (1993).

[41] R. Guerrero, F. Aliev, R. Villar, R. Ortega-Hertogs, W. Park, and J. Moodera, Journal of Physics D: Applied Physics **35**, 1761 (2002).

[42] A. Grigorenko and D. Mapps, Journal of Physics D: Applied Physics **36**, 791 (2003).

[43] E. Paperno and B.-Z. Kaplan, Magnetics, IEEE Transactions on **31**, 3161 (1995).

[44] L. Kirschenbaum, C. Rogers, S. Russek, and S. Sanders, Magnetics, IEEE Transactions on **31**, 3943 (1995).

[45] K. Hung, P.-K. Ko, C. Hu, and Y. C. Cheng, Electron Device Letters, IEEE **11**, 90 (1990).

[46] G. D. Fuchs, N. C. Emley, I. N. Krivorotov, P. M. Braganca, E. M. Ryan, S. I. Kiselev, J. C. Sankey, D. C. Ralph, R. A. Buhrman, and J. A. Katine, Applied Physics Letters **85**, 1205 (2004).

[47] J. Slonczewski, Journal of Magnetism and Magnetic Materials **159**, 0 (1996).

[48] D. Ralph and M. Stiles, Journal of Magnetism and Magnetic Materials **320**, 1190 (2008).

[49] A. Brataas, A. D. Kent, and H. Ohno, Nature Materials **11**, 372 (2012).

[50] C. Kittel, *Introduction to Solid State Physics, 8th edition* (Wiley, New York, 2004).

[51] J.-G. Zhu, Journal of Applied Physics **91**, 7273 (2002).

[52] Y. Guan, J. Z. Sun, X. Jiang, R. Moriya, L. Gao, and S. S. P. Parkin, Applied Physics Letters **95**, 082506 (2009).

[53] Y. Zhou, A. Roesler, and J.-G. Zhu, Journal of Applied Physics **91**, 7276 (2002).

[54] Z. Diao, Z. Li, S. Wang, Y. Ding, A. Panchula, E. Chen, L.-C. Wang, and Y. Huai, Journal of Physics Condensed Matter **19**, 165209 (2007).

[55] W. Gallagher and S. Parkin, IBM Journal of Research and Development **50**, 5 (2006).

[56] D. Houssameddine, S. H. Florez, J. A. Katine, J.-P. Michel, U. Ebels, D. Mauri, O. Ozatay, B. Delaet, B. Viala, L. Folks, B. D. Terris, and M.-C. Cyrille, Applied Physics Letters **93**, 022505 (2008).

[57] Z. Zeng, G. Finocchio, and H. Jiang, Nanoscale **5**, 2219 (2013).

[58] J.-V. Kim, V. Tiberkevich, and A. N. Slavin, Phys. Rev. Lett. **100**, 017207 (2008).

[59] M. Quinsat, D. Gusakova, J. F. Sierra, J. P. Michel, D. Houssameddine, B. Delaet, M.-C. Cyrille, U. Ebels, B. Dieny, L. D. Buda-Prejbeanu, J. A. Katine, D. Mauri, A. Zeltser, M. Prigent, J.-C. Nallatamby, and R. Sommet, Applied Physics Letters **97**, 182507 (2010).

[60] J. S. Moodera, L. R. Kinder, T. M. Wong, and R. Meservey, Phys. Rev. Lett. **74**, 3273 (1995).

[61] T. Miyazaki and N. Tezuka, Journal of Magnetism and Magnetic Materials **139**, 0 (1995).

[62] J. S. Moodera, J. Nassar, and G. Mathon, Annual Review of Materials Science **29**, 381 (1999).

[63] E. R. Nowak, M. B. Weissman, and S. S. P. Parkin, Applied Physics Letters **74**, 600 (1999).

[64] L. Jiang, E. Nowak, P. Scott, J. Johnson, J. Slaughter, J. Sun, and R. Dave, Phys. Rev. B **69**, 1 (2004).

[65] L. Jiang, J. F. Skovholt, E. R. Nowak, and J. M. Slaughter, in *Second International Symposium on Fluctuations and Noise* (International Society for Optics and Photonics, 2004) pp. 13–27.

[66] P. K. George, Y. Wu, R. M. White, E. Murdock, and M. Tondra, Applied Physics Letters **80**, 682 (2002).

[67] R. Guerrero, F. G. Aliev, Y. Tserkovnyak, T. S. Santos, and J. S. Moodera, Phys. Rev. Lett. **97**, 266602 (2006).

[68] Y. Nazarov and J. Struben, Phys. Rev. B **53**, 15466 (1996).

[69] S. Garzon, Y. Chen, and R. Webb, Physica E: Low-dimensional Systems and Nanostructures **40**, 133 (2007).

[70] S. S. Safonov, A. K. Savchenko, D. A. Bagrets, O. N. Jouravlev, Y. V. Nazarov, E. H. Linfield, and D. A. Ritchie, Phys. Rev. Lett. **91**, 136801 (2003).

[71] D. Wang, C. Nordman, J. Daughton, Z. Qian, and J. Fink, Magnetics, IEEE Transactions on **40**, 2269 (2004).

[72] D. Wang, C. Nordman, J. Daughton, Z. Qian, and J. Fink, Magnetics, IEEE Transactions on **40**, 2269 (2004).

[73] S. Ikeda, J. Hayakawa, Y. Ashizawa, Y. M. Lee, K. Miura, H. Hasegawa, M. Tsunoda, F. Matsukura, and H. Ohno, Applied Physics Letters **93**, 082508 (2008).

[74] C. Tiusan, F. Greullet, M. Sicot, M. Hehn, C. Bellouard, F. Montaigne, S. Andrieu, and A. Schuhl, Journal of Applied Physics **99**, 08 (2006).

[75] R. Guerrero, D. Herranz, F. G. Aliev, F. Greullet, C. Tiusan, M. Hehn, and F. Montaigne, Applied Physics Letters **91**, 132504 (2007).

[76] K. Sekiguchi, T. Arakawa, Y. Yamauchi, K. Chida, M. Yamada, H. Takahashi, D. Chiba, K. Kobayashi, and T. Ono, Applied Physics Letters **96**, 252504 (2010).

[77] T. Arakawa, K. Sekiguchi, S. Nakamura, K. Chida, Y. Nishihara, D. Chiba, K. Kobayashi, A. Fukushima, S. Yuasa, and T. Ono, Applied Physics Letters **98**, 202103 (2011).

[78] K. Liu, K. Xia, and G. E. W. Bauer, Phys. Rev. B **86**, 020408 (2012).

[79] E. R. Nowak, R. D. Merithew, M. B. Weissman, I. Bloom, and S. S. P. Parkin, Journal of Applied Physics **84**, 6195 (1998).

[80] S. Ingvarsson, G. Xiao, R. A. Wanner, P. Trouilloud, Y. Lu, W. J. Gallagher, A. Marley, K. P. Roche, and S. S. P. Parkin, Journal of Applied Physics **85**, 5270 (1999).

[81] S. Ingvarsson, G. Xiao, S. S. Parkin, W. J. Gallagher, G. Grinstein, and R. H. Koch, Phys. Rev. Lett. **85**, 3289 (2000).

[82] F. G. Aliev, R. Guerrero, D. Herranz, R. Villar, F. Greullet, C. Tiusan, and M. Hehn, Applied Physics Letters **91**, 232504 (2007).

[83] A. Gokce, E. R. Nowak, S. H. Yang, and S. S. P. Parkin, Journal of Applied Physics **99**, 8 (2006).

[84] R. Guerrero, F. G. Aliev, R. Villar, J. Hauch, M. Fraune, G. Güntherodt, K. Rott, H. Brückl, and G. Reiss, Appl. Phys. Lett. **87**, 042501 (2005).

[85] R. Guerrero, F. Aliev, R. Villar, J. Hauch, M. Fraune, G. Guntherodt, K. Rott, H. Bruckl, and G. Reiss, J. Magn. Magn. Mater. **300**, 132 (2006).

[86] D. Herranz, F. Bonell, A. Gomez-Ibarlucea, S. Andrieu, F. Montaigne, R. Villar, C. Tiusan, and F. G. Aliev, Appl. Phys. Lett. **96**, 202501 (2010).

[87] D. Herranz, R. Guerrero, J. P. Cascales, F. G. Aliev, M. Hehn, and C. Tiusan, Acta Physica Polonica A **121** (2012).

[88] G. Feng, S. Van Dijken, and J. M. D. Coey, Applied Physics Letters **89**, 162501 (2006).

[89] J. Scola, H. Polovy, C. Fermon, M. Pannetier-Lecoeur, G. Feng, K. Fahy, and J. M. D. Coey, Applied Physics Letters **90**, 252501 (2007).

[90] W. G. Wang, J. Jordan-sweet, G. X. Miao, C. Ni, A. K. Rumaiz, L. R. Shah, X. Fan, P. Parsons, R. Stearrett, E. R. Nowak, J. S. Moodera, and J. Q. Xiao, Applied Physics Letters **95**, 242501 (2009).

[91] R. Stearrett, W. G. Wang, L. R. Shah, J. Q. Xiao, and E. R. Nowak, Applied Physics Letters **97**, 243502 (2010).

[92] R. Stearrett, W. G. Wang, L. R. Shah, A. Gokce, J. Q. Xiao, and E. R. Nowak, Journal of Applied Physics **107**, 064502 (2010).

[93] D. Herranz, A. Gomez-Ibarlucea, M. Schíďfers, A. Lara, G. Reiss, and F. G. Aliev, Applied Physics Letters **99**, 062511 (2011).

[94] D. Li, J. Feng, G. Yu, H. Wei, X. Han, and J. Coey, Magnetics, IEEE Transactions on **49**, 5204 (2013).

[95] S. Ikegawa, Y. Asao, Y. Saito, S. Takahashi, T. Kai, K. Tsuchida, and H. Yoda, Japanese Journal of Applied Physics **42**, L745 (2003).

[96] A. Iovan, S. Andersson, Y. G. Naidyuk, A. Vedyaev, B. Dieny, and V. Korenivski, Nano Letters **8**, 805 (2008).

[97] S. Colis, G. Gieres, L. Bíďr, and J. Wecker, Applied Physics Letters **83**, 948 (2003).

[98] G. Feng, S. van Dijken, J. F. Feng, J. M. D. Coey, T. Leo, and D. J. Smith, Journal of Applied Physics **105**, 033916 (2009).

[99] Y. Tserkovnyak and A. Brataas, Phys. Rev. B **64**, 214402 (2001).

[100] M. Wilczynski and J. Barnaś, Journal of Magnetism and Magnetic Materials **221**, 373 (2000).

[101] J. S. Moodera, J. Nowak, L. R. Kinder, P. M. Tedrow, R. J. M. van de Veerdonk, B. A. Smits, M. van Kampen, H. J. M. Swagten, and W. J. M. de Jonge, Phys. Rev. Lett. **83**, 3029 (1999).

[102] D. Herranz, F. G. Aliev, C. Tiusan, M. Hehn, V. K. Dugaev, and J. Barnaś, Phys. Rev. Lett. **105**, 047207 (2010).

[103] A. N. Useinov, J. Kosel, N. K. Useinov, and L. R. Tagirov, Phys. Rev. B **84**, 085424 (2011).

[104] G. Q. Yu, Z. Diao, J. F. Feng, H. Kurt, X. F. Han, and J. M. D. Coey, Applied Physics Letters **98**, 112504 (2011).

[105] J. C. Cuevas and E. Scheer, *Molecular electronics: an introduction to theory and experiment*, Vol. 1 (World Scientific, 2010).

[106] W. Naber, S. Faez, and W. van der Wiel, Journal of Physics D: Applied Physics **40**, R205 (2007).

[107] V. Podzorov, E. Menard, A. Borissov, V. Kiryukhin, J. A. Rogers, and M. E. Gershenson, Phys. Rev. Lett. **93**, 086602 (2004).

[108] G. G. R. Farchioni, *Organic Electronic Materials: Conjugted Polymers and Low Molecular Weight Electronic Solids* (Springer, 2001).

[109] R. W. I. de Boer, M. E. Gershenson, A. F. Morpurgo, and V. Podzorov, physica status solidi (a) **201**, 1302 (2004).

[110] H. Klauk (Editor), *Organic Electronics: Materials, Manufacturing, and Applications* (Wiley, 2006).

[111] W. G. van der Wiel, S. De Franceschi, J. M. Elzerman, T. Fujisawa, S. Tarucha, and L. P. Kouwenhoven, Rev. Mod. Phys. **75**, 1 (2002).

[112] S. Datta, Nanotechnology **15**, S433 (2004).

[113] H. Haug and A. Jauho, *Quantum Kinetics in Transport and Optics of Semiconductors*, Springer Series in Solid-State Sciences (Springer, 2007).

[114] A. R. Rocha, V. Garcia-Suarez, S. W. Bailey, C. J. Lambert, J. Ferrer, and S. Sanvito, Nature Materials **4**, 335 (2005).

[115] J. Kalinowski, M. Cocchi, D. Virgili, P. D. Marco, and V. Fattori, Chemical Physics Letters **380**, 710 (2003).

[116] A. H. Davis and K. Bussmann, Journal of Applied Physics **93**, 7358 (2003).

[117] V. Dediu, M. Murgia, F. Matacotta, C. Taliani, and S. Barbanera, Solid State Communications **122**, 181 (2002).

[118] Z. H. Xiong, D. Wu, Z. Valy Vardeny, and J. Shi, Nature **427**, 821 (2004).

[119] S. Majumdar, R. Laiho, P. Laukkanen, I. J. Vayrynen, H. S. Majumdar, and R. Osterbacka, Applied Physics Letters **89**, 122114 (2006).

[120] J. Kumar, R. K. Singh, P. Siwach, H. Singh, R. Singh, R. Rastogi, and O. Srivastava, Solid State Communications **138**, 422 (2006).

[121] V. Dediu, L. E. Hueso, I. Bergenti, A. Riminucci, F. Borgatti, P. Graziosi, C. Newby, F. Casoli, M. P. De Jong, C. Taliani, and Y. Zhan, Phys. Rev. B **78**, 115203 (2008).

[122] H.-W. Liu, H.-J. Chang, G.-P. Li, and M. Bachman, Electron Device Letters, IEEE **30**, 346 (2009).

[123] B. Li, C.-Y. Kao, J.-W. Yoo, V. N. Prigodin, and A. J. Epstein, Advanced Materials **23**, 3382 (2011).

[124] T. S. Santos, J. S. Lee, P. Migdal, I. C. Lekshmi, B. Satpati, and J. S. Moodera, Phys. Rev. Lett. **98**, 016601 (2007).

[125] W. Xu, G. J. Szulczewski, P. LeClair, I. Navarrete, R. Schad, G. Miao, H. Guo, and A. Gupta, Applied Physics Letters **90**, 072506 (2007).

[126] G. Szulczewski, H. Tokuc, K. Oguz, and J. M. D. Coey, Applied Physics Letters **95**, 202506 (2009).

[127] T. Wen, D. Liu, C. K. Luscombe, and K. M. Krishnan, Applied Physics Letters **95**, 082509 (2009).

[128] C. Barraud, P. Seneor, R. Mattana, S. Fusil, K. Bouzehouane, C. Deranlot, P. Graziosi, L. Hueso, I. Bergenti, and V. Dediu, Nature Physics **6**, 615 (2010).

[129] A. Aviram and M. A. Ratner, Chemical Physics Letters **29**, 277 (1974).

[130] M. Reed, C. Zhou, C. Muller, T. Burgin, and J. Tour, Science **278**, 252 (1997).

[131] H. Song, Y. Kim, H. Jeong, M. A. Reed, and T. Lee, The Journal of Physical Chemistry C **114**, 20431 (2010).

[132] D. Goldhaber-Gordon, J. Göres, H. Shtrikman, D. Mahalu, U. Meirav, and M. Kastner, Nature **391**, 156 (1998).

[133] W. G. van der Wiel, S. D. Franceschi, T. Fujisawa, J. M. Elzerman, S. Tarucha, and L. P. Kouwenhoven, Science **289**, 2105 (2000).

[134] J. R. Petta, S. K. Slater, and D. C. Ralph, Phys. Rev. Lett. **93**, 136601 (2004).

[135] J. Chen, M. Reed, A. Rawlett, and J. Tour, Science **286**, 1550 (1999).

[136] K. S. Ralls, R. A. Buhrman, and R. C. Tiberio, Applied Physics Letters **55**, 2459 (1989).

[137] R. Guerrero, *Conductancia y ruido en uniones túnel Magnéticas*, Ph.D. thesis, Universidad Autónoma de Madrid, Spain (2007).

[138] D. Herranz, *Electron transport and noise in magnetic tunnel junctions with MgO barriers*, Ph.D. thesis, Universidad Autónoma de Madrid, Spain (2012).

[139] S. Petit-Watelot, *Influence du couple de transfert de spin sur les fluctuations magnétiques thermiquement activées dans les jonctions tunnel magnétiques*, Ph.D. thesis, Université Joseph Fourier (Grenoble I) (2007).

[140] L. Berger, Phys. Rev. B **54**, 9353 (1996).

[141] M. Tsoi, A. G. M. Jansen, J. Bass, W.-C. Chiang, M. Seck, V. Tsoi, and P. Wyder, Phys. Rev. Lett. **80**, 4281 (1998).

[142] J. Sun, Journal of Magnetism and Magnetic Materials **202**, 157 (1999).

[143] E. B. Myers, D. C. Ralph, J. A. Katine, R. N. Louie, and R. A. Buhrman, Science **285**, 867 (1999).

[144] J. A. Katine, F. J. Albert, R. A. Buhrman, E. B. Myers, and D. C. Ralph, Phys. Rev. Lett. **84**, 3149 (2000).

[145] D. Houssameddine, U. Ebels, B. Delaët, B. Rodmacq, I. Firastrau, F. Ponthenier, M. Brunet, C. Thirion, J.-P. Michel, L. Prejbeanu-Buda, *et al.*, Nature materials **6**, 447 (2007).

[146] G. Yu, P. Upadhyaya, Y. Fan, J. G. Alzate, W. Jiang, K. L. Wong, S. Takei, S. A. Bender, L.-T. Chang, Y. Jiang, *et al.*, Nature nanotechnology (2014).

[147] S. I. Kiselev, J. C. Sankey, I. N. Krivorotov, N. C. Emley, R. J. Schoelkopf, R. A. Buhrman, and D. C. Ralph, Nature **425**, 380 (2003).

[148] J. Xiao, A. Zangwill, and M. D. Stiles, Phys. Rev. B **72**, 014446 (2005).

[149] J. C. Sankey, Y.-T. Cui, J. Z. Sun, J. C. Slonczewski, R. A. Buhrman, and D. C. Ralph, Nature Physics **4**, 67 (2007).

[150] H. Kubota, A. Fukushima, K. Yakushiji, T. Nagahama, S. Yuasa, K. Ando, H. Maehara, Y. Nagamine, K. Tsunekawa, and D. D. Djayaprawira, Nature Physics **4**, 37 (2007).

[151] J. C. Sankey, P. M. Braganca, A. G. F. Garcia, I. N. Krivorotov, R. A. Buhrman, and D. C. Ralph, Phys. Rev. Lett. **96**, 227601 (2006).

[152] A. A. Tulapurkar, Y. Suzuki, A. Fukushima, H. Kubota, H. Maehara, K. Tsunekawa, D. D. Djayaprawira, N. Watanabe, and S. Yuasa, Nature **438**, 339 (2005).

[153] A. Helmer, S. Cornelissen, T. Devolder, J.-V. Kim, W. van Roy, L. Lagae, and C. Chappert, Phys. Rev. B **81**, 094416 (2010).

[154] J.-V. Kim, Q. Mistral, C. Chappert, V. S. Tiberkevich, and A. N. Slavin, Phys. Rev. Lett. **100**, 167201 (2008).

[155] V. Tiberkevich, A. Slavin, and J.-V. Kim, Applied Physics Letters **91**, 192506 (2007).

[156] Q. Mistral, J.-V. Kim, T. Devolder, P. Crozat, C. Chappert, J. A. Katine, M. J. Carey, and K. Ito, Applied Physics Letters **88**, 192507 (2006).

[157] S. Petit, C. Baraduc, C. Thirion, U. Ebels, Y. Liu, M. Li, P. Wang, and B. Dieny, Phys. Rev. Lett. **98**, 077203 (2007).

[158] D. Houssameddine, U. Ebels, B. Dieny, K. Garello, J.-P. Michel, B. Delaet, B. Viala, M.-C. Cyrille, J. A. Katine, and D. Mauri, Phys. Rev. Lett. **102**, 257202 (2009).

[159] D. Houssameddine, *Magnetization dynamics in spin torque microwave nano-oscillators*, Theses, Université Joseph-Fourier - Grenoble I (2009).

[160] D. V. Dimitrov, Z. Gao, X. Wang, W. Jung, X. Lou, and O. G. Heinonen, Applied Physics Letters **94**, 123110 (2009).

[161] A. Vedyayev, N. Ryzhanova, B. Dieny, and N. Strelkov, Phys. Lett. A **355**, 243 (2006).

[162] G. Finocchio, M. Carpentieri, L. Torres, G. Consolo, A. Romeo, L. Lopez-Diaz, and B. Azzerboni, Physica B: Condensed Matter **403**, 364 (2008), proceedings of the Sixth International Symposium on Hysteresis Modeling and Micromagnetics.

[163] G. Finocchio, physica status solidi (c) **5**, 2396 (2008).

[164] B. Zhong, Y. Chen, S. Garzon, T. M. Crawford, and R. A. Webb, Journal of Applied Physics **109**, 07 (2011).

[165] J.-G. Zhu, Journal of Applied Physics **97**, 10 (2005).

[166] H. Meng and J.-P. Wang, Magnetics, IEEE Transactions on **41**, 2612 (2005).

[167] G. Finocchio, G. Consolo, M. Carpentieri, A. Romeo, B. Azzerboni, L. Torres, and L. Lopez-Diaz, Applied Physics Letters **89**, 262509 (2006).

[168] T. Devolder, L. Bianchini, J.-V. Kim, P. Crozat, C. Chappert, S. Cornelissen, M. Op de Beeck, and L. Lagae, Journal of Applied Physics **106**, 103921 (2009).

[169] J.-G. Zhu and X. Zhu, Magnetics, IEEE Transactions on **40**, 182 (2004).

[170] A. Eklund, S. Bonetti, S. R. Sani, S. Majid Mohseni, J. Persson, S. Chung, S. Amir Hossein Banuazizi, E. Iacocca, M. íŰstling, J. íĚkerman, and B. Gunnar Malm, Applied Physics Letters **104**, 092405 (2014).

[171] J.-V. Kim, V. Tiberkevich, and A. N. Slavin, Phys. Rev. Lett. **100**, 017207 (2008).

[172] F. Montaigne, C. Tiusan, and M. Hehn, Journal of Applied Physics **108**, 063912 (2010).

[173] J. Alvarez-Hérault, *Magnetic memory using a thermally assisted spin polarized current writing*, Theses, Université de Grenoble (2010).

[174] A. Gokce, E. R. Nowak, S. H. Yang, and S. S. P. Parkin, Journal of Applied Physics **99**, 08 (2006).

[175] J. M. Almeida, P. Wisniowski, and P. Freitas, Magnetics, IEEE Transactions on **44**, 2569 (2008).

[176] J. P. Cascales, D. Herranz, J. L. Sambricio, U. Ebels, J. A. Katine, and F. G. Aliev, Applied Physics Letters **102**, 092404 (2013).

[177] G. Finocchio, A. Prattella, G. Consolo, L. Torres, A. Faba, E. Cardelli, and B. Azzerboni, Magnetics, IEEE Transactions on **46**, 1519 (2010).

[178] K. V. Thadani, G. Finocchio, Z.-P. Li, O. Ozatay, J. C. Sankey, I. N. Krivorotov, Y.-T. Cui, R. A. Buhrman, and D. C. Ralph, Phys. Rev. B **78**, 024409 (2008).

[179] V. K. J. Bednarík, J. Kova and P. Kollar, J. Electr. Eng. **53** (2002).

[180] M. J. Donahue, D. G. Porter, N. I. of Standards, and T. (U.S.), *OOMMF user's guide [microform] / M.J. Donahue, D.G. Porter*, version 1.0. ed. (U.S. Dept. of Commerce, Technology Administration, National Institute of Standards and Technology Gaithersburg, MD, 1999) pp. iii, 83 p. and.

[181] D. Aurelio, L. Torres, and G. Finocchio, Journal of Applied Physics **108**, 083911 (2010).

[182] F. Liu, Y. Ding, R. Kemshetti, K. Davies, P. Rana, and S. Mao, Journal of Applied Physics **105**, 07 (2009).

[183] J. P. Cascales, D. Herranz, F. G. Aliev, T. Szczepański, V. K. Dugaev, J. Barnaś, A. Duluard, M. Hehn, and C. Tiusan, Phys. Rev. Lett. **109**, 066601 (2012).

[184] T. Szczepański, V. K. Dugaev, J. Barnaś, J. P. Cascales, and F. G. Aliev, Phys. Rev. B **87**, 155406 (2013).

[185] J. P. Cascales, L. Martin, A. Dulluard, M. Hehn, C. Tiusan, T. Szczepański, V. K. Dugaev, J. Barnaś, and F. G. Aliev, IEEE Transactions on Magnetics **49**, 4347 (2013).

[186] G. Schmidt, D. Ferrand, L. W. Molenkamp, A. T. Filip, and B. J. van Wees, Phys. Rev. B **62**, R4790 (2000).

[187] A. Fert and H. Jaffrs, Phys. Rev. B **64**, 184420 (2001).

[188] A. Gokce, R. Stearrett, E. R. Nowak, and C. Nordman, Fluctuation and Noise Letters **10**, 381 (2011).

[189] T. Nozaki, N. Tezuka, and K. Inomata, Phys. Rev. Lett. **96**, 027208 (2006).

[190] Y. Wang, Z.-Y. Lu, X.-G. Zhang, and X. F. Han, Phys. Rev. Lett. **97**, 087210 (2006).

[191] C. Tiusan, F. Greullet, M. Hehn, F. Montaigne, S. Andrieu, and A. Schuhl, Journal of Physics: Condensed Matter **19**, 165201 (2007).

[192] J. Faure-Vincent, C. Tiusan, C. Bellouard, E. Popova, M. Hehn, F. Montaigne, and A. Schuhl, Phys. Rev. Lett. **89**, 107206 (2002).

[193] L. Berger, Journal of Applied Physics **93**, 7693 (2003).

[194] A. Vedyayev, N. Ryzhanova, B. Dieny, and N. Strelkov, Physics Letters A **355**, 243 (2006).

[195] I. Theodonis, A. Kalitsov, and N. Kioussis, Phys. Rev. B **76**, 224406 (2007).

[196] J. B. M. Wilczyński, R. Świrkowicz, Acta Physica Polonica A **115**, 269 (2009).

[197] M. Watanabe, J. Okabayashi, H. Toyao, T. Yamaguchi, and J. Yoshino, Appl. Phys. Lett. **92**, 082506 (2008).

[198] F. Quinlan, T. M. Fortier, H. Jiang, A. Hati, C. Nelson, Y. Fu, J. C. Campbell, and S. A. Diddams, Nature Photonics , 290Ű (2013).

[199] M. Chshiev, D. Stoeffler, A. Vedyayev, and K. Ounadjela, EPL (Europhysics Letters) **58**, 257 (2002).

[200] F. Greullet, C. Tiusan, F. Montaigne, M. Hehn, D. Halley, O. Bengone, M. Bowen, and W. Weber, Phys. Rev. Lett. **99**, 187202 (2007).

[201] G. Iannaccone, G. Lombardi, M. Macucci, and B. Pellegrini, Phys. Rev. Lett. **80**, 1054 (1998).

[202] V. Nam Do, P. Dollfus, and V. Lien Nguyen, Comput. Electron **6**, 125 (2007).

[203] S. Hershfield, J. H. Davies, P. Hyldgaard, C. J. Stanton, and J. W. Wilkins, Phys. Rev. B **47**, 1967 (1993).

[204] C. W. J. Beenakker and M. Büttiker, Phys. Rev. B **46**, 1889 (1992).

[205] G. X. Du, S. G. Wang, Q. L. Ma, Y. Wang, R. C. C. Ward, X.-G. Zhang, C. Wang, A. Kohn, and X. F. Han, Phys. Rev. B **81**, 064438 (2010).

[206] I. Žutić, J. Fabian, and S. Das Sarma, Rev. Mod. Phys. **76**, 323 (2004).

[207] G. Szulczewski, S. Sanvito, and M. Coey, Nature Materials **8**, 693 (2009).

[208] R. Guerrero, M. Pannetier-Lecoeur, C. Fermon, S. Cardoso, R. Ferreira, and P. P. Freitas, J. Appl. Phys. **105**, 113922 (2009).

[209] H. Kroemer, Rev. Mod. Phys. **73**, 783 (2001).

[210] M. Z. Hasan and C. L. Kane, Rev. Mod. Phys. **82**, 3045 (2010).

[211] T. Schlenk, M. Bianchi, M. Koleini, A. Eich, O. Pietzsch, T. O. Wehling, T. Frauenheim, A. Balatsky, J.-L. Mi, B. B. Iversen, J. Wiebe, A. A. Khajetoorians, P. Hofmann, and R. Wiesendanger, Phys. Rev. Lett. **110**, 126804 (2013).

[212] K. D. Belashchenko, J. Velev, and E. Y. Tsymbal, Phys. Rev. B **72**, 140404 (2005).

[213] L. D. Bell and W. J. Kaiser, Phys. Rev. Lett. **61**, 2368 (1988).

[214] F. Bonell, T. Hauet, S. Andrieu, F. Bertran, P. Le Fvre, L. Calmels, A. Tejeda, F. Montaigne, B. Warot-Fonrose, B. Belhadji, A. Nicolaou, and A. Taleb-Ibrahimi, Phys. Rev. Lett. **108**, 176602 (2012).

[215] R. F. Berger, C. J. Fennie, and J. B. Neaton, Phys. Rev. Lett. **107**, 146804 (2011).

[216] M. Bowen, V. Cros, F. Petroff, A. Fert, C. MartÄśÌĄnez Boubeta, J. L. Costa-Kríďmer, J. V. Anguita, A. Cebollada, F. Briones, J. M. de Teresa, L. Morellíşn, M. R. Ibarra, F. Gíijell, F. Peiríş, and A. Cornet, Applied Physics Letters **79**, 1655 (2001).

[217] J. Faure-Vincent, C. Tiusan, E. Jouguelet, F. Canet, M. Sajieddine, C. Bellouard, E. Popova, M. Hehn, F. Montaigne, and A. Schuhl, Applied Physics Letters **82**, 4507 (2003).

[218] D. A. Stewart, Nano Letters **10**, 263 (2010).

[219] P.-J. Zermatten, G. Gaudin, G. Maris, M. Miron, A. Schuhl, C. Tiusan, F. Greullet, and M. Hehn, Phys. Rev. B **78**, 033301 (2008).

[220] I. Rungger, O. Mryasov, and S. Sanvito, Phys. Rev. B **79**, 094414 (2009).

[221] T. Harada, I. Ohkubo, M. Lippmaa, Y. Sakurai, Y. Matsumoto, S. Muto, H. Koinuma, and M. Oshima, Phys. Rev. Lett. **109**, 076602 (2012).

[222] R. C. Jaklevic and J. Lambe, Phys. Rev. Lett. **17**, 1139 (1966).

[223] J. M. Teixeira, J. Ventura, J. P. Araujo, J. B. Sousa, P. Wisniowski, S. Cardoso, and P. P. Freitas, Phys. Rev. Lett. **106**, 196601 (2011).

[224] D. Wortmann, H. Ishida, and S. Blügel, Phys. Rev. B **72**, 235113 (2005).

[225] K. Nikolić and A. MacKinnon, Phys. Rev. B **50**, 11008 (1994).

[226] G. Xu, C. M. Torres, E. B. Song, J. Tang, J. Bai, X. Duan, Y. Zhang, and K. L. Wang, Nano Letters **10**, 4590 (2010).

[227] F. Bonell, S. Andrieu, F. Bertran, P. Lefevre, A. Ibrahimi, E. Snoeck, C.-V. Tiusan, and F. Montaigne, Magnetics, IEEE Transactions on **45**, 3467 (2009).

[228] F. Bonell, S. Andrieu, C. Tiusan, F. Montaigne, E. Snoeck, B. Belhadji, L. Calmels, F. Bertran, P. Le Fvre, and A. Taleb-Ibrahimi, Phys. Rev. B **82**, 092405 (2010).

[229] M. Sicot, S. Andrieu, C. Tiusan, F. Montaigne, and F. Bertran, J. Appl. Phys. **99**, 08D301 (2006).

[230] F. Bonell, A. M. Bataille, S. Andrieu, C. Tiusan, B. Kierren, G. Lengaigne, and D. Lacour, Eur. Phys. J. Appl. Phys **361**, 357 (2008).

[231] S. Fahy, A. Lindsay, H. Ouerdane, and E. P. O'Reilly, Phys. Rev. B **74**, 035203 (2006).

[232] R. Jayaraman and C. Sodini, Electron Devices, IEEE Transactions on **36**, 1773 (1989).

[233] E. Borovitskaya and M. Shur, Solid-State Electronics **45**, 1067 (2001).

[234] Y. Lu, H.-X. Yang, C. Tiusan, M. Hehn, M. Chshiev, A. Duluard, B. Kierren, G. Lengaigne, D. Lacour, C. Bellouard, and F. Montaigne, Phys. Rev. B **86**, 184420 (2012).

[235] G. Kresse and J. Hafner, Phys. Rev. B **47**, 558 (1993).

[236] G. Kresse and J. Furthmüller, Phys. Rev. B **54**, 11169 (1996).

[237] G. Kresse and J. Furthmíijller, Computational Materials Science **6**, 15 (1996).

[238] P. E. Blöchl, Phys. Rev. B **50**, 17953 (1994).

[239] G. Kresse and D. Joubert, Phys. Rev. B **59**, 1758 (1999).

[240] Y. Wang and J. P. Perdew, Phys. Rev. B **44**, 13298 (1991).

[241] J. P. Cascales, J.-Y. Hong, I. Martinez, M.-T. Lin, T. Szczepański, V. K. Dugaev, J. Barnaś, and F. G. Aliev, Applied Physics Letters **105**, (2014).

[242] T. D. Nguyen, E. Ehrenfreund, and Z. V. Vardeny, Science **337**, 204 (2012).

[243] S. Sanvito, Chemical Society Reviews **40**, 3336 (2011).

[244] J. S. Jiang, J. E. Pearson, and S. D. Bader, Phys. Rev. Lett. **106**, 156807 (2011).

[245] R. Vincent, S. Klyatskaya, M. Ruben, W. Wernsdorfer, and F. Balestro, Nature **488**, 357 (2012).

[246] N. Clément, S. Pleutin, O. Seitz, S. Lenfant, and D. Vuillaume, Phys. Rev. B **76**, 205407 (2007).

[247] A. A. Balandin, Nature Nanotechnology **8**, 549 (2013).

[248] P. Rocha, H. Gomes, L. Vandamme, D. De Leeuw, S. Meskers, and P. van de Weijer, in *Noise and Fluctuations (ICNF), 2013 22nd International Conference on* (2013) pp. 1–4.

[249] M. Tsutsui, M. Taniguchi, and T. Kawai, Nat Commun **1** (2010).

[250] J. Schaffert, M. Cottin, A. Sonntag, H. Karacuban, C. Bobisch, N. Lorente, J.-P. Gauyacq, and R. Muller, Nature Materials **12**, 223 (2012).

[251] K.-S. Li, Y.-M. Chang, S. Agilan, J.-Y. Hong, J.-C. Tai, W.-C. Chiang, K. Fukutani, P. A. Dowben, and M.-T. Lin, Phys. Rev. B **83**, 172404 (2011).

[252] H. Vinzelberg, J. Schumann, D. Elefant, R. B. Gangineni, J. Thomas, and B. Buchner, Journal of Applied Physics **103**, 093720 (2008).

[253] F. Wang, F. Macià, M. Wohlgenannt, A. D. Kent, and M. E. Flatté, Phys. Rev. X **2**, 021013 (2012).

[254] T. Tanaka, T. Arakawa, M. Maeda, K. Kobayashi, Y. Nishihara, T. Ono, T. Nozaki, A. Fukushima, and S. Yuasa, Applied Physics Letters **105**, 042405 (2014).

[255] T. L. Keevers, A. Danos, T. W. Schmidt, and D. R. McCamey, Nat. Nanotech. **8**, 886 (2013).

[256] J.-Y. Hong, K.-H. Ou Yang, B.-Y. Wang, K.-S. Li, H.-W. Shiu, C.-H. Chen, Y.-L. Chan, D.-H. Wei, F.-H. Chang, H.-J. Lin, W.-C. Chiang, and M.-T. Lin, Applied Physics Letters **104**, 083301 (2014).

[257] J. J. H. M. Schoonus, P. G. E. Lumens, W. Wagemans, J. T. Kohlhepp, P. A. Bobbert, H. J. M. Swagten, and B. Koopmans, Phys. Rev. Lett. **103**, 146601 (2009).

[258] N. Mott, Philosophical Magazine **19**, 835 (1969).

[259] J. H. Shim, K. V. Raman, Y. J. Park, T. S. Santos, G. X. Miao, B. Satpati, and J. S. Moodera, Phys. Rev. Lett. **100**, 226603 (2008).

[260] K. V. Raman, S. M. Watson, J. H. Shim, J. A. Borchers, J. Chang, and J. S. Moodera, Phys. Rev. B **80**, 195212 (2009).

[261] Y. Yamauchi, K. Sekiguchi, K. Chida, T. Arakawa, S. Nakamura, K. Kobayashi, T. Ono, T. Fujii, and R. Sakano, Phys. Rev. Lett. **106**, 176601 (2011).

[262] E. Onac, F. Balestro, B. Trauzettel, C. F. J. Lodewijk, and L. P. Kouwenhoven, Phys. Rev. Lett. **96**, 026803 (2006).

[263] Y. Okazaki, S. Sasaki, and K. Muraki, Phys. Rev. B **87**, 041302 (2013).

[264] N. Lambert, R. Aguado, and T. Brandes, Phys. Rev. B **75**, 045340 (2007).

[265] G. Kießlich, E. Schöll, T. Brandes, F. Hohls, and R. J. Haug, Phys. Rev. Lett. **99**, 206602 (2007).

[266] W. Belzig, Phys. Rev. B **71**, 161301 (2005).

[267] D. A. Bagrets and Y. V. Nazarov, Phys. Rev. B **67**, 085316 (2003).

[268] H. Vázquez, R. Oszwaldowski, P. Pou, J. Ortega, R. Pérez, F. Flores, and A. Kahn, EPL (Europhysics Letters) **65**, 802 (2004).

[269] S. Yogev, R. Matsubara, M. Nakamura, U. Zschieschang, H. Klauk, and Y. Rosenwaks, Phys. Rev. Lett. **110**, 036803 (2013).

[270] S. Braun, W. R. Salaneck, and M. Fahlman, Advanced Materials **21**, 1450 (2009).

[271] M. Prezioso, A. Riminucci, I. Bergenti, P. Graziosi, D. Brunel, and V. A. Dediu, Advanced Materials **23**, 1371 (2011).

[272] A. K. Jonscher, *Electronic processes in non-crystalline materials: By N. F. Mott and E. A. Davis, Clarendon Press: Oxford Univ. Press, Oxford, 1971 and 437 pp.* (Wiley, New York, 2004).

[273] V. V. Kuznetsov, E. E. Mendez, X. Zuo, G. L. Snider, and E. T. Croke, Phys. Rev. Lett. **85**, 397 (2000).

[274] C. L. Kane and E. J. Mele, Science **314**, 1692 (2006).

[275] K. v. Klitzing, G. Dorda, and M. Pepper, Phys. Rev. Lett. **45**, 494 (1980).

[276] D. J. Thouless, M. Kohmoto, M. P. Nightingale, and M. den Nijs, Phys. Rev. Lett. **49**, 405 (1982).

[277] C. L. Kane and E. J. Mele, Phys. Rev. Lett. **95**, 146802 (2005).

[278] L. Fu, C. L. Kane, and E. J. Mele, Phys. Rev. Lett. **98**, 106803 (2007).

[279] M. König, S. Wiedmann, C. Br´une, A. Roth, H. Buhmann, L. W. Molenkamp, X.-L. Qi, and S.-C. Zhang, Science **318**, 766 (2007).

[280] H. Zhang, C.-X. Liu, X.-L. Qi, X. Dai, Z. Fang, and S.-C. Zhang, Nature Physics **5**, 438 (2009).

[281] Y. Xia, D. Qian, D. Hsieh, L. Wray, A. Pal, H. Lin, A. Bansil, D. Grauer, Y. Hor, R. Cava, *et al.*, Nature Physics **5**, 398 (2009).

[282] Y. Ando, arXiv prOPTeprint arXiv:1304.5693 (2013).

[283] C. Li, O. vanŚt Erve, J. Robinson, Y. Liu, L. Li, and B. Jonker, Nature nanotechnology (2014).

[284] D. Hsieh, D. Qian, L. Wray, Y. Xia, Y. S. Hor, R. Cava, and M. Z. Hasan, Nature **452**, 970 (2008).

[285] C. Jozwiak, C.-H. Park, K. Gotlieb, C. Hwang, D.-H. Lee, S. G. Louie, J. D. Denlinger, C. R. Rotundu, R. J. Birgeneau, Z. Hussain, *et al.*, Nature Physics **9**, 293 (2013).

[286] C.-X. Liu, H. Zhang, B. Yan, X.-L. Qi, T. Frauenheim, X. Dai, Z. Fang, and S.-C. Zhang, Phys. Rev. B **81**, 041307 (2010).

[287] Y. Zhang, K. He, C.-Z. Chang, C.-L. Song, L.-L. Wang, X. Chen, J.-F. Jia, Z. Fang, X. Dai, W.-Y. Shan, *et al.*, Nature Physics **6**, 584 (2010).

[288] Y. L. Chen, J. G. Analytis, J.-H. Chu, Z. K. Liu, S.-K. Mo, X. L. Qi, H. J. Zhang, D. H. Lu, X. Dai, Z. Fang, S. C. Zhang, I. R. Fisher, Z. Hussain, and Z.-X. Shen, Science **325**, 178 (2009).

[289] J. Zhang, C.-Z. Chang, Z. Zhang, J. Wen, X. Feng, K. Li, M. Liu, K. He, L. Wang, X. Chen, *et al.*, Nature communications **2**, 574 (2011).

[290] Y. Zhao, C.-Z. Chang, Y. Jiang, A. DaSilva, Y. Sun, H. Wang, Y. Xing, Y. Wang, K. He, X. Ma, *et al.*, Scientific reports **3** (2013).

[291] S. Urazhdin, D. Bilc, S. D. Mahanti, S. H. Tessmer, T. Kyratsi, and M. G. Kanatzidis, Phys. Rev. B **69**, 085313 (2004).

[292] Z. Alpichshev, J. G. Analytis, J.-H. Chu, I. R. Fisher, Y. L. Chen, Z. X. Shen, A. Fang, and A. Kapitulnik, Phys. Rev. Lett. **104**, 016401 (2010).

[293] R. Yoshimi, A. Tsukazaki, K. Kikutake, J. G. Checkelsky, K. S. Takahashi, M. Kawasaki, and Y. Tokura, Nature Materials **13**, 253 (2014).

[294] T. Yokoyama and Y. Tserkovnyak, Phys. Rev. B **89**, 035408 (2014).

[295] W. Brinkman, R. Dynes, and J. Rowell, Journal of Applied Physics **41**, 1915 (1970).

[296] F. G. Aliev, J. P. Cascales, A. Hallal, M. Chshiev, and S. Andrieu, Phys. Rev. Lett. **112**, 216801 (2014).

[297] L. Zhao, H. Deng, I. Korzhovska, Z. Chen, M. Konczykowski, A. Hruban, V. Oganesyan, and L. Krusin-Elbaum, Nature Materials **13**, 580 (2014).